Scuola Internazionale Superiore di Studi Avanzati

Ph.D. Thesis

Coevolution of Supermassive Black Holes and Galaxies across cosmic times

Author:
Rossella Aversa

Supervisors:
Andrea Lapi
Luigi Danese
Paolo Salucci

A thesis submitted in fulfilment of the requirements for the degree of Doctor of Philosophy

at

SISSA

October 2015

Declaration of Authorship

I, Rossella Aversa, declare that this thesis titled 'Coevolution of Supermassive Black Holes and Galaxies across cosmic times' and the work presented in it are my own.

I confirm that:

- This work was done while in candidature for the degree of Doctor of Philosophy at SISSA.
- Where I have consulted the published work of others, this is always clearly attributed.
- Where I have quoted from the work of others, the source is always given. With the exception of such quotations, this thesis is entirely my own work.
- I have acknowledged all main sources of help.
- This thesis is mainly based on the Lapi et al. (2014) and the Aversa et al. (2015) papers.

Abstract

Understanding how supermassive black holes (SMBHs) and galaxies coevolve within their host dark matter (DM) halos is a fundamental issue in astrophysics. This thesis is aimed to shed light on this topic.

As a first step, we employ the recent wide samples of far-infrared (FIR) selected galaxies followed-up in X-rays, and of X-ray/optically selected active galactic nuclei (AGNs) followed-up in the FIR band, along with the classic data on AGN and stellar luminosity functions at redshift $z \gtrsim 1.5$, to probe different stages in the coevolution of SMBHs and their host galaxies. The results of this analysis indicate the following scenario:

(i) the star formation in the host galaxy proceeds within a heavily dust-enshrouded medium, at an almost constant rate, over a timescale $\lesssim 0.5 - 1$ Gyr, and then abruptly declines due to quasar feedback;

(ii) part of the interstellar medium loses angular momentum, reaches the circum-nuclear regions, at a rate proportional to the star formation, and is temporarily stored into a massive reservoir/proto-torus, wherefrom it can be promptly accreted;

(iii) the black hole (BH) grows by accretion in a self-regulated regime with radiative power that can slightly exceed the Eddington limit ($L/L_{\rm Edd} \lesssim 4$), particularly at the highest redshifts;

(iv) the ensuing energy feedback from massive BHs, at its maximum, exceeds the stellar one and removes the interstellar gas, thus stopping the star formation and the fueling of the reservoir;

(v) afterwards, if the gas stored in the reservoir is enough, a phase of supply-limited accretion follows, whose rate exponentially declines with a timescale of ~ 3 e-folding times.

We also discuss how the detailed properties and the specific evolution of the reservoir can be investigated via coordinated, high-resolution observations of starforming, strongly lensed galaxies in the (sub-)mm band with ALMA, and in the X-ray band with *Chandra* and the next generation of X-ray instruments.

According to the scenario described above, we further investigate the coevolution of galaxies and hosted SMBHs throughout the history of the Universe by applying a statistical, model-independent approach, based on the continuity equation and the abundance matching technique. We present analytical solutions of the continuity equation without source term, to reconstruct the SMBH mass function (BHMF) at different redshifts

from the AGN luminosity function. Such an approach includes the physically-motivated AGN lightcurves we have tested and discussed, which describe the evolution of both the Eddington ratio and the radiative efficiency from slim- to thin-disc conditions. We nicely reproduce the local estimates of the BHMF, the AGN duty cycle as a function of mass and redshift, along with the Eddington ratio function and the fraction of galaxies hosting an AGN with given Eddington ratio.

We employ the same approach to reconstruct the observed stellar mass function (SMF) at different redshifts, starting from the ultraviolet (UV) and FIR luminosity functions associated to star formation in galaxies. Our results imply that the buildup of stars and BHs in galaxies occurs via *in-situ* processes, with dry mergers playing a marginal role, at least for stellar masses $\lesssim 3 \times 10^{11}\, M_{\odot}$ and BH masses $\lesssim 10^{9}\, M_{\odot}$, where the statistical data are more secure and less biased by systematic errors.

In addition, we develop an improved abundance matching technique, to link the stellar and BH content of galaxies to the gravitationally dominant DM component. The resulting relationships constitute a testbed for galaxy evolution models, highlighting the complementary role of stellar and AGN feedback in the star formation process. They may also be operationally implemented in numerical simulations to populate DM halos, or to gauge subgrid physics. Moreover, they can be exploited to investigate the galaxy/AGN clustering as a function of redshift, stellar/BH mass, and/or luminosity. The clustering properties of BHs and galaxies are found to be in full agreement with current observations, so further validating our results from the continuity equation.

Finally, our analysis highlights that:

(i) the fraction of AGNs observed in the slim-disc regime, where anyway most of the BH mass is accreted, increases with redshift;

(ii) already at $z \gtrsim 6$, a substantial amount of dust must have formed, over timescales $\lesssim 10^{8}$ yr, in strongly starforming galaxies, making these sources well within the reach of ALMA surveys in (sub-)millimeter bands.

Contents

List of Figures

List of Tables

Abbreviations

AGN: active galactic nucleus
AGN LF: active galactic nucleus luminosity function
BH: black hole
BHMF: black hole mass function
BLR: broad line region
B/T: bulge-to-total
CDM: cold dark matter
DM: dark matter
ETG: early-type galaxy
FIR: far-infrared
FUV: far-ultraviolet
FWHM: full width at half maximum
GHMF: galactic halo mass function
HMF: halo mass function
HOD: halo occupation distibution
HON: halo occupation number
IMF: initial mass function
IR: infrared
IRX: infrared to ultraviolet emission ratio
ISM: interstellar medium
LBG: Lyman break galaxy
LF: luminosity function
MIR: mid-infrared
M/L: mass-to-light
MF: mass function
NIR: near-infrared
NUV: near-ultraviolet
PAH: polycyclic aromatic hydrocarbon
sBHAR: specific black hole accretion rate

SED: spectral energy distribution
SFH: star formation history
SFR: star formation rate
SFR-LF: star formation rate luminosity function
SLF: stellar luminosity function
SMF: stellar mass function
SMBH: supermassive black hole
SN (SNe): supernova (supernovae)
sSFR: specific star formation rate
TP-AGB star: thermally pulsing asymptotic giant branch star
QSO: quasar
UV: ultraviolet

Chapter 1

Introduction

The joint formation and the coevolution of galaxies and active galactic nuclei/quasars (AGNs/QSOs)[1] are still a major problem in astrophysics and cosmology. One of the key points has been the discovery, via kinematic and photometric observations, that the very central regions of local, early-type galaxies (ETGs) and massive bulges exhibit black holes (BHs) with masses $M_{\rm BH} \gtrsim 10^6\,M_\odot$ (Dressler 1989; Kormendy & Richstone 1995; Magorrian et al. 1998, for a recent review see Kormendy & Ho 2013).

The correlations between the central BH mass and galaxy properties, such as the mass in old stars (Kormendy & Richstone 1995; Magorrian et al. 1998; Marconi & Hunt 2003; Häring & Rix 2004; McLure & Dunlop 2004; Ferrarese & Ford 2005; Graham 2007; Sani et al. 2011; Beifiori et al. 2012; McConnell & Ma 2013; Kormendy & Ho 2013), the velocity dispersion (Ferrarese & Merritt 2000; Gebhardt et al. 2000a; Tremaine et al. 2002; Gültekin et al. 2009b; McConnell & Ma 2013; Kormendy & Ho 2013; Ho & Kim 2014), and the inner light distribution (Graham et al. 2001; Lauer et al. 2007; Graham & Driver 2007; Kormendy & Bender 2009), imply the existence of a strong tie between the formation and evolution of the supermassive BH (SMBH) and that of the old stellar population in the host galaxy (for a recent review see King 2014). This relationship is possibly imprinted by the QSO feedback (but also stellar feedback can contribute); such an idea has been proposed by Silk & Rees (1998) based on an energy argument, and by Fabian (1999) based on a momentum one, further developed by King (2003, 2005), Murray, Quataert & Thompson (2005), and recently reviewed by King & Pounds (2015).

[1] In this thesis, we will use the terms QSO and AGN without distinction. Quasars are not different from their low-luminosity counterparts, AGNs: they both represent stages of building up supermassive black holes, and they interact with the host galaxies in a self-regulated way (e.g., Silk & Rees 1998; Magorrian et al. 1998; Ferrarese & Merritt 2000; Gebhardt et al. 2000a; Kauffmann & Haehnelt 2000; Wyithe & Loeb 2002, 2003; King 2003; Di Matteo, Springel & Hernquist 2005; Croton et al. 2006; Shen et al. 2009)

The way dark matter (DM) halos and associated baryons assemble play a central role in this evolution. So far, the most popular among the models have been the *merging* and the *fast collapse* ones. Concerning the baryons, the contribution of 'wet' and 'dry' mergers, or a mixture of the two processes, have been often implemented (for a recent review see Somerville & Davé 2014). On the other hand, detailed analysis of DM halo assembly indicate a two-stage process: an early fast collapse during which the central regions rapidly reach a dynamical quasi-equilibrium, followed by a slow accretion that mainly affects the halo outskirts (e.g., Zhao et al. 2003; Wang et al. 2011a; Lapi & Cavaliere 2011). Thus, the rapid star formation episodes in the central regions during the fast collapse can be considered the leading processes in galaxy formation (e.g., Lapi et al. 2011, 2014; Cai et al. 2013). Plainly, the main difference between merging and fast collapse models relates to the amount of stars formed *in situ* (e.g., Moster, Naab & White 2013).

While $N-$body simulations of DM halo formation and evolution are nowadays quite robust (though details of their results are not yet fully understood), the outcomes of hydrodynamical simulations including star formation and central BH accretion are found to feature large variance (Scannapieco et al. 2012; Frenk & White 2012). This is expected, since most of the relevant processes involving baryons, such as cooling, gravitational instabilities, angular momentum dissipation, star formation and BH accretion, occur on spatial and temporal scales well below the current resolution.

On the other hand, observations at many wavelengths of AGNs and galaxies at different stages of their evolution have spectacularly increased in the last decade. In particular, the AGN luminosity function (LF) is rather well assessed up to $z \sim 6$, though with different uncertainties, in the X-ray (Aird et al. 2010, 2015; Fiore et al. 2012; Ueda et al. 2014; Buchner et al. 2015), ultraviolet (UV)/optical (Richards et al. 2006; Fan et al. 2006; Croom et al. 2009; Jiang et al. 2009; Willott et al. 2010b; Masters et al. 2012; Ross et al. 2012), and IR bands (Richards et al. 2006; Fu et al. 2010; Assef et al. 2011; Ross et al. 2012); these observation allow to infer the SMBH accretion rate functions at various redshifts. In addition, luminosity functions of galaxies are now available up to $z \sim 10$ in the UV (Wyder et al. 2005; Reddy & Steidel 2009; Oesch et al. 2010; Cucciati et al. 2012; Bouwens et al. 2015; Finkelstein et al. 2014; Weisz, Johnson & Conroy 2014), and up to $z \sim 4$ in the far-infrared (FIR) band (Lapi et al. 2011; Gruppioni et al. 2013; Magnelli et al. 2013); these determinations allow to estimate the star formation rates (SFRs) at various redshifts.

The distribution function of the luminosity associated to the formation of massive stars, in galaxies selected by their mid-IR (MIR) and FIR emission, shows that at $z \lesssim 4$ the number density of galaxies endowed with star formation rates $\dot{M}_\star \gtrsim 10^2\, M_\odot\ \mathrm{yr}^{-1}$

is $N(\log \dot{M}_\star) \gtrsim 10^{-3}$ Mpc^{-3}. For $\dot{M}_\star \approx 10^3\,M_\odot$ yr^{-1}, the density is still significant, $N(\log \dot{M}_\star) \gtrsim 10^{-5}$ Mpc^{-3}. The UV selection, instead, elicits galaxies forming stars at much lower rates ($\dot{M}_\star \lesssim 30\,M_\odot$ yr^{-1}) up to $z \sim 10$. The complementarity between the two selections is ascribed to the increasing amount of dust in galaxies with larger SFR (Steidel, Pettini & Adelberger 2001; Mao et al. 2007; Bouwens et al. 2013, 2014; Fan et al. 2014; Cai et al. 2014; Heinis et al. 2014). Observations at high spatial resolution of sub-mm selected, high redshift galaxies with the Submillimeter Array (SMA) and follow-ups at radio wavelengths with the Very Large Array (VLA) show that $z \lesssim 6$ galaxies exhibiting $\dot{M}_\star$ of the order of a few $10^3\,M_\odot$ yr^{-1} have a number density $N \sim 10^{-6}$ Mpc^{-3} (Barger et al. 2012, 2014), fully in agreement with the results of Lapi et al. (2011) and Gruppioni et al. (2013) based on *Herschel* (single dish) surveys. However, deep, high resolution surveys with the Atacama Large Millimeter/submillimeter Array (ALMA) at (sub-)mm wavelengths have given hints of possible source blending at fluxes $S_{870\,\mu\mathrm{m}} \gtrsim 10$ mJy (Karim et al. 2013; Ono et al. 2014).

Studies in the sub-mm band on individual galaxies show that several of these objects at high redshift exhibit $\dot{M}_\star \gtrsim 10^3\,M_\odot$ yr^{-1} concentrated on scales $\lesssim 10$ kpc (e.g., Finkelstein et al. 2014; Neri et al. 2014; Rawle et al. 2014; Riechers et al. 2014; Ikarashi et al. 2014; Simpson et al. 2014; Scoville et al. 2014). Size ranging from a few to several kpc of typical high$-z$ strongly star forming galaxies has been confirmed by observations of many gravitational lensed objects (e.g., Negrello et al. 2014). Furthermore, high spatial resolution observations around optically selected quasars put in evidence that a non negligible fraction of host galaxies exhibits $\dot{M}_\star \gtrsim 10^3\,M_\odot$ yr^{-1} (Omont et al. 2001, 2003; Carilli et al. 2001; Priddey et al. 2003; Wang et al. 2008; Bonfield et al. 2011; Mor et al. 2012).

The clustering properties of luminous sub-mm selected galaxies (Webb et al. 2003; Blain et al. 2004; Weiß et al. 2009; Hickox et al. 2012; Bianchini et al. 2015) indicate that they are hosted by large halos with masses $M_\mathrm{H} \gtrsim 10^{12}\,M_\odot$ and that the star formation timescale is $\sim 0.5 - 1$ Gyr. The same characteristic halo mass is suggested by the clustering-strength measurements of X-ray selected AGNs over the redshift range $z \approx 0 - 3$, with no strongly significant trend with obscuration or luminosity (e.g., Coil et al. 2009; Hickox et al. 2009; Cappelluti et al. 2010; Koutoulidis et al. 2013).

The statistics on the presence of AGNs along the various stages of galaxy assembling casts light on the possible reciprocal influence between star formation and BH accretion (for a recent review, see Heckman & Best 2014 and references therein), although the fine interpretation of the data is still debated. On one side, some authors suggest that star formation and BH accretion are strongly coupled via feedback processes, while others support the view that the two processes are only loosely related, and that the

final relationships among BH mass and galaxy properties are built up along the entire Hubble time, with a relevant role of dry merging processes.

From a statistical point of view, the coevolution of the host galaxies and their SMBHs could be reconstructed if the stellar mass/SFR distribution for the hosts and the BH mass/accretion rate distribution for the AGNs/QSOs at different redshifts were available. These pieces of information would provide insights at least on space- and time-averaged quantities. Progress in this respect has been tremendous in the last decade, and nowadays we have sound estimates even at substantial redshift of:

1. Luminosity functions of AGNs/QSOs in the X-ray (e.g., Fiore et al. 2012; Ueda et al. 2014; Aird et al. 2015) and in the optical bands (e.g., Richards et al. 2006; Fan et al. 2006; Croom et al. 2009; Jiang et al. 2009; Willott et al. 2010b; Masters et al. 2012; Ross et al. 2012);

2. BH masses (see Shen 2013 for a comprehensive review) and Eddington ratios (see Kelly & Shen 2013 and references therein; Schulze et al. 2015);

3. BH mass function (BHMF) estimates up to $z \sim 6$ (Willott et al. 2010a; Li, Ho & Wang 2011; Ueda et al. 2014);

4. FIR luminosity/SFR function in massive galaxies (e.g., Rodighiero et al. 2010; Lapi et al. 2011; Magnelli et al. 2013; Gruppioni et al. 2013);

5. Stellar luminosity/mass functions (e.g., Stark et al. 2009; Santini et al. 2012a; Ilbert et al. 2013; Bernardi et al. 2013; Duncan et al. 2014).

The coevolution has been also explored by searching for nuclear activity in starforming galaxies and, vice versa, searching for star formation in AGNs/QSOs. Specifically, large statistics have been recently obtained on:

1. Nuclear activity, by exploiting the follow-up in X-rays of galaxies with large SFRs mainly selected at FIR/sub-mm wavelengths or in the $K-$band (e.g., Borys et al. 2005; Alexander et al. 2005, 2008; Laird et al. 2010; Symeonidis et al. 2010; Xue et al. 2010; Georgantopoulos, Rovilos & Comastri 2011; Carrera et al. 2011; Melbourne et al. 2011; Rafferty et al. 2011; Mullaney et al. 2012a; Johnson et al. 2013; Wang et al. 2013c; Rodighiero et al. 2015) and of galaxies forming stars at a lower rates, hence more easily selected at UV wavelengths via the stacking technique (e.g., Fiore, Puccetti & Mathur 2012; Treister et al. 2011; Willott 2011; Basu-Zych et al. 2013);

2. The star formation in AGN host galaxies, by exploiting the follow-up at FIR and (sub-)mm wavelengths of X-ray selected AGNs (e.g., Page et al. 2004, 2012; Stevens et al. 2005; Lutz et al. 2010; Shao et al. 2010; Mainieri et al. 2011; Harrison et al. 2012; Mullaney et al. 2012b; Rosario et al. 2012; Rovilos et al. 2012; Santini et al. 2012b) and of optically selected QSOs (Omont et al. 1996, 2001, 2003; Carilli et al. 2001; Priddey et al. 2003; Wang et al. 2008, 2013b; Walter et al. 2009; Serjeant et al. 2010; Bonfield et al. 2011; Mor et al. 2012; Willott, Bergeron & Omont 2015).

These two complementary blocks of observations are of paramount relevance in determining the way stellar and BH masses grew at early times in the ETG progenitors.

In the fist part of our thesis, we will provide definite descriptions of the SFR and AGN lightcurves in terms of a few physical parameters. We will show how the comparison with the current data can clarify the main aspects of the galaxy/AGN coevolution process, even though additional observations in X-ray, optical, and FIR bands are strongly required in order to test the overall picture in detail. We will also show that the wealth of data at $z \gtrsim 1$ strongly supports the view that galaxies with final stellar mass $M_\star \gtrsim 10^{11}\,M_\odot$ proceed with their star formation at an almost constant rate over $\sim 0.5 - 1$ Gyr, within a dusty interstellar medium (ISM).

At the same time, several physical mechanisms related to the star formation, such as gravitational instabilities in bars or dynamical friction among clouds of starforming gas or radiation drag (Norman & Scoville 1988; Shlosman, Frank & Begelman 1989; Shlosman, Begelman & Frank 1990; Shlosman & Noguchi 1993; Hernquist & Mihos 1995; Noguchi 1999; Umemura 2001; Kawakatu & Umemura 2002; Kawakatu, Umemura & Mori 2003; Thompson, Quataert & Murray 2005; Bournaud, Elmegreen & Elmegreen 2007; Bournaud et al. 2011; Hopkins & Quataert 2010, 2011), can make a fraction of the ISM lose angular momentum and flow into a reservoir around the seed BH. The accretion from the reservoir to the BH can be as large as $30-50$ times the Eddington rate, leading to slim-disc conditions (Abramowicz et al. 1988; Watarai, Mizuno & Mineshige 2001; Blandford & Begelman 2004; Li 2012; Begelman 2012; Madau, Haardt & Dotti 2014; Volonteri, Silk & Dubus 2015), with an Eddington ratio $\lambda_{\rm Edd} \lesssim 4$ and an average radiative efficiency $\epsilon \lesssim 0.1$. This results in an exponential increase of the BH mass and of the AGN luminosity, with an $e-$folding timescale $\tau_{\rm ef}$ ranging from a few to several 10^7 years. Eventually, the AGN at its maximum power can effectively transfer energy and momentum to the ISM, removing a large portion of it from the central regions, and so quenching the star formation in the host. The reservoir around the BH is no more fed by additional gas, so that even the accretion and the nuclear activity come to an end.

In the second part of the thesis, we will implement the lightcurves for the luminosity associated to the star formation and to the BH accretion in a continuity equation approach. In the context of quasar statistics, the continuity equation has been introduced by Cavaliere, Morrison & Wood (1971) to explore the optical quasar luminosity evolution and its possible relation with the radiosource evolution. Soltan (1982) and Chokshi & Turner (1992) exploited the mass-energy conservation to derive an estimate of the present mass density of inactive SMBHs.

The extension and the derivation of the BHMF have been pioneered by Small & Blandford (1992), who first attempted to connect the local BHMF to the AGN luminosity evolution. A simplified version in terms of mass-energy conservation has been used by Salucci et al. (1999), who have shown that the distribution of the mass accreted onto the central SMBHs during AGN activity well matches the massive dark object (MDO) mass function of local inactive galaxies. A detailed discussion of the continuity equation applied to QSOs and SMBHs has been presented by Yu & Lu (2004, 2008). In the last decade, the continuity equation has been widely used, though the AGN lightcurve, one of the fundamental ingredients, was largely based on assumptions (e.g., Marconi et al. 2004; Shankar, Weinberg & Miralda-Escudé 2009, 2013; Merloni & Heinz 2008; Cao 2010). Results on the BHMF through the continuity equation have been reviewed by Kelly & Merloni (2012) and Shankar (2013).

We will also implement the continuity equation for the stellar content of galaxies. This has become possible because the UV surveys for Lyman Break Galaxies (LBGs), and the wide surveys *Herschel* Multi-tiered Extragalactic Survey (HerMES) and *Herschel*-ATLAS (H-ATLAS) obtained with the *Herschel* space observatory have allowed to reconstruct the SFR function in the Universe up to $z \sim 6$ for $\dot{M}_\star \sim 10 - 1000\, M_\odot\ \mathrm{yr}^{-1}$. Therefore, we can exploit the continuity equation, adopting an analogous approach as the one routinely used for AGNs; the SMBH mass is replaced by the stellar mass, and the bolometric luminosity due to the accretion process is replaced by the luminosity generated by the formation of young, massive stars.

The stellar mass function (SMF) is estimated by exploiting the observed luminosity function in the wavelength range of the spectral energy distribution (SED) dominated by the emission from older, less massive stars. The passage from stellar luminosity to mass is plagued by several problems, which result in uncertainties of the order of a factor of 2, increasing for young, dusty galaxies (e.g., Cappellari et al. 2013; Conroy, Graves & van Dokkum 2014). Therefore, the mass estimate is more robust for galaxies with quite low star formation and/or passively evolving. All in all, the SMF of galaxies is much easier to estimate, and hence much better known, than the BHMF, particularly at high redshift. Reliable SMFs are available both for local and high redshift (up to

$z \sim 6$) galaxy samples (e.g., Stark et al. 2009; González et al. 2011; Santini et al. 2012a; Bernardi et al. 2013; Maraston et al. 2013; Ilbert et al. 2013; Duncan et al. 2014). The comparison between the observed SMF and the results from the continuity equation sheds light on the relative contribution of dry merging and of *in-situ* star formation. We will solve the continuity equation for AGNs and for the stellar component after including the corresponding lightcurves derived in the first part of the thesis and from the data analysis of Lapi et al. (2011).

Once the stellar and the BH mass functions at different redshifts are known, they can also be compared with the abundance of DM halos, to obtain interesting relationships between halo mass and galaxy/BH properties. Such a technique, dubbed abundance matching, has been exploited by several authors (e.g., Vale & Ostriker 2004; Shankar et al. 2006; Moster et al. 2010; Moster, Naab & White 2013; Behroozi, Wechsler & Conroy 2013; Behroozi & Silk 2015). We will refine the technique and will use it in connection with the outcomes of the continuity equation to tackle the following open issues in galaxy formation and evolution:

1. Is the BHMF reflecting the past AGN activity? What was the role of merging in shaping it?
2. How does the BH duty cycle evolve? What can we infer on the radiative efficiency and on the Eddington ratio of active BHs?
3. Is there any correlation between the central BH mass and the halo mass? How does it evolve with time?
4. Which is the relationship between the AGN bolometric luminosity and the host halo mass? Can we use this relationship with the duty cycle to produce large simulated AGN catalogs?
5. Which are the bias properties of AGNs? Do they strongly depend on luminosity and redshift?
6. Can the evolution of the SMF be derived through the continuity equation as in the case of the BHMF, by replacing the accretion rate with the SFR? Does dry merging play a major role in shaping the SMF of galaxies? What is the role of the dust in the star formation process within galaxies?
7. Which is the relationship between the SFR, the stellar mass of the galaxies, and the mass of the host halo? Does the star formation efficiency (i.e., the fraction of baryons going into stars) evolve with the cosmic time?

8. Which is the relationship between the bolometric luminosity of galaxies due to star formation and the host halo mass? Can we combine this relationship with the stellar duty cycle to produce large simulated catalogs of star forming galaxies?

9. Which are the bias properties of star forming and passively evolving galaxies?

10. How does the specific star formation rate (sSFR) evolve with redshift and stellar mass?

11. Which is the relationship between the BH mass and the stellar mass at the end of the star formation and BH mass accretion epoch? Does it evolve with time?

12. How and to what extent can we extrapolate the relationships for both galaxies and hosted AGNs to higher, yet unexplored, redshift?

To answer to these questions, we have organized the thesis as follows.

Chapters 2 and 3 are dedicated to an overview of the main topics that we are going to deal with. In particular, Chapter 2 is devoted to BH basics, while Chapter 3 to stellar basics. In Chapter 4, we will present a simple prescription for the time-averaged evolution of the SFR and BH accretion rate, following the guidance of physically motivated basics, and we will show that it fits the statistics obtained by X-ray follow-up of FIR selected starforming galaxies and by FIR follow-up of X-ray and optically selected AGNs/QSOs, and additional observations, somewhat less systematic but of great relevance, such as the BH-to-stellar mass ($M_{\rm BH}/M_{|}star$) ratio in optically selected QSOs, the relative abundance of obscured to unobscured AGNs/QSOs, and the measured QSO outflow rates. Finally, we will discuss the prospects for direct detection of the large gas reservoir around the SMBHs predicted by our prescriptions, and our understanding of the gas path from the interstellar medium to the accretion disc around the SMBH. In Chapter 5 we will connect the luminosity information to the mass growth: we will solve the continuity equation to derive the BH and stellar mass functions at different redshifts. Comparison with recent data are also presented. In Chapter 6, we will exploit the abundance matching technique to infer relationships among the properties of the BH, stellar, and DM components in galaxies. We will also provide a discussion about the results present in the literature. Chapter 7 will offer a final discussion, important remarks, and a summary of our findings.

Throughout this thesis, we will adopt the concordance cosmology (see *Planck* Collaboration XVI et al. 2014; *Planck* Collaboration XIII et al. 2015), i.e., a flat Universe with round parameter values: matter density $\Omega_M = 0.3$, baryon density $\Omega_b = 0.05$, Hubble constant $H_0 = 100\,h$ km s^{-1} Mpc^{-1} with $h = 0.7$, and mass variance $\sigma_8 = 0.8$ on a scale of $8\,h^{-1}$ Mpc. Stellar masses and FIR luminosities (or conversely SFRs) of galaxies are

evaluated assuming the Chabrier (2003) initial mass function (IMF) and the SED of SMM J2135-0102, a typical high-redshift starbursting galaxy (very similar to the local ULIRG Arp220; see Lapi et al. 2011 for details). By FIR we will consider the restframe wavelength range from $\lambda \approx 40\,\mu$m to $\lambda \approx 500\,\mu$m. In general, we can assume that this spectral region is dominated by the emission of dust associated with star formation, although a contribution from a torus around an AGN may be not completely negligible (e.g., Granato & Danese 1994; Leipski et al. 2013). We will indicate with $L_{\rm AGN}$ the bolometric output of the nuclear emission, and with $L_B = L_{\rm AGN}/k_B$, $L_X = L_{\rm AGN}/k_X$ the powers in the optical and in the $2-10$ keV X-ray bands, adopting the bolometric corrections k_B and k_X by Hopkins, Richards & Hernquist (2007, see also Marconi et al. 2004; Vasudevan & Fabian 2007; Runnoe, Brotherton & Shang 2012; Lusso et al. 2012). The values depend on the AGN luminosity (or on the Eddington ratio), and span the ranges $k_B \sim 8-15$ and $k_X \sim 15-100$ for $L_{\rm AGN} \sim 10^{43}-10^{47}$ erg s^{-1}. Further information about bolometric corrections are given in Sec. 2.7.1. Note that we will restrict ourselves to $L_X \gtrsim 10^{42}$ erg s^{-1}, to avoid appreciable contaminations of the X-ray emission by star formation (see Symeonidis et al. 2011). The only exception could be the rare extreme starburst galaxies in the distant Universe, such as luminous sub-mm galaxies, which can exceed this threshold without an AGN being present (Brandt & Alexander, 2015).

Chapter 2

Basics of Black Hole Growth

Active SMBHs in galactic centers have been known since the early discovery of QSOs in the 1960s. However, the idea that most galaxies, especially those with dynamically relaxed bulges, contain dormant SMBHs in their centers took much longer time to develop. Detailed studies of the stellar velocity field and gas motion in nearby galaxies suggest the existence of such objects (see Sec. 2.8). Moreover, there seems to be strong correlations between the BH mass and the bulge properties of the host galaxy.

Systematic and extensive observations of active SMBHs show that such systems must have been present very early in the history of the Universe. In fact, observations of AGNs at high redshift show that BH masses of the order of $10^9 M_\odot$ have already been in place at $z \sim 6$. Some of these sources are accreting material at a very high rate, close to the theoretical upper limits of such processes (see Sec. 2.2). Thus, the evolution of SMBHs and their host galaxies have been linked since very early times, probably already at $z \sim 10$.

In this Chapter, we will describe the relevant characteristics of SMBHs, the basic theory of BH growth, and recent observational results. We will also introduce the main quantities useful for further discussions.

2.1 Accretion

AGNs are extragalactic sources powered by a compact central engine, consisting of a SMBH. Such sources produce very high luminosities (up to 10^{48} erg s^{-1}, outshining all of the stars in its host galaxy) in a tiny volume ($\lesssim 10^{14}$ cm). The only process through which so high powers in such small volumes can be produced is accretion onto a compact object, in which the rest-mass energy can be converted into radiation with an efficiency

$\epsilon \sim 0.1$ (see Sec. 2.3), to be compared to the nuclear stellar efficiencies, which are of the order of ~ 0.007. Given a mass accretion rate $\dot{M}_{\rm acc}$ infalling onto a BH, this is converted with an efficiency ϵ into a bolometric luminosity:

$$L_{\rm bol} = \epsilon \dot{M}_{\rm BH} c^2 \tag{2.1}$$

while growing the BH mass by a quantity:

$$\dot{M}_{\rm BH} = (1-\epsilon)\dot{M} \ . \tag{2.2}$$

2.2 Eddington limit and related quantities

In spherical symmetry, let us consider a central point source with mass $M_{\rm BH}$, total luminosity $L_{\rm bol}$ and monochromatic luminosity L_ν. Let us also assume a fully ionized gas at a distance r from the source. The radiation pressure force acting on a gas particle is:

$$f_{\rm rad} = \frac{N_e \sigma_T}{4\pi r^2 c} \int_0^\infty {\rm d}\nu \, L_\nu = \frac{N_e \sigma_T}{4\pi r^2 c} L_{\rm bol} \ , \tag{2.3}$$

where N_e is the electron density and $\sigma_T = 6.65 \times 10^{-25}$ cm^2 is the Thomson cross section. The gravitational force per particle is:

$$f_{\rm g} = \frac{G M_{\rm BH} \mu m_p N_e}{r^2} \ , \tag{2.4}$$

where μ is the mean molecular weight, defined as the mean number of protons and neutrons per electron ($\mu \sim 1.17$ for a fully ionized gas with solar composition). Spherical accretion onto the central object can proceed as long as $f_g > f_{\rm rad}$. The limiting requirement for accretion, $f_{\rm rad} = f_g$, leads to the definition of the Eddington luminosity:

$$L_{\rm Edd} = \frac{4\pi c G M_{\rm BH} \mu m_p}{\sigma_T} \sim 1.38 \times 10^{38} \left(\frac{M_{\rm BH}}{M_\odot} \right) {\rm erg\,s^{-1}} \ , \tag{2.5}$$

where the factor 1.38×10^{38} depends on the exact value of μ. The value of $L_{\rm Edd}$ defined in this way represents the maximum luminosity allowed for objects that are powered by a steady-state accretion in spherical symmetry over a long period.

The accretion rate required to produce a total luminosity equal to $L_{\rm Edd}$, namely the Eddington accretion rate, is:

$$\dot{M}_{\rm Edd} = \frac{L_{\rm Edd}}{\epsilon c^2} \sim 3 \left(\frac{M_{\rm BH}}{10^8} \right) \left(\frac{\epsilon}{0.1} \right)^{-1} M_\odot \, {\rm yr^{-1}} \tag{2.6}$$

and the typical time associated to this accretion rate, namely the Eddington time, writes:

$$t_{\rm Edd} = \frac{M_{\rm BH}}{\dot{M}_{\rm Edd}} \sim 4 \times 10^8 \,{\rm yr} \ . \tag{2.7}$$

With this terminology, we can write the Eddington Luminosity also as:

$$L_{\rm Edd} = \frac{M_{\rm BH} \epsilon c^2}{t_{\rm Edd}} \ . \tag{2.8}$$

The last important quantity to be defined is the Eddington ratio:

$$\lambda_{\rm Edd} = \frac{L_{\rm bol}}{L_{\rm Edd}} \ , \tag{2.9}$$

which relates the AGN bolometric luminosity to the Eddington luminosity and, through Eq. 2.5, to the SMBH mass.

2.3 Radiative efficiency

In order to accrete onto a BH, the orbiting material has to lose a fraction of its rest mass energy, which in turn is emitted as a radiation. The radiative efficiency ϵ is defined as the fraction of mass inflow, namely the accretion rate $\dot{M}$, that is converted into radiation $L_{\rm bol}$:

$$\epsilon = \frac{L_{\rm bol}}{\dot{M} c^2} \tag{2.10}$$

The radiative efficiency is closely related to the energy output appearing as a jet/wind outflow. Such outflows can interact with the surrounding gas more efficiently than radiation, and may significantly affect the host galaxy evolution giving rise to the correlations of the BH mass with the galaxy properties (e.g., Magorrian et al. 1998; Vasudevan & Fabian 2007; King & Pounds 2015). As we will see in Sec. 2.4, the radiative efficiency is related to the spin a of the BH: without torques, the maximum value of the total efficiency is $\epsilon = 0.4$ for $a = 1$, or $\epsilon = 0.32$ for $a = 0.998$, which is the maximal spin within an accretion disc (Thorne 1974).

Following the Soltan (1982) argument, the global AGN average radiative efficiency ϵ is commonly estimated by comparing the total mass accreted onto SMBHs per unit volume and the total AGN luminosity per unit volume integrated over time. Later works used a related method to determine the average accretion efficiency by measuring the X-ray background (Fabian & Iwasawa 1999; Elvis, Risaliti & Zamorani 2002).

In studies of AGN evolution, where the redshift-dependent AGN LF is compared with the local BHMF (Small & Blandford 1992; Salucci et al. 1999; Yu & Tremaine 2002;

Marconi et al. 2004; Merloni 2004; Raimundo & Fabian 2009; Shankar, Weinberg & Miralda-Escudé 2009), the accretion efficiency is one of the free parameters associated with the accretion process. These can be determined on average for AGNs, but the derived values are significantly uncertain; in fact, when taking the observed values for the Eddington ratio and obscuration into account, the possible parameter range is very wide (Raimundo & Fabian 2009).

Davis & Laor (2011) discussed a method to derive ϵ in individual AGNs. They have estimated the accretion rate by fitting radiatively efficient thin accretion disc model SEDs to the optical emission in a sample of 80 Palomar-Green QSOs with well determined $L_{\rm bol}$. The BH masses were estimated using single epoch methods (see Sec. 2.8.6), as well as the $M_{\rm BH} - \sigma$ relationship for those objects with bulge stellar velocity dispersion measurements. The radiative efficiency was then calculated for each source from Eq. 2.10. Their resulting mean efficiency is consistent with the estimates based on the Soltan argument, and seems to be correlated with the BH mass, but a follow-up study suggests that the correlation is an artifact induced by selection effects (Raimundo et al. 2012).

Adopting an approach similar to that of Davis & Laor (2011), Trakhtenbrot (2014) derived constraints on the radiative efficiencies of the accretion discs powering a sample of 72 luminous, unobscured AGNs at $1.5 \lesssim z \lesssim 3.5$.

2.4 Spin

When the spacetime is described by the Kerr metric, an isolated BH is fully characterized by just its mass $M_{\rm BH}$ and angular momentum J, usually specified in terms of the dimensionless spin parameter:

$$a = \frac{Jc}{GM_{\rm BH}^2} \ , \tag{2.11}$$

where $|a| \lesssim 1$.

According to the standard accretion disc theory of AGNs (Shakura & Sunyaev 1973), the BH spin determines the radiative efficiency ϵ, because it sets the radius beyond which the material is assumed to fall into the BH without losing further energy (the marginally stable orbit). Thus, the spin determines also the BH mass growth efficiency, through Eq. 2.2.

Since the total efficiency is a rising monotonic function of the spin, the measured ϵ provides a lower limit on a. Several numerical studies investigated the spin evolution: it was shown that if the SMBH grew mostly through a single event (major mergers or

continuous gas accretion), then a is expected to "spin up", and it will be close to $a \sim 1$; alternatively, if the growth of the SMBH was characterized by a series of independent events (minor mergers or episodic accretion), a is expected to "spin down", reaching $a \sim 0$ (e.g., Hughes & Blandford 2003; Gammie, Shapiro & McKinney 2004; Volonteri et al. 2005; Volonteri, Sikora & Lasota 2007; Berti & Volonteri 2008; King & Pringle 2006; King, Pringle & Hofmann 2008; Dotti et al. 2013).

There are 3 main methods for the determination of the SMBH spin:

1. Estimating the accretion efficiency;
2. Fitting the shape of the broad Fe Kα line to X-ray data;
3. Fitting the accretion disc continuum to the broad-band data with disc models.

The first method is applied in the statistical approach to the whole QSO population. The estimates made by Soltan (1982) have indicated the overall accretion efficiency to be of the order of $\epsilon \sim 0.1$, corresponding to a moderate BH spin, $a \sim 0.67$. Subsequent studies based on the same approach claimed similar values (e.g. Elvis, Risaliti & Zamorani 2002; Marconi et al. 2004; Martínez-Sansigre & Taylor 2009; Shankar, Weinberg & Miralda-Escudé 2009), with some evidence for higher spins at higher redshifts (e.g., Wang et al. 2009; Shankar, Weinberg & Shen 2010; Li 2012). A semi-analytical galaxy formation model has been developed by Barausse (2012) to study the mass and spin evolution in a self-consistent way. Their model follows the evolution of DM haloes and of the baryonic component (hot gas, stellar and gaseous bulges, plus stellar and gaseous galactic discs) along merger trees, and takes into account the effect of the gas present in galactic nuclei during both accretion phases and mergers. The limitation of all these approaches is that they cannot probe the spins of individual objects.

The second method has been employed for a number of AGNs, mostly nearby Seyfert galaxies with high-quality X-ray spectra (Brenneman & Reynolds 2006, 2009; Goosmann et al. 2006; Schmoll et al. 2009; de La Calle Pérez et al. 2010; Risaliti et al. 2013, see Reynolds 2014 for a recent review). A major advantage of this method is that knowledge of the SMBH mass, its distance or accretion disc inclination, is not required in order to derive the spin; Indeed, X-ray reflection spectroscopy allows to measure the inclination concurrently with the SMBH spin.

The third method can be used to infer the spin in single AGNs (Czerny et al. 2011; Done et al. 2013), even though its application is limited, since it requires the broad-band spectrum to be disc-dominated, and the spectral region corresponding to the maximum of the disc emission to be clearly visible. The second condition is particularly difficult to meet in AGNs, since it is often challenging to measure the full SED.

Recently, Wang et al. (2014) proposed a new approach to estimate a in AGNs using reverberation mapping of the Hβ line (see Sec. 2.8.5). Studying the broad-line region (BLR) size-luminosity relation based on a standard accretion disc model, they found the BLR size to be very sensitive to the spin of the SMBH: the shortest Hβ lags correspond to the lowest spins or to retrograde accretion. Applying this technique to the currently available sample of ~ 50 AGNs with reliable reverberation mapping measurements, the authors found a predominance of fast-rotating SMBHs.

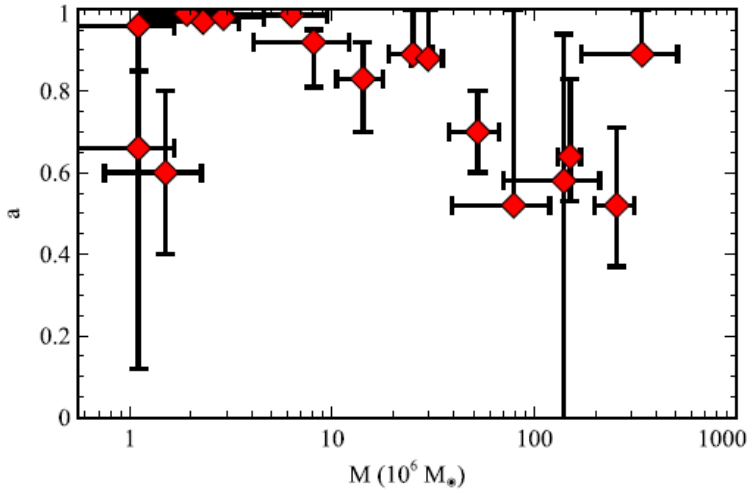

FIGURE 2.1: Spins against SMBH masses from the sample of Reynolds (2013). Masses are marked with 1σ error bars, when available; otherwise, an error of $0.5\mathrm{M}_\odot$ is adopted. Spins are marked with 90% error ranges. The figure has been taken from Reynolds (2014).

In the last years, the number of published SMBH spin measurements based on relativistic reflection spectra has increased, including two major works that used the public data archives (Patrick et al. 2012; Walton et al. 2013). The same method was applied by Reynolds (2014) in 20 low-redshift AGNs with $M_{\mathrm{BH}} \sim 10^6 - 3 \times 10^8 M_\odot$, providing the measurements shown in Fig. 2.1. Uncertainties are large, however it seems that a significant fraction of SMBHs in these AGNs are rapidly spinning ($a \gtrsim 0.8$), at least in the mass range $10^6 - 2 \times 10^7 M_\odot$. This suggests that the growth of these SMBHs occurred via coherent, rather than chaotic, accretion (King & Pringle 2006) or major merger (Volonteri et al. 2005). Moreover, there are hints that the most massive BHs in the sample ($M_{\mathrm{BH}} \gtrsim 10^8 M_\odot$), as well as the least massive BHs ($M_{\mathrm{BH}} \lesssim 10^6 M_\odot$) may have lower spins. If confirmed by more rigorous analyses, these trends would provide direct evidence for the increased role of chaotic accretion and/or major mergers at the two extreme ends of SMBH masses.

2.5 Accretion disc models

Mass is generally accreted onto the SMBH from the outskirts of the host galaxy. The infalling gas will be endowed with substantial angular momentum, which prevents it from directly reaching the central SMBH, making it settle into a disc structure. Thus, some form of friction is required to allow gas to lose angular momentum and accrete the BH. Magnetic fields have been shown to efficiently trigger an instability that leads to turbulence, angular momentum transport, and energy dissipation, allowing accretion to proceed (e.g., Balbus & Hawley 1998).

As suggested by Abramowicz & Fragile (2013), we will classify accretion discs into four categories: thick, thin, slim, and Advection-Dominated Accretion Flow (ADAF). They can be characterized in terms of: relative thickness $h = H/R$, where H is the thickness of the disc at radius R; dimensionless accretion rate $\dot{m} = 0.1\dot{M}c^2/L_{\rm Edd}$; optical depth τ; and accretion efficiency ϵ. Their properties are listed in Table 2.1.

Disc type	h	$\dot{m}$	τ	ϵ
Thin disc	$\ll 1$	$\lesssim 1$	$\gg 1$	~ 0.1
Thick disc	> 1	$\gg 1$	$\gg 1$	$\ll 0.1$
ADAF	< 1	$\ll 1$	$\ll 1$	$\ll 0.1$
Slim disc	~ 1	$\gtrsim 1$	$\gg 1$	$\lesssim 0.1$

TABLE 2.1: Classification of accretion discs

During phases characterized by high accretion rate, the energy is radiated away on a timescale shorter than the one needed by the gas to flow into the SMBH. As a consequence, the gas cools rapidly, and a geometrically thin, optically thick disc forms (Shakura & Sunyaev 1973; Frank, King & Raine 2002). On the other hand, if the gas cannot radiate its energy away, it settles into a hot thick accretion disc with $\epsilon \ll 0.1$.

During periods of modest accretion, a hot, radiatively inefficient ($\epsilon \ll 0.1$) accretion flow, namely ADAF, forms (e.g. Narayan & Yi 1994; Abramowicz et al. 1995; Narayan & McClintock 2008). In these discs, the inflow timescale is much shorter than the cooling one. Thus, the accretion energy cannot be radiated away, and is either advected inwards or released in a wind or radio jet (adiabatic inflow-outflow solutions, ADIOS; Blandford & Begelman 1999, 2004).

Finally, slim disc conditions are predicted when the accretion onto the BH is large, up to $30-50$ times the Eddington rate (Abramowicz et al. 1988; Watarai, Mizuno & Mineshige 2001; Blandford & Begelman 2004; Li 2012; Begelman 2012; Madau, Haardt & Dotti 2014; Volonteri, Silk & Dubus 2015). The radiative efficiency has relatively low values

($\epsilon \lesssim 0.1$), and $\lambda_{\rm Edd}$ is high; the result is that the radiation pressure dominates over the gas pressure, and that the disc is geometrically thick.

The data analysis by Netzer & Trakhtenbrot (2014) suggests that statistically the fraction of slim discs should increase toward higher redshifts. A recent work by Wang et al. (2013a) suggests that extreme slim discs, with $\lambda_{\rm Edd} \gg 1$, can be used as a new type of standard candles for cosmological studies, since their bolometric luminosity is directly proportional to the BH mass, with only a weak (logarithmic) dependence on the accretion rate.

Results of several numerical simulations and analytic works (Abramowicz et al. 1988; Mineshige et al. 2000; Watarai, Mizuno & Mineshige 2001; Blandford & Begelman 2004; Li 2012; Begelman 2012; Madau, Haardt & Dotti 2014), indicate a simple prescription to relate the efficiency ϵ and the Eddington ratio $\lambda_{\rm Edd}$ in both slim and thin disc conditions:

$$\epsilon_{\rm slim} = \frac{\epsilon_{\rm thin}}{2} \frac{\lambda_{\rm Edd}}{e^{\lambda_{\rm Edd}/2} - 1} \ ; \tag{2.12}$$

here $\epsilon_{\rm thin}$ is the efficiency during the thin disc phase, which may range from 0.057 for a non-rotating to 0.32 for a maximally rotating Kerr BH (Thorne 1974). In this thesis, we will adopt $\epsilon_{\rm thin} = 0.1$ as our fiducial value. In conditions of mildly super-Eddington accretion with $\lambda_{\rm Edd} \gtrsim 1$, the radiative efficiency $\epsilon_{\rm slim} \lesssim 0.3\,\epsilon_{\rm thin}$ applies, while in sub-Eddington accretion regime with $\lambda_{\rm Edd} \lesssim 1$, it quickly approaches the thin disc value $\epsilon_{\rm slim} = \epsilon_{\rm thin}$.

2.6 AGN Spectral Energy Distribution

The AGN luminosity is emitted primarily in a broad continuum spectrum carrying significant power over several decades, from the radio to the X-ray bands. The continuum in each spectral region can be ascribed to distinct energy generation mechanisms: jets in the radio (see e.g. Harris & Krawczynski 2006 for a review), dust in the IR (e.g., McAlary & Rieke 1988; Sanders et al. 1989), accretion disc in the optical-UV and soft X-rays (e.g., Shakura & Sunyaev 1973; Rees 1984; Czerny & Elvis 1987), and Compton up-scattering by hot coronae in the hard X-rays (e.g. Zamorani et al. 1981; Laor, Netzer & Piran 1990; Haardt & Maraschi 1991; Williams et al. 1992; Zdziarski, Poutanen & Johnson 2000; Kawaguchi, Shimura & Mineshige 2001; Mateos et al. 2005; Mainieri et al. 2007).

SEDs are generally plotted as $\log \nu f_\nu$ as a function of $\log \nu$: since νf_ν is the flux per logarithmic frequency interval, such plots give the best indication of the frequency ranges where most of the energy is released. Fig. 2.2 shows the typical SEDs for both radio

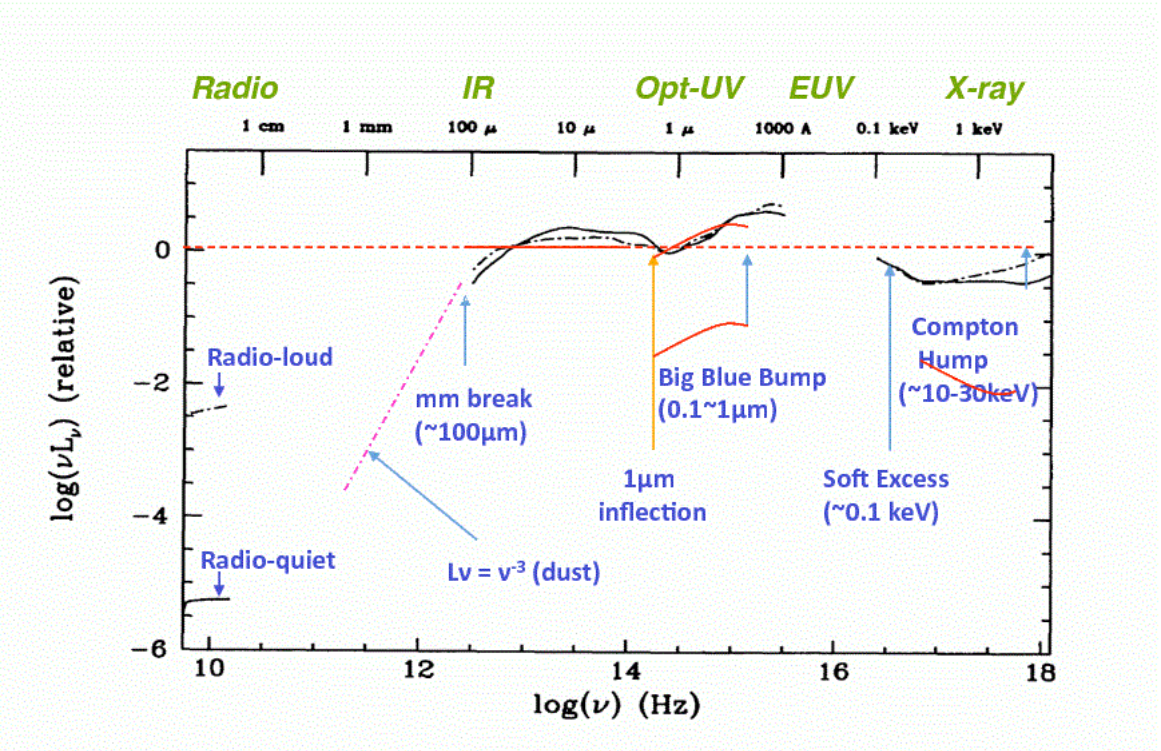

FIGURE 2.2: The radio to X-ray continuum quasar SED. On the top, observing bands are written in green. Spectral features are indicated by the arrows in the plot. Radio-quiet AGNs are represented by a black solid line, radio-loud AGNs by a black dot-dashed line. Horizontal red line shows equal power per decade. The figure has been updated from Elvis et al. (1994).

loud and radio quiet AGNs. A quasar keeps its power output almost constant from the FIR ($\sim 100\,\mu$m) to X-rays (~ 10 keV), with excursions of only a factor of a few. In general, no data are available in the extreme UV gap beyond the Lyman limit, because our Galaxy is opaque at these frequencies. The more prominent features in a SED are the following:

1. The millimeter break (labeled mm break in Fig. 2.2) at $\sim 100\,\mu$m: The AGN power always drops in the sub-mm band, but the extent of it varies from object to object. In radio loud AGNs, the drop is usually 2 orders of magnitude, while in radio quiet AGNs it can be 5 or even 6 orders of magnitudes. Radio loud AGNs have a powerful jet moving at relativistic speeds made up of energetic particles, themselves moving near the speed of light in a magnetic field. This causes them to radiate light by the synchrotron process. The millimeter break in the strongest feature in the QSO continuum, although it is less strong in radio-selected objects;

2. The IR bump at $\sim 30 - 40\,\mu$m: this feature is due to the reprocessed thermal emission of the optical-UV radiation by hot ($T \sim 10^3$ K) dust located in the proximity of the accretion disc, probably in a torus (e.g., Antonucci 1993);

3. The near-IR (NIR) inflection at $1\,\mu$m: The wavelength range between 1 μm and 1.5 μm is marked by an inflection between the rising Wien tail of emission from hot dust and the power law $f_\nu \propto \nu^{1/3}$ of the Big Blue Bump in the optical caused by the emission of the accretion disc. Because its location is easy to identify, the $1\,\mu$m wavelength is usually chosen as a normalization point (Elvis et al. 1994);

4. The Big Blue Bump, in the range $\sim 0.1 - 1\,\mu$m: The optical-UV continuum rises above the IR in a "bump". This feature dominates the QSO emission by a modest factor. It is likely due to thermal emission from an accretion disc around the central SMBH, with temperatures ranging from $\sim 10^3$ K to $\sim 10^5$ K;

5. The soft excess at ~ 0.1 keV: Many AGNs show an enhanced emission below ~ 1 keV with respect to an extrapolation of the power law spectrum in the $2 - 10$ keV band attributed to the hot corona. This extra emission is generally approximated by a thermal shape, and is well fitted by a black body of energy $\sim 0.1 - 0.2$ keV. However, its physical origin is still unclear. Several models have been suggested to account for it, including ionized reflection of X-rays from the inner part of the accretion disc (Ross & Fabian 2005; Crummy et al. 2006; Walton et al. 2013; Vasudevan et al. 2014), ionized winds/absorbers (e.g., Gierliński & Done 2004), or Comptonization of inner-disc photons (e.g., Done et al. 2012).

6. The Compton hump in the range $\sim 10 - 30$ keV: The X-ray continuum in AGNs is believed to arise from the Comptonization of thermal photons that are emitted from the accretion disc by a plasma of extremely energetic particles, most likely electrons, around the BH, called corona (Sunyaev & Trümper 1979). Above 10 keV, photons are not photoelectrically absorbed and reprocessed, but they are Compton scattered. This produces an excess of photons in the 20-30 keV range (e.g., Kara et al. 2015; Wilkins & Gallo 2015).

The SEDs depend on the main selection of the objects (e.g., X-ray, UV, optical, IR), possibly on the Eddington ratio (Vasudevan et al. 2010; Lusso et al. 2012), and on the bolometric luminosity (Hopkins, Richards & Hernquist 2007). In principle, changes in the continuum with redshift (Kelly et al. 2007), bolometric luminosity, BH mass or Eddington ratio might be expected; However, the recent analysis of Hao et al. (2014) found no significant dependencies on any of these quantities of the mean SEDs for a sample of about 400 X-ray selected Type 1 AGNs, although a large dispersion is signalled.

2.7 AGN Luminosity Function

The evolution of the AGN luminosity function (LF) with redshift is a key observational constraint on the growth of SMBHs over cosmic time. The behaviour of the AGN LF places constraints on the duty cycles, on the growth history of SMBHs, and on their coevolution with their host galaxies (e.g., Ueda et al. 2003; Hopkins et al. 2006; Aird et al. 2013; Shankar, Weinberg & Miralda-Escudé 2013; Schulze et al. 2015). Thus, accurate measurement of the LF is of paramount importance in the study of AGNs.

2.7.1 Bolometric corrections

Since AGN LFs are determined in a limited energy band, suitable bolometric corrections k_b are needed to recover the bolometric luminosity, as:

$$L_{\rm AGN} = k_b \cdot L_b \ , \tag{2.13}$$

where L_b is the LF observed in a given band b. Bolometric corrections are based on studies of SEDs for large samples of AGNs (e.g., Elvis et al. 1994; Richards et al. 2006; Hopkins, Richards & Hernquist 2007; Lusso et al. 2010, 2012; Vasudevan et al. 2010; Hao et al. 2014). In the literature, several optical and X-ray bolometric corrections have been proposed (see Marconi et al. 2004; Hopkins, Richards & Hernquist 2007; Shen et al. 2011; Lusso et al. 2012; Runnoe, Brotherton & Shang 2012). Those by Marconi et al. (2004) and Lusso et al. (2012) are somewhat smaller by $\lesssim 40\%$ in the optical and by $\lesssim 30\%$ in the hard X-ray band with respect to the ones by Hopkins, Richards & Hernquist (2007). In fact, since bolometric corrections are intrinsically uncertain by a factor of ~ 2 (e.g., Vasudevan & Fabian 2007; Lusso et al. 2012; Hao et al. 2014), these systematic differences among various determinations are not relevant. We will show in Sec. 5.1.3 that our results marginally feel the effect of bolometric corrections.

In this thesis, we convert the optical and X-ray luminosities to bolometric ones by using the Hopkins, Richards & Hernquist (2007) corrections[1], reported in Fig. 2.3.

[1]Most of the optical data are given in terms of magnitude M_{1450} at 1450 Å. First, we convert them to $B-$band (4400 Å) using the relation $M_B = M_{1450} - 0.48$ (Fan et al. 2001), then we pass to $B-$band luminosities in solar units $\log L_B/L_{B,\odot} = -0.4\,(M_B - 5.48)$, and finally we go to bolometric in solar units after $L_{\rm AGN}/L_\odot = k_B\, L_B/L_{B,\odot} \times L_{B,\odot}/L_\odot$. For this last step, we recall that the $B-$band luminosity of the Sun $L_{B,\odot} \approx 2.13 \times 10^{33}$ erg s^{-1} $\approx L_\odot/2$ is about half its bolometric one $L_\odot \approx 3.9 \times 10^{33}$ erg s^{-1}. In some other instances the original data are expressed in terms of a $z = 2$ K-corrected $i-$band magnitude $M_i(z = 2)$. We adopt the relation with the 1450 magnitude $M_{1450} = M_i(z = 2) + 1.486$ (Richards et al. 2006) and then convert to bolometric as above.

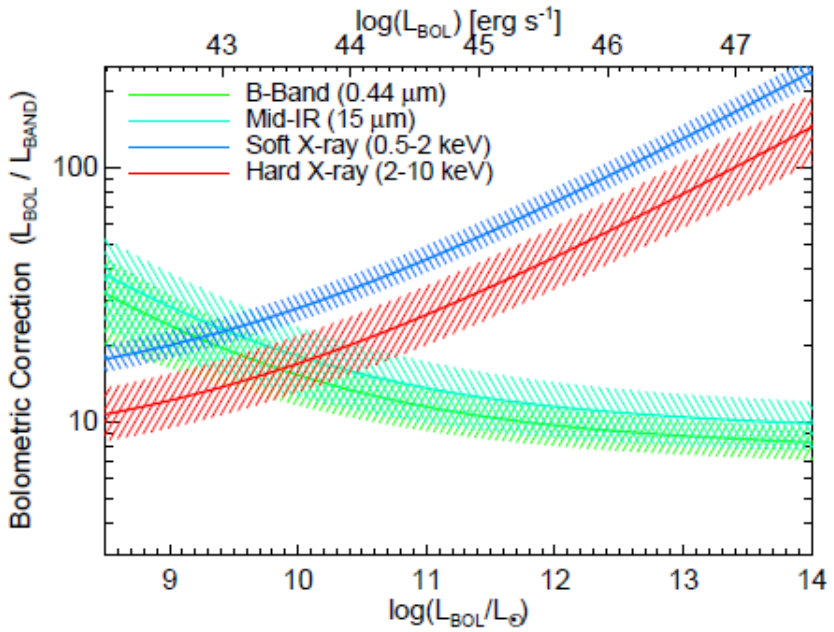

FIGURE 2.3: Bolometric corrections for B-band (green), MIR (cyan), soft (blue) and hard X-ray (red) bands as a function of luminosity, determined by Hopkins, Richards & Hernquist (2007) and adopted in this thesis. The shaded range for each band represents the lognormal dispersion in the distribution of bolometric corrections at fixed L. The figure has been taken from Hopkins, Richards & Hernquist (2007).

2.7.2 X-ray obscuration

Many AGNs are surrounded by gas and dust that can obscure their emission at certain wavelengths. Basic X-ray spectral analyses of the detected AGNs in deep X-ray surveys found that the majority of these objects shows evidence for obscuration (e.g., Dwelly & Page 2006; Tozzi et al. 2006; Merloni et al. 2014). Thus, it is fundamental to understand the role of obscuration in AGNs, in order to obtain accurate measurements of the LF, to reveal whether SMBHs undergo significant periods of obscured growth, and when they take place during the AGN lifetimes.

Revealing the extent of obscuration requires large, unbiased samples of AGNs selected over the widest possible range of redshifts and luminosities. Optical surveys, combined with follow-up spectroscopy, can efficiently cover wide areas, but are biased towards the most luminous, unobscured sources. Instead, X-ray surveys can efficiently identify AGNs over a wide luminosity range, including low-luminosity sources. Nevertheless, soft X-ray emission (at energies $\lesssim$ 2 keV) is absorbed by gas and dust, thus soft X-ray samples are generally dominated by mildly obscured AGNs, and may be partly contaminated by X-ray emission from starforming regions.

A large number of deep and wide X-ray surveys have been carried out, taking advantage of the efficiency and power of X-ray selection (see Brandt & Alexander 2015 for a recent

review). The inferred column-density distribution of the underlying obscured population, appears to peak around $N_H \sim 10^{23}$ cm^2. This result implies that a substantial fraction of AGNs will be highly obscured and even Compton-thick. For example, in the local Universe, even hard X-ray surveys as the Rossi X-Ray Timing Explorer (RXTE) and the High Energy Astronomical Observatory 1 (HEAO-1) may be missing a number of extremely obscured AGN. In the case of Compton-thick AGNs, at column densities $> 10^{24}$ cm^{-2}, a large fraction of the intrinsic flux will be absorbed.

For $z < 1$, the fraction of AGNs showing X-ray obscuration has a strong luminosity dependence, dropping from $\sim 70\%$ at $L_{2-10\mathrm{keV}} = 10^{43}$ erg s^{-1} to $\sim 20\%$ at $L_{2-10\mathrm{keV}} = 10^{45}$ erg s^{-1}. The fraction of AGNs showing X-ray obscuration, after allowing for luminosity effects, also appears to rise with redshift as $(1 + z)^{0.4-0.6}$, at least up to $z \sim 2$, beyond which the uncertainties become important (e.g., Treister & Urry 2006; Hasinger 2008; Hiroi et al. 2012; Iwasawa et al. 2012; Vito et al. 2013, 2014; Brightman et al. 2014; Merloni et al. 2014; Ueda et al. 2014). Whether this redshift evolution applies for all AGNs or primarily for the most luminous ones, is still debated (e.g., Iwasawa et al. 2012; Vito et al. 2013; Merloni et al. 2014; Ueda et al. 2014).

In this thesis, we correct the number density for the fraction of obscured (including Compton thick) objects as prescribed by Hopkins, Richards & Hernquist (2007) for the optical data, and according to Ueda et al. (2014, see also Ueda et al. 2003) for the hard X-ray data.

2.7.3 The observed AGN LF

The AGN LF $N(\log L_{\mathrm{AGN}}, z)$ is defined as the number of AGNs per unit volume, per unit logarithmic luminosity. It is usually estimated in discrete luminosity bins, using the standard $1/V_{\mathrm{max}}$ estimator (Schmidt 1968), in an equivalent manner as for the stellar luminosity function of galaxies. Details on the method will be given in Sec. 3.5.1.

In the optical, QSOs have been traditionally selected using colour thresholds to avoid stellar contamination from the host galaxy (Schmidt & Green 1983; Boyle et al. 2000). Instead, AGN X-ray selections are based on:

- Luminosity tresholds: to avoid appreciable contaminations of the X-ray emission by star formation (see Symeonidis et al. 2011), sources with 0.5-10 keV luminosities above $\sim 10^{42}$ erg s^{-1} are considered. Only rare extreme starburst galaxies in the distant Universe, such as luminous sub-mm galaxies, can exceed this threshold without an AGN being present;

- X-ray-to-optical/NIR flux ratios: AGNs tend to have higher ratios with respect to starburst/normal galaxies. Typical thresholds used to select 90-95% of AGNs in a sample are $\log(f_{0.5-10\mathrm{keV}}/f_R) > -1$ using the observed-frame R-band, or $\log(f_{0.5-10\mathrm{keV}}/f_{3.6\mu\mathrm{m}}) > -1$ using the observed-frame 3.6 μm band from *Spitzer* (e.g., Werner et al. 2004);

- Effective power-law photon indices: sources with $\Gamma_{\mathrm{eff}} < 1.0$ in the 0.5-10 keV band are generally obscured AGNs.

The sky density of QSOs derived from optical surveys is $\sim 10^4$ deg^2, typically at least an order of magnitude lower than the one derived from X-ray surveys (Georgantopoulos et al. 2009). This is because the colour selection is biased toward high luminosity AGNs, in contrast to the X-ray selection. Thus, the optical LF (Richards et al. 2006; Croom et al. 2009; Masters et al. 2012; Ross et al. 2012; Fan et al. 2006; Jiang et al. 2009; Schulze, Wisotzki & Husemann 2009; Willott et al. 2010b) is a powerful diagnostic tool for the understanding of luminous AGNs, enabling uniform sample selection at many redshifts, but misses substantial populations of obscured or heavily reddened quasars. On the other hand, the X-ray LF (Ueda et al. 2003, 2011, 2014; Fiore et al. 2012; Aird et al. 2015) can reach distant AGNs (objects similar to local moderate luminosity Seyfert galaxies can be identified out to $z \sim 5$), including obscured systems and objects that are up to ~ 100 times less bolometrically luminous than those found in wide-field quasar surveys.

2.7.4 Computing the bolometric AGN LF

One of the basic inputs in this thesis is constituted by the *bolometric* AGN LF, that we build up as follows. We start from the AGN luminosity functions at different redshifts, observed in the optical band by Richards et al. (2006), Croom et al. (2009), Masters et al. (2012), Ross et al. (2012), Fan et al. (2006), Jiang et al. (2009), Willott et al. (2010b), and in the hard X-ray band by Ueda et al. (2014), Fiore et al. (2012), Aird et al. (2010). Then, as already mentioned in Sec. 2.7.1 and in Sec. 2.7.2, we apply the Hopkins, Richards & Hernquist (2007) and Ueda et al. (2003, 2014) corrections.

Given the non-homogeneous nature and diverse systematics affecting the datasets exploited to build up the bolometric LF, a formal minimum χ^2-fit is not warranted. We have instead worked out an analytic expression, providing a sensible rendition of the data in the relevant range of luminosity and redshift. For this purpose, we use a modified Schechter function with evolving characteristic luminosity and slopes. The luminosity

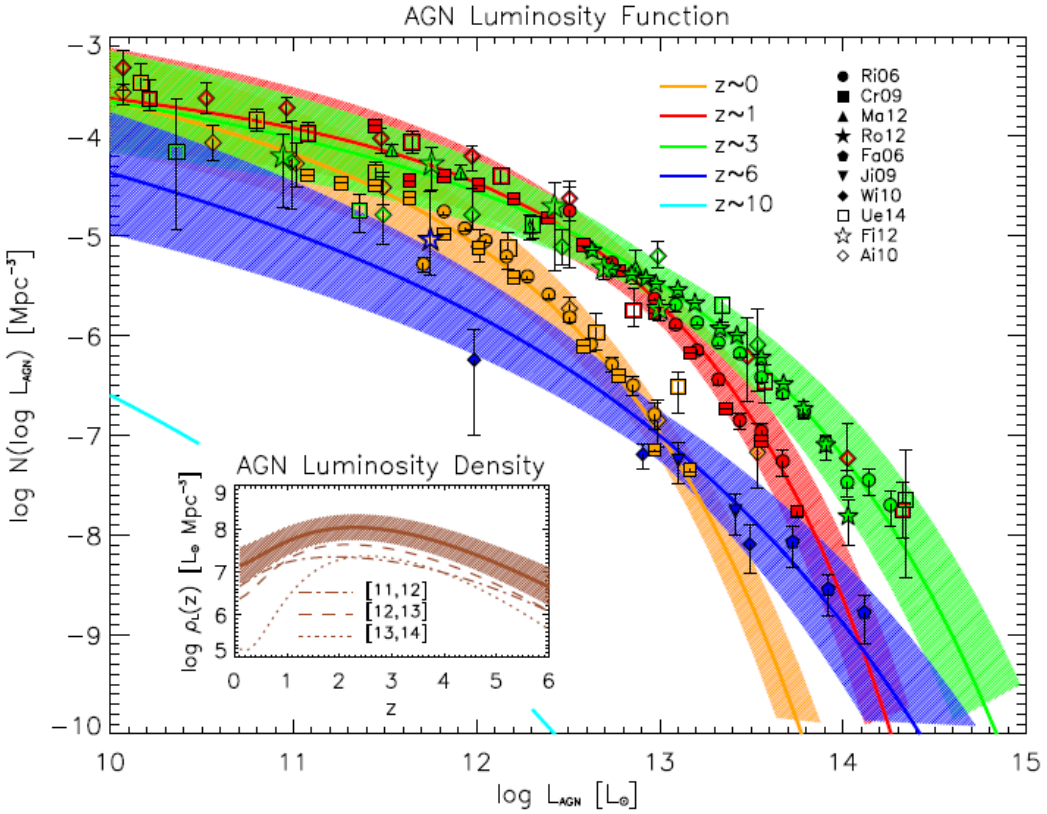

FIGURE 2.4: The bolometric AGN LF $N(\log L_{\rm AGN})$ at redshift $z = 0$ (orange), 1 (red), 3 (green), and 6 (blue). Optical data are from Richards et al. (2006, filled circles), Croom et al. (2009, filled squares), Masters et al. (2012, filled triangles), Ross et al. (2012, filled stars), Fan et al. (2006, filled pentagons), Jiang et al. (2009, filled reversed triangles), Willott et al. (2010b, filled diamonds); X-ray data are from Ueda et al. (2014, open squares), Fiore et al. (2012, open stars), and Aird et al. (2010, open diamonds). The optical and X-ray luminosities have been converted to bolometric ones by using the Hopkins, Richards & Hernquist (2007) corrections, while the number densities have been corrected for the presence of obscured AGNs according to Ueda et al. (2003, 2014). The solid lines illustrate the analytic rendition of the luminosity functions as described in Sect. 2.7.4, while the hatched areas represent the associated uncertainty; the cyan line is the extrapolation to $z = 10$, plotted for illustration. The inset shows the AGN luminosity density as a function of redshift, for the overall luminosity range probed by the data (solid line with hatched area), and for AGN bolometric luminosity $\log L_{\rm AGN}/L_{\odot}$ in the ranges $[11, 12]$ (dot-dashed line), $[12, 13]$ (dashed line), $[13, 14]$ (dotted line).

function in logarithmic bins $N(\log L_{\rm AGN}, z) = N(L_{\rm AGN}, z)\, L_{\rm AGN}\, \ln(10)$ writes:

$$N(\log L_{\rm AGN}, z) = \Phi(z) \left[\frac{L_{\rm AGN}}{L_c(z)}\right]^{1-\alpha(z)} \exp\left\{-\left[\frac{L_{\rm AGN}}{L_c(z)}\right]^{\omega(z)}\right\} . \qquad (2.14)$$

The normalization $\log \Phi(z)$, the characteristic luminosity $\log L_c(z)$, and the characteristic slopes $\alpha(z)$ and $\omega(z)$ evolve with redshift according to the same parametrization:

$$p(z) = p_0 + k_{p1}\, \chi + k_{p2}\, \chi^2 + k_{p3}\, \chi^3 , \qquad (2.15)$$

with $\chi = \log[(1+z)/(1+z_0)]$ and $z_0 = 0.1$. The parameter values are reported in Table 6.1. We stress that the results presented in this thesis are insensitive to the specific parametrization adopted for the luminosity function and its evolution, provided that the quality in the rendition of the data is similar to ours.

In Fig. 2.4, we illustrate the bolometric AGN LF at various redshifts, including both our data collection and our analytic parametrization of Eq. 2.14, with an estimate of the associated 1σ uncertainty; the $z = 10$ extrapolation is also shown, for illustration. In the inset, we plot the evolution with redshift of the AGN luminosity density, computed as:

$$\rho_{L_{\rm AGN}}(z) = \int {\rm d}\log L_{\rm AGN}\, N(\log L_{\rm AGN}, z)\, L_{\rm AGN}\ , \tag{2.16}$$

and the contribution to the total by specific luminosity ranges.

2.8 BH mass estimates

All galaxies, independent of their morphology, seem to host a SMBH. Several techniques have been employed to measure their masses. The methods adopted are different whether they are applied for the SMBH search in active or quiescent galaxies, locally or at high z. In particular, the presence of a SMBH in the central region of inactive galaxies is tested through the velocity dispersion of bulge stars, gas, and water masers. In active galaxies, mass determinations are performed using reverberation mapping or single-epoch spectroscopy of broad emission lines (Hβ, MgII, CIV), depending on redshifts, with the adoption of empirical correlations found between the radius of the BLR and the luminosity of the continuum at different wavelengths. In this section, we will give an overview of the various methods.

2.8.1 Milky Way

The Milky Way provides the most compelling empirical evidence and the most precise measure of the mass of a SMBH. Due to its proximity (D$\sim 8.29 \pm 0.33$ kpc), individual stars can be resolved, and detailed orbital studies are possible, as shown in Fig. 2.5. In particular, star S2 has the shortest orbital period (15.8 yr, Ghez et al. 2008), and has already completed the whole orbit. The motions of all the 28 monitored stars in the central parsec around the SMBH are traced by combining information from the proper motion (projected motion on the sky) and the radial velocity (e.g., Ghez et al. 2005; Gillessen et al. 2009b). The SMBH mass has been obtained by fitting the orbit

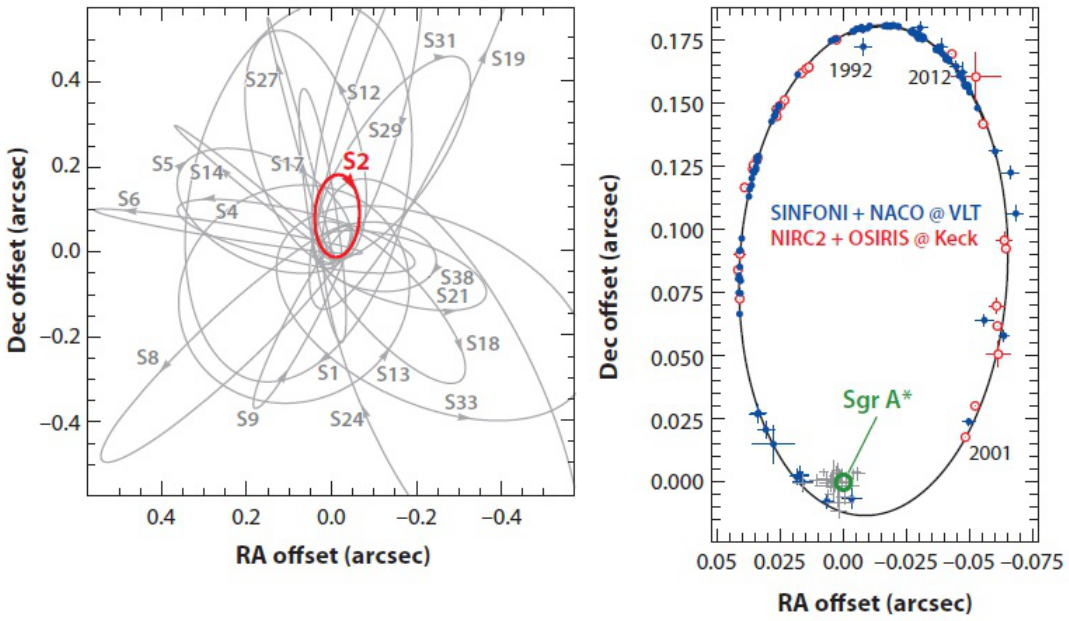

FIGURE 2.5: Left panel: Orbits of individual stars near the Galactic center. The arrows show the direction of the motion. Right panel: Orbit of the star S2 around the SMBH associated to the radio source Sgr A* (large green open circle), based on observation of its position from 1992 to 2012. Red open circles have been obtained by Ghez et al. (2008), blue filled dots have been obtained by Gillessen et al. (2009a). The figure has been updated from Genzel, Eisenhauer & Gillessen (2010) and reported by Kormendy & Ho (2013).

parameters under the assumption that the monitored stars are moving into the gravitational potential of the SMBH, represented by a point mass. The most recent estimate is $M_{\rm BH} = (4.31 \pm 0.36) \times 10^6 M_\odot$ (Gillessen et al. 2009b).

2.8.2 Stellar dynamics

Due to the crowded fields, it is not possible to resolve individual star orbits even in nearby galaxies. Thus, measurements of the rotational velocity and/or velocity dispersion of the stellar distribution in the bulge are used to infer the presence of a SMBH. This method requires the measurement of the stellar velocity from the width of absorption lines, and the modelling of the stellar motions. Both photometry, to measure the density distribution of the stars, and spectroscopy, to measure their kinematics, are needed. Stellar photometric and kinematics observations have been performed for several objects with the *Hubble Space Telescope* (HST) or with ground-based telescopes with adaptive optics (e.g., Magorrian et al. 1998; Gebhardt et al. 2000b; Ferrarese & Merritt 2000; Krajnović et al. 2009; Gültekin et al. 2009a; McConnell et al. 2011, 2012).

Concerning the modelling, impressive improvements have been made since the seminal paper by Sargent et al. (1978), who used spherical, isotropic models to estimate the

BH mass of M87). At present, the most widely adopted are the three-integral models based on Schwarzschild (1979, 1993) orbit superposition method, which allow to choose axisymmetric or triaxial potentials. While most dynamical models assume axisymmetry (e.g., van den Bosch & de Zeeuw 2010; Cappellari et al. 2009), a modelling code for triaxial systems has also been developed and applied to measure SMBH masses (e.g., Cappellari et al. 2006; van den Bosch et al. 2008; Walsh et al. 2012).

The dynamical models are asked to fit weighted and superposed stellar orbits to line-of-sight velocity distributions (LOSVDs) extracted from spectroscopic data; the quantities to be determined are the central SMBH mass and the mass-to-light (M/L) ratio of the stellar population, usually assumed to be constant with radius. Because of this radial independence, the contribution of the DM halo to the potential in the dynamical models is an important issue.

Until 2009, the potential was calculated from the contribution of only the SMBH and the stars, without DM halo. Including it makes the estimated SMBH mass increase, because some of the mass density at large radii is attributed to DM, an so the M/L ratio (being constant) must decrease not only there, but also in the central regions. To maintain a good fit to the kinematics data, the SMBH mass has necessarily to be increased. This problem has been discussed first by Gebhardt & Thomas (2009), and then further examined in depth by, e.g., Schulze & Gebhardt (2011) and Rusli et al. (2013).

To constrain the models, the inclination i of the galaxy is needed. Constrains on i are weak, because it couples with the SMBH mass and the M/L ratio. This is the reason why variations of i cause only little systematic effect. Usually, in stellar dynamics modelling, galaxies are assumed to be edge-on (e.g., Gebhardt et al. 2003; Gültekin et al. 2009a).

2.8.3 Gas dynamics

Emission lines originating from a circumnuclear rotating disc can be used as a tool to interpret the dynamics of the ionized gas. Optical nebular line emission is detectable at ground-based and HST resolution (Hughes et al. 2005; Shields et al. 2007) in the central few hundred parsecs of all spirals, and in roughly half of S0 and elliptical galaxies. The observed line velocities are compared to the predictions of a model where the gas is confined in a thin disc that rotates in Keplerian motion, $V(r) \propto r^{-1/2}$, around the SMBH (e.g., Macchetto et al. 1997; van der Marel & van den Bosch 1998; Barth et al. 2001; Maciejewski & Binney 2001; Marconi et al. 2001, 2003). The aim is to match the observed velocities, velocity dispersions, and surface brightness distribution of the line emission, with the BH mass, the inclination i of the disc, and its projected position angle

as free parameters. Also in this case, i is often poorly constrained using just kinematics of the discs, so a significant fraction of the error bar in the estimate of the SMBH mass is due to the uncertainty in the disc orientation, since $M_{\rm BH} \propto 1/\sin^2 i$.

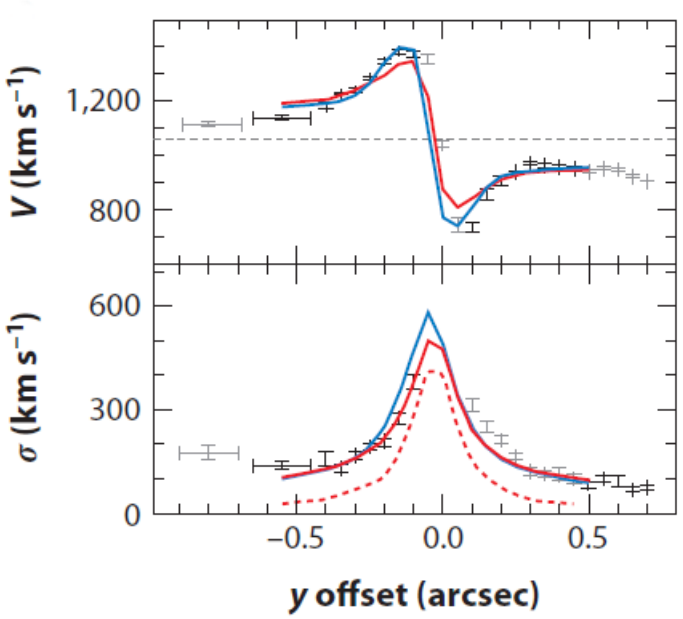

FIGURE 2.6: The radial profiles of [NII] λ6583 mean velocity and velocity dispersion (in km s^{-1}) along the central slit position, as analysed by Walsh, Barth & Sarzi (2010), obtained with the Space Telescope Imaging Spectrograph (STIS) by Bower et al. (1998). Superposed are predictions of the best BH model with (blue curve) and without (red solid curve) correction for asymmetric drift. The red dotted curve shows the contribution from rotational line broadening. The figure has been taken from Kormendy & Ho (2013).

The main assumption is that the gas motion is influenced only by gravitational forces from the stars and the central SMBH. This requirement is often not fulfilled by the majority of galaxies, spirals and S0 in particular, since the gas can be influenced by turbulence, radiation pressure, shocks, hydromagnetic acceleration, and other nongravitational perturbations. Moreover, the instrumental resolution is an other issue.

NGC 4374 (Walsh, Barth & Sarzi 2010), shown in Fig. 2.6, is the only galaxy, among the ones studied with HST, whith a sphere of influence at so high resolution that is possible to see the Keplerian rotation. All considered, dynamical analysis is successful in determining the SMBH mass only in roughly 20% of nearby bulges.

However, gas-dynamics methods made possible to obtain a considerable quantity of upper limits (Ratnam & Salucci 2000; Sarzi et al. 2002; Verdoes Kleijn, van der Marel & Noel-Storr 2006; Beifiori et al. 2009, 2012), which have been used to put constraints on BH-host galaxy or BH-DM halo scaling relations.

2.8.4 Water maser dynamics

Among dynamical methods, the observation of water maser is one of the most accurate ones, because it allows to reach an excellent angular resolution, up to a few milliarcseconds. This technique consists in measuring strong stimulated emission at radio wavelengths from the circum-BH molecular gas disc. Moreover, it allows to study objects which are difficult to explore with other methods, such as gas rich starforming galaxies, optically obscured sources, or AGNs. In fact, it works particularly well for Seyfert 2 galaxies, where the dust torus around the central SMBH is seen edge-on, as water maser emission is seen only when observing almost in the orbital plane of the emission.

The best example for the use of this technique is the Seyfert 2 galaxy NGC 4258 (for a complete literature, see Lo 2005). Very Large Baseline Array (VLBA) observations reveal that the high velocity (~ 1000 km s^{-1}) water emission originates from molecular clouds that trace a thin and nearly edge-on gas disc (Miyoshi et al. 1995; Moran 2008), making their dynamics easy to interpret. The emission region defines nearly perfect Keplerian orbits, shown in Fig. 2.7, constraining the SMBH mass through $M_{\rm BH} = V^2 r/G$ to be $(3.81 \pm 0.04) \times 10^7$ M$_\odot$ for an adopted distance of 7.27 Mpc. (Herrnstein et al. 2005; Siopis et al. 2009; Kormendy & Ho 2013). Similar measurements were done for other sources (e.g., Greenhill et al. 2009; Reid et al. 2009; Braatz et al. 2010; Greene et al. 2010, 2013; Kuo et al. 2011; Wardle & Yusef-Zadeh 2012). However, the maser emission can be observed only in limited cases: it is detected in about 10% of the nearby Seyfert 2 galaxies (Kondratko, Greenhill & Moran 2006), as it requires particular inclination and relatively low absorption (Czerny & Nikołajuk 2010).

2.8.5 Reverberation mapping

Dynamical methods requiring good spatial resolution are generally not applicable to AGNs, because they are typically far away, and because the active nuclei overwhelm the stellar spectral features. The most robust method to obtain the mass of the central SMBH powering an AGN is the reverberation mapping of the BLR, which consists in analyzing the non-thermal continuum and the broad emission lines seen in the spectrum. This technique is particularly useful to determine SMBH masses in Type 1 AGNs, in which the BLR is not hidden by the dust torus.

The continuum is due to accretion onto the SMBH, that radiates energy and excited the surrounding gas, so Doppler-broadening the emission lines of the BLR. Thus, the broad line variations are interpreted as a delayed response to the continuum ones. The size of the BLR ($R_{\rm BLR}$) can be inferred by measuring this time lag τ and assuming light travel

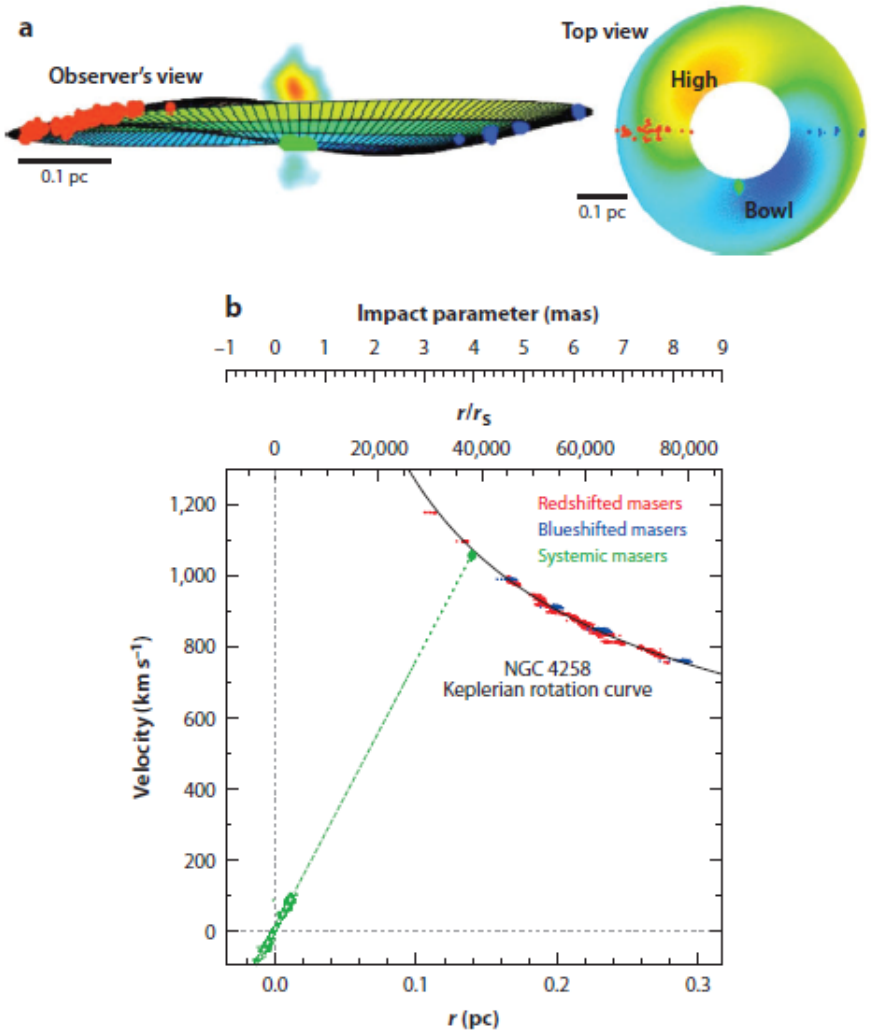

FIGURE 2.7: (a) Schematic views of the almost edge-on, warped maser disc of NGC 4258 (from Moran 2008) with warp parameters from Herrnstein et al. (2005), including the inner contours of the radio jet. The relative positions of the receding, near-systemic, and approaching masers are indicated by red, green, and blue spots, respectively. (b) NGC 4258 rotation curve V(r) as a function of radius in units of parsecs (bottom axis), Schwarzschild radii (top axis), and milliarcseconds (extra axis). The black curve is a Keplerian fit to 4255 velocities of red- and blue-shifted masers (red and blue dots, respectively). The small green points and line show 10036 velocities of near-systemic masers and a linear fit to them. The green filled circle is the corresponding mean V(r) point. The maser data are taken from Argon et al. (2007). The figure has been taken from Kormendy & Ho (2013).

time, through $R_{\rm BLR} = c\tau$. Applying the virial theorem, and assuming that the motion of the emitting clouds is dominated by the gravitational field of the central SMBH, its mass can be derived by measurable quantities, namely the time delay and the width of the emission lines, as (following the notation of Shen 2013):

$$M_{\rm BH} = \frac{V_{\rm vir}^2 R_{\rm BLR}}{G} = f\frac{W_{\rm line}^2 R_{\rm BLR}}{G} \ , \tag{2.17}$$

where $V_{\rm vir}^2$ is the virial velocity, and $W_{\rm line}^2$ is the width of the broad line, used for practical purposes as an indicator of the virial velocity, under the assumption that the lines are broadened by the virial motion of the emitting gas. The quantity f is called virial coefficient, or geometrical factor, and takes into account the details on the structure of the gas (inclination, geometry), though with a rather high degree of uncertainty. Its value depends not only on the assumed geometry, but also on the choice of using the "full-width-at-half-maximum" (FWHM) or the line dispersion ($\sigma_{\rm line}$) as a measure of the line width.

As an example, for BLR clouds in randomly orientated orbits, $f = 3/4$ if $W_{\rm line} = {\rm FWHM}$, or $f = 3$ if $W_{\rm line} = \sigma_{\rm line}$ (Peterson 2014). Nowadays, the value of f is empirically determined requiring an external calibration of the zero-point through correlations between SMBH masses and host-galaxy properties (mainly imposing that the masses obtained with the reverberation mapping lie on the $M_{\rm BH} - \sigma$ relation of local inactive galaxies), which are assumed to be the same for the host galaxies of active and quiescent SMBHs (e.g., Gebhardt et al. 2000b; Onken et al. 2004; Peterson 2014; Grier et al. 2013). The most commonly adopted values are $f = 1.4$ if $W_{\rm line} = {\rm FWHM}$, or $f = 5.5$ if $W_{\rm line} = \sigma_{\rm line}$, even though calibration for individual objects can give slightly different values. The uncertainty in reverberation mapping mass estimations is dominated by the uncertainty on f, and is typically $0.4 - 0.5$ dex (Peterson 2014).

An alternative to the problem of the unknown geometry has been proposed by Pancoast, Brewer & Treu (2014), who presented a phenomenological model of the BLR. They used direct modelling of the integrated emission line light curve to measure the mean time lag, and the full spectroscopic dataset of emission line profiles to constrain the geometry and the dynamics of the BLR. In this way, the BH mass can be inferred without the need of the factor f, and the uncertainty in the mass determination reduces to $0.05 - 0.25$ dex.

The most remarkable finding of reverberation mapping is that the time lag for the emission-line response to continuum variations is longer in more luminous objects. This traduces in a tight correlation between the BLR size and the optical continuum luminosity (typically measured at $\lambda \sim 5100$ Å, restframe), $R_{\rm BLR} \propto L^{1/2}$ (Kaspi et al. 2000, 2005;

Bentz et al. 2009a). This is well-established only for Hβ, but the more limited reverberation results for CIV are consistent with the same relationship. This radius-luminosity (R-L) relationship provides the underpinning for indirect methods of measuring SMBHs of quasars over cosmic times.

2.8.6 Single epoch determinations

Reverberation mapping is the only method that is potentially extendable to high redshift, through the R-L relationship. In this case, BH masses are estimated with the so called single epoch determinations, also known as BH mass scaling methods.

The BLR size is estimated by measuring the quasar continuum luminosity L and then using the R-L relationship. Combining this result with the measured width W of a specific broad emission line, with opportune coefficients, the mass estimators read as (following the notation of Shen 2013):

$$\log\left(\frac{M_{\rm BH}}{M_\odot}\right) = a + b\log\left(\frac{L}{10^{44}{\rm erg/s}}\right) + c\log\left(\frac{W}{\rm km/s}\right) \ , \tag{2.18}$$

where a, b, and c are calibrated from the sample of local AGNs with reverberation mapping mass estimates (e.g., Kaspi et al. 2000, 2005; Bentz et al. 2009b). In some cases, in which the continuum can be significantly contaminated by the host starlight (e.g., Greene & Ho 2005) or by jet emission in radio-loud objects (e.g., Wu et al. 2004), line luminosities are preferred to the continuum luminosity, even though their correlation with the BLR size is more scattered. In the literature, different line or continuum luminosities, in optical, UV or X-ray bands, have been used (e.g., Wandel, Peterson & Malkan 1999; Vestergaard 2002; McLure & Jarvis 2002; McLure & Dunlop 2004; Vestergaard & Peterson 2006; Kollmeier et al. 2006; Onken & Kollmeier 2008; Wang et al. 2009; Vestergaard & Osmer 2009; Greene, Peng & Ludwig 2010; Shen et al. 2011; Shen & Liu 2012; Trakhtenbrot & Netzer 2012).

The most commonly used line-luminosity pairs are Hβ (or eventually Hα) with L_{5100}, MgII with L_{3000}, and CIV with L_{1350} or L_{1450}. All the continuum luminosities and several line luminosities correlate to each other, with different scatters. While the MgII FWHM correlates with Hβ FWHM reasonably well, the correlation between the CIV FWHM and MgII FWHM is poor (see also, e.g., Shen et al. 2008; Fine et al. 2008, 2010), as illustrated in Fig. 2.8, showing some correlations between different continuum luminosities, obtained using the spectral measurements of Sloan Digital Sky Survey (SDSS) quasars from Shen et al. (2011). It seems that the high-ionization CIV line is a biased virial mass estimator (e.g., Baskin & Laor 2005; Sulentic et al. 2007; Netzer et al. 2007; Shen et al. 2008; Marziani & Sulentic 2012, and references therein), because

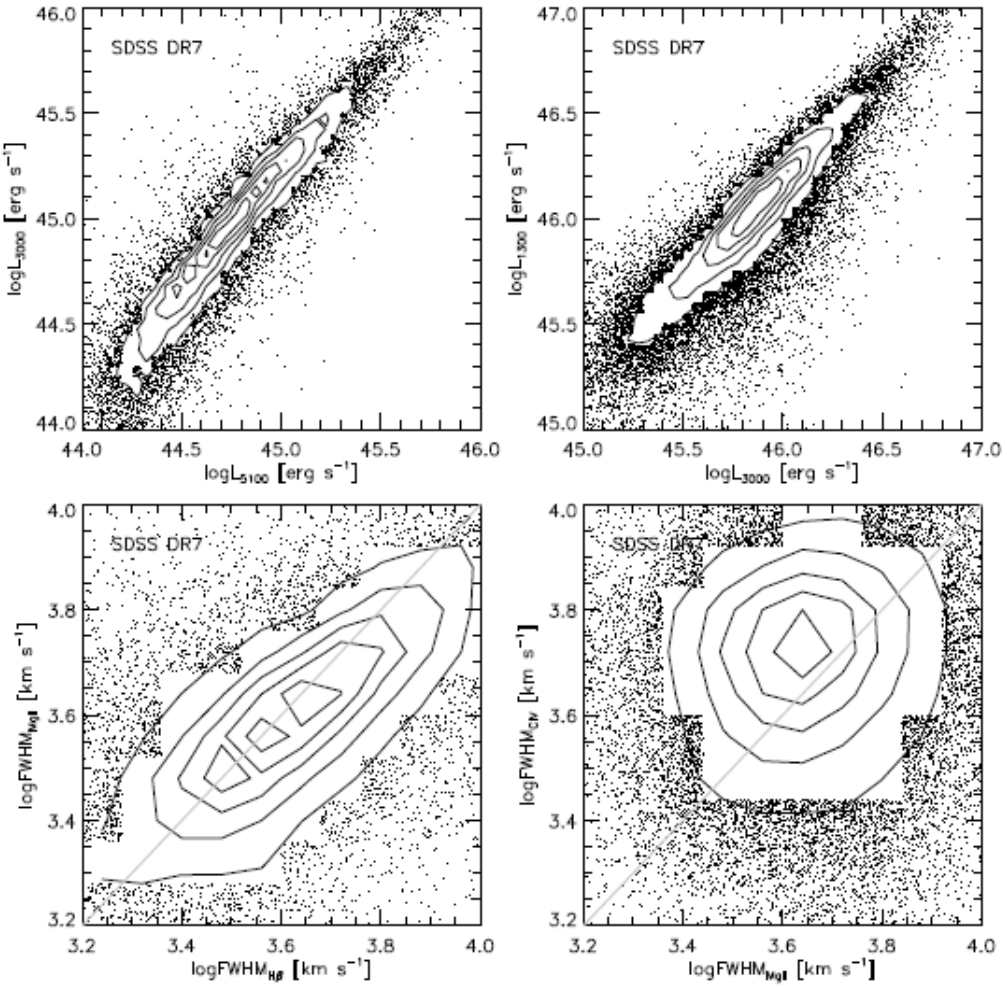

FIGURE 2.8: Comparisons between different continuum luminosities and line FWHMs, using SDSS quasar spectra that cover two lines. Shown here are the local point density contours. Measurements are taken from Shen et al. (2011). The upper panels show the correlations between continuum luminosities, and the bottom panels show the correlations between line FWHMs. The figure has been taken from Shen et al. (2011).

it is probably affected by a non-virial component, such as a radiatively-driven (and/or MHD-driven) accretion disc wind (e.g., Konigl & Kartje 1994; Murray et al. 1995; Proga, Stone & Kallman 2000; Everett 2005), especially for high-luminosity objects.

At present, calibrations exist for Hα (McLure & Dunlop 2001), Hβ (Georgakakis et al. 2009), MgII (McLure & Dunlop 2002; McLure & Jarvis 2002; Merloni 2004), and CIV (Georgakakis et al. 2009). The statistical scatter in the virial mass estimates is currently evaluated to be ~ 0.4 dex (Georgakakis et al. 2009), although there are indications that the scatter may be smaller, at least for the most luminous quasars (Merritt & Ferrarese 2001; Merloni, Heinz & di Matteo 2003; Merloni, Heinz & Di Matteo 2005; Merloni et al. 2010; Merloni & Heinz 2008). The statistical scatters for Hβ and CIV are estimated by comparing masses derived from these lines with those derived from reverberation

mapping (Georgakakis et al. 2009). Instead, there is currently no direct estimate of the statistical scatter in MgII-based virial mass estimates, because the calibration is obtained by enforcing consistency in the mean values of this mass estimator and the Hβ and CIV ones. All considered, Hβ seems to be the most reliable line to use for single epochs estimates, but it can be measured only up to $z \lesssim 1$. In absence of the Balmer lines, MgII can be used up to $z \sim 2$. CIV can be observed up to much higher redshifts ($z \lesssim 5$), but its application should proceed with some caution. Fig. 2.9 shows a sample of SDSS BH masses, obtained with different emission lines. The redshift ranges in which each line is reliable are clearly visible.

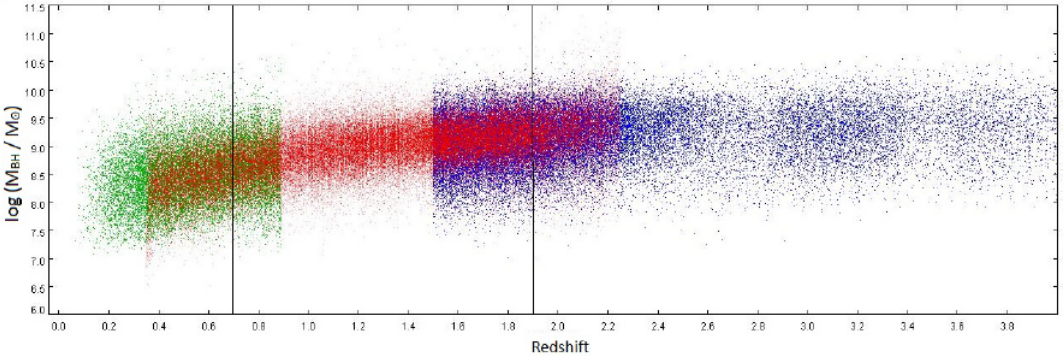

FIGURE 2.9: BH masses estimated for a SDSS catalogue of 105783 quasars, obtained with different emission lines, Hβ (green dots, Vestergaard & Peterson 2006), MgII (red dots, Shen et al. 2011), CIV (blue dots, Vestergaard & Peterson 2006). Figure curtesy of R. D'Agostino.

2.9 SMBH Mass Function

The BH mass function (BHMF) in logarithmic bins, denoted as:

$$N(\log M_{\rm BH}, z) = N(M_{\rm BH}, z)\, M_{\rm BH}\, \ln(10)\ , \tag{2.19}$$

is the number of sources per comoving cosmic volume $V(z)$ with BH masses in the range $\log M_{\rm BH}, \log M_{\rm BH} + d\log M_{\rm BH}$. It describes the evolution of the distribution of BH masses at each redshift.

The BHMF is observationally determined from large surveys, but two caveats are in order (Kelly, Vestergaard & Fan 2009):

1. As can be inferred from Sec. 2.8, it is not possible to obtain reliable mass estimators for large numbers of SMBHs through dynamical or virial direct methods, due to the large uncertainties of the determinations. Thus, scaling relationships between BH mass and host galaxy properties, or single epoch estimators are invoked. However,

this relationships have in turn an intrinsic scatter, that amounts to 0.29 ± 0.02 dex when correlating $M_{\rm BH}$ with σ, and 0.30 ± 0.01 dex with the $K-$band magnitude (Kormendy & Ho 2013) or the IR luminosiy of the bulge (Marconi & Hunt 2003; Sani et al. 2011). The intrinsic BHMF has to be convolved with this scatter, resulting in a broadening of the BHMF, in particular at the high mass end, as clearly illustrated in Fig. 2.10. At present, this problem cannot be avoided, because the scaling relationships constitute the only feasible way to estimate BH mass for the huge number of sources in the surveys.

2. Surveys are usually selected on flux, not mass, criteria. At a given SMBH mass, there is a distribution of luminosities, and so some masses can scatter around the flux limit. This creates a so called selection function, defined as the probability of including an object in a sample as a function of its measured quantities, which is less sensitive to SMBH mass, and can cause incompleteness of the survey, even in every mass bin.

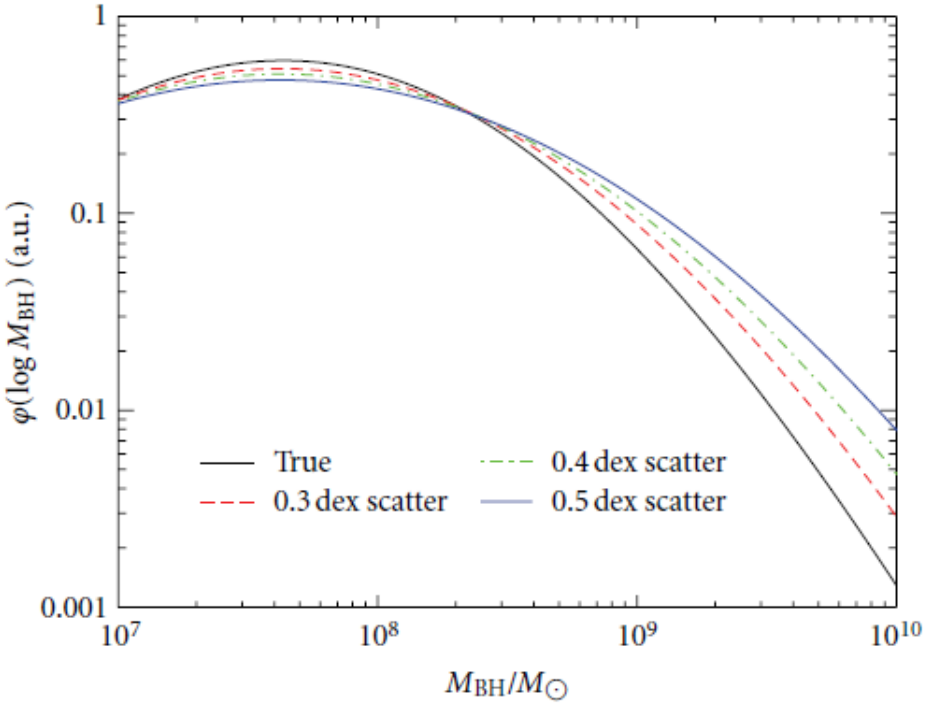

FIGURE 2.10: Illustration of the bias in the estimated BHMF derived from mass estimates. The true mass function is shown (thick solid black line) for a simulated sample, together with the mass function derived from the mass estimates with a scatter of 0.3 dex (red dashed line), 0.4 dex (green dot-dashed line), and 0.5 dex (solid blue thin line). The mass function derived from the mass estimates is more biased with increasing BH mass and scatter. The figure has been taken from Kelly & Merloni (2012).

2.9.1 BHMF at $z = 0$

There are two ways to estimate the local BHMF. The first method allows to obtained an unbiased mass function. The basic steps are the following:

1. Assume a BHMF;
2. Calculate the distribution of mass estimates and of observable quantities, used to select the sample, implied by the assumed mass function. This step needs the assumption of the relationships between the mass function and the observable quantities, but is necessary to correct for incompleteness;
3. Impose the selection function for the sample;
4. Compare the predictions with the observed distributions; if they are not consistent, the assumed BHMF and/or the relationship between the mass function and the observable quantity can be ruled out. In practice, this is done by deriving the likelihood function for the BHMF.

The second method is commonly used to estimate the local BHMF, using the empirical BH-galaxy scaling relationships to calibrate the total mass distribution of BHs (e.g., Marconi et al. 2004; Shankar, Weinberg & Miralda-Escudé 2013), once the galaxy distribution, expressed as a function of a given measured variable (e.g., the stellar velocity dispersion or bulge luminosity/stellar mass) is known. The basic implicit assumption is that all galaxies host a SMBH. Specifically, the BHMF is computed taking into account the scatter in the $M_{\rm BH}$-galaxy relations (e.g., Salucci et al. 1999). In a statistical sense, the two methods should provide equivalent results.

Recent attempts in this direction have been made by a number of groups (e.g., Hopkins et al. 2006, 2008; Cao & Li 2008; Yu & Lu 2008; Shankar, Weinberg & Miralda-Escudé 2009), leading to significant conclusions. Their BHMF construction methods vary: some of them convolve the $M_{\rm BH} - L$ relation with the AGN luminosity function (Salucci et al. 1999; Shankar, Weinberg & Miralda-Escudé 2009; Vika et al. 2009), while others use the $M_{\rm BH} - \sigma$ relation with the local velocity dispersion function (VDF; Aller & Richstone 2002), and some use both (McLure & Dunlop 2004; Shankar et al. 2004; Shankar, Weinberg & Miralda-Escudé 2013).

Shankar et al. (2012) estimated the BHMF for pseudobulges, which are significantly undermassive with respect to the scaling relations followed by their counterpart BHs in classical bulges (Hu 2008; Greene, Ho & Barth 2008; Graham & Li 2009).

Meanwhile, Tundo et al. (2007) discussed whether L or σ is a better predictor of BHMF, given the inconsistency in the BHMFs derived from the two relationships. Two considerations are in order: The first one is the assumption that the $M_{\rm BH}$-host property relationship is a single power law; this is still an open question, although many authors (e.g., Cirasuolo et al. 2005; Lauer et al. 2007; Bernardi et al. 2007) suggest that the $M_{\rm BH}-\sigma$ relation is unlikely to be a single power law. The second issue concerns the intrinsic scatter of the relationships. It is generally believed that a better estimate of the $M_{\rm BH}$ distribution can be obtained by adopting the relation with smaller scatter. Indeed, Marconi et al. (2004) stated that relationships with similar scatter should provide equivalent descriptions of the distribution of $M_{\rm BH}$. However, even when the scatter has been accounted for, the $M_{\rm BH}-\sigma$ relationship predicts fewer massive BHs than the $M_{\rm BH}-L$ does. This is because the $\sigma-L$ relation in the currently available BH samples is inconsistent with that in the samples from which the distributions of L or σ are based: the BH samples have smaller L for a given σ, or larger σ for a given L.

2.9.2 BHMF at $z > 0$

Assuming that SMBHs assemble their mass predominantly through accretion during luminous phases of quasar activity, it is possible to identify the BHMF as an integral quantity mapped by the AGN LF. Expanding the Soltan (1982) argument, the BHMF at any cosmic time t can be calculated as the accreted mass distribution implied by the AGN LF integrated up to that time. This can be operationally exploited through a continuity equation formalism (Small & Blandford 1992), which describes the evolution of the SMBH number density:

$$\partial_t N(M_{\rm BH},t) + \partial_{M_{\rm BH}}[\langle \dot{M}_{\rm BH}\rangle\, N(M_{\rm BH},t)] = S(M_{\rm BH},t)\ ; \tag{2.20}$$

where $\partial_x = \partial/\partial x$, $\langle \dot{M}_{\rm BH}\rangle$ is the mean accretion rate, and $S(M_{\rm BH},t)$ is a source term describing the triggering rate of nuclear activities of BHs, in particular dry merging.

Knowing from Sec. 2.1 that the accretion rate of matter onto the BH is related to the bolometric luminosity through the radiative efficiency ϵ as $L = \epsilon \dot{M}_{\rm acc} c^2$, and that the growth rate of the SMBH is $\dot{M}_{\rm BH} = (1-\epsilon)\dot{M}_{\rm acc}$ because of radiative losses, Eq. 2.20 can be written as:

$$\partial_t N(M_{\rm BH},t) + \frac{1-\epsilon}{\epsilon c^2}\partial_{M_{\rm BH}}[\langle L(M_{\rm BH},t)\rangle\, N(M_{\rm BH},t)] = S(M_{\rm BH},t)\ . \tag{2.21}$$

Using this equation, the BHMF can be calculated at any redshift corresponding to t, assuming a lightcurve and a distribution of radiative efficiencies, which can be constrained by observations of the local BHMF and the AGN LF. A bolometric correction needs also

to be assumed, which itself depends on both BH mass and Eddington ratio $\lambda_{\rm Edd}$, and suffers considerable uncertainty, as already illustrated in Sec. 2.7.1.

Many authors have employed Eq. 2.21, assuming a lightcurve in which the Eddington ratio is constant (Yu & Tremaine 2002; Marconi et al. 2004; Shankar et al. 2004; Shankar, Weinberg & Miralda-Escudé 2009), slightly dependent on L (Salucci et al. 1999), on z and $M_{\rm BH}$ (Shankar, Weinberg & Miralda-Escudé 2009), or on the different population of AGNs (obscured or not obscured, Raimundo & Fabian 2009). A quasar lightcurve undergoing a powerlaw decay has been modeled by, e.g., Yu & Lu (2008) and Cao (2010). Ueda et al. (2014) determined the BHMF at $z \sim 3$ using the hard X-ray luminosity function and assuming, following Li (2012), that the Eddington ratio distribution function is log-normal, and is independent of luminosity and redshift.

Willott et al. (2010a) estimated the BHMF at $z \sim 6$ through the observed luminosity function (Willott et al. 2010b) obtained from 40 optically selected quasars from the SDSS and the Canada-France High-z Quasar Survey (CFHQS) and the $\lambda_{\rm Edd}$ distribution obtained using the BH masses of 17 CFHQS+SDSS quasars, determined with the MgII emission line widths and L_{3000}. Their approach is slightly different from other authors, because rather than attempt to invert the observed luminosity function to determine the BHMF, they instead use model BHMFs to produce luminosity functions which are then fit to the quasar samples.

Tamura, Ohta & Ueda (2006) investigated the SMBH mass function up to $z \sim 1$ from spheroids luminosity functions, assuming a z-dependent $M_{\rm BH} - L_{\rm sph}$ correlation, given by the passive evolution of $L_{\rm sph}$. The most important source of uncertainty suffered by this derivation of the BHMF is related to the scatter in the local scaling relationships, especially at the high-mass end, as already mentioned (see Fig. 2.10. Other uncertainties may be due to the loose constrains on the bulge-to-total (B/T) luminosity ratio, and to the choice of the passive evolution.

Li, Ho & Wang (2011) have derived the mass function of inactive SMBHs up to $z \sim 2$ using the K-band galaxy luminosity obtained by Cirasuolo et al. (2010) and the stellar mass function computed by Pérez-González et al. (2008) for a sample of galaxies for which they could obtain rest-frame NIR photometry using Spitzer/Infrared Array Camera observations, and were able to calculate stellar masses by fitting the SEDs from the UV to the MIR bands. The BHMF has been estimated adopting a B/T ratio to transform the total galaxy luminosity to the spheroid luminosity, $M_{\rm BH} - L_{\rm bulge}$ and $M_{\rm BH} - M_{\rm bulge}$ scaling relationships to pass from measured spheroid luminosities or masses to BH masses, and a prescription for the passive evolution with redshift of the scaling relationships to account for the evolution of the stellar population. Since this method is very similar to the one used by Tamura, Ohta & Ueda (2006), the derivation of the BHMF suffers the

same limitations mentioned above. In this case, an other source of uncertainty can be ascribed to the IMF assumed to compute stellar masses (see Sec. 3.1).

An alternative way to infer the BHMF, avoiding the assumption of a quasar lightcurve, is to empirically estimate the accretion rate from the observed distribution of $\lambda_{\rm Edd}$ using the BH fundamental plane (linking BH mass, radio luminosity, and X-ray luminosity), as was done by Merloni, Heinz & di Matteo (2003), and Merloni & Heinz (2008). A limit of this method is that the BH fundamental plane is defined only for objects with $\lambda_{\rm Edd} \lesssim 10^{-2}$, so it has to be extrapolated to higher accretion rates, where most of the BH mass growth seems to occur. Moreover, the uncertainties on the bolometric corrections and the radiative efficiency also apply here.

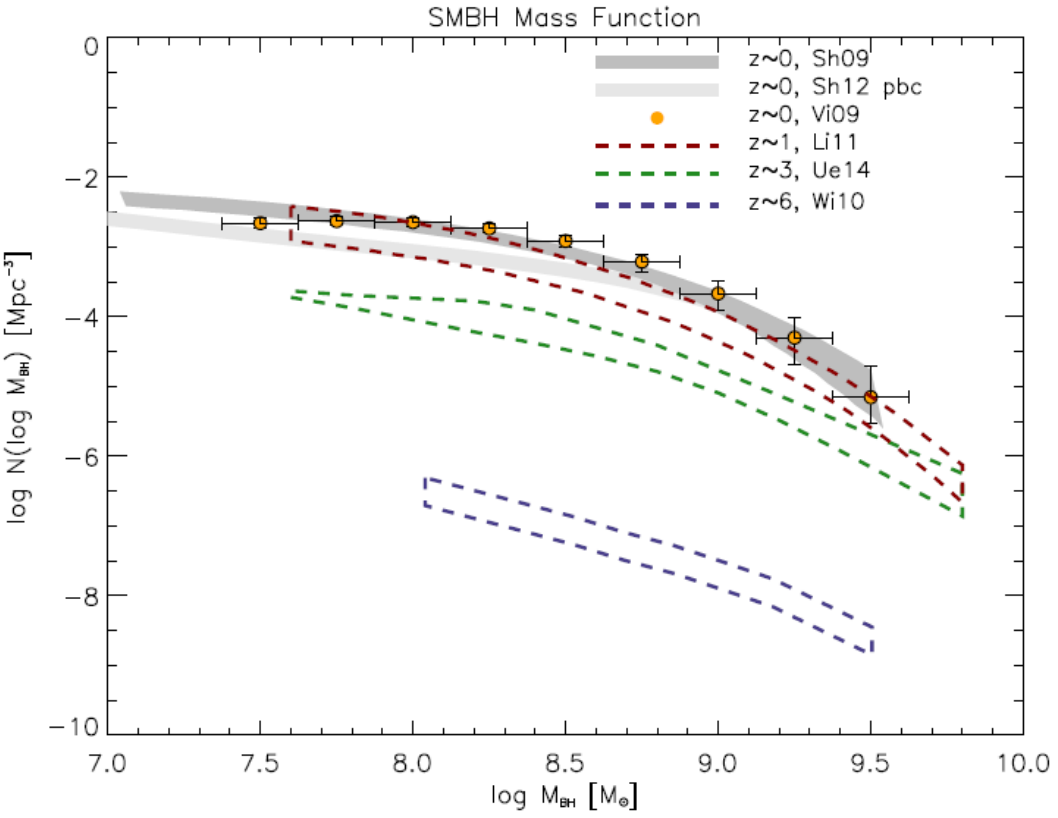

FIGURE 2.11: Observational estimates of the BHMF. The dark grey shaded area illustrates the collection of estimates at $z = 0$ by Shankar, Weinberg & Miralda-Escudé (2009), built by combining the SMF or the VDF with the $M_{\rm BH} - M_\star$ or $M_{\rm BH} - \sigma$ relations of elliptical galaxies; the light grey shaded area is the $z = 0$ determination by Shankar et al. (2012), corrected to take into account the different relations followed by pseudobulges. The orange circles are the determination at $z = 0$ by Vika et al. (2009). The red dashed area illustrates the determination at $z \sim 1$ by Li, Ho & Wang (2011), the green dashed area shows the range of models by Ueda et al. (2014) at $z \sim 3$, and the blue dashed area the estimate by Willott et al. (2010a) at $z \sim 6$.

We illustrate in Fig. 2.11 a collection of recent BHMF estimates available in the literature, at $z = 0$ (Shankar, Weinberg & Miralda-Escudé 2009; Shankar et al. 2012; Vika

et al. 2009), $z \sim 1$ (Li, Ho & Wang 2011); $z \sim 3$ (Ueda et al. 2014), and at $z \sim 6$ (Willott et al. 2010a).

2.9.3 BHMF of broad line AGNs

As already seen in Sec. 2.8.6, SMBH masses of broad line AGNs can be estimated from single epoch measurements, provided that the scaling relationship between the continuum luminosity and the BLR size derived locally from reverberation mapping is applicable also at high redshift.

Once virial masses are available, they can be binned up applying the $1/V_{\rm max}$ correction to estimate the BHMF of broad line AGNs (e.g., Wang, Chen & Zhang 2006; Greene & Ho 2007; Vestergaard et al. 2008; Vestergaard & Osmer 2009), in a similar way as done for luminosity function observations.

In detail, Vestergaard et al. (2008) estimated the BHMF for broad line AGNs at $0.3 < z < 5$ using data from the SDSS data release (DR) 3, while Greene & Ho (2007) presented the local broad line AGNs BHMF obtained from the SDSS DR4, and Vestergaard & Osmer (2009) estimated the BHMF for the brightest broad line AGNs up to $z = 5$; Nobuta et al. (2012) used quasars from the Subaru XMM-Newton Deep Survey (SXDS) and BH masses estimated from MgII and L_{3000} to build up the BHMF and the Eddington ratio distribution function of X-ray-selected broad line AGNs at $z \sim 1.4$. The mass functions obtained by all these authors have been derived from measurements on individual sources, so provide a more direct estimate with respect to those based on the continuity equation (e.g., Tamura, Ohta & Ueda 2006). However, the results are biased by both the large statistical scatter in the single epoch masses, as pointed out in Sec. 2.8.6, and by the incompleteness in $M_{\rm BH}$, which cannot be solved by a luminosity-based $1/V_{\rm max}$ correction, as the BH mass selection function is not equivalent to the flux selection function, as explained in Sec. 2.10. Kelly, Vestergaard & Fan (2009) tried to correct for both these problems: first, they derived the likelihood function relating the broad line AGNs BHMF to the observed distribution of redshifts, luminosities, and broad emission line widths, and then developed a Bayesian approach to obtain the BHMF when single epoch masses are used.

Other authors presented different methods: Shen et al. (2008) employed a forward-modelling approach to estimate broad line AGNs BHMF and Eddington ratio distribution by matching the observed mass and luminosity distributions to the ones implied by their model, while Shen & Kelly (2010, 2012), and Kelly & Shen (2013) adopted a Bayesian method to estimate the BHMF for broad line AGNs and the Eddington ratio distribution up to $z \lesssim 5$ using the SDSS DR7. Incompleteness and statistical

scatter in mass estimates are taken into account by all these autors. Also Schulze & Wisotzki (2010), and Schulze et al. (2015) were able to correct for incompleteness, using a maximum-likelihood technique to estimate the BHMF for broad line AGNs and the Eddington ratio at $z = 0$ and $1 < z < 2$, respectively, from different optical surveys. However, they do not take into account the scatter in single epoch mass estimates.

As a final remark, it must be noted that broad line AGNs mass functions are only representative of a poorly constrained (in particular as a function of BH mass) fraction of the whole active SMBH population.

2.10 Seed Black Holes

Observations of AGNs at $z \gtrsim 6$ (e.g., Fan 2006; Mortlock et al. 2011) confirm the existence of BHs with masses $M_{\rm BH} \sim 10^9 M_\odot$ when the age of the Universe was only ~ 1 Gyr. Observational limitations prevent the discovery of smaller BHs at such high redshifts. However, it is likely that the number of smaller mass BHs far exceed that of the most massive objects. This implies that massive BHs must have been rather common in the early universe, short after the first stars were born. The first stage of growth of the SBMHs is represented by the so called *seed* BHs, which are thought to be in place as early as $z \sim 10 - 20$. There are three main scenarios describing the physical processes that lead to the formation of seed BHs, schematically illustrated in Fig. 2.12 (see Volonteri 2010 for a review). We will briefly describe them in the following.

2.10.1 Population III stars

The theory of structure formation in a Universe dominated by cold dark matter (CDM) involves a bottom-up collapse of local perturbations on larger and larger scales (White & Rees 1978. This hierarchical growth takes place when the initial density perturbations enter the nonlinear regime. The first galaxies form from the baryons in the first halos, and started their growth where the age of the Universe was less that 0.5 Gyr. The cooling of the baryons leads to the formation of the first stars, and of the first generation of seed BHs. The Population III (Pop III) stars are very massive objects, with masses $\gtrsim 100\, M_\odot$ and very short lifetime (a few Myr), which were formed from zero-metallicity gas. Low-metallicity stars of $M_\star \sim 100\, M_\odot$ are thought to directly form BHs with masses which are roughly half of their initial stellar mass. When $M_\star \sim 200\, M_\odot$, pair production becomes important, and leads to supernova (SN) explosions without a compact remnant. At still higher mass, $M_\star \lesssim 250\, M_\odot$, BHs with about half the initial mass are the final result of the stellar evolution. Thus, Pop III remnant BHs with masses $M_{\rm BH} \sim 100\, M_\odot$

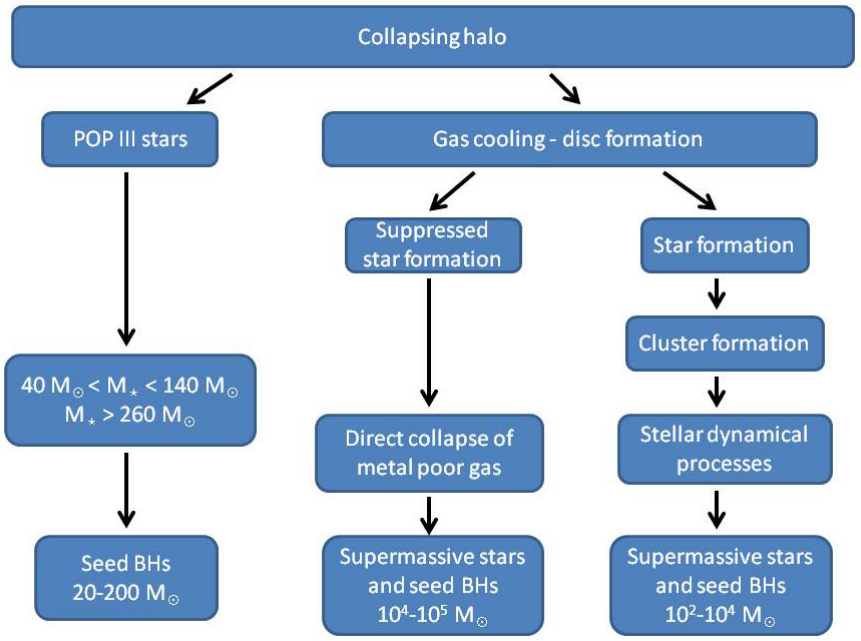

FIGURE 2.12: Schematic view of different scenarios for the formation of seed BHs in high redshift galaxies. The figure has been adapted from Volonteri (2010).

are predicted by some models (Haiman & Loeb 2001; Abel, Bryan & Norman 2000, 2002; Bromm & Larson 2004; Volonteri & Rees 2006; Tanaka & Haiman 2009) to possibly grow up to the observed SMBHs.

2.10.2 Direct collapse

An other class of seed BHs is speculated to result from the direct collapse of very massive clouds of dense gas (Haehnelt & Rees 1993; Loeb & Rasio 1994; Eisenstein & Loeb 1995; Bromm & Loeb 2003; Koushiappas, Bullock & Dekel 2004; Begelman, Volonteri & Rees 2006; Lodato & Natarajan 2006; Choi, Shlosman & Begelman 2013, 2015). Such metal-poor clouds are thought to exist in the center of protogalaxies. Unlike metal-enriched gas clouds, very low-metallicity ones are inefficient in cooling, hence they retain their original mass and temperature, without fragmenting. If the angular momentum of the cloud is low, than collapse can happen. The final product of collapse are supermassive stars, which evolve and produce BHs which continue to accrete from the surrounding gas. Seeds BHs with masses in the range $10^4 - 10^5 M_\odot$ can be formed at the end of this process.

2.10.3 Dynamical stellar processes

The last suggested scenario involves dynamical interactions in dense stellar systems formed at the earlier stages of the collapse (Begelman & Rees 1978; Ebisuzaki et al. 2001; Miller & Hamilton 2002; Portegies Zwart & McMillan 2002; Portegies Zwart et al. 2004; Freitag, Rasio & Baumgardt 2006; Freitag, Gürkan & Rasio 2006). Fragmentation and formation of low mass stars happen after gas has been enriched by Pop III star formation in small halos (Omukai, Schneider & Haiman 2008). This efficient star formation can cause the formation of very compact nuclear star clusters, where stellar dynamical processes, as star collisions, can lead to the formation of massive stars ($M_\star \lesssim 100\,M_\odot$) and consequently to seed BHs with typical masses of $10^2 - 10^4 M_\odot$ (Devecchi & Volonteri 2009; Lupi et al. 2014).

Chapter 3

Basics of Star Formation in galaxies

The mass and luminosity functions of the stellar component in galaxies impose important constraints on star formation theories. As an example, conversion of the stellar luminosity function (SLF) to a mass function (SMF) through a mass-luminosity relation gives information about how many stars form in a given mass interval, and how the stellar mass has grown. It is worth recalling that the contribution to the stellar mass content is mainly due to old, low mass stars ($M \lesssim 1\,M_{\odot}$), emitting primarily in the K-band, while high mass stars ($M \gtrsim 1\,M_{\odot}$), emitting in the UV, are the major contributors to the stellar luminosity.

In this Chapter, we will present the basic issues concerning the star formation process in galaxies, highlighting the important role of dust. We also show some recent observational results, which show how the complementarity of UV and FIR data is essential when dealing with strongly starforming objects.

3.1 Initial Mass Function

The stellar initial mass function (IMF) describes the relative probability of stars of different masses that were initially formed along the main sequence. It underlies the relation between mass, light and age of a stellar population, and gives information about the ratio of bright, high mass, UV emitting stars, that dominate the light, to faint, low mass, K-band emitting stars, that dominate the mass. Moreover, it regulates the luminosity and color evolution of the integrated stellar population, as the evolution rate depends on the stellar mass.

The most widely used functional form is a power law, as originally proposed by Salpeter (1955) for stellar masses in the range $\sim 1 - 100\,M_{\odot}$:

$$\xi(\log m) = \frac{dN}{d\log m} = C\,m^{-x}\ , \tag{3.1}$$

where N is the stellar number density per logarithmic mass bin, C is a normalization constant, and x is the power law exponent, which is still rather uncertain; Scalo (1986) claimed $x \sim 1.7$ to adequately describe the IMF of massive ($m \gtrsim 1\,M_{\odot}$) stars, however the Salpeter value $x = 1.35$ is usually adopted as a reference.

The second widely adopted form for the IMF is a Gaussian distribution, as suggested by Miller & Scalo (1979), which extends below $1\,M_{\odot}$:

$$\xi(\log m) = \frac{A}{\sqrt{2\pi}\sigma}\exp\left[-\frac{(\log m - \log m_c)^2}{2\sigma^2}\right]\ , \tag{3.2}$$

where A is a normalization constant, while $\log m_c$ and $\sigma^2 = (\log m - \log\langle m\rangle)^2$ denote the mean mass and the variance in $\log m$, respectively.

Other commonly used forms of the IMF are the Kroupa (2001) broken power law, and the Chabrier (2003), well described by a power law form at $m \gtrsim 1\,M_{\odot}$, and a log-normal form below this limit.

Fig 3.1 compares different IMFs by plotting the mass fraction per dex versus stellar mass, i.e., normalized so that the integral under each curve is unity. The Kennicutt (1983), the Kroupa (2001), the Baldry & Glazebrook (2003) and the Chabrier (2003) IMFs (indicated as solid lines) are considered the best renditions, for reasonable M/L ratios and galaxy colors. The Baldry & Glazebrook analysis favoured a slope shallower than the Salpeter one at the high-mass end, based on constraints from local luminosity densities and cosmic star-formation history (SFH); IMFs with high-mass slopes steeper than the Kennicutt were ruled out as candidates for a universal IMF. The extrapolation of the Salpeter IMF (dotted line) below $1\,M_{\odot}$ results in an excess of low mass stars. On the other hand, the Miller & Scalo (1979), the Scalo (1986)), and the Kroupa, Tout & Gilmore (1993) IMFs (indicated as dashed lines) have too few high mass stars. They were based on galactic disc measurements, which cannot be used to accurately infer the high-mass end, because of the complicated SFH of the Galaxy.

The Salpeter IMF, being too rich in low-mass stars, might overestimate the stellar masses. Those derived with the Chabrier IMF are smaller than the Salpeter ones by a factor of ~ 1.7 (e.g., Pozzetti et al. 2007). This lead to a decrease of the SMF at the low-mass end by a factor of $\sim (1.7)^{1+\alpha}$. For a characteristic value $\alpha \sim -1.2$ (Pérez-González et al. 2008), the SMF decreases slightly by ~ 0.05 dex (Li, Ho & Wang 2011).

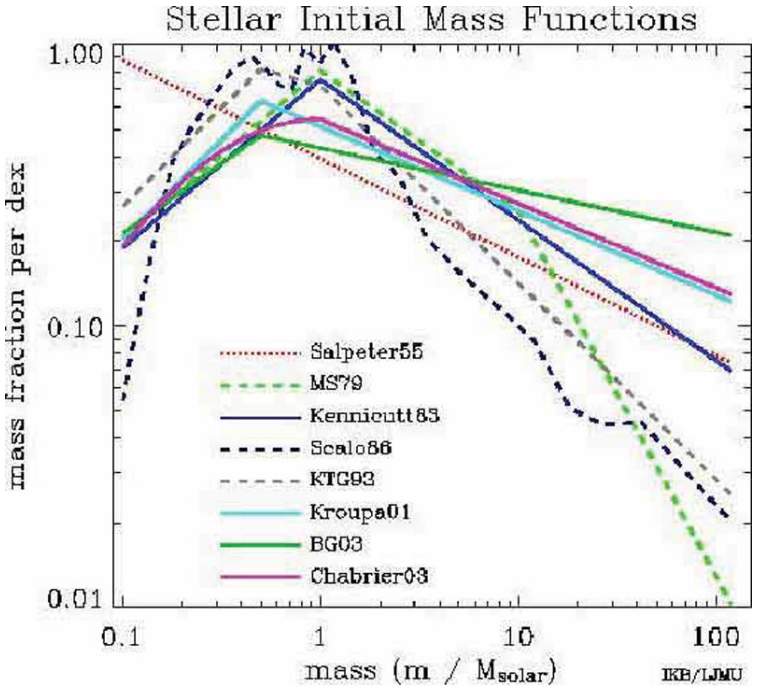

FIGURE 3.1: Comparison of different IMFs. The fraction per dex (i.e., normalized so that the integral under each curve is unity) is plotted as a function of stellar mass. Red dotted line: Salpeter (1955); Green dashed line: Miller & Scalo (1979); Blue solid line: Kennicutt (1983); Black dashed line: Scalo (1986); Grey dashed line: Kroupa, Tout & Gilmore (1993); Cyan solid lines: Kroupa (2001); Green solid line: Baldry & Glazebrook (2003)); Magenta solid line: Chabrier (2003). They are assumed to be valid from 0.1 to 120 $M_{\odot}$. The figure has been taken from Ivan Baldry's Research webpage.

Moreover, the different IMFs result in different luminosities and SEDs for a stellar population, as well as different overall rates of gas return and metal ejection from dying stars. Following the notation of Madau & Dickinson (2014), the restituted fraction R, i.e. the mass fraction that is put back into the ISM, and the metal ejection y, i.e. the mass of heavy elements ejected into the ISM, can be derived from:

$$R = \int_{m_0}^{m_{max}} \mathrm{d}m\, \xi(m)(m - m_r) \ , \tag{3.3}$$

where m_r is the remnant stellar mass, and from:

$$y(1 - R) = \int_{m_0}^{m_{max}} \mathrm{d}m\, \xi(m) y_m\, m \ , \tag{3.4}$$

where y_m is the stellar yield, i.e. the fraction of the stellar mass m that is converted to heavy elements and ejected. Taking $m_0 = 1\, M_{\odot}$ as the dividing stellar mass for instantaneous recycling[1], the restituted fraction is $R_{\mathrm{Salp}} \sim 0.3$ for a Salpeter IMF and

[1]Under the assumption of instantaneous recycling, the release and mixing of the nucleosynthesis products occur on a timescale $t \ll t_H$ for stars with $m > m_0$, and $t \gg t_H$ for stars with $m < m_0$, i.e. they live forever.

$R_{\rm Chabr} \sim 0.4 > R_{\rm Salp}$ for a Chabrier IMF, because it is more weighted toward short-lived massive stars; the metal ejections are $y_{\rm Salp} \sim 0.2$, and $y_{\rm Chabr} \sim 0.3$ for a Salpeter and a Chabrier IMF, respectively. The exact values depends on the assumed domain of integration, stellar yield, metallicity, and time elapsed from the burst. In fact, for the Chabrier IMF, the mass in old, less massive stars approaches $(1 - R_{\rm Chabr}) \approx 0.5$ when the time elapsed is larger than a few Gyr. Since we shall exploit the continuity equation also at relatively short cosmic times ($z \gtrsim 1$), in this thesis we adopt the value $(1 - R) \approx 0.6$, corresponding to $\tau_{\rm burst} \sim 1$ Gyr (see Chapter 4).

The IMF is not directly observed. It cannot be uniquely inferred from photometric measurements of the integrated light of galaxies, because there is a strong degeneracy among metallicities, ages and colors. Usually, the most direct constraints on the IMF come from:

- The present-day SLF by using a stellar mass-age-luminosity relation, obtained from theories of stellar evolution, together with a model of how the SFR varies with time;
- Counts of sub-solar dwarf stars as a function of mass in resolved, nearby stellar population;
- Integrated kinematics measurements (velocity dispersion or rotation curve) of the M/L ratio in galaxies or star clusters, in order to derive a mass, which is then compared to the luminosity.

These methods are difficult to apply for faint galaxies at high redshift, so a universal IMF is usually assumed, with the same shape at each z and for each galaxy.

3.2 Dust

When the radiation hits a dust particle, it can be scattered as well as absorbed. Therefore, the total amount of radiation screened by the dust particle in the line of sight is the sum of the absorbed and scattered intensities. This quantity is defined as the total extinction by the dust particles. Dust extinction is an effect that must often be assumed or inferred, rather than directly measured. In order to understand the nature of the material responsible for producing the interstellar extinction, it is necessary to know the variation of the extinction as a function of the wavelength of the incident radiation. This curve is generally known as extinction curve, or extinction law, and its shape depends on the properties of the dust grains causing the extinction. The simplest

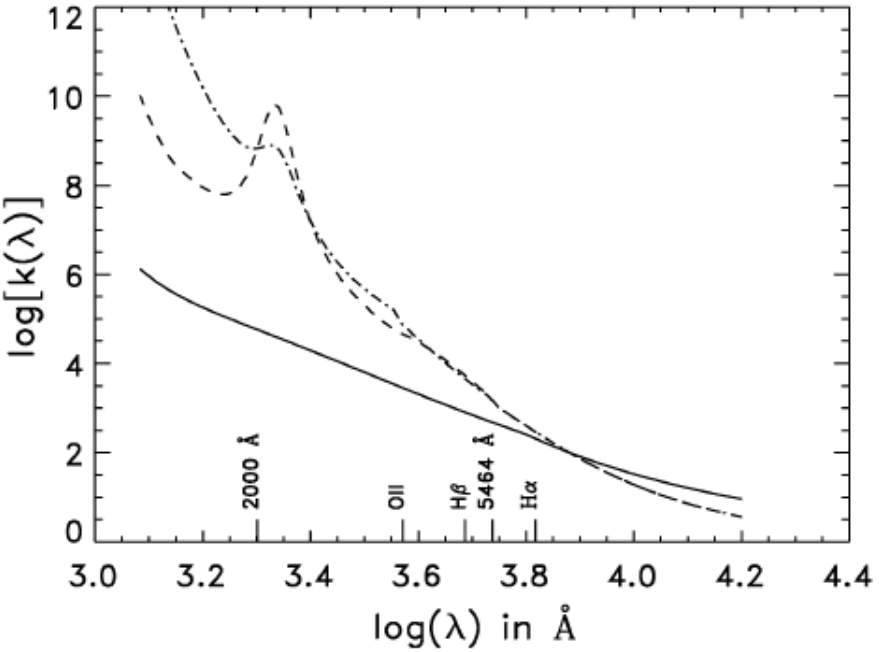

FIGURE 3.2: Extinction curves. The solid line is the empirical relation given by Calzetti (1999); the dashed line is the curve for the Galaxy by Seaton (1979) and Howarth (1983); the dot-dashed line is the curve for the Large Magellanic Cloud by Howarth (1983). The figure has been taken from Rosa-González, Terlevich & Terlevich (2002).

way to get the wavelength dependence of the extinction is by comparing two stars of the same spectral type, one of which has plenty of material in front, while the other has not. The difference in their observed intensities with wavelength arises mainly due to the properties of the intervening material. Extinction curves have been derived for the Milky Way (e.g., Seaton 1979; Howarth 1983), for the Large Magellanic Cloud (e.g., Howarth 1983), and for other local galaxy samples both empirically (e.g., Calzetti, Kinney & Storchi-Bergmann 1994; Calzetti 1999; Calzetti et al. 2000) and using theoretical modeling (Charlot & Fall 2000). Fig. 3.2 shows some of these extinction curves.

For observations of a single star, photons may be absorbed by dust or scattered out of the observed line of sight. This problem is even more serious in galaxies, where photons may be scattered both into and out of the line of sight, and the optical depth of dust will be different for each star. These effects are generally grouped together into the simplifying assumption of a mean dust attenuation curve. However, there are many differences among galaxies, and no mean attenuation law is equally appropriate for all of them. Galaxies with huge star formation activity are completely obscured by dust, especially in the UV part of the spectrum (Buat et al. 2005; Burgarella, Buat & Iglesias-Páramo 2005). Uncorrected UV luminosities can underestimate the SFRs by more than one order of magnitude, with more starforming galaxies suffering higher attenuations (e.g.,

Wang & Heckman 1996; Treyer et al. 2007; Hao et al. 2011). Appropriate corrections for dust attenuation are therefore essential.

The most common approaches used to estimate the dust attenuation in the UV are:

- The power law slope of the UV continuum β ($f_\lambda \propto \lambda^\beta$), in the wavelength range $1300 - 2600$ Å(Calzetti, Kinney & Storchi-Bergmann 1994; Calzetti 1999; Calzetti et al. 2000; Bouwens et al. 2012, 2014; Mashian, Oesch & Loeb 2015): this estimator is based on the strong assumption that β is only sensitive to dust attenuation, so it does not depend on, e.g., the mean age of the dust-heating population, the dust/star geometry, or the dust properties;
- The ratio of IR to UV emission (often referred to as IRX): the amount of dust attenuation can be inferred by considering the FIR radiation as the reprocessed emission of all the starlight absorbed by the dust at optical and UV wavelengths (energy balance argument; e.g., Wang & Heckman 1996; Heckman et al. 1998; Meurer, Heckman & Calzetti 1999; Hao et al. 2011). In principle, the IRX ratio is a more reliable dust attenuation indicator with respect to the Calzetti power law slope, because it is almost independent of the dust properties and the relative distribution of dust and stars (e.g., Buat & Xu 1996; Gordon et al. 2000; Cortese et al. 2006, 2008);
- The attenuation in the Hα line, derived from the Balmer line ratio Hα/Hβ (also referred to as the Balmer decrement): starting from the idea that the SFR derived from dust-corrected Hα luminosity matches that from dust-corrected UV luminosity, the attenuation can be estimated either by using the observed Hα/UV emission ratio, or by assuming a dust attenuation law (e.g., Buat et al. 2002; Treyer et al. 2007). However, this indicator suffer large systematic uncertainties, because it is strongly model dependent.

In a recent work, Hao et al. (2011) applied the second method to derive attenuation corrections in a sample of local galaxies, both using the IR to far-UV (FUV) luminosity ratio and the far-near UV (FUV-NUV) color. As the authors noticed, color corrected-FUV luminosities underestimate the SRFs for galaxies which are strongly forming stars, and show large luminosity-dependent uncertainties: a dust correction based only on UV colors is not enough, proving the fundamental importance of IR data for investigating dust extinction. However, it must be stressed that the sample used by Hao et al. (2011) is composed by sources with SFR $\lesssim 100\, M_\odot \mathrm{yr}^{-1}$, so it is not representative of strongly dust-enshrouded starforming galaxies at $z \gtrsim 1$, which can reach SFR $\gtrsim 10^3\, M_\odot\ \mathrm{yr}^{-1}$ (Lapi et al. 2011; Gruppioni et al. 2013). On the other hand, for IRX $\gtrsim 10$, the FUV

information becomes dominated by high uncertainties, and so the estimation of the attenuation correction is less reliable.

When only UV data are available, the correlation between the β and the IRX ratio is largely used to estimate the dust attenuation (Meurer, Heckman & Calzetti 1999). While initially proposed only for low redshift galaxies, the method has been tested and applied also to high redshifts (Reddy et al. 2010; Overzier et al. 2011; Bouwens et al. 2013, 2014). However, for large values of β and of the attenuation, the spread around the correlation becomes huge (Overzier et al. 2011; Reddy et al. 2010) and the estimate of attenuation becomes quite uncertain, even in local samples (e.g., Howell et al. 2010; Hao et al. 2011). On the other hand, the estimate of attenuation for UV-selected samples is less dispersed for galaxies with low SFRs ($\dot{M}_\star \lesssim 1\,M_\odot\ \mathrm{yr}^{-1}$). In such instances, the correction to UV luminosity is more secure, and relatively small on average (Bouwens et al. 2013). In fact, this is also suggested by the UV attenuation inferred by combining the Hα attenuation and the Calzetti extinction curve (Hopkins et al. 2001; Mancuso et al. 2015).

The mean dust attenuation increases with redshift up to $z \sim 1 - 1.5$, where it reaches a maximum. After the peak, it decreases rapidly with increasing z. As shown by Madau & Dickinson (2014) and Cai et al. (2014), the mean dust attenuation is low at $z \gtrsim 6$, when the metallicity of the intergalactic medium (IGM) is lower than the solar value by a factor $\sim 10^{-3}$. Thus, UV measurements are likely to be a reliable SFR diagnostic at these redshifts, being IR measurements not possible due to current instrumental limits. However, we caution that a few galaxies with high SFRs and substantial dust extinction have been found by Riechers et al. (2013) and Watson et al. (2015)).

3.3 Galaxy Spectral Energy Distribution

The SEDs of galaxies are shaped by their physical properties and contain information on galaxy stellar, gaseous, and dust content. In particular, properties as redshift, age of the stellar population, IMF, total mass in stars, metallicity, physical state and quantity of gas and dust can be inferred via the SED fitting. This procedure consists in comparing theoretical templates to observations, in order to find the properties of the models that best resemble the data. The most extensively used SED modeling technique is the stellar population synthesis, which is a method for creating a galactic spectrum through the sum of the spectra of its stars (e.g., Charlot & Bruzual 1991; Bruzual A. & Charlot 1993; Bressan, Chiosi & Fagotto 1994; Worthey 1994; Fioc & Rocca-Volmerange 1997; Maraston 1998; Leitherer et al. 1999; Vazdekis 1999, see also the review papers by Walcher et al. 2011; Conroy 2013). In the last 20 years, models have been developed to

simultaneously and self-consistently predict galaxy SEDs from the UV to the FIR (e.g., Silva et al. 1998; Devriendt, Guiderdoni & Sadat 1999; da Cunha, Charlot & Elbaz 2008; Groves et al. 2008; Noll et al. 2009). An example of model fit from the UV to the FIR SED, obtained by da Cunha, Charlot & Elbaz (2008), is shown in Fig 3.3. Their phenomenological model includes intrinsic starlight emission (the blue line), a dust attenuation model (which depresses the starlight emission at sub-mm wavelengths in order to fit the data, black line), an empirical spectrum for the polycyclic aromatic hydrocarbons (PAHs) emission (seen in the region centered at $\sim 10\,\mu$m), and the dust emission, separated into dust in the diffuse ISM (solid green line) and dust in starforming regions (dotted green line).

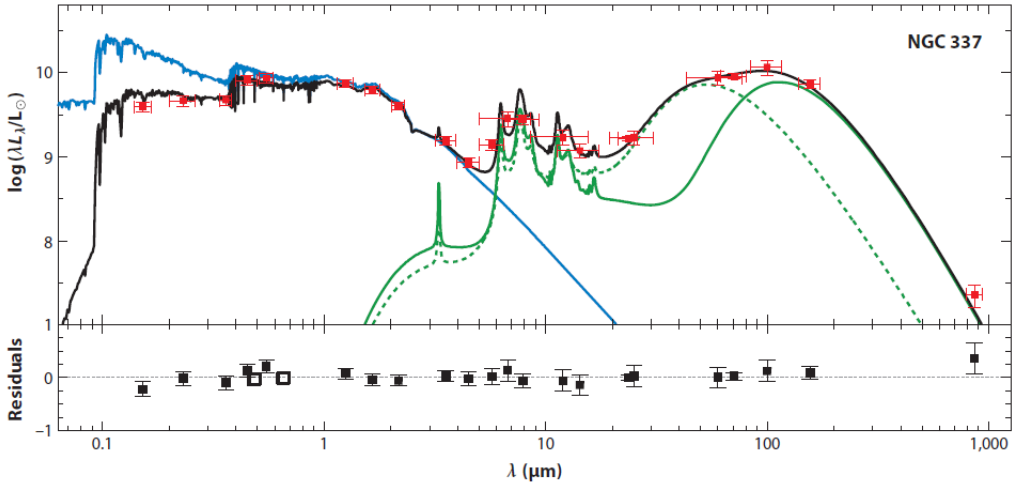

FIGURE 3.3: Model fit from the FIR to the UV SED of NGC 337. Observational data point are in red. The black line is the best-fit model. Also shown are the unattenuated model starlight (blue line) and the dust emission, separated into dust in the diffuse ISM (solid green line) and dust in starforming regions (dotted green line). The figure has been taken from da Cunha, Charlot & Elbaz (2008).

The bulk of the emission from galaxies is produced from UV to sub-mm wavelengths ($\sim 0.1 - 1000\,\mu$m; e.g., Kennicutt & Evans 2012). It is primarily due to stellar light and, if present, to the AGN. The peak of the intrinsic emission from the stellar population is located at UV-NIR wavelengths, and corresponds to the (approximate) blackbody radiation from stars over a range of masses and ages (Kurucz 1979). Starlight is often attenuated by the presence of dust, due to young or still forming stars, which thermally re-radiate the emission at FIR wavelengths ($\lambda \sim 100\,\mu$m). Thus, the emission from galaxies undergoing intense star formation is most efficiently detected at FIR wavelengths, while the majority of the emission from quiescent galaxies is observed at UV-NIR wavelengths. An explicative comparison between a dusty (starforming) and a non-dusty (quiescent) galaxy SED, as obtained from composite stellar populations modeling, is shown in Fig. 3.4.

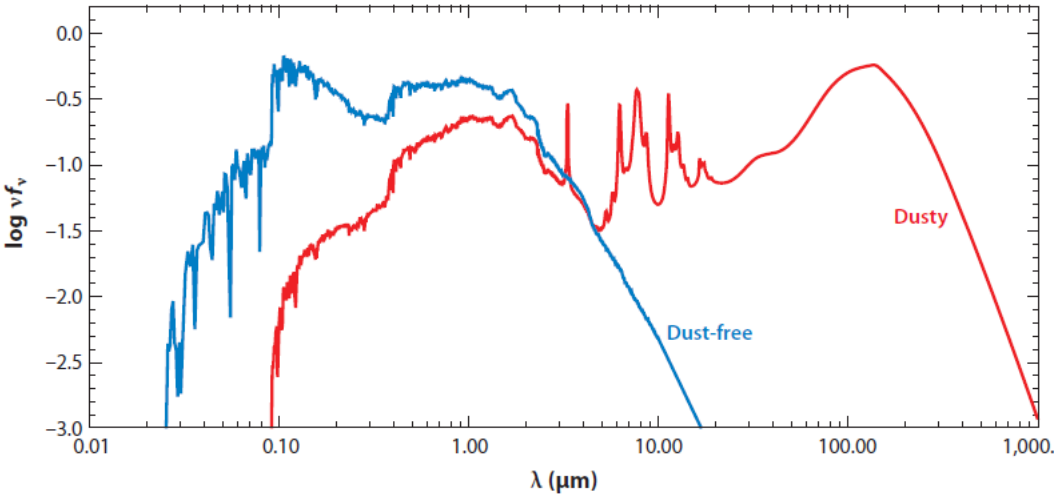

FIGURE 3.4: Models of a dusty (red) and a dust-free (blue) SED from composite stellar populations. The figure has been taken from Conroy (2013).

As already mentioned, also AGNs are luminous in the IR band, due to the thermal emission from the dusty torus around the accretion disc. However, the temperature of the torus dust is a least one order of magnitude higher than that of the stellar dust. Thus, the emission from the AGN is peaked to shorter MIR wavelengths ($\sim 40\,\mu$m; e.g., Netzer et al. 2007; Mullaney et al. 2011) and does not contaminate IR-based SFR estimates. In general, we can assume that the FIR portion of the spectra is reliable for SFR estimates, as it is dominated by the emission of dust associated with star formation, although a contribution from the torus may be not completely negligible (e.g., Granato & Danese 1994; Vega et al. 2008; Leipski et al. 2013).

A full panchromatic SED analysis should include also radio emission, as it constitutes an independent constraint on the star formation in starbursting galaxies (Bressan, Silva & Granato 2002; Prouton et al. 2004; Vega et al. 2008; Mancuso et al. 2015). As an example, we show in Fig. 3.5 the broadband SED of IRAS 14348-1447, modeled by Vega et al. (2008) using the population synthesis code GRASIL (Silva et al. 1998). Both thermal (orange three dots-dashed line) and non-thermal (green long dashed line) radio emission are included. The cyan dot-dashed line represents the AGN component, which contributes to 8.4% of the IR emission from this source.

3.4 Star Formation rate diagnostics

There are several well established diagnostic methods for measuring the SFR in star forming galaxies (see the reviews of Kennicutt 1998; Kennicutt & Evans 2012). The SFR can be estimated from lines (mainly Lyα and Hα) or from continuum emission (FUV, IR, radio and X-ray). Each indicator has its own limits: for example, we already

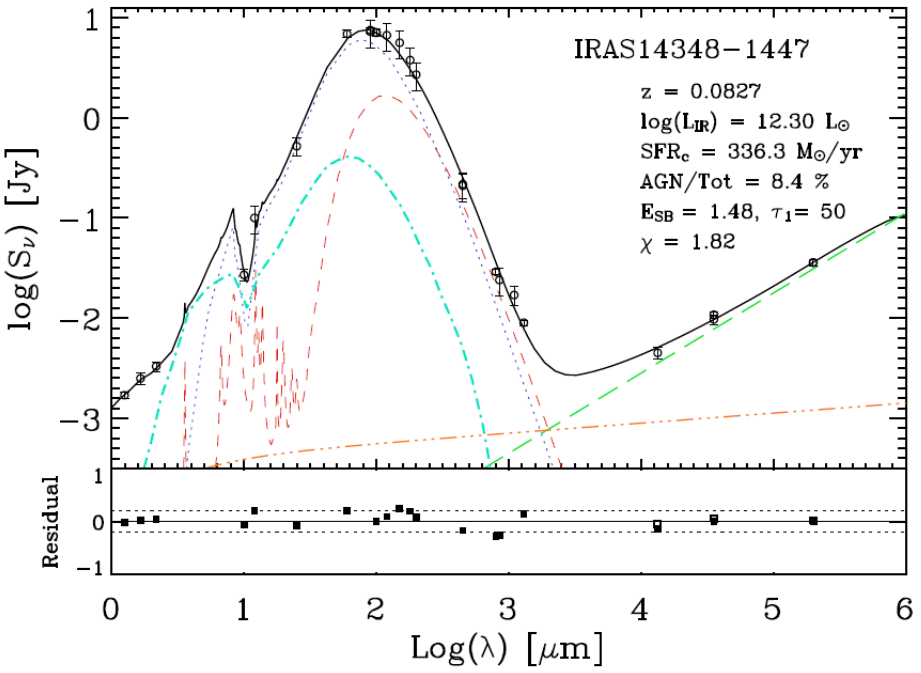

FIGURE 3.5: Broadband SED (open circles), including radio data, of IRAS 14348-1447. The best-fit model (black solid line) has been obtained from a library generated with the population synthesis code GRASIL. The different emission components are: the diffuse medium (red short dashed line), the molecular clouds (blue dotted line), thermal radio emission (orange three dots-dashed line), and the non-thermal radio emission (green long dashed line), and additional emission from the AGN (cyan dot-dashed line). The figure has been taken from Vega et al. (2008).

mentioned that the FUV luminosity is highly sensitive to dust extinction, while the IR luminosity may be contaminated by AGN emission. We will now give a brief overview of the most used SFR diagnostic tools.

3.4.1 UV luminosity

The SFR is directly proportional to the FUV luminosity, which traces the integrated emission by young, massive stars. The launch of the *Galaxy Evolution Explorer* (*GALEX*) mission (Martin et al. 2005) has largely improved SFR estimated based on observations in this wavelength range, providing integrated NUV and FUV fluxes for hundreds of thousands of galaxies, also at high redshift. Over the past decade, several studies have been published based on observations made with the *XMM Optical Monitor* (Mason et al. 2001), the *Swift UV/Optical Telescope* (Roming et al. 2005), the *Ultraviolet Imaging Telescope* on the ASTRO missions (Stecher et al. 1997; Marcum et al. 2001), and the HST (primarily for nearby galaxies in the NUV).

However, the UV band is severely affected by dust absorption, that may drastically reduce the luminosity to a few percent, or even less, of its intrinsic value. Even though

many independent estimates of the dust attenuation exist (see Sec. 3.2), more weight is being applied to SFRs based on combinations of UV with IR measurements (see Sec. 3.4.6).

3.4.2 Emission lines

Among emission lines, the most widely used as SFR indicators are in the optical and NIR bands, tracing ionized gas around massive young stars. The Hα luminosity, measured from the FIR/sub-mm reprocessed emission by stellar dust, can be contamined by radiation from old stellar populations or by the AGN. Nonetheless, it is rather widely used at low redshift.

At higher z, the luminosity of the Lyα line ($\lambda_{\rm rest} = 1216$ Å) has been used as a tracer of starforming galaxies over the past decade (e.g., Ouchi et al. 2009, 2010). However, also this line is subject to strong quenching by the ISM. As a result, its measurements suffer large scatter and systematic uncertainties. Thus, Lyα surveys have been mainly used for identifying large samples of distant starforming galaxies.

3.4.3 IR emission

The SFR of galaxies undergoing intense star formation can be indirectly estimated from the FIR luminosity emitted by the dust. The majority of early applications of dust emission as a tracer of the SFR were based on the integrated total IR emission. This effectively represents the bolometric luminosity of a completely dust-enshrouded stellar population (Kennicutt 1998).

Dust emission does not account for the starlight which is not absorbed, so the IR luminosity systematically underestimates the SFR if the missing fraction of star formation is not considered into the calibrations (e.g., Hirashita et al. 2001). On the other hand, evolved stars may significantly contribute to dust heating, which tends to cause the IR luminosity to overestimate the SFR (e.g., Sauvage & Thuan 1992; Walterbos & Greenawalt 1996; Cortese et al. 2008; Kennicutt et al. 2009; Hao et al. 2011).

An other component that may contribute a fraction f to the FIR emission and may affect the SFR estimates comes from diffuse dust emission (cirrus). The FIR luminosity ascribable to the cirrus depends on several aspects, such as stellar content (mass, age and chemical composition), dust content, and spatial distribution. The cirrus dust is characterized by rather low dust temperature ($\sim$ 25 K). Thus, cirrus emits at larger wavelengths with respect to star formation in molecular clouds (Silva et al. 1998; Rowlands et al. 2014). Some local galaxies with quite low SFR, whose FIR luminosity is

dominated by cirrus emission, have been observed. For example, Hao et al. (2011) found $(1 - f) \sim 0.5$ for a sample of nearby starforming galaxies with $\dot{M}_\star \lesssim 30\,M_\odot$ yr^{-1}. However, the fraction $(1 - f)$ strongly reduces with increasing star formation (e.g., Clemens et al. 2013). For strong local starbursting galaxies with $\dot{M}_\star \gtrsim 100\,M_\odot$ yr^{-1} and $L_{\rm IR} \gtrsim 10^{12}\,L_\odot$, such as Arp 220, $(1 - f)$ is only a few percent (Silva et al. 1998; Rowlands et al. 2014).

3.4.4 Radio emission

The radio continuum emission of galaxies consists of a flat spectrum free-free component, expected to show up at frequencies of tens of GHz, and a steeper spectrum synchrotron component from charged particles produced by SNe, which dominates the integrated radio emission at $\nu \lesssim 5$ GHz. Observations have largely confirmed a tight correlation between the low-frequency radio continuum and the non-thermal FIR emission from galaxies, favouring its application as a SFR tracer (see Helou, Soifer & Rowan-Robinson 1985; Condon 1992; Yun, Reddy & Condon 2001; Ivison et al. 2010; Jarvis et al. 2010; Bourne et al. 2011; Mao et al. 2011). However, many physical processes related to this correlation, such as propagation of relativistic electrons, strength and structure of the magnetic field, size and composition of dust grains, are not yet completely understood (Bell 2003; Lacki & Thompson 2010). Moreover, faint nuclear radio activity may contaminate the synchrotron emission, even by a large factor.

A more direct radio SFR indicator is the free-free emission from the gas ionized by massive young stars (Murphy 2009; Murphy et al. 2011). This emission is directly proportional to the production rate of ionising photons, so it allows to estimate the SFR avoiding the problems related to dust attenuation. The data at these frequencies may be contaminated by "anomalous" dust emission (*Planck* Collaboration XX et al. 2011, and references therein), probably due to spinning dust grains (e.g., Draine & Lazarian 1998), even though the contribution of this component to the global emission of galaxies does not seem to be significant (Murphy et al. 2012; *Planck* Collaboration XXV et al. 2014).

Radio observations deep enough to detect starforming galaxies at high redshift are difficult to obtain. With the advent of the Square Kilometer Array (SKA) observations, SFR estimates based on free-free emission are expected to improve, allowing to efficiently detect also high-z galaxies.

3.4.5 X-ray flux

In the absence of an AGN, the X-ray emission is dominated by massive X-ray binaries, SNe, SN remnants, and massive stars. All this radiation is associated with young stellar populations and recent star formation. Moreover, the 2-10 keV fluxes of galaxies are observed to be strongly correlated with their IR and non-thermal radio continuum fluxes (e.g., Bauer et al. 2002; Ranalli, Comastri & Setti 2003; Symeonidis et al. 2011), even though this correlation needs to be calibrated from IR or radio emission (Ranalli, Comastri & Setti 2003; Persic et al. 2004). Over the past decade, the integrated hard X-ray emission of galaxies has been increasingly applied as a SFR tracer (e.g., Colbert et al. 2004; Lehmer et al. 2010), widely based on the calibration by Ranalli, Comastri & Setti (2003). Measures of individual starforming galaxies are possible up t $z \sim 1$ in the deepest *Chandra* fields; fainter fluxes have been reached with stacking measurements of UV-selected galaxies at $1 < z < 4$, and upper limits have been reported at higher redshifts (Reddy & Steidel (2004); Lehmer et al. (2005); Laird et al. (2005, 2006); Basu-Zych et al. (2013)).

3.4.6 Multi-λ indicators

Ideal estimates would be based on both the UV ($L_{\rm UV}$) and the FIR ($L_{\rm IR}$) observed luminosities for large galaxy samples at relevant redshifts. This would allow to derive the total luminosity proportional to the SFR as (following the notation of Kennicutt & Evans 2012):

$$L_{\rm SFR} = L_{\rm UV}^{\rm corr} = L_{\rm UV} + f\, L_{\rm IR} \ ; \tag{3.5}$$

where the fraction f is meant to subtract from the budget the FIR luminosity due to the cirrus (see Sec. 3.4.3), absorbing the light from less massive, older stars.

Actually, the SFR functions are inferred from UV or FIR-selected samples. In both cases, calibrations and corrections are included (Calzetti et al. 2000; Hao et al. 2011; Murphy et al. 2011; Kennicutt & Evans 2012). The calibration constants between SFR and luminosity in UV and FIR are nearly the same, as expected on energy conservation arguments (Kennicutt 1998; Kennicutt & Evans 2012); for the FIR luminosity we have:

$$\log \frac{\rm SFR}{M_\odot\ {\rm yr}^{-1}} \approx -9.81 + \log f\, \frac{L_{\rm IR}}{L_\odot} \ , \tag{3.6}$$

while for the dust-corrected UV luminosity we have:

$$\log \frac{\rm SFR}{M_\odot\ {\rm yr}^{-1}} \approx -7.42 - 0.4\, M_{\nu_{\rm UV}}^{\rm corr} \approx -9.76 + \log \frac{\nu_{\rm UV} L_{\nu_{\rm UV}}^{\rm corr}}{L_\odot} \ , \tag{3.7}$$

with $\nu_{\rm UV}$ being the frequency corresponding to 1550 Å.[2]

Hereafter, in this thesis, we will assume that $f = 1$ for $L_{\rm IR} \gtrsim 10^{12}\, L_\odot$, and that the SFR is traced by the FIR at such large luminosities. At low luminosity, instead, the SFR is better estimated from UV emission.

3.5 Stellar Luminosity Function

The stellar luminosity function (SLF) is a fundamental statistics for galaxy formation and evolution. It provides one of the key tools to probe the distribution of galaxies over cosmological times and to establish the relative contribution of bright and faint sources either to the energy budget at a given redshift, or to the cosmic SFR density. Moreover, in combination with other quantities, like the SMF and the DM halo distribution, it allows to have information about the efficiency of star formation and the effects of feedback at different mass scales (Rees & Ostriker 1977; Silk & Rees 1998; Dekel & Birnboim 2006; Behroozi, Wechsler & Conroy 2013; Aversa et al. 2015; Mashian, Oesch & Loeb 2015).

The SLF $N(\log L_\star, z)$ is defined as the distribution of the galaxy comoving number density as a function of their intrinsic luminosity, at a given redshift. To estimate it, the $1/V_{\rm max}$ estimator (Schmidt 1968) is usually adopted to account for the different detection limits of adopted surveys at different redshift.

3.5.1 $1/V_{\rm max}$ estimator

The maximum observable comoving volume $V_{{\rm obs},i}$ in which a galaxy i can be detected in a survey is given by:

$$V_{{\rm obs},i} = \int_\omega \int_{z_{{\rm min},i}}^{z_{{\rm max},i}} \frac{{\rm d}^2 V}{{\rm d}\omega {\rm d}z} {\rm d}\omega {\rm d}z \ , \tag{3.8}$$

where ω is the effective solid angle of the survey, and V is the comoving volume. The LF in terms of absolute magnitude $N_R(M)$, measured in a reference filter R, is expressed in discrete magnitude bins of width ${\rm d}M$ as:

$$N_R(M) = \sum_k N_{R,k}\, W(M_{R,k} - M) \ , \tag{3.9}$$

[2]Some UV data are given at a restframe wavelength different from 1550 Å; Eq. 3.7 still holds, provided that on the right hand side the correction $-\log \lambda/1550$ Å is added. E.g., for $\lambda = 1350$ Å, the correction amounts to 0.06 and the zero point calibration becomes −7.36.

where W is the window function of the survey, and $N_{R,k}$ are the discrete values of the LF derived in each bin k as:

$$N_{R,k}\mathrm{d}M = \frac{1}{V_{\mathrm{obs},i}} \sum_i W(M_{R,k} - M_{R,i}) \tag{3.10}$$

This method is formulated under the implicit assumption of a uniform galaxy distribution, which is not necessarily true. Other estimators were developed, such as the STY (Sandage, Tammann & Yahil 1979), the C^- (Lynden-Bell 1971), and the stepwise maximum-likelihood (SWML, Efstathiou, Ellis & Peterson 1988), to overcome this assumption (see Ilbert et al. 2004 for a comprehensive comparison). With some exceptions (e.g. Cucciati et al. 2012), the $1/V_{\mathrm{max}}$ method is the most used in high-z surveys, due to its simplicity. A word of caution is needed, however: due to the spectral type dependency of the k-corrections, the $1/V_{\mathrm{max}}$ method tends to underestimate the LF in the faintest magnitude bins, within a given redshift range, because galaxies will not be equally visible to the same absolute magnitude limit (Ilbert et al. 2004).

3.5.2 The observed stellar LF

As we have seen, massive star formation is in principle directly traced by the UV LF, but the radiation absorbed from dust and remitted at IR or sub-mm wavelengths must be accounted for. Thus, the FIR LF is essential to provide an unbiased study of the SFR.

Some instrumental limits arise, however. Rest-frame IR observations at high redshift are usually ~ 2000 times less sensitive than those in the UV, which are also not limited by spatial resolution. Thus, due to source confusion and low detector sensitivity, the FIR population have been probed from $z = 0$ up to $z \sim 4 - 5$ (Rodighiero et al. 2010; Lapi et al. 2011; Magnelli et al. 2013; Gruppioni et al. 2010, 2013; Patel et al. 2013).

On the other hand, the UV LF has been extensively studied up to $z \sim 6$ (Wyder et al. 2005; Reddy & Steidel 2009; Oesch et al. 2010; Cucciati et al. 2012; Weisz, Johnson & Conroy 2014; Finkelstein et al. 2014). Moreover, rather robust samples of galaxies at $z > 6$ have been collected (Bouwens et al. 2010; McLure et al. 2013; Oesch et al. 2010, 2013; Finkelstein et al. 2012, 2015; Bowler et al. 2014), with a few candidates up to $z \sim 10$ (McLure et al. 2013; Lorenzoni et al. 2013; Oesch et al. 2013, 2015; Bouwens et al. 2011, 2015).

3.5.3 Computing the SFR-luminosity function

Given all the considerations we made in Sec. 3.2 and in Sec. 3.4, we aim at tracing the SFR in the most complete way. We thus take into account both UV and FIR data, and build up an *overall* SFR-luminosity function (SFR-LF) as follows. We start from the SLFs at different redshifts, observed in the FIR band by Magnelli et al. (2013), Gruppioni et al. (2013), Lapi et al. (2011), and in the UV band by Bouwens et al. (2014), Oesch et al. (2010), Reddy & Steidel (2009), and Wyder et al. (2005). The data are reported in Fig. 3.6. In passing, note that the SFR and the $L_{\rm SFR}$ scales, on the upper and lower axis, have been related assuming the approximate relation:

$$\log \frac{\rm SFR}{M_\odot~{\rm yr}^{-1}} \approx -9.8 + \log \frac{L_{\rm SFR}}{L_\odot}~, \tag{3.11}$$

and so the number density per unit SFR or per unit luminosity are the same.

For the FIR samples, we assume $f = 1$, while for the UV samples at redshift $z \gtrsim 2$ we have employed the dust correction suggested by Meurer, Heckman & Calzetti (1999) and Bouwens et al. (2013, 2014)). At lower redshift ($z \lesssim 2$) the attenuation has been kept to the values found by Bouwens et al. (2013) for $z \approx 2.5$ galaxies. This assumption produces at $z \lesssim 1$ an UV attenuation somewhat in between those proposed by Wyder et al. (2005) and Cucciati et al. (2012), and the one proposed by Hopkins et al. (2001). However, we stress that for galaxies with $L_{\rm UV} \lesssim 10^{10}\,L_\odot$ the correction is anyway smaller than a factor of ~ 2.

Fig. 3.6 shows that, at any redshifts, we lack a robust determination of the SFR-LF at intermediate luminosities. This occurs for two reasons:

1. UV data almost disappear above $L_{\rm UV} \approx 10^{11}\,L_\odot$ (see also Reddy et al. (2010)) because of dust extinction, while FIR data progressively disappear below $L_{\rm UV} \approx 10^{12}\,L_\odot$ because of current observational limits
2. UV correction for $L_{\rm UV} \gtrsim 10^{10}\,L_\odot$, corresponding to $\dot{M}_\star \gtrsim 1\,M_\odot~{\rm yr}^{-1}$, becomes progressively uncertain, as discussed in Sec. 3.2.

To fill in the gap, we render the overall SFR distribution with a continuous function, whose shape is basically determined by the FIR data at the bright end, and by the UV data at the faint end. Specifically, we adopt the same modified-Schechter functional shape of Eq. (2.14), with evolving characteristic luminosity and slopes:

$$N(\log L_{\rm SFR}, z) = \Phi(z)\,\left[\frac{L_{\rm SFR}}{L_c(z)}\right]^{1-\alpha(z)}\,\exp\left\{-\left[\frac{L_{\rm SFR}}{L_c(z)}\right]^{\omega(z)}\right\}~. \tag{3.12}$$

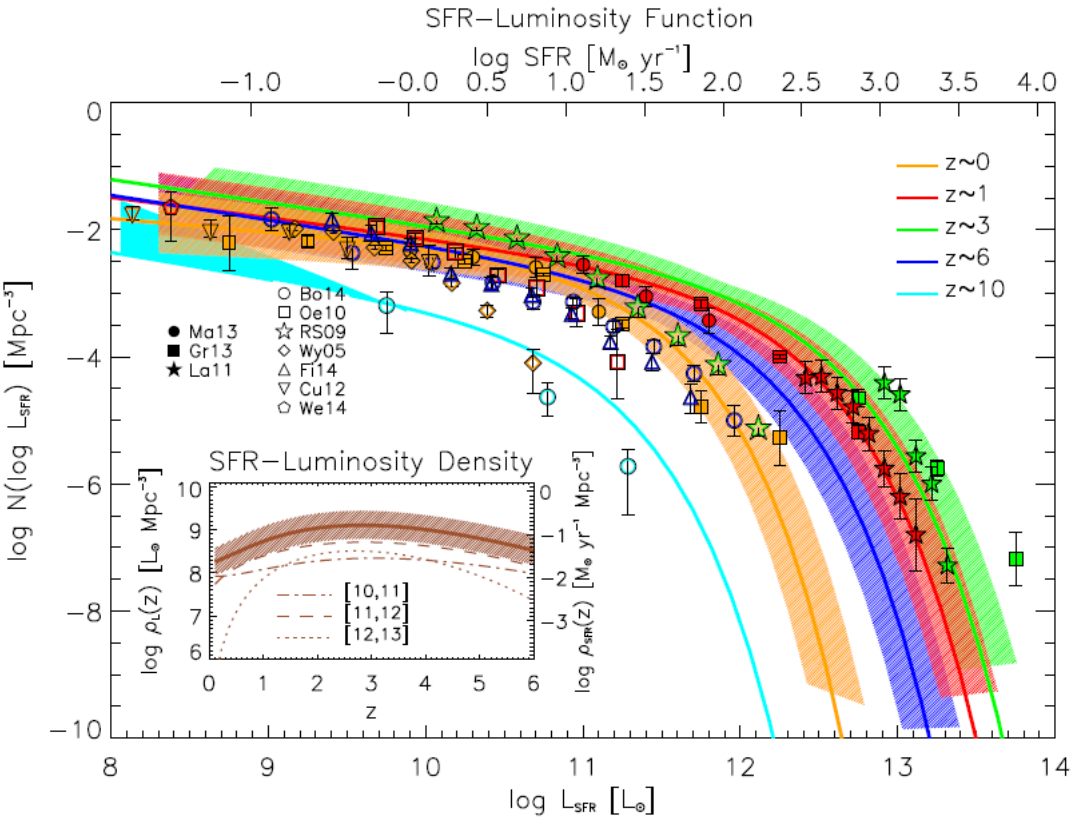

FIGURE 3.6: The SFR-LF $N(\log L_{\rm SFR})$ at redshift $z = 0$ (orange), 1 (red), 3 (green), and 6 (blue), vs. the bolometric luminosity $L_{\rm SFR}$ associated to the SFR (lower axis) and vs. the SFR (upper axis). IR data are from Magnelli et al. (2013, filled circles), Gruppioni et al. (2013, filled squares), and Lapi et al. (2011, filled stars); UV data (dust corrected, see text) are from Bouwens et al. (2014, open circles), Oesch et al. (2010, open squares), Reddy & Steidel (2009, open stars), Wyder et al. (2005, open diamonds), Finkelstein et al. (2014, open triangles), Cucciati et al. (2012, open reversed triangles), Weisz, Johnson & Conroy (2014, pentagons). The solid lines illustrate the analytic rendition of the SLF described in Sect. 3.5.3, while the hatched areas represent the associated uncertainty; the cyan line is the extrapolation to $z = 10$, plotted for illustration, with the shaded area representing the uncertainty on the faint-end slope. The inset shows the SFR-luminosity density as a function of redshift, for the overall luminosity range probed by the data (solid line with hatched area), and for bolometric luminosity $\log L_{\rm SFR}/L_\odot$ in the ranges $[10, 11]$ (dot-dashed line), $[11, 12]$ (dashed line), $[12, 13]$ (dotted line)

The normalization $\log \Phi(z)$, the characteristic SFR-luminosity $\log L_c(z)$, and the characteristic slopes $\alpha(z)$ and $\omega(z)$ evolve with redshift according to the same parametrization:

$$p(z) = p_0 + k_{p1}\,\chi + k_{p2}\,\chi^2 + k_{p3}\,\chi^3 \ . \tag{3.13}$$

with $\chi = \log[(1+z)/(1+z_0)]$ and $z_0 = 0.1$. The parameter values are reported in Table 6.1. The UV data, at the faint, and FIR data, at the bright, are smoothly connected by our analytic renditions. We also illustrate an estimate of the associated 1σ uncertainty. In the inset, we plot the evolution with redshift of the SFR-luminosity density, and the contribution to the total by specific luminosity ranges. Whenever

possible, we have performed a formal minimum χ^2-fit to the data. We have checked that our rendition os almost indistinguishable from it.

It happens that our rendition of the data closely follows the models proposed by Mao et al. (2007) and Cai et al. (2014), wherein the extinction is strongly differential with increasing SFR (and gas metallicity). In such models, the faint end of the UV LF at high redshift is dictated by the rate of halo formation, while the bright end is modeled by the dust content in rapidly starforming galaxies. At $z \gtrsim 6$, reliable statistics concern only UV-selected galaxies endowed with low SFR.

At high luminosity, we have extrapolated the behavior from lower redshift ($z \lesssim 4$), finding a good agreement with the model proposed by Cai et al. (2014). This extrapolation implies a significant fraction of dusty galaxies with $\dot{M}_\star \gtrsim 10^2\, M_\odot\ \mathrm{yr}^{-1}$ at $z \gtrsim 6$, which are missed by the UV selection. Clues of such a population are scanty, but not totally missing. Riechers et al. (2014) detected a dust obscured galaxy at $z \approx 6.34$ with $\dot{M}_\star \approx 2900\, M_\odot\ \mathrm{yr}^{-1}$, and Finkelstein et al. (2014) found an other one at $z \approx 7.51$ with $\dot{M}_\star \approx 300\, M_\odot\ \mathrm{yr}^{-1}$. The high-SFR end at $z \gtrsim 6$ will be probed in the near future by ALMA and *JWST* observations.

In Fig. 3.6, we also report the extrapolation of the SFR-LF to $z = 10$ (cyan line). It is interesting to compare it with the recent estimates from UV observations by Bouwens et al. (2014). At $L_{\mathrm{UV}} \approx 10^{9.7}\, L_\odot$, our extrapolation matches the observed number density around 10^{-3} Mpc^{-3}. We remark that the slope of the LF is highly uncertain for smaller UV luminosities ($L_{\mathrm{UV}} \lesssim 10^{9.7}\, L_\odot$); our data extrapolation suggests a slope in the range from -1.65 to -2, as illustrated by the cyan shaded area. At the other end, for $L_{\mathrm{UV}} \approx 10^{10.4}\, L_\odot$, the extrapolated number density is around 10^{-4} Mpc^{-3}, ~ 3 times larger than that observed in the UV. This possibly suggests that dust affects the UV data toward the bright end already at $z \approx 10$, as it happens at lower redshifts.

3.6 Stellar masses

The stellar mass is among the most fundamental parameters in the study of galaxy formation. It is related to many properties, such as SFR, stellar metallicity, galaxy formation efficiency, DM halo mass, and feedback processes.

3.6.1 Stellar mass measurements

The widely used method to derive stellar mass estimates of galaxies is to fit their observed broadband SEDs to templates generated from the population synthesis models. The

templates consist of a large sample of model SEDs with given parameters, including redshift, SFH, age, prescription for dust extinction and metallicity. Assuming a stellar IMF, the best-fit model is associated to the observed galaxy. A measure of the stellar M/L ratio (see Sec. 3.6.3), and thus of the galaxy luminosity, is also needed.

However, the fitting techniques do not necessarily yield unique models. For local galaxies, resolved color-magnitude diagrams can be useful to constrain the distribution of stellar properties, but the observed quantity in the vast majority of galaxies is the integrated light, so that some degeneracies (especially regarding broadband colors) arise. For example, age, metallicity and dust can all redden the spectrum of a galaxy, and are well known to be degenerate (e.g., Worthey 1994); the interplay among parameters can affect mass etimates with $\lesssim 0.2$ dex uncertainties (Mobasher et al. 2015). Moreover, SFHs are barely constrained by population synthesis model fitting (Gallazzi & Bell 2009). An other significant issue is the still uncertain treatment of the emission from thermally pulsing asymptotic giant branch (TP-AGB) stars, at red and NIR wavelenghts (Maraston 2005; Maraston et al. 2006; Marigo et al. 2008; Kriek et al. 2010). This contribution leads to lower M/L ratios and to redder colors, and can affect the derived stellar masses by a factor of 2, or even more (Maraston et al. 2006).

The dominant contribution to the stellar mass in a galaxy is given by low-mass stars, that emit most of their light at red optical and NIR wavelengths. Thus, NIR to MIR measurements are critical for deriving stellar masses (Madau & Dickinson 2014), even though some authors concluded that NIR data give no such an improvement (Taylor et al. 2011), except in case of strong dust absorption (Conroy 2013).

3.6.2 Stellar mass measurements at high z

Galaxies with high SFRs can in principle contain a large population of old, red stars, whose contribution may be difficult to disentangle when modeling a SED (Papovich, Dickinson & Ferguson 2001). This issue becomes more severe towards higher redshifts, where SFRs tends to increase, and makes the analysis of high-redshift galaxy SEDs more complicated. However, it seems that stellar masses derived by SED modeling are rather independent on old stars contribution at $z \sim 7 - 8$ (Finkelstein et al. 2010; Curtis-Lake et al. 2013). At higher redshifts ($z \gtrsim 10$), estimating stellar masses may become even simpler, because the age of the oldest stellar population will eventually become comparable to the star formation timescale probed by the restframe UV band (Conroy 2013). Thus, stellar masses can be reasonably inferred by the SFR traced by UV measurements, multiplied by the age of the Universe.

Concerning the available instrumentations, the HST Wide Field Camera 3 (WFC3) can only sample optical rest-frame radiation at $z < 3$, so *Spitzer* is still the better instrument for deriving stellar masses at higher redshifts: *JWST* will provide a major advance in the next future.

3.6.3 M/L ratio measurements

As we have seen in Sec. 3.6.1, in order to derive the mass of stars in galaxies, both their luminosity and the stellar M/L ratio have to be measured. The M/L ratio associated to the star component can be derived by studies of stellar evolution, with uncertainties associated to poor knowledge of details in the IMF (see e.g. Bell (2003,?); Fukugita & Peebles (2004); Baldry et al. (2004); Panter, Heavens & Jimenez (2004); Conroy (2013); Roediger & Courteau (2015)). In fact, the uncertainties related to the IMF and SFH imply $\sim 30\%$ of uncertainty in the M/L ratio, to be added to statistical uncertainties of $\sim 20\%$.

The most popular methods to estimate the stellar M/L ratio are:

1. The use of tabulated relations between M/L and colors, derived from stellar population synthesis models (Bell & de Jong 2001; Bell 2003; Zibetti, Charlot & Rix 2009; Gallazzi & Bell 2009). The adoption of these relations has the advantages of requiring photometry only in two bands, and of avoiding explicit modeling;
2. The broadband photometry modeling and SED fitting (Sawicki & Yee 1998; Gallongo et al. 1998; Brinchmann & Ellis 2000; Papovich, Dickinson & Ferguson 2001; Shapley et al. 2001; Salim et al. 2007). Obviously, this technique requires the construction of a set of template libraries.

3.7 Stellar Mass Function

Stellar mass assembly in galaxies can be the result of internal processes, such as star formation from in-situ or accreted gas, or from major or minor mergers. The star formation may also be quenched by AGN feedback for galaxies residing in more massive DM halos, or by SN-driven winds in less massive halos. The SMF and its integral over masses, the stellar mass density, are a key tool to describe the assembly of stellar mass through cosmic times, as well as a sensitive test of modern galaxy evolutionary models.

As already said in Sec. 3.6.1, stellar masses in galaxies are usually estimated through SED fitting or through colors. Both these methods allows to determine the SMF (SalucciPersic99, Bell03, Baldry08, Baldry12, Santini12, Bernardi13, Moustakas13).

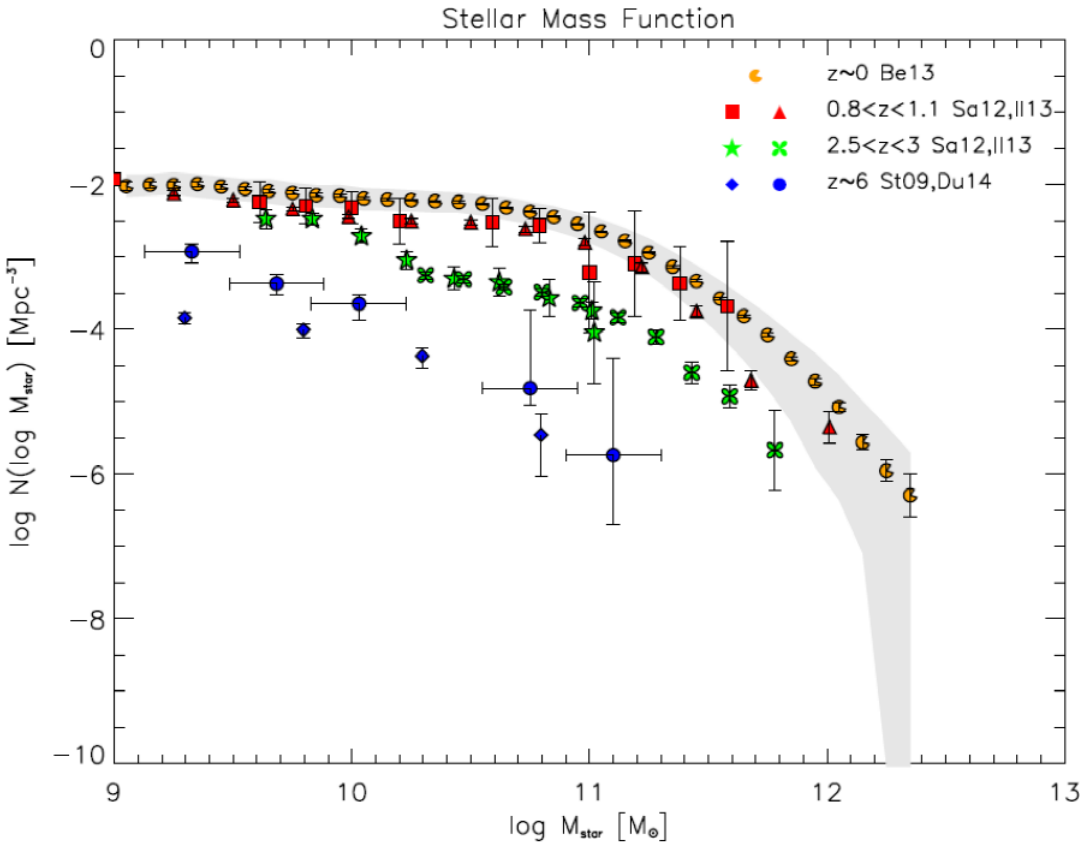

FIGURE 3.7: Observational estimates of the SMF. High redshift data are from Ilbert et al. (2013, $z \sim 1$ red triangles, $z \sim 3$ green clovers), Santini et al. (2012a, $z \sim 1$ red squares, $z \sim 3$ green stars), Stark et al. (2009, $z \sim 6$ blue diamonds), and Duncan et al. (2014, $z \sim 6$ blue circles). Local data are from Bernardi et al. (2013): orange pacmans with errorbars illustrate their fiducial measurements with the associated statistical uncertainty, while the shaded area shows the systematic uncertainty related to light profile fitting.

We show in Fig. 3.7 a collection of recent SMF estimates available in the literature, at $z = 0$ (Bernardi et al. 2013), $z \sim 1$ (Santini et al. 2012a; Ilbert et al. 2013), $z \sim 3$ (Santini et al. 2012a; Ilbert et al. 2013), and $z \sim 6$ (Stark et al. 2009; Duncan et al. 2014). The various SMFs presented in the literature generally agree at $z \sim 0 - 5$, although disagreements exist (Marchesini et al. 2009, 2010; Caputi et al. 2011; González et al. 2011; Mortlock et al. 2011; Bernardi et al. 2013). The main source of uncertainty seems to be associated to the stellar M/L ratio measurements (for example, mismatched stellar templates, or mass dependence of the adopted IMF).

At higher redshifts, the available estimates of the SMF are based on UV-selected samples (Stark et al. 2009; Duncan et al. 2014), thus are potentially incomplete in mass. Moreover, the SMF at the low-mass end is highly uncertain at intermediate and high redshifts, since current samples are not deep enough to establish its slope with good accuracy, due to observational limitations.

Again, we stress the importance of the FIR, in addition to the UV data, in probing the star formation process in high-redshift galaxies. In fact,even when dust corrected, the UV data are unable to fully account for the population of strongly starforming galaxies seen in the FIR band (Hao et al. 2011; Lapi et al. 2011; Santini et al. 2012b; Gruppioni et al. 2013; Aversa et al. 2015). This mismatch can hardly be recovered by mass additions from dry merging events, since a factor 10 in mass is needed from $z \approx 3$ to $z \approx 0$ (Aversa et al. 2015. We will examine in depth this topic in Sec 5.2.

Chapter 4

Constraints on the growth of Black Holes and Galaxies

Powerful quasars hosting SMBHs with masses $M_{\rm BH} \sim 10^8 - 10^9 M_\odot$ have been observed at $z > 6$, when the age of the Universe is ~ 1 Gyr (Barth et al. 2003; Willott et al. 2005; Fan 2006; Mortlock et al. 2011; Venemans et al. 2012, 2013). This evidence sets two important contraints:

1. Seed BHs must have formed at early times, probably at $z \gtrsim 10 - 20$;
2. The mass growth must have been very fast.

Accretion onto the BH results to be the most validated option to solve this issue. In fact, the accretion causes the BH mass to increase as:

$$M_{\rm BH}(\tau) = M_{\rm seed}\, e^{\tau/\tau_{\rm ef}} \ , \tag{4.1}$$

where τ is the galactic (internal) time, and the e-folding time is expressed in terms of the mass-energy conversion efficiency ϵ and the Eddington ratio $\lambda_{\rm Edd}$:

$$\tau_{\rm ef} = \frac{\epsilon}{(1-\epsilon)} \frac{t_{\rm Edd}}{\lambda_{\rm Edd}} \ . \tag{4.2}$$

Thus, to reach a final mass $M_{\rm BH} \sim 10^8 M_\odot$ from a BH seed of $M_{\rm seed} \sim 100\, M_\odot$, the required number of e-folding is:

$$\frac{\tau}{\tau_{\rm ef}} = \ln\left(\frac{M_{\rm BH}}{M_{\rm seed}}\right) \sim 14 \ . \tag{4.3}$$

Reversing the argument, $\lambda_{\rm Edd}$ and ϵ set the value of $\tau_{\rm ef}$ through Eq. 4.2. To make a rough calculation, let us take constant values $\lambda_{\rm Edd} = 1$, $\epsilon = 0.1$, so $\tau_{\rm ef} \sim 4 \times 10^7$ yr.

Assuming a BH seed of $M_{\rm seed} \sim 100\,M_{\odot}$ formed at $z \sim 20$, we obtain:

$$\frac{t(z=6) - t(z=20)}{\tau_{\rm ef}} \sim 20\ , \tag{4.4}$$

allowing the seed BH to grow its mass by a factor $e^{20} \sim 5 \times 10^8$, perfectly explaining the observed quasar masses at high redshift. Thus, the growth of the SMBH mass traced by an exponential ascending phase (up to a peak value) in the AGN lightcurve is physically motivated and rather commonly adopted in the literature (e.g., Yu & Lu 2004, 2008; Shankar, Weinberg & Miralda-Escudé 2009, 2013).

Concerning the stellar component, there are three time-honored assumptions describing the behavior of the SFR as a function of galactic age: exponentially rising (Maraston et al. 2010; González et al. 2014), powerlaw (Smit et al. 2012), and constant (Lee et al. 2011). The last instance corresponds to the exponential case when a long timescale is adopted, or to the powerlaw case when a flat index is chosen. Hence, we assume a simple, constant lightcurve, motivated by the recent FIR data from the *Herschel* satellite for high-redshift, luminous starbursting galaxies (Lapi et al. 2011, 2014).

On the other hand, the observed correlations between SMBH masses and host galaxy properties suggest a common evolution, driving their assembly and their growth. The coevolution of AGNs and of their host galaxies at high redshift ($z \gtrsim 1.5$) is mainly traced by observations aimed at estimating the relationship between the star formation in the host and the nuclear activity due to accretion onto the central SMBH. There are two main ways to proceed:

1. In the first one, galaxies are selected on the basis of their SFR and followed up with X-ray observations, looking for nuclear activity;

2. In the second one, AGNs are selected in X-rays and then followed up with FIR observations, looking for star formation in the hosts.

The main outcomes of these observations are statistics on detections and on properties such as stellar mass in the host galaxy and SMBH mass. These statistics depend on the limiting flux/luminosity of the selection, and of the ensuing follow-up.

In this Chapter, we will show how these data are powerful in probing the different stages of our basic coevolution scenario, and in setting the timescales of the AGN and stellar lightcurves (Lapi et al. 2014).

4.1 Coevolution framework

We take as a guidance the framework originally proposed by Granato et al. (2004), which has been successful in reproducing the statistics of galaxies selected at 850 μm, of passively evolving galaxies, and of AGNs/QSOs at substantial redshift. Lapi et al. (2006, 2011) and Cai et al. (2013) further developed the original formulation, and showed that it fits the galaxy number counts at (sub-)mm wavelengths (e.g., Clements et al. 2010; Vieira et al. 2010, 2013), and the luminosity functions of sub-mm selected galaxies (Eales et al. 2010; Lapi et al. 2011; Gruppioni et al. 2013). Furthermore, the scenario has been used to estimate the number of sub-mm selected gravitationally lensed galaxies (Perrotta et al. 2003; Negrello et al. 2007; Lapi et al. 2012), a prediction fully confirmed by observations (Negrello et al. 2010; González-Nuevo et al. 2012; Weiß et al. 2013).

The scenario envisages that the early growth of the BH occurs in a gas rich and strongly dust-enshrouded ISM (Lapi et al. 2014; see also Chen et al. 2015). The BH accretes in a demand-limited regime, with values of $\lambda_{\rm Edd}$ appreciably greater than unity, though ϵ may keep low values, because slim-disc conditions develop. Since the BH mass is still small, the nuclear luminosity, though appreciably super-Eddington, is much lower than that of the starforming host galaxy, and the whole system behaves as a sub-mm bright galaxy with an X-ray nucleus.

At this stage, the gas inflowing from the ISM can be either directly accreted onto the BH or piled up into a *reservoir*, which can be related to the so called torus, observed in nearby AGNs and called for to explain the AGN phenomenology (e.g., Antonucci 1993; Granato & Danese 1994; Urry & Padovani 1995). Observations, at least of low redshift objects (see, e.g., Davies et al. 2007; Müller Sánchez et al. 2009; Krips et al. 2011; Diamond-Stanic & Rieke 2012; Sani et al. 2012; Storchi-Bergmann et al. 2012; Hönig et al. 2013), have revealed the presence of such reservoirs, with sizes from a few to several tens of parsecs; the reservoirs have been found to be rich in molecular gas and dust, and often accompanied by localized star formation. The amount of gas piled up in the reservoir is large enough to sustain the accretion during the final part of the ascending lightcurve, when the QSO reaches its maximum luminosity and the BH acquires most of its final mass.

Close to the peak of the AGN lightcurve, the BH mass has grown to large values, and the nuclear emission becomes comparable to, or even overwhelms, that of the surrounding galaxy. Strong winds from the nucleus remove gas and dust from the ambient medium, quenching the star formation in the host, while the whole system shines as an optical quasar. If residual gas mass is still present in the central regions, it can be accreted in a supply-driven regime, so originating the declining part of the lightcurve; this phase

corresponds to the onset of the standard thin disc accretion, which yields the observed SEDs of UV/optically-selected Type 1 AGNs (Elvis et al. 1994; Hao et al. 2014).

Actually, the data concerning the fraction of starforming galaxies in optically-selected quasar samples suggest such a descending phase to be present only for luminous objects, while in low-luminosity ones tiny residual mass is present, and the AGN fades more drastically after the peak.

When the accreting gas mass is exhausted, the BH becomes quiet, while the stellar populations in the galaxy evolve passively. For the most massive objects, the outcome will be a local ETG with a central relic SMBH.

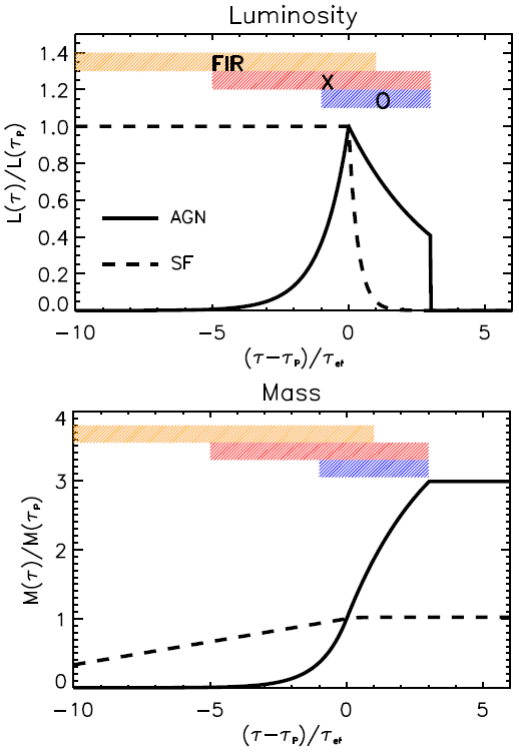

FIGURE 4.1: Time evolution of the luminosity (top panel) and mass (bottom panel), normalized to the value at time of the AGN luminosity peak. Solid lines refer to AGN-related, and dashed lines to star-formation related quantities. The colored areas highlight the stages when the system shines as a FIR bright source (orange), as an X-ray AGN (red), and as an optical QSO (blue).

A schematic view of the evolution with the galactic age τ of the AGN luminosity and the SFR-luminosity is sketched in the top panel of Fig. 4.1, while the corresponding growth of the BH mass and of the stellar mass is illustrated in the bottom panel. We also indicate with colors the stages when the galaxy is detectable as a FIR bright source (orange), and when the nucleus is detectable as an X-ray AGN (red) and as an optical QSO (blue), according to the framework described above.

4.2 Lightcurves

We adopt the following lightcurve for the AGN (Yu & Lu 2004, 2008):

$$\begin{aligned} L_{\rm AGN}(\tau|M_{\rm BH},t) &= \frac{\lambda_0\, M_{\rm BH,P}\, c^2}{t_{\rm Edd}}\, e^{\frac{(\tau-\tau_{\rm P})}{\tau_{\rm ef}}} \qquad 0 \le \tau \le \tau_{\rm P} \\ &= \frac{\lambda_0\, M_{\rm BH,P}\, c^2}{t_{\rm Edd}}\, e^{-\frac{(\tau-\tau_{\rm P})}{\tau_{\rm D}}} \qquad \tau_{\rm P} \le \tau \le \tau_{\rm P}+\zeta\tau_{\rm D} \\ &= 0 \qquad\qquad\qquad\qquad\qquad\qquad \tau > \tau_{\rm P}+\zeta\tau_{\rm D} \end{aligned} \tag{4.5}$$

This includes two phases:

1. An early one, up to a peak time $\tau_{\rm P}$, when the BH grows exponentially with a timescale $\tau_{\rm ef}$ to a mass $M_{\rm BH,P}$ and emits with an Eddington ratio λ_0 until it reaches a peak luminosity:
$$L_{\rm P} = \frac{\lambda_0\, M_{\rm BH,P}\, c^2}{t_{\rm Edd}}\ ; \tag{4.6}$$
2. A late one, when the luminosity declines exponentially on a timescale $\tau_{\rm D}$ up to a time $\tau_{\rm P}+\zeta\tau_{\rm D}$, when it shuts off.

We denote with λ_0 and ϵ_0 the average Eddington ratio and radiative efficiency during the early, ascending phase. The $e-$folding time associated to them is:

$$\tau_{\rm ef} = \frac{\epsilon_0}{(1-\epsilon_0)}\frac{t_{\rm Edd}}{\lambda_0}\ . \tag{4.7}$$

The epoch of the peak $\tau_{\rm P}$, the timescale of the descending phase τ_D, and its duration ζ (in units of τ_D) will be determined from the observations in the following sections.

We fiducially assume that the Eddington ratio of the ascending phase λ_0 depends on the cosmic time t (or redshift z) as:

$$\lambda_0(z) = 4\left[1-\frac{1}{2}\,{\rm erfc}\left(\frac{z-2}{3}\right)\right]\ , \tag{4.8}$$

as illustrated in Fig. 4.2. As shown by Lapi et al. (2006, 2014), such moderately super-Eddington values at high redshift ($z \gtrsim 4$) are necessary to explain the bright end of the quasar LF (see also Shankar, Weinberg & Miralda-Escudé 2009, 2013). During the demand-limited, ascending phase of the lightcurve, λ_0 exceeds the characteristic value $\lambda_{\rm thin} \approx 0.3$ for the onset of a slim accretion disc (Laor & Netzer 1989). On the other hand, during the declining phase of the lightcurve, the Eddington ratio decreases almost

exponentially, so that after the characteristic time $\tau_{\rm thin} \approx \tau_{\rm D}\ \log(\lambda_0/\lambda_{\rm thin})$, the transition to a thin accretion disc takes place. At high redshift, where $\lambda_0 \approx 4$, the thin-disc regime sets in only after a time $\tau_{\rm thin} \approx 2.5\,\tau_{\rm D}$ after the peak, while at low redshift, where $\lambda_0 \lesssim 1$, it sets in about $\tau_{\rm thin} \approx 1.2\,\tau_{\rm D}$ after the peak. We notice that, statistically, the fraction of slim discs should increase toward high redshift, as suggested by the data analysis of Netzer & Trakhtenbrot (2014), paving the way for their use as standard candles for cosmological studies (Wang et al. 2013a). The time-averaged value of $\lambda_{\rm Edd}$ during the declining phase is, to a good approximation, given by:

$$\langle\lambda_{\rm Edd}\rangle \simeq \frac{\lambda_0\,(1-e^{-\zeta})}{\zeta} \approx \frac{\lambda_0}{\zeta}\ , \tag{4.9}$$

while the time-averaged value during the thin disc regime

$$\langle\lambda_{\rm Edd}\rangle \simeq \frac{\lambda_{\rm thin} - \lambda_0\,e^{-\zeta}}{\zeta - \log\left(\frac{\lambda_0}{\lambda_{\rm thin}}\right)} \tag{4.10}$$

ranges from 0.1 at $z \lesssim 1$ to 0.3 at $z \gtrsim 3$. We will see that such values of $\langle\lambda_{\rm Edd}\rangle$, averaged over the Eddington distribution associated to the adopted lightcurve, well reproduce the observational determinations (Vestergaard & Osmer 2009; Kelly & Shen 2013).

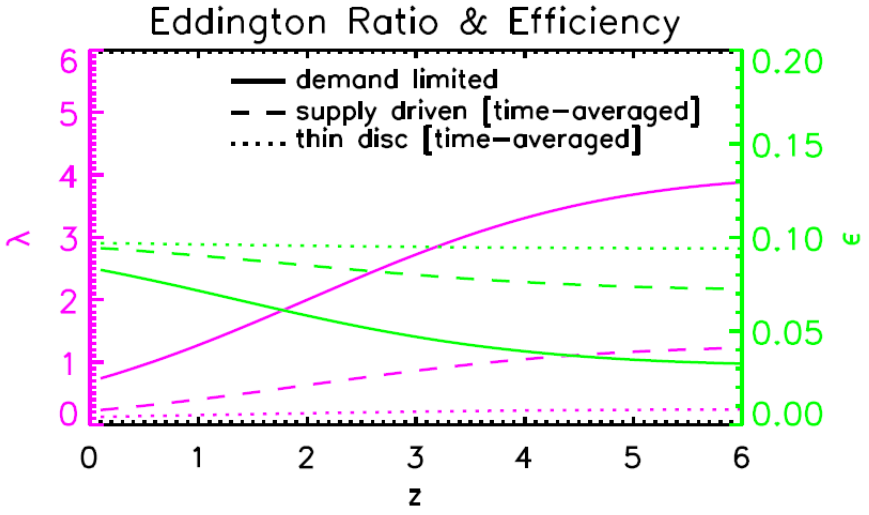

FIGURE 4.2: The adopted Eddington ratio (magenta lines and left axis) and radiative efficiency (green line and right axis) as a function of redshift. The values during the ascending, demand-limited phase (solid lines) and the time-averaged values during the descending, supply-driven phase (dashed lines) and during the thin-disc regime (dotted lines) are shown.

As to the radiative efficiency ϵ, we relate it and the Eddington ratio $\lambda_{\rm Edd}$ in both slim and thin disc conditions through Eq. 2.12, with $\epsilon_{\rm thin} = 0.1$ as our fiducial value. We also take into account that, along the declining portion of the lightcurve, ϵ increases, following the almost exponential decrease of $\lambda_{\rm Edd}$. The time averaged values $\langle\epsilon\rangle$ of the

efficiency during the declining phase and during the thin disc regime are illustrated in Fig. 4.2. We expect the redshift dependence of the average efficiency to be negligible during the thin disc regime; this is in qualitative agreement with the findings by Wu et al. (2013), based on spectral fitting in individual Type 1 quasars (see also Davis & Laor 2011 for a low-z determination), and by Cao (2010), based on a continuity equation analysis.

The final BH mass $M_{\rm BH}$ is easily linked to the mass at the peak $M_{\rm BH,P}$ appearing in Eq. 4.5:

$$M_{\rm BH} = \int_0^{\tau_{\rm P}+\zeta\,\tau_{\rm D}} d\tau' \frac{1-\epsilon}{\epsilon\,c^2}\,L_{\rm AGN}(\tau') = M_{\rm BH,P}\,\left[1 + f_\epsilon\,\frac{\tau_{\rm D}}{\tau_{\rm ef}}\,(1-e^{-\zeta})\right]\,. \tag{4.11}$$

The correction factor f_ϵ takes into account the modest change of the quantity $(1-\epsilon)/\epsilon$ along the declining phase. We have checked that $f_\epsilon \approx 0.8$ for any reasonable value of $\epsilon_{\rm thin}$. Notice that at high redshift, where $\lambda_0 \approx 4$, the fraction of BH mass accumulated in thin-disc conditions is only 5% of the total, while it can be as large as 20% at low redshift, where $\lambda_0 \approx 1$.

For the stellar component, we adopt a constant lightcurve:

$$\begin{aligned} L_{\rm SFR}(\tau|M_\star,t) &= \kappa_\star\,\dot{M}_\star \qquad\qquad \tau \le \tau_{\rm burst} \\ &= 0 \qquad\qquad\qquad\quad \tau > \tau_{\rm burst} \end{aligned} \tag{4.12}$$

where $\tau_{\rm burst}$ is the timescale for the duration of the starburst, and $\kappa_\star$ is a dimensional constant converting the SFR into bolometric luminosity.

For a Chabrier IMF, $\kappa_\star \approx 2.5\times10^{43}$ yr erg s$^{-1}/M_\odot \approx 6.5\times10^9$ yr $L_\odot/M_\odot$. The constant SFR

$$\dot{M}_\star = \frac{M_{\star,\rm burst}}{\tau_{\rm burst}} \tag{4.13}$$

represents an average over the fiducial period of the burst $\tau_{\rm burst}$, with the *total* (final) mass of formed stars amounting to $M_{\star,\rm burst}$.

The most recent observations with ALMA have undoubtedly confirmed that the SFR in massive high-redshift galaxies must have proceeded over a timescale of $\lesssim 0.5$ Gyr at very high rates ($\gtrsim$ a few $10^2\,M_\odot$ yr^{-1}) under heavily dust-enshrouded conditions (e.g., Scoville et al. 2014, 2015, their Table 1). The observed fraction of FIR-detected host galaxies in X-ray (e.g., Page et al. 2012; Mullaney et al. 2012b; Rosario et al. 2012) and optically selected (e.g., Mor et al. 2012; Wang et al. 2013b; Willott, Bergeron & Omont 2015) AGNs points toward a SFR abruptly shutting off after this period of time. In our

framework (see also Lapi et al. 2014), this rapid quenching is interpreted as due to the energy feedback from the SMBH growing at the center of the starbursting galaxy.

In the first stages of galaxy evolution, the BH is still rather small and the nuclear luminosity is much less than that associated to the star formation in the host. The SFR is then regulated by feedback from SN explosions, and stays roughly constant with time, while the AGN luminosity exponentially increases. In massive galaxies, after a period $\lesssim 1$ Gyr the nuclear luminosity becomes dominant, blowing away most of the gas and dust from the ambient medium and hence quenching the star formation.

On this basis, we adopt a timescale for the duration of the starburst given by:

$$\tau_{\rm burst}(z) \sim 1\,{\rm Gyr}\,\left(\frac{1+z}{3.5}\right)^{-3/2}\ ; \tag{4.14}$$

We note that the redshift dependence mirrors that of the dynamical/condensation time:

$$t_{\rm cond}(z) \propto \frac{1}{\sqrt{G\rho(z)}} \propto (1+z)^{-3/2}\ , \tag{4.15}$$

reflecting in turn the increase of the average density in the ambient medium.

4.3 Computing detected fractions

The fraction of objects $f_{\rm FIR\to X}$ selected in the FIR with luminosity $L_{\rm FIR}$ within the bin $[L_{\rm FIR}^{\rm INF}, L_{\rm FIR}^{\rm SUP}]$, that are detected in X-rays, with an AGN luminosity $L_{\rm X}$ above the limit $L_{\rm X}^{\rm LIM}$, is formally computed as:

$$f_{\rm FIR\to X} \equiv \frac{\int {\rm d}L_{\rm FIR}\ \frac{{\rm d}N(L_{\rm FIR},t)}{{\rm d}L_{\rm FIR}}\,\Delta t_{\rm FIR\to X}}{\int {\rm d}L_{\rm FIR}\ \frac{{\rm d}N(L_{\rm FIR},t)}{{\rm d}L_{\rm FIR}}}\ , \tag{4.16}$$

where $\Delta t_{\rm FIR\to X}$ is the time that an object with X-ray luminosity above the detection limit $L_X^{\rm LIM}$ spends at FIR luminosity $L_{\rm FIR}^{\rm INF} < L_{\rm FIR} < L_{\rm FIR}^{\rm SUP}$. This quantity is the only unknown, which will be determined through the comparison with the observed fractions.

The average of a given quantity $Q(t)$ among the detected sources is computed as:

$$< Q >_{\rm FIR\to X} \equiv \frac{\int {\rm d}L_{\rm FIR}\ \frac{{\rm d}N(L_{\rm FIR},t)}{{\rm d}L_{\rm FIR}}\int_{\Delta t_{\rm FIR\to X}} {\rm d}t\ Q(t)}{\int {\rm d}L_{\rm FIR}\ \frac{{\rm d}N(L_{\rm FIR},t)}{{\rm d}L_{\rm FIR}}\,\Delta t_{\rm FIR}}\ . \tag{4.17}$$

We recall that, in this analysis, we are dealing with the observations of massive galaxies, for which the SFR can be estimated by the FIR luminosity. So, for practical purposes,

the FIR LF $N(L_{\rm FIR}, z)$ in Eq. 4.16 and in Eq. 4.17 can be replaced with the SFR-LF $N(L_{\rm SFR}, z)$, presented in Sec. 3.5.3.

The same formalism applies when computing the fraction of objects $f_{\rm X\rightarrow FIR}$ selected in X rays and detected in the FIR, or the fraction of objects $f_{\rm O\rightarrow FIR}$ selected in the optical band and detected in the FIR, provided that the SFR-LF is replaced by the AGN bolometric LF.

4.4 The relationship between SFR and AGN luminosity

We begin by discussing X-ray observations of massive galaxies at $z \gtrsim 1.5$, mainly selected on the basis of their SFR. We compare our predictions with the accurate statistics derived from FIR and X-ray observations. The purpose is to constrain the evolution of the star formation in the host and the BH growth, deriving the parameters of the lightcurves introduced in Sec. 4.2. We stress that the available statistics already strongly support the conclusion that during an early phase, the AGN luminosity exponentially increases, while the SFR stays almost constant.

4.4.1 FIR and (sub-)mm galaxies in X-rays

In Fig. 4.3, we present the fraction of AGNs detected in X-rays (2-10 keV band) as a function of the host FIR luminosity and of the X-ray detection threshold. We caution that, for different data samples, the minimum X-ray luminosity for detection is somewhat uncertain, depending on flux limit, absorption correction, and redshift. Our theoretical results agree with the data in predicting an increasing detection fraction with increasing SFR (or $L_{\rm FIR}$) at given X-ray detection threshold L_X.

The FIR luminosity is constant for most ($\gtrsim 80\%$) of the star formation duration, while the AGN luminosity is exponentially increasing on a timescale $\tau_{\rm ef}$ (see top panel of Fig. 4.1). As a consequence, the time lapse during which the central AGN is brighter than the X-ray detection threshold is only a fraction of the starburst duration.

The increasing fraction of detected AGNs with increasing SFR of the host galaxy reflects the higher power that can be attained by more massive BHs in more massive galaxies. Plainly, at given $L_{\rm FIR}$, the higher the X-ray detection threshold, the shorter the fraction of time spent by the AGN above that limit.

We also predict a slight redshift dependence, due to the combined effect of the increase in Eddington ratio $\lambda_{\rm Edd}$ described by Eq. 4.8 (implying a decrease of $\tau_{\rm ef}$ through Eq. 4.7), and of the decrease in the star formation duration with increasing redshift.

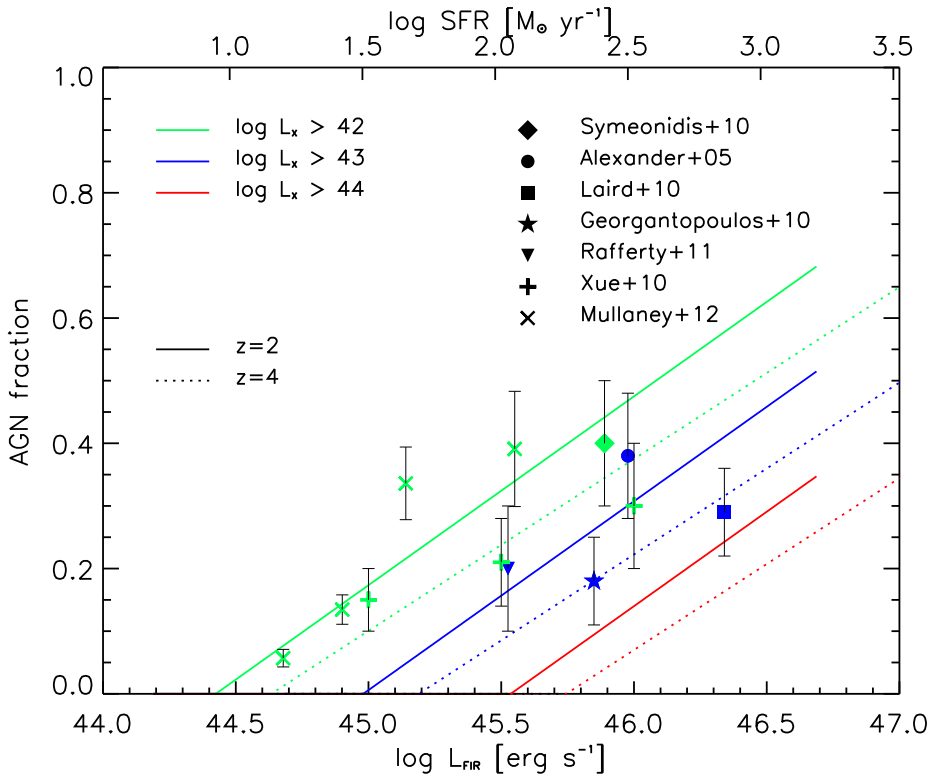

FIGURE 4.3: Fraction of X-ray detected AGNs in FIR/K-band selected galaxies, as a function of the FIR luminosity (lower scale) and of the SFR (upper scale). Our predictions are provided for galaxies at $z = 2$ (solid lines) and $z = 4$ (dotted lines) for different X-ray (2-10 keV band) detection thresholds: $L_X = 10^{42}$ (green), 10^{43} (blue), and 10^{44} erg s^{-1} (red); data (same color code) are from Alexander et al. (2005, circles), Georgantopoulos, Rovilos & Comastri (2011, stars), Laird et al. (2010, squares), Symeonidis et al. (2010, diamonds), Xue et al. (2010, plus signs), Rafferty et al. (2011, triangles), Mullaney et al. (2012a, crosses).

Conversely, a shorter or a longer timescale for the evolution of the AGN luminosity would imply detection rates higher or lower than observed, respectively. For instance, let us consider the hypothesis that the accretion rate during the star formation epoch is proportional to the large-scale SFR (e.g., Mullaney et al. 2012a; Silk 2013):

$$\dot{M}_{\rm acc} \approx \Gamma_0 \, \dot{M}_\star \ , \tag{4.18}$$

where $\Gamma_0 = M_{\rm BH}/M_\star \approx 3 \times 10^{-3}$ is the mean observed ratio between the stellar and BH masses in local massive ETGs and bulges (Magorrian et al. 1998; Gebhardt et al. 2000b; Marconi & Hunt 2003; Häring & Rix 2004; Ferrarese & Ford 2005; Bennert et al. 2011; Graham et al. 2011; Beifiori et al. 2012; McConnell & Ma 2013; Kormendy & Ho 2013).

We get:

$$\frac{L_{\rm FIR}}{L_{\rm AGN}} \propto \epsilon^{-1} \ . \tag{4.19}$$

Then, the expected X-ray luminosity would be:

$$L_X \approx 10^{42} \left(\frac{k_X}{25}\right)^{-1} \left(\frac{\Gamma_0}{3\times10^{-3}}\right) \left(\frac{\dot{M}_\star}{M_\odot\,{\rm yr}^{-1}}\right) {\rm erg\,s^{-1}} \gtrsim 10^{43} {\rm erg\,s^{-1}} \tag{4.20}$$

whenever $\dot{M}_\star \gtrsim 10\,M_\odot\ {\rm yr}^{-1}$ and $L_{\rm FIR} \gtrsim 3\times10^{44}$ erg s^{-1}. Such an AGN X-ray luminosity would imply that, in galaxies with $L_{\rm FIR} \gtrsim 3\times10^{44}$ erg s^{-1}, the nuclear activity should *always* be detected, in contrast with the observations presented in Fig. 4.3.

To escape the limits set by observations, we should assume that all AGNs hosted by FIR bright galaxies have extreme X-ray absorbing column densities ($N_{\rm H} \gg 10^{24}$ cm^{-2}). This would yield a selection bias, which would allow us to detect only the objects with lower column densities, implying a reduced detection fraction. Although quite large column densities ($N_{\rm H} \gtrsim 3\times10^{23}$ cm^{-2}) have been observed in several (sub-)mm selected galaxies, a significant fraction of objects exhibits lower column densities (Alexander et al. 2005; Laird et al. 2010; Georgantopoulos, Rovilos & Comastri 2011; Rafferty et al. 2011); in particular, no clear correlation between FIR luminosity and column density have been observed.

The FIR/sub-mm selection elicits galaxies with $L_{\rm SFR}/L_{\rm AGN} \gtrsim 1$ (Alexander et al. 2005; Georgantopoulos, Rovilos & Comastri 2011; Laird et al. 2010; Rafferty et al. 2011; Johnson et al. 2013; Wang et al. 2013b). The few objects that exhibit a ratio $L_{\rm SFR}/L_{\rm AGN} \sim 1$ have large X-ray power ($L_X \gtrsim 3\times10^{44}$ erg s^{-1}) and high Hα luminosity (Alexander et al. 2008). In our framework, the AGN bolometric luminosity approaches and possibly exceeds the galaxy FIR luminosity only for a couple of e-folding times before the peak (see Fig. 4.1). In addition, to get $L_X \gtrsim 10^{44}$ erg s^{-1}, the minimum X-ray luminosity often assumed to define X-ray QSOs, a value $\dot{M}_\star \gtrsim 100\,M_\odot\ {\rm yr}^{-1}$, or correspondingly $L_{\rm FIR} \gtrsim 3\times10^{45}$ erg s^{-1}, is required.

4.4.2 K-band selected starforming galaxies

The sample analyzed by Mullaney et al. (2012a), primarily selected in the K-band (with BzK color criteria chosen to ensure the presence of star formation), allows us to introduce the mass of the stellar component, trough Eq. 4.13, in the study of the relationship between star formation and AGN activity. In the following, we will focus on the sample at $z \approx 2$, relevant for our work. In this sample, the star formation can be probed down to small rates, because of the spectral coverage from the UV to 24 μm and of the low detection limits. The AGN activity is inferred from X-ray observations

with 4 Ms exposure time, thus reaching a detection threshold of $L_X \approx 10^{42}$ erg s^{-1} at $z \approx 2$. Such a luminosity corresponds to central SMBHs of relatively low mass, $M_{\rm BH} \sim 10^5 - 10^6\, M_\odot$.

As can be seen in Fig. 4.3, the detected AGN fraction as a function of FIR luminosity for the sample of Mullaney et al. (2012a) is very similar to the results obtained for FIR or (sub-)mm selected galaxies. This implies that the primary K-band selection is not introducing a relevant bias with respect to a pure FIR selection. Moreover, the average ratio of SFR-luminosity to AGN bolometric luminosity is large ($4 \lesssim L_{\rm SFR}/L_{\rm AGN} \lesssim 9$), as found for (sub-)mm selected galaxies.

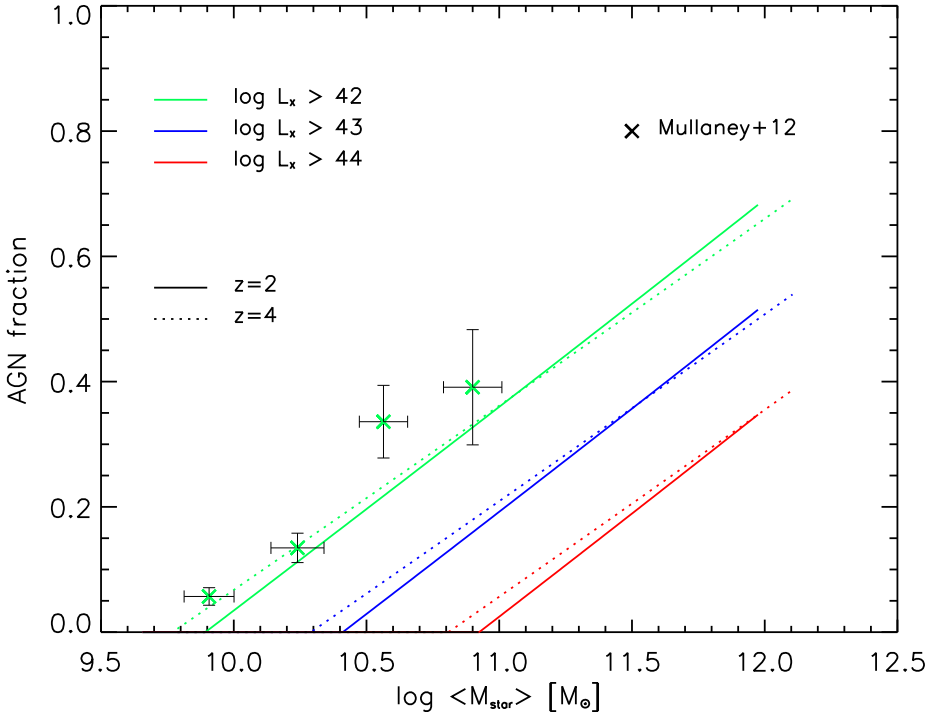

FIGURE 4.4: Fraction of X-ray detected AGN in K-band selected galaxies, as a function of the average stellar mass. Linestyles and colors as in Fig. 4.3. Data (for both detected and undetected sources, with the former dominating) are from Mullaney et al. (2012a, crosses).

In Fig. 4.4 we show that the AGN detection fraction increases with the stellar mass. This result is not independent of that presented in Fig. 4.3. To illustrate this, we present in Fig. 4.5 the average stellar mass in FIR/K-band selected galaxies, as a function of the FIR luminosity (lower scale) and of the SFR (upper scale). The data from Mullaney et al. (2012a) are also plotted. Though they refer to both detected and undetected

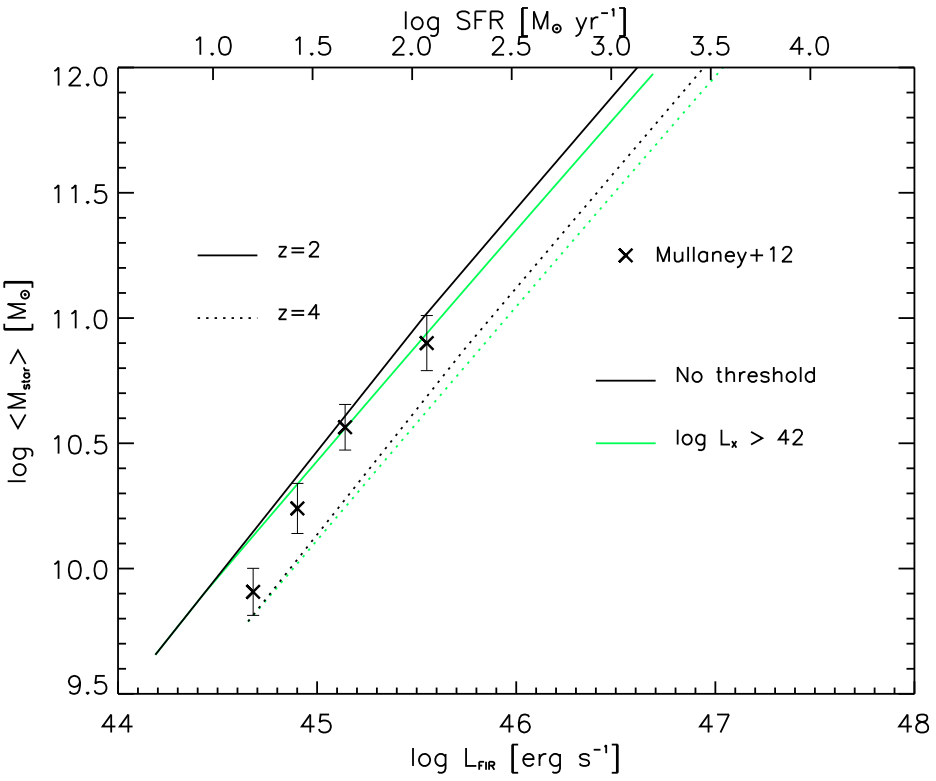

FIGURE 4.5: Average stellar mass in FIR/K-band selected galaxies, as a function of the FIR luminosity (lower scale) and of the SFR (upper scale). Our predictions are provided at redshifts $z = 2$ (solid lines) and $z = 4$ (dotted lines), for an X-ray detection threshold $L_X = 10^{42}$ erg s^{-1} (green lines), and for no threshold (black lines); data (for both detected and undetected sources, with the former dominating) are from Mullaney et al. (2012a, crosses).

sources, the authors point out that the X-ray counts for each bin in mass are dominated ($\gtrsim 80\%$) by X-ray detected galaxies. The data show an approximately linear dependence of the stellar mass on FIR luminosity or, equivalently, on SFR. The solid black line shows the relation $M_\star - L_{\rm SFR}$ between the average final stellar mass and the SFR-luminosity prescribed for star forming galaxies at redshift $z \approx 2$, independently of the nuclear activity. Starting from Eq. 4.12 and Eq. 4.13, it reads:

$$M_\star \propto \dot{M}_\star \left(\frac{\tau}{\tau_{\rm burst}}\right) \cdot \tau_{\rm burst} \propto L_{\rm SFR} \left(\frac{\tau}{\tau_{\rm burst}}\right) \cdot \tau_{\rm burst} \approx L_{\rm SFR} \cdot \tau_{\rm burst} \ , \tag{4.21}$$

where the last equality holds because K-band observations select galaxies when their final mass is roughly in place, i.e. when $\tau \approx \tau_{\rm burst}$. We notice that the results show very weak or no dependence on the X-ray detection threshold, since the relationship is dictated only by the SFH. The redshift dependence of the $M_\star - L_{\rm SFR}$ relation, apparent in Fig. 4.5, is inherited by the redshift depencence of $\tau_{\rm burst}$ (see Eq. 4.14). This also

explains why the fraction of detected AGNs at fixed stellar mass is almost redshift independent (see Fig. 4.4).

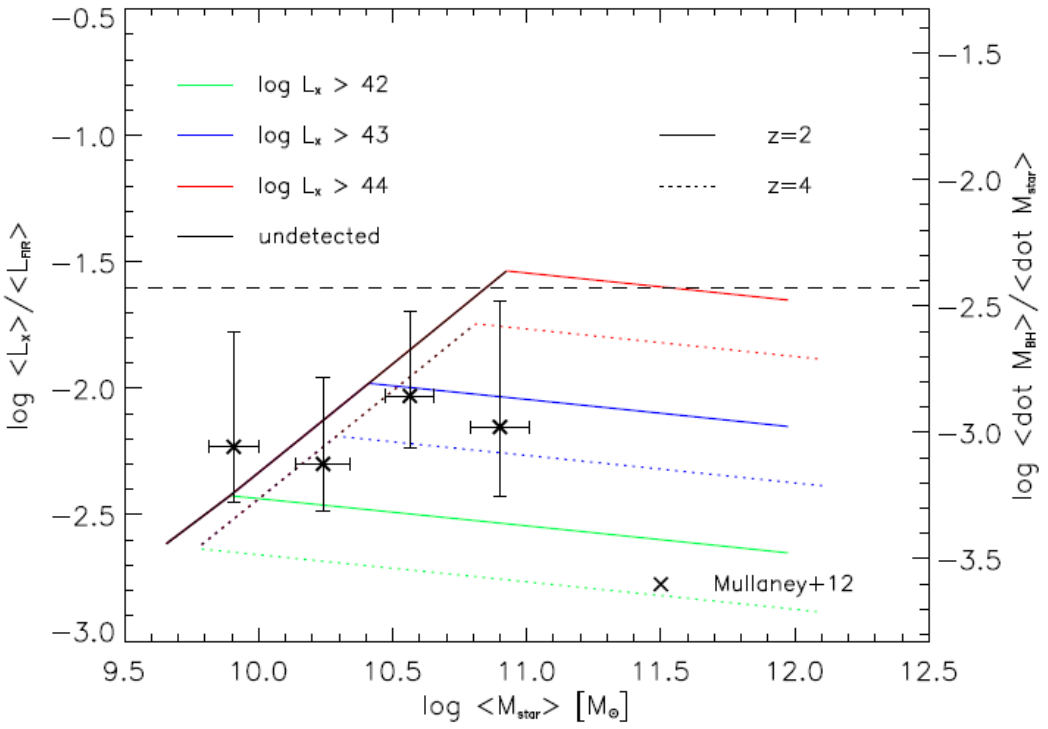

FIGURE 4.6: Ratios of average X-ray to FIR luminosity (left scale) and of average BH accretion rate to SFR (right scale) in K-band selected galaxies, as a function of the average stellar mass. Linestyles and colors are the same as in Fig. 4.3. The black lines show our predictions for undetected galaxies. The dashed line corresponds to $L_{\rm SFR} = L_{\rm AGN}$. Data (for both detected and undetected sources, with the former dominating) are from Mullaney et al. (2012a, crosses), and refer to $10^{42} \lesssim L_X \lesssim 10^{43}$ erg s^{-1}.

Fig. 4.6 illustrates our predictions for the ratio $\langle L_X \rangle / \langle L_{\rm FIR} \rangle$ between the average X-ray and FIR luminosities of FIR-selected galaxies as a function of the stellar mass. We compare our outcomes with the data by Mullaney et al. (2012a). For masses large enough to allow detection, the ratio keeps almost constant. This comes from the primary selection in the K-band, which biases toward late times of the evolution, where $L_{\rm AGN}$ is rapidly approaching $L_{\rm FIR}$. Specifically, from the data it appears that the AGN bolometric luminosity is still a factor of several below $L_{\rm FIR}$, and it will take another couple of e-folding time to attain it.

Recent data at $z \sim 2$ by Rodighiero et al. (2015) at $M_\star \gtrsim 10^{11}\, M_\odot$ would suggest a weak dependence of the ratio on the stellar mass:

$$\frac{L_X}{L_{\rm FIR}} \propto M_\star^{0.4 \pm 0.1} \,, \tag{4.22}$$

although this result may be partly driven by a still predominant fraction of undetected sources in the sample ($36/46 \sim 80\%$; see the black line in Fig. 4.6).

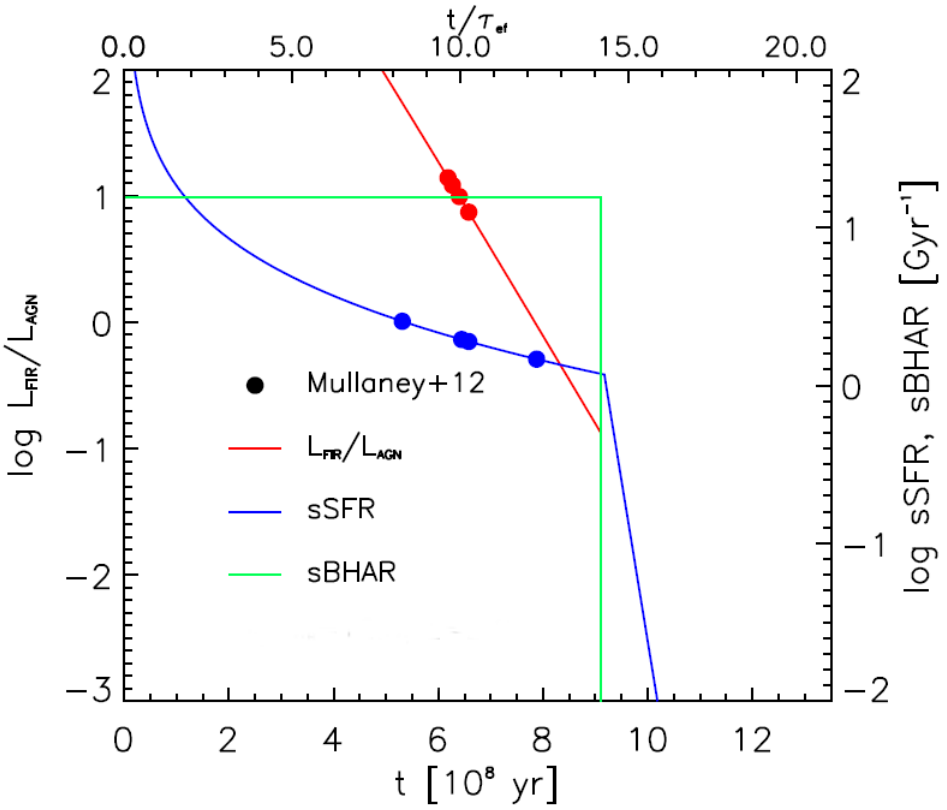

FIGURE 4.7: Evolution of the bolometric FIR to AGN luminosity ratio (red lines, left scale), of the specific SFR (blue lines, right scale), and of the specific BH accretion rate (green line, right scale) in galaxies with mass $M_\star = 6 \times 10^{10}\, M_\odot$ at redshift $z = 2$; the quantities are plotted as a function of the galactic age in units of 10^8 yr (lower scale) and of the e-folding time $\tau_{\rm ef} \approx 2 \times 10^7$ yr (upper scale). The values of $L_{\rm FIR}/L_{\rm AGN}$ and of the sSFR observed by Mullaney et al. (2012a, dots) are marked onto the respective predictions.

In Fig. 4.7, we show the ratio $L_{\rm FIR}/L_{\rm AGN}$, the specific SFR (sSFR) $\dot{M}_\star/M_\star$, and the specific BH accretion rate (sBHAR) $\dot{M}_{\rm BH}/M_{\rm BH}$ as a function of galactic time, calculated for a starforming galaxy at redshift $z \approx 2$; we focus on a stellar mass of $M_\star \approx 6 \times 10^{10}\, M_\odot$, typical of the sample considered by Mullaney et al. (2012a). The range of the observed values of the sSFR and of the luminosity ratio are marked on the corresponding predictions. We note that the sBHAR stays constant at values around 10 Gyr^{-1}, mirroring the exponential time behavior of the BH accretion. It appears that the data on the luminosity ratio single out a galaxy age $\approx 9 - 11\, \tau_{\rm ef}$, corresponding to $70 - 80\%$ of the star formation duration. In terms of the sSFR, the data span a larger time range, possibly due to the larger uncertainties in the mass estimates. Therefore, the selection of Mullaney et al. (2012a) picks out objects that are detected on the average $\sim 2 - 3$ e-folding times before the peak of the AGN activity; as a consequence, they should exhibit a $M_{\rm BH}/M_\star$ ratio lower than the local one by a factor $\sim 5 - 10$. This value is close

to the estimate obtained by Alexander et al. (2008) for a sample of (sub-)mm selected galaxies exhibiting nuclear activity.

In conclusion, the data of Mullaney et al. (2012a) concur with the FIR-selected samples in supporting the view that the BH and stellar mass are assembling in parallel, but on different timescales. While the stellar mass increases almost linearly with galactic time for a period $\tau_{\rm burst} \approx 7 \times 10^8$ yr $\sim 10 - 15\,\tau_{\rm ef}$ at $z \approx 2.5$, the BH mass is exponentially increasing on a timescale $\sim \tau_{\rm burst}/15$. Such a timescale indicates that, during this epoch, the BH accretion is in a self-regulated regime.

We will see in Sec. 4.6.1 that this conclusion is also supported by the estimates of the central BH mass in FIR and (sub-)mm selected galaxies. More detailed statistics on the nuclear activity in FIR-selected galaxies would allow us to determine with higher precision the ratio between the duration of the star formation and the e-folding timescale of the BH accretion.

4.5 Quenching of the SF and of the nuclear activity

The data discussed in the previous section allowed us to reconstruct the ascending phase of the nuclear activity, when the BH mass is growing and the star formation in the host galaxy is still significant. We recall that such epoch is characterized by objects with $L_{\rm SFR}/L_{\rm AGN} \gtrsim 1$.

In this Section, we show that determinations of the SFR in high-z, X-ray or optically selected AGNs, allow us to explore the phases in which the AGN/QSO approaches its maximum mass/luminosity, and the quenching of the star formation and of the nuclear activity sets in.

4.5.1 Star formation in X-ray selected AGNs

We present in Fig. 4.8 the results relative to the statistics of the X-ray selected AGNs whose host galaxy has been detected in the FIR/(sub-)mm range. We warn that some caution must be used in interpreting data obtained with different luminosity thresholds in the FIR.

Nevertheless, it appears that only a few powerful X-ray AGNs with $L_X \gtrsim 10^{44}$ erg s^{-1} are detected in the FIR. Such a small fraction suggests that the most luminous AGNs extend their X-ray emission beyond the epoch of constant and large SFR, into a phase when the star formation has been quenched more rapidly than the nuclear activity. According

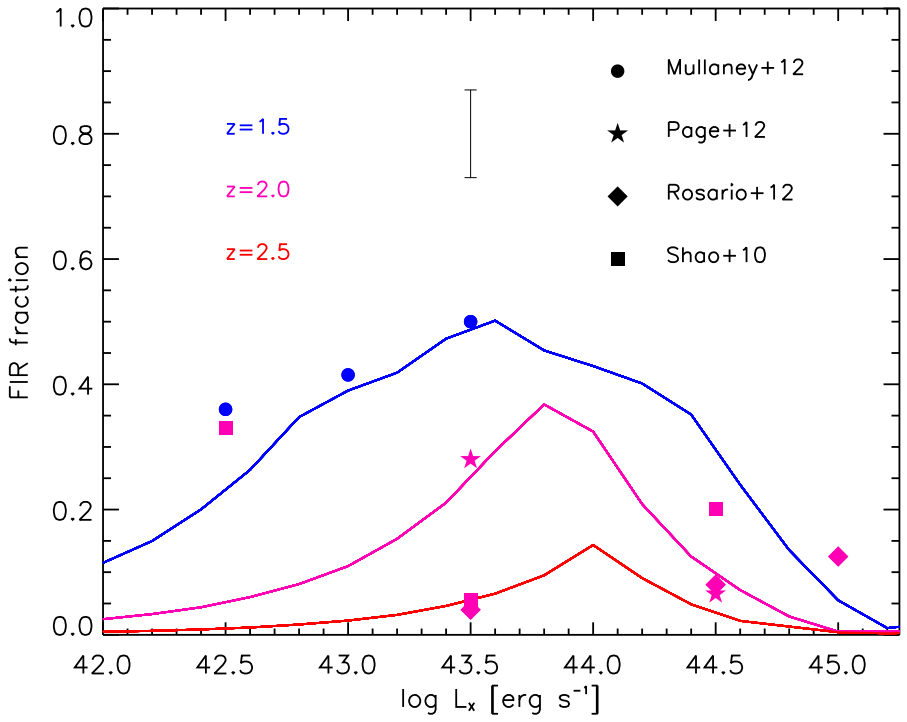

FIGURE 4.8: Fraction of FIR detected hosts in X-ray selected AGNs, as a function of the X-ray luminosity. Our predictions (solid lines) are provided at $z = 1.5$ (blue), 2 (magenta), and 2.5 (red), for FIR detection thresholds $\log L_{\rm FIR} = 44.8$, 45.3, and 45.8 erg s^{-1}, respectively. Data (same color code) are from Shao et al. (2010, squares), Mullaney et al. (2012b, circles), Page et al. (2012, stars), and Rosario et al. (2012, diamonds); the typical error bar is also shown near the legend.

to our framework, this later phase is present only if the reservoir is not exhausted when the feedback quenches the star formation; in such a case, the accretion can continue for some additional time.

When moving to lower luminosities, AGNs do not feature a prolonged declining phase. If they did, the low-luminosity tails of their LFs would exceed observational determinations (see also the discussion by Granato et al. 2006; Lapi et al. 2014; Aversa et al. 2015). Similar constraints come also from statistical matching arguments between the AGN accreted mass function and the local BH mass functions (see Yu & Lu 2004).

The mass in the reservoir is determined by the efficiency of the mechanisms capable to transfer the angular momentum of the cold gas involved in the star formation process, which reflects into the distribution of Γ_0; we recall that local samples suggest $\Gamma_0 \approx 3 \times 10^{-3}$ with a small, but positive dependence on the stellar mass, and with $1\,\sigma$ spread of ≈ 0.4 dex.

By setting the AGN quenching timescale (i.e., the timescale of the descending phase) $\tau_D = 3\,\tau_{\rm ef}$ and the SFR quenching timescale $\tau_{\rm SFR} = \tau_{\rm ef}/2$, we obtain a good representation of the available statistics on AGNs detected in the FIR, as shown in Fig. 4.8. We note that $\tau_{\rm SFR} \lesssim 10^7$ yr is consistent with the estimates by Daddi et al. (2007) and Maiolino et al. (2012).

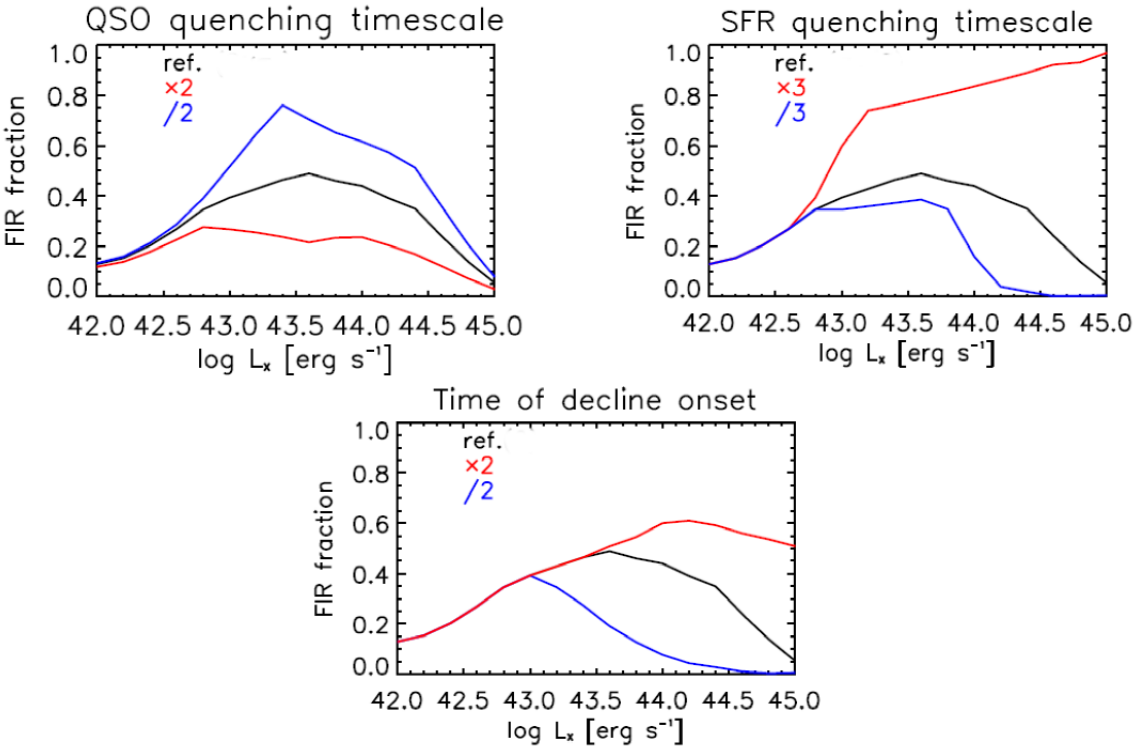

FIGURE 4.9: Dependence on the parameters of the FIR detected fraction of X-ray selected AGNs at $z = 2$: quenching timescale of the AGN emission τ_D (top left); quenching timescale of the SFR $\tau_{\rm SFR}$ (top right); time of the onset of the declining phase (bottom). In each panel, three curves are shown: the black ones refer to a reference value of the parameter (see tect), the red ones to an increased value, and the blue ones to a reduced value, as detailed in the legend.

In the top panels of Fig. 4.9, the effect of changing the AGN quenching timescale (left) and the SFR quenching timescale (right) is illustrated. Keeping $\tau_{\rm SFR}$ fixed, but reducing τ_D would imply a much higher fraction of detected AGNs. The opposite is true when prolonging τ_D. By the same token, if the star formation is switched off too early with respect to the AGN accretion, then the detection fraction decreases, while it increases if the star formation is still significant during the last phases of AGN activity. The bottom panel of Fig. 4.9 shows the effects of varying the time when the decline of the star formation and nuclear activity sets in. Increasing this time makes the FIR bright phase of the X-ray selected AGNs longer, so raising the detection fraction, and viceversa.

An additional test for the quenching of the star formation and of the nuclear activity is the observed average FIR luminosity of the AGN hosts as a function of their X-ray

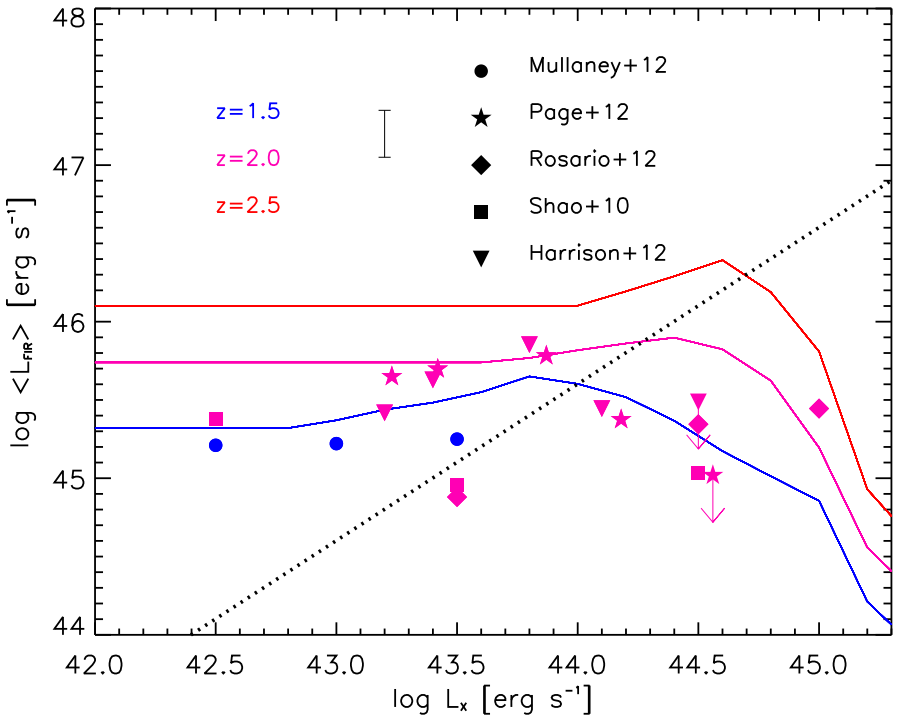

FIGURE 4.10: Average FIR luminosity of FIR-detected hosts of X-ray selected AGNs, as a function of the X-ray luminosity. Linestyles and colors as in Fig. 4.8. Data are from Shao et al. (2010, squares), Harrison et al. (2012, triangles), Mullaney et al. (2012b, circles), Page et al. (2012, stars), and Rosario et al. (2012, diamonds). The dotted line corresponds to $L_{\rm FIR} = L_{\rm AGN}$ where the bolometric correction by Hopkins, Richards & Hernquist (2007)) has been adopted.

luminosity, shown in Fig. 4.10. We stress that the redshift dependence apparent in our predictions is almost entirely due to different thresholds at different z, that reflect the data sampling. (cf. Fig. 4.8) The statistics of these averages depend on the flux/luminosity distribution of detected and undetected sources around the X-ray detection threshold. It is clear that the X-ray primary selection picks out AGNs with $L_{\rm SFR}/L_{\rm AGN} \gtrsim 1$ for $L_X \lesssim 10^{44}$ erg s^{-1}, while ratios $L_{\rm SFR}/L_{\rm AGN} \lesssim 1$ are typical at larger X-ray luminosities.

Though caution is mandatory, due to different detection limits, this behavior is nevertheless consistent with the fact that the declining phase of the X-ray luminosity is present on average in AGNs with $L_X \gtrsim 10^{44}$ erg s^{-1}, i.e., in massive galaxies endowed with substantial BH masses. Meanwhile, in AGNs with $L_X \lesssim 10^{44}$ erg s^{-1}, the quenching of the AGN activity occurs on a timescale of the same order (or even smaller) than that of the quenching of the star formation. All in all, the data suggest that the decline sets up at around $L_{\rm SFR} \sim L_{\rm AGN}$.

The faster decline of the star formation in luminous X-ray AGNs is also supported by the results of Page et al. (2012), who claimed the detection of a strong reduction in the SFR with increasing X-ray luminosity, by stacking AGN positions with flux derived from HerMES maps. This finding is not fully confirmed by Harrison et al. (2012), who remarks that, within the error bars, it is possible that the SFR keeps constant with increasing X-ray luminosity. However, their suggestion depends on an upper limit to the SFR at $L_X \approx 3 \times 10^{44}$ erg s^{-1}, larger by a factor of 3 with respect to that in Page et al. (2012).

It is worth noticing that, as pointed out by several authors (Harrison et al. 2012; Mullaney et al. 2012b; Rosario et al. 2012), at high luminosities a contribution from the AGN could add to the power from the star formation. The amount depends on the wavelength of observation, since the AGN emission is less important at (sub-)mm than at FIR restframe wavelengths (Richards et al. 2006; Polletta et al. 2007; Cai et al. 2013).

Exploiting optical and NIR photometry, Mullaney et al. (2012b) estimated the stellar mass in the host galaxy of AGNs with luminosity $10^{42} \lesssim L_X \lesssim 10^{44}$ erg s^{-1}. They concluded that the FIR-detected host galaxies exhibit $\langle M_\star \rangle \approx 5 \times 10^{10}\, M_\odot$, increasing by a factor of ~ 2 when the X-ray luminosity changes by about two orders of magnitude, and possibly tracing a power law $M_\star \propto L_X^{1/7}$ relationship. In our framework, the exponential growth of the AGN luminosity, coupled with the almost constant SFR, implies that $M_\star$ depends only very weakly on $L_{\rm AGN}$, according to:

$$M_\star(\tau) \propto \dot{M}_\star \times \ln L_{\rm AGN}(\tau) \ . \tag{4.23}$$

If mass estimates are available, the sSFR of the galaxies can be investigated. In Fig. 4.11, we show the average sSFR of FIR-detected hosts of X-ray selected AGNs, as a function of their X-ray luminosity. We predict a decrease in the sSFR at large X-ray luminosities, $L_X \gtrsim 10^{44}$ erg s^{-1}. This is a straightforward consequence of the decline in the SFR (seen in Fig. 4.10) during the final phase of the AGN and galaxy coevolution, when the stellar mass is already piled up. The present data do not show a clear trend. In particular, we notice that the lack of data at high X-ray luminosities ($L_X \gtrsim 5 \times 10^{44}$ erg s^{-1}) depends on the limited volume covered by current surveys (see Rovilos et al. 2012, their Fig. 6).

All studies of X-ray selected AGNs agree in claiming very weak or no correlation between the X-ray absorbing column density and the FIR luminosity (e.g., Stevens et al. 2005; Shao et al. 2010; Lutz et al. 2010; Rosario et al. 2012; Rovilos et al. 2012). This result suggests that most of the X-ray absorption may not originate from the gas and dust directly involved in the star formation process, but may be more related to the very central regions (see the review by Turner & Miller 2009). The same conclusion has been reached by Page et al. (2011), through direct studies of $z \sim 2$ heavily absorbed QSOs.

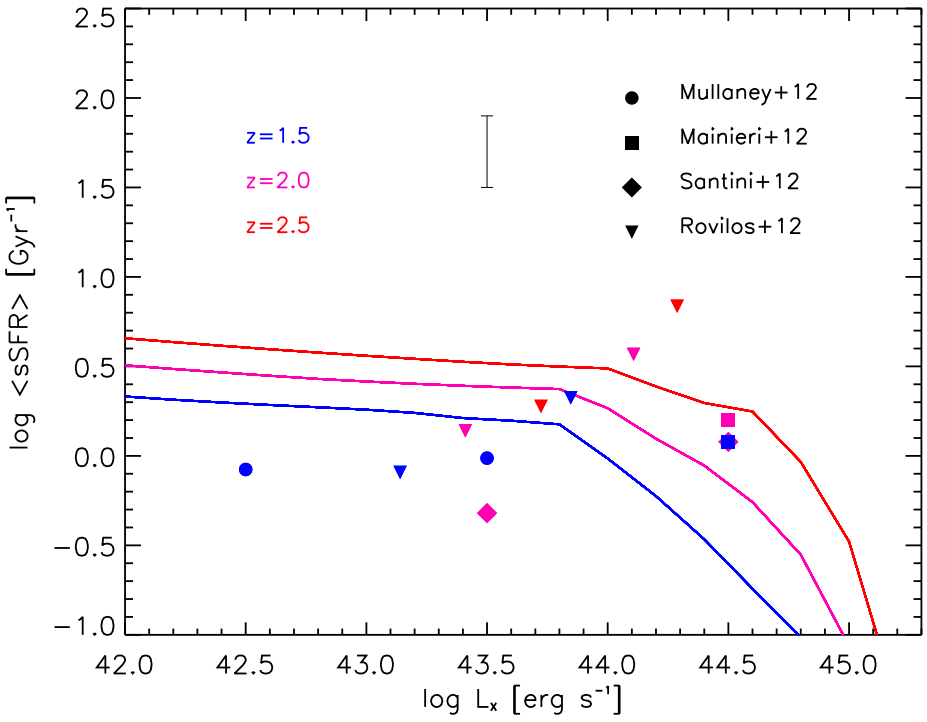

FIGURE 4.11: Average sSFR of FIR-detected hosts of X-ray selected AGNs, as a function of the X-ray luminosity. Linestyles and colors as in Fig. 4.8. Data are from Mainieri et al. (2011, squares), Mullaney et al. (2012b, circles), Rovilos et al. (2012, reversed triangles), and Santini et al. (2012b, diamonds).

On the other hand, Brusa et al. (2010) show that the fraction of obscured AGNs (i.e., with $N_{\rm H} \gtrsim 10^{22}$ cm^{-2}) strongly decreases with increasing X-ray luminosity, and ranges from $\sim 80-90\%$ at $L_X \sim 10^{42-43}$ erg s^{-1} to $\sim 10-20\%$ at $L_X \gtrsim 6\times10^{45}$ erg s^{-1}, with an abrupt transition around $L_X \sim 10^{44}$ erg s^{-1}. For X-ray selected AGNs, this luminosity corresponds, on average, to the transition from the bolometric luminosity dominated by the star formation to that dominated by the nuclear activity (see Fig. 4.10).

These findings can be understood recalling that an unbiased X-ray selection can pick up objects either *before* or *after* the SFR quenching (see Fig 4.1). Specifically, in the early epoch dominated by star formation, the gas is abundant both in the reservoir and in the central regions of the galaxy, and both settings can contribute to the obscuration.

When the AGN reaches its maximum power, the ISM is rapidly blown away by winds on a timescale $\sim \tau_{\rm ef}/2$, so its possible contribution to the obscuration drastically decreases. On the other hand, the QSO winds may also affect the reservoir/proto-torus and the

innermost X-ray absorbing regions, for instance peeling off the gas at higher latitude and reducing the covering factors.

Interestingly, the high fraction ($\sim 40\%$) of FIR detections in a sample of highly absorbed X-ray QSOs with $N_{\rm H} \gtrsim 10^{22}$ cm^{-2} and $L_X \gtrsim 10^{45}$ erg s^{-1} found at $z \sim 1.5-2$ by Stevens et al. (2005) can be understood on the same grounds. Since these authors select *highly obscured* QSOs, they pick up on average objects with a huge reservoir and a large amount of gas in their ISM, which can still maintain a high SFR. Taking into account that the space density of absorbed QSOs is $\sim 15\%$ of that of the unabsorbed ones at given X-ray luminosity (Page et al. 2011), the $\sim 40\%$ of FIR detections for highly absorbed QSOs is still consistent with the low fraction ($\lesssim 10\%$) for an unbiased selection at large X-ray luminosities (Rosario et al. 2012; Page et al. 2012; Harrison et al. 2012).

The results of Stevens et al. (2005) are also confirmed by Mainieri et al. (2011) and by Carrera et al. (2011, 2013), who have shown that a major fraction of all obscured QSO hosts at $z \gtrsim 1$ are forming stars at significant rates. More quantitatively, the absorbed X-ray selected QSOs exhibit luminosity ratios in the range $0.3 \lesssim L_{\rm SFR}/L_{\rm AGN} \lesssim 5$ (Stevens et al. 2005; Vignali et al. 2009; Gilli et al. 2011; Feruglio et al. 2011), supporting the view that these objects typically reach their large X-ray luminosity when the star formation is still vigorous.

To make our analysis more clear, we show in Fig. 4.12 a schematic illustration of the different phases, as traced by the ratio $L_{\rm SFR}/L_{\rm AGN}$. Inspecting the figure, it appears that, for obscured X-ray QSOs, the observed ratios $L_{\rm SFR}/L_{\rm AGN}$ correspond to a time interval $\sim 3\,\tau_{\rm ef}$ before the AGN decline phase sets in (cyan box). During this epoch, both the reservoir and the ISM are rich in gas and dust, so X-ray obscured QSOs are obscured also in the UV-optical bands. As a consequence, they are on average extremely 'red' (e.g., Fiore et al. 2009). After the onset of the QSO winds, the SFR rapidly decreases and, as mentioned above, the covering factor of the reservoir also decreases. In fact, X-ray unobscured QSOs exhibit $L_{\rm SFR}/L_{\rm AGN} \lesssim 0.3$ (e.g., Page et al. 2004), and they look similar to the pure optically selected QSOs (green box).

In conclusion, the above considerations illustrate that the study of star formation in well defined samples of X-ray selected AGNs can be extremely useful to statistically define the observational framework to which a sensible theory of coevolution must conform. As a matter of fact, the X-ray selected objects may lie not only on the rising branch of the X-ray luminosity curve, when the SFR is almost constant, but also in the declining phase of the SFR and nuclear activity. The number of objects with $L_{\rm SFR}/L_{\rm AGN} \gtrsim 1$ relative to that with $L_{\rm SFR}/L_{\rm AGN} \lesssim 1$ is an important clue on the timescale of the SFR quenching by the AGN feedback, and on the timescale over which the nuclear activity itself switches off.

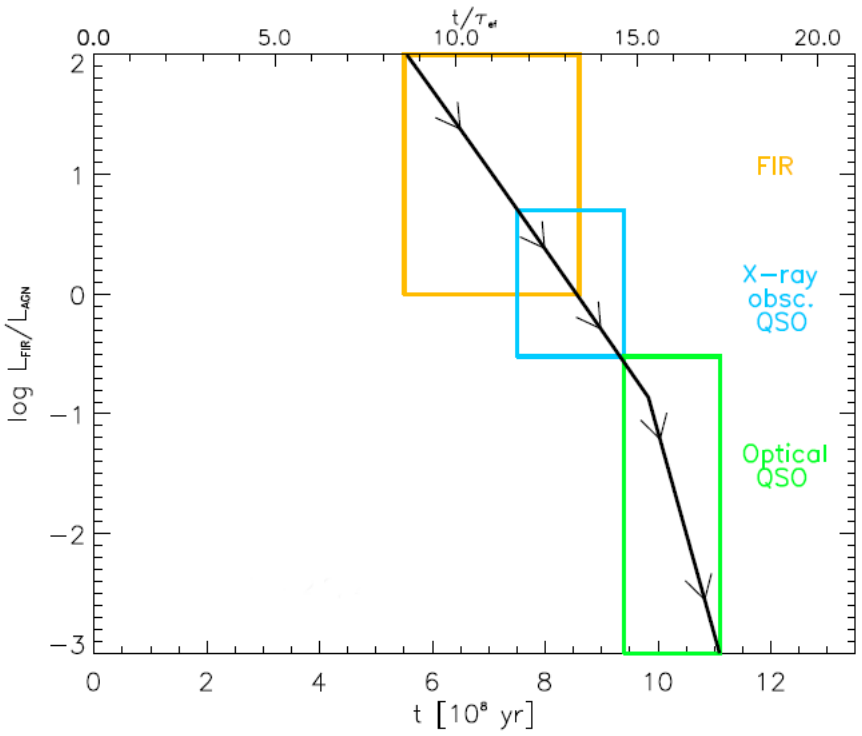

FIGURE 4.12: A schematic illustration of the different phases, marked by the colored boxes, of our galaxy/AGN coevolution scenario, as traced by the ratio $L_{\rm SFR}/L_{\rm AGN}$. The orange box refers to the FIR bright phase, the cyan box to the obscured X-ray QSO phase, and the green box to the optically bright QSO phase. We also note that an X-ray selection unbiased to obscuration can pick up objects with very different values of $L_{\rm SFR}/L_{\rm AGN}$, as shown in Fig. 4.10 and pointed out in the text.

4.5.2 Star formation in optically selected QSOs

Star formation in some galaxies hosting an optically selected QSO has been clearly detected in the (sub-)mm, even at very high redshifts (see Omont et al. 1996, 2001, 2003; Carilli et al. 2001; Priddey et al. 2003; Wang et al. 2008; Serjeant et al. 2010; Bonfield et al. 2011; Mor et al. 2012), up to $z \sim 7$ (Venemans et al. 2012). Most of these observations have targeted QSOs endowed with very large bolometric luminosities ($L_{\rm AGN} \approx 4 \times 10^{47}$ erg s^{-1}).

Omont et al. (2001, 2003), Carilli et al. (2001), and Priddey et al. (2003) observed more than 100 optically selected QSOs ($2 \lesssim z \lesssim 4$) at mm wavelengths, with a detection rate of $\approx 30\%$. At variance with the X-ray absorbed QSOs, the optically selected ones exhibit $L_{\rm SFR}/L_{\rm AGN} \lesssim 0.3$, with an average value of ~ 0.12 for detected sources. Millimeter flux stacking on undetected targets yields $\langle L_{\rm SFR}\rangle/\langle L_{\rm AGN}\rangle \approx 1.5 \times 10^{-2}$. The typical average ratio for the detected and undetected QSOs is $\langle L_{\rm SFR}\rangle/\langle L_{\rm AGN}\rangle \approx 0.06$. The five optically selected QSOs at $z \sim 4.8$, detected by Mor et al. (2012) in the sub-mm bands with *Herschel*, show larger ratios ($0.25 \lesssim L_{\rm SFR}/L_{\rm AGN} \lesssim 0.6$). However, as pointed out

by the authors, such values must be taken as upper limits, since the sub-mm fluxes refer to regions within $10''$ from the targeted QSOs, and they are close to, or below, the source confusion limit.

Small $L_{\rm SFR}/L_{\rm AGN}$ ratios for high redshift QSOs are fully confirmed by the results of the *Herschel*-ATLAS survey (Serjeant et al. 2010; Bonfield et al. 2011), which include also objects with lower bolometric luminosities ($L_{\rm AGN} \sim 10^{46}$ erg s^{-1}).

The (sub-)mm searches have also been performed by targeting more than 60 optically selected QSOs at $z \sim 6$, once more favoring quite powerful sources, even though there are already attempts to observe also QSOs fainter than $L_{\rm AGN} \lesssim 10^{47}$ erg s^{-1} (Willott et al. 2007; Wang et al. 2008, 2010, 2011b; Omont et al. 2013; Leipski et al. 2013). The fraction of detected luminous QSOs with $L_{\rm AGN} \approx 3 \times 10^{47}$ erg s^{-1} turns out to be $\approx 30\%$, remarkably close to what is found at lower redshifts. The average maximum ratio $\langle L_{\rm SFR}\rangle/\langle L_{\rm AGN}\rangle \lesssim 0.3$, the minimum value ≈ 0.02, derived by stacking undetected sources, and the average value ≈ 0.12, for detected objects, are quite close to those in lower redshift samples.

Can our framework cope with the results for bright QSOs? The (positive) answer is in Fig. 4.13, where we show the fraction of FIR-detected hosts of optically selected QSOs, as a function of the AGN bolometric luminosity (lower scale) and of the B-band magnitude (upper scale). We recall that, according to our scenario, the bright QSOs are associated to massive galaxy halos formed at high redshift, in agreement with the clustering data (e.g., Hickox et al. 2011). If the optically bright QSOs appear, on average, when the declining phase sets in, i.e., at a time $\tau \gtrsim \tau_{\rm P}$ when $L_{\rm SFR}/L_{\rm AGN} \lesssim 0.3$ (only a handful of observed QSOs exceed this limit), the subsequent evolution of the ratio is:

$$\frac{L_{\rm FIR}}{L_{\rm AGN}}(\tau \gtrsim \tau_{\rm P}) = \frac{L_{\rm FIR}}{L_{\rm AGN}}(\tau_{\rm P})\,\frac{e^{-\frac{(\tau-\tau_{\rm P})}{\tau_{\rm SFR}}}}{e^{-\frac{(\tau-\tau_{\rm P})}{\tau_D}}}\ . \tag{4.24}$$

Recalling that we have set $\tau_D = 3\,\tau_{\rm ef}$, and $\tau_{\rm SFR} = \tau_{\rm ef}/2$, and substituting in the above equation, we obtain:

$$\frac{L_{\rm FIR}}{L_{\rm AGN}}(\tau \gtrsim \tau_{\rm P}) \approx \frac{L_{\rm FIR}}{L_{\rm AGN}}(\tau_{\rm P})\,e^{-\frac{5}{3}\frac{(\tau-\tau_{\rm P})}{\tau_{\rm ef}}} \approx 0.3\,e^{-\frac{5}{3}\frac{(\tau-\tau_{\rm P})}{\tau_{\rm ef}}}\ . \tag{4.25}$$

According to Eq. 4.25, the time lapse between the larger ratio $L_{\rm FIR}/L_{\rm AGN} \approx 0.3$ and the ratio $L_{\rm FIR}/L_{\rm AGN} \approx 0.02$ obtained by stacking non-detections amounts to:

$$\Delta t \approx \frac{3}{5} \times \ln\left(\frac{0.3}{0.02}\right)\,\tau_{\rm ef} \approx 1.6\,\tau_{\rm ef}\ . \tag{4.26}$$

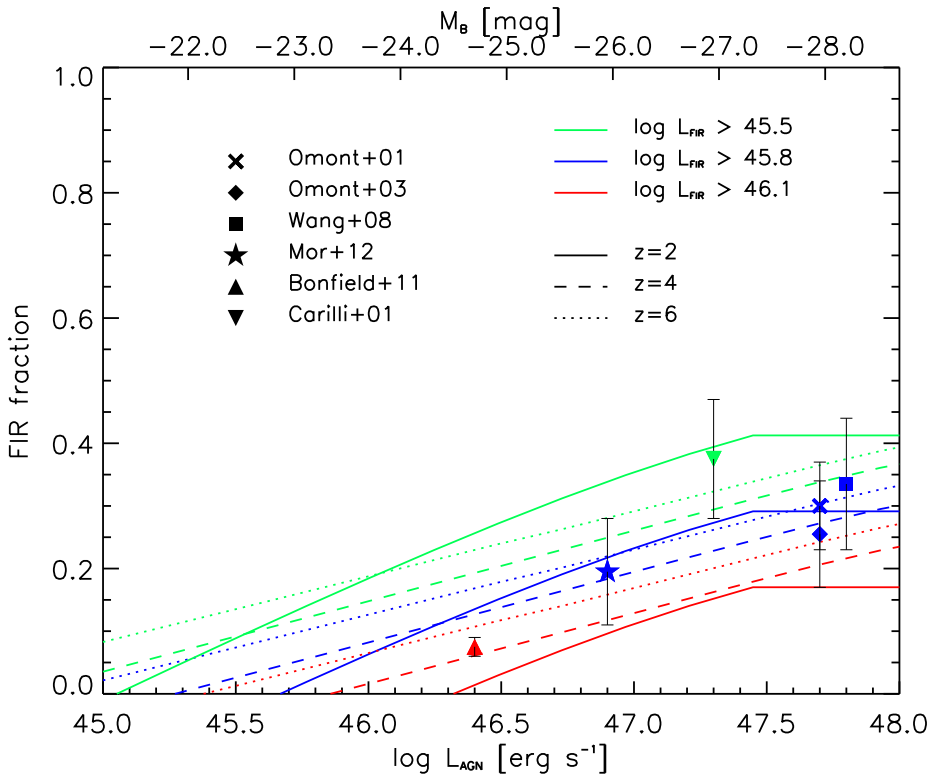

FIGURE 4.13: Fraction of FIR-detected hosts of optically selected QSOs, as a function of the AGN bolometric luminosity (lower scale) and of the B-band magnitude (upper scale). Our predictions are provided at redshift $z = 2$ (solid lines), 4 (dashed lines), and 6 (dotted lines), for different values of the FIR detection threshold: $\log L_{\rm FIR} = 45.5$ (green lines), 45.8 (blue lines), and 46.1 (red lines) erg s^{-1}. Data (same color code) are from Carilli et al. (2001, reversed triangle), Omont et al. (2001, cross), Omont et al. (2003, diamond), Wang et al. (2008, square), Bonfield et al. (2011, triangle), and Mor et al. (2012, star).

This is an estimate of the time interval between the onset of the optical phase and the time when bright QSOs are, on average, no longer detected at mm wavelengths. Over this time, the optical luminosity decreases by a factor of ~ 2, while the FIR luminosity decreases by a factor of ~ 30. Recalling that the ratio for detected objects is $L_{\rm FIR}/L_{\rm AGN} \approx 0.12$, the average time interval during which the bright QSOs are detectable at mm wavelengths is given by:

$$\Delta t \approx \frac{3}{5} \times \ln\left(\frac{0.3}{0.12}\right) \tau_{\rm ef} \approx 0.54\,\tau_{\rm ef} \ . \tag{4.27}$$

As a result, the expected detection fraction amounts to $0.54/1.6 \sim 33\%$. In this context, the similarity of the detected fraction ($\sim 30\%$) observed for bright QSOs at both low and high redshifts can be understood on the basis of the above equations, i.e., ascribed to

the similarity of the physical processes in action at redshift $z \gtrsim 1.5$. Although the above estimates are somewhat uncertain, since the statistics depend on the FIR-detection threshold, nevertheless they highlight the potential of refined data on $L_{\rm FIR}/L_{\rm AGN}$ to trace this phase of the bright QSO evolution.

These results refer to QSOs with bolometric luminosity $L_{\rm AGN} \gtrsim 6 \times 10^{47}$ erg s^{-1}. The detection rate decreases to $\lesssim 5-10\%$ when fainter QSOs with magnitude $M_{1450} \gtrsim -25$, or $L_{\rm AGN} \lesssim 6 \times 10^{46}$ erg s^{-1} are considered, as pointed out by Omont et al. (2013). The same authors found $\langle L_{\rm SFR}\rangle/\langle L_{\rm AGN}\rangle \approx 0.07$ for their observed 20 QSOs, in agreement with the findings for brighter ones. Willott, Omont & Bergeron (2013) studied with ALMA two *faint* QSOs with $M_{1450} \gtrsim -25$. One of the objects has been detected and features $L_{\rm FIR}/L_{\rm AGN} \approx 0.05$, while the second one has not been detected, providing an upper limit $L_{\rm SFR}/L_{\rm AGN} \lesssim 0.02$. Also Bonfield et al. (2011) found that the fraction of detections decreases to $\sim 8\%$ when lower luminosity QSOs ($L_{\rm AGN} \sim 10^{45}$ erg s^{-1}) are included in the target sample. In our framework, two effects cooperate to get such results:

1. At a given final BH mass, the decrease of the nuclear luminosity corresponds to a faster decrease of the SFR;

2. Less luminous QSOs are on average associated with less massive BHs and, as a consequence, with host galaxies exhibiting lower SFRs (see Fig. 4.13).

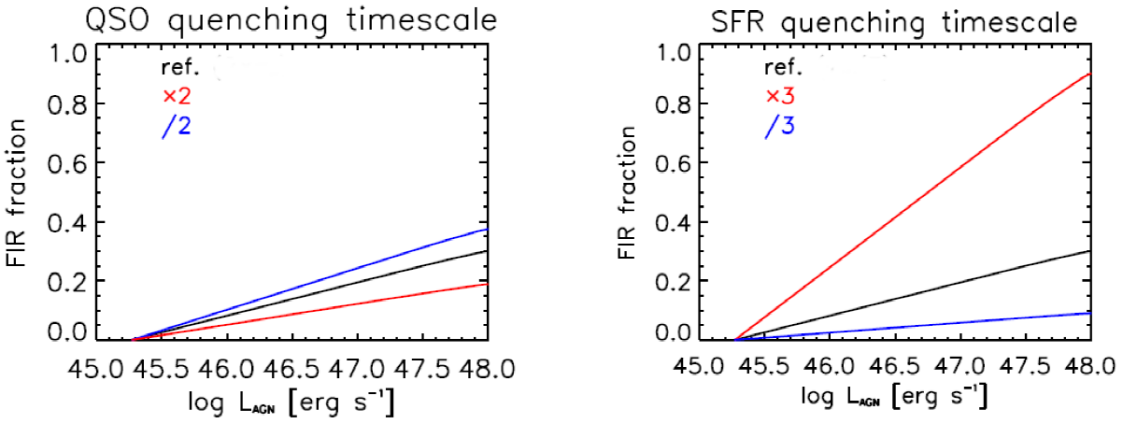

FIGURE 4.14: Dependence on parameters of the FIR-detected fraction of optically selected AGNs at $z = 4$: AGN quenching timescale τ_D (left); SFR quenching timescale $\tau_{\rm SFR}$ (right). In each panel, three curves are shown: the black ones refer to the fiducial value of the parameter (see text), the red ones to an increased value, and the blue ones to a reduced value, as detailed in the legend.

In Fig. 4.14, we show how the FIR-detection fraction of optically selected QSOs depends on the model parameters. In particular, we illustrate how it changes when varying the

AGN (left) and the SFR (right) quenching timescales. The same comments to Fig. 4.9 hold, so we do not repeat them here.

The observational data suggest that the X-ray absorbed QSOs and the optically selected QSOs are representative of two adjacent and subsequent phases, encompassing the time when the AGN luminosity overcomes the SFR luminosity of the host, while the QSO winds remove the ISM and reshape the reservoir around the BH (see Fig. 4.12). The handful of optically selected QSOs with $L_{\rm SFR}/L_{\rm AGN} \gtrsim 0.3$ can be understood as peculiar objects, wherein the obscuration usually associated with large $L_{\rm SFR}/L_{\rm AGN}$ does not preclude them to be selected in optical surveys. For instance, the QSO J0129-0035 at $z = 5.78$, the faintest one found in the SDSS, exhibits $L_{\rm SFR}/L_{\rm AGN} \approx 0.83$ (Wang et al. 2013b). This object also features a quite weak Lyα line emission (Jiang et al. 2009), as expected for a partially obscured object.

On the other hand, we recall that, when $L_{\rm SFR}/L_{\rm AGN} \lesssim 0.3$, the AGN feedback fully removes the cold gas and stops any flow toward the reservoir/torus, which shrinks down in mass and size. Therefore, during this epoch, the optical and X-ray emissions are on average less obscured (see Sec. 4.7). Thus, the selected objects appear as unobscured AGNs, exhibiting the well known correlation between UV/Optical and X-ray emission (e.g., Lusso et al. 2010).

According to our framework, luminous objects evolve along the following sequence, already illustrated in Fig. 4.12: at first, the galaxies are violently forming stars, growing up a SMBH in their centers. The BH manifests its mass accretion in hard X-rays, because the obscuration for these energetic photons is less dramatic. Then, the QSO winds clear up the ISM and an optical bright phase follows, until the exhaustion of the fuel in the reservoir.

The sequence looks similar to that suggested by Sanders et al. (1988), although major mergers are not the leading phenomenon in our framework. It is quite remarkable that, even at high redshift, the stage of strong star formation in a QSO precursor has been already detected. This is the case of HFSL3 at $z \approx 6.3$ (Riechers et al. 2013). Its gas mass $M_{\rm gas} \approx 10^{11}\,M_{\odot}$, about 40% of the dynamical mass, is distributed within a radius $\lesssim 2$ kpc, and its properties are consistent with our scenario. Such system is predicted to evolve into a QSO like SDSSJ114816.64+525150.3 at $z \approx 6.42$ within a few e-folding times. As a matter of fact, Walter et al. (2009) have detected in SDSSJ114816.64+525150.3 a huge SFR ($\dot{M}_{\star} \approx 1700\,M_{\odot}$ yr^{-1}) within a radius $\lesssim 1$ kpc. We notice that this object has a ratio $L_{\rm FIR}/L_{\rm AGN} \approx 0.2$, as expected from our framework (see Fig. 4.12).

An additional prediction of our overall picture is that the mass in stars and the BH mass are already settled to their final values in optically selected QSOs, since both star formation and BH accretion are exponentially declining during the optical bright phase. In conclusion, even though the AGN light curve around and after the peak of the activity has been prescribed in order to fit the behavior of X-ray selected AGNs, it nicely describes also the statistics of optically selected QSOs.

4.6 Additional observational constraints

Additional observations, concerning the evolution of the $M_{\rm BH}/M_\star$ ratio, the obscured to unobscured AGN fraction, and the QSO outflows, are less systematic because of their inherent difficulty, but still provide useful constraints. In this section, we aim to discuss these observations within our framework.

4.6.1 Stellar and BH masses in QSOs

As recalled at the beginning of this Chapter, the mass of the old stellar population correlates with the mass of the central SMBH in local ETGs. On the other hand, it has been claimed by many authors that the relationship changes with cosmic time. While individual BH and stellar mass estimates for high redshift AGNs must be taken with caution, the data are nevertheless rather informative.

The first relevant piece of evidence is that the optically selected QSOs at $z \gtrsim 2$ exhibit on average a $M_{\rm BH}/M_\star$ ratio $3-20$ times higher than the local value, $\Gamma_0 \approx 3 \times 10^{-3}$, (e.g., McLure & Dunlop 2004; Peng et al. 2006; Coppin et al. 2008; Decarli et al. 2010; Merloni et al. 2010; Wang et al. 2010; Targett, Dunlop & McLure 2012; Omont et al. 2013; Wang et al. 2013b). We claim that such a finding is due to a selection bias. In fact, the high luminosity tail ($L_{\rm AGN} \gtrsim 10^{47}$ erg s^{-1}) of the LF of optically selected AGNs at $z \gtrsim 3$ includes objects that are on the high side ($\gtrsim 3\,\sigma$) of the local Γ_0 distribution (e.g., Wyithe & Loeb 2003; Mahmood, Devriendt & Silk 2005; Lapi et al. 2006, see their Fig. 4; Lauer et al. 2007). Considering the scatter of 0.4 dex of the local ratio, our predicted value for optically selected QSOs is $M_{\rm BH}/M_\star \gtrsim 10^{-2}$, in good agreement with the observational data.

Note that our framework predicts that optically selected QSOs have already assembled most of their final stellar and BH masses. This does not exclude that some mass is subsequently added, but the later evolution must have a minor impact, on average.

The complementary view of the BH and stellar mass evolution is given by (sub-)mm selected galaxies with detectable AGN activity. The results of Borys et al. (2005), Alexander et al. (2005, 2008), Melbourne et al. (2011), and Carrera et al. (2011) strongly suggest that, in these galaxies, the ratio $M_{\rm BH}/M_{\star} \lesssim (0.1-0.3)\,\Gamma_0 \approx 3-9\times10^{-4}$ applies. This is consistent with the view that in (sub-)mm selected galaxies the BH mass is still piling up. The almost constant SFR, coupled with the exponential increase of the BH accretion rate, makes this ratio increase almost exponentially before the declining phase.

4.6.2 Fraction of obscured to unobscured AGNs

AGNs are mainly classified as obscured on the basis of their emission line spectra, X-ray absorption $N_{\rm H} \gtrsim 10^{23}$ cm^{-2}, and reddening $E(B-V)$. Such a classification criteria have been recently applied by several authors to objects selected in X-rays (see Bongiorno et al. 2012) or in the NIR (Glikman et al. 2007; Banerji et al. 2012, 2013), with the purpose of understanding the fraction of obscured to unobscured AGNs/QSOs, and of searching for clues on the connection between the obscuration and the host galaxy star formation activity. We recall that, in this Chapter, we are focusing on sources with $z \gtrsim 1-1.5$. The fraction of red QSOs has been found to be significant. For instance, Glikman et al. (2007) found that the fraction of reddened QSOs with $K \lesssim 14$ can range from 25% to 60% of the total underlying population. With different selection criteria on color and limiting magnitude, Banerji et al. (2012) found that at very bright luminosities $M_i \lesssim -30$, the red QSOs are ~ 5 times more numerous than the UV bright ones. However, just below that limit, the fraction significantly decreases to values close to those found by Glikman et al. (2007).

According to our framework, we expect that an obscured AGN phenomenology occurs before the action of the QSO wind, when $L_{\rm SFR}/L_{\rm AGN} \gtrsim 0.3$, and the UV-optical lines and continuum emission of the AGN are heavily absorbed by the reservoir/torus and by the dust-rich ISM. Contrarily, unobscured sources are more likely selected after the onset of the QSO wind, when the ISM and the reservoir have been significantly depleted.

Before the setting of QSO winds, during the obscured phase, the size of the highly ionized region of the ISM surrounding the QSOs is limited, since most of the UV and ionizing photons are heavily absorbed.

The small size of the ionized region around ULASJ112001.48+064124.3 at $z \approx 7.1$ (the highest redshift QSO detected so far), claimed by Mortlock et al. (2011), can be ascribed to such an effect, as also supported by the radiative transfer simulations by Bolton et al. (2011). These authors found that the UV bright phase should have lasted for $\sim 10^7$ yr, implying that the estimated $M_{\rm BH} \sim 10^9 M_{\odot}$ should have grown in a previous dust

obscured phase. Interestingly, this example suggests that the early, dusty phase of QSOs at very high redshift can be easily probed by JWST (http://www.jwst.nasa.gov) with the Near Infrared Camera (NIRCam) and the Mid-Infrared Instrument (MIRI), as it can be explored at lower redshift with the Wide-field Infrared Survey Explorer (WISE) All Sky Survey (Wright et al. 2010; Banerji et al. 2013).

4.6.3 Large-scale outflows

The AGN feedback on the ISM should manifest itself in terms of large outflows (see King & Pounds 2015 for a recent review), signaling the rapid expulsion of gas and the dramatic shutoff of the star formation. Large outflows have been observed in relatively nearby galaxies hosting an active nucleus (Feruglio et al. 2010; Rupke & Veilleux 2011; Sturm et al. 2011; Greene, Zakamska & Smith 2012). At $z \gtrsim 1$, QSOs winds associated with large mass outflows have been detected by several studies (e.g., Maiolino et al. 2001, 2004; D'Odorico et al. 2004; Brusa et al. 2015; Cicone et al. 2015). Optically thick gas, moving at large velocity around QSOs up to a distance of 100 kpc, has been detected by Prochaska & Hennawi (2009), possibly associated with quite massive outflows.

Broad-absorption line QSOs constitute the most basic and longstanding aspects of outflow phenomenology; line-driven outflows are expected in the form of winds, that can form just above the accretion disc by a combination of radiation and gas/magnetic pressure (see Zubovas & King 2013). In fact, massive outflows have been confirmed in such objects by many X-ray observations (Brandt & Gallagher 2000; Chartas, Brandt & Gallagher 2003; Chartas et al. 2009). Recently, Borguet et al. (2013) detected the most energetic QSO outflow to date, with a kinetic power of $\sim 10^{46}$ erg s^{-1} and an associated mass flow rate of $\sim 400\, M_{\odot}$ yr^{-1}.

The most evident massive QSO outflow has been detected by Maiolino et al. (2012) with highly accurate and detailed observations of the C[II] line in SDSSJ114816.64+525150.3 at $z = 6.42$. The authors estimate an outflow rate of $\approx 3000\, M_{\odot}$ yr^{-1}, capable of removing the gas in the host galaxy within 6×10^6 yr. Thus, for massive BHs, we prescribe outflow rates ranging from several hundreds to several thousands of $M_{\odot}$ yr^{-1}.

Our scenario also requires, before the peak of the nuclear activity, weaker galactic winds mainly driven by stellar feedback, as observed in some starforming galaxies at substantial redshift (Alexander et al. 2010; Genzel et al. 2012). Both AGN and stellar feedbacks can remove a huge amount of cold gas from the central regions of galaxies, though on different timescales. For instance, in SDSSJ114816.64+525150.3 the dynamical mass within a radius of ~ 2.5 kpc is about twice the gas mass (Wang et al. 2010). The results of Maiolino et al. (2012) suggest that the central regions of the host are deprived of

about half of their mass in less than 10^7 yr. Hence, these outflows must affect the inner structure of the host galaxies, as pointed out by several authors (see Fan et al. 2008, 2010, 2013; Damjanov et al. 2009; Zubovas et al. 2013).

It is worth mentioning that, while usually the AGN feedback is invoked to turn off the star formation, the latter may occur in the outflowing shell (see Ishibashi & Fabian 2012; Silk 2013; Zubovas et al. 2013; King & Pounds 2015). Since FIR-selected samples show that the SFR is high even when the AGN luminosity (and hence the feedback) is low, this mechanism can originate only a fraction of the total stellar mass, while still relevant with respect to the size of the host galaxy (Ishibashi & Fabian 2012). In particular, in the early phases of the evolution, the SN feedback is energetically dominant with respect to the AGN one, and the observations reveal large stellar masses associated with huge gas abundance and weak AGN activity (i.e., low mass BHs).

In summary, large outflows able to remove most of the ISM from AGN hosts are detected at least in one case, and possibly in several others. We recall that even the short duration of the phase can significantly depress the statistics of outflow detection. For instance, in the case of SDSSJ114816.64+525150.3, the gas within a scale of $5 - 10$ kpc is going to be removed in $\approx 6 \times 10^6$ yr, which is 20% of the duration of the QSO optical phase.

4.7 Discussion

Here we first discuss the observational evidence and the properties of the circumnuclear structures in local AGNs, related to the presence of a massive gas reservoir, as predicted by our coevolution framework (see Sec. 4.1). Then, by extrapolating the results of the local observations to higher redshifts, we show that ALMA high resolution imaging and coordinated X-ray high resolution observations of strongly lensed (sub-)mm selected galaxies can cast light on the epoch of stellar and BH mass growth. In the light of our scenario, we point out several physical mechanisms operating on different scales, which can lead to the accretion of a fraction of the ISM.

4.7.1 The reservoir

As already enunciated, our framework predicts that a gas reservoir soon sets up around the central SMBH. Its formation stems from the requirement of funnelling gas of low angular momentum at a rate proportional to the SFR, while the BH accretes in a self-regulated regime. Such a structure could constitute a (proto-)torus around the BH, of the same kind as that observed at low redshift and often called for in order to explain

the diversity of unobscured and obscured AGNs (see Sec. 4.6.2). This torus/reservoir, with size ranging from a few to several tens of parsecs, has been studied in detail only in nearby AGNs. High spatial resolution observations reveal that molecular gas and dust are largely present (e.g., Müller Sánchez et al. 2009; Krips et al. 2011; Diamond-Stanic & Rieke 2012; Sani et al. 2012; Hönig et al. 2013), often accompanied by star formation (e.g., Davies et al. 2007; Storchi-Bergmann et al. 2012). The dust distribution looks quite complex: the hot component is located in compact structures, while the warm one is more diffuse (see Hönig et al. 2013).

The studies of Kawakatu et al. (2007), Spaans & Meijerink (2008), and Maiolino (2008) concluded that a reservoir/torus with mass $M_{\rm res} \approx 10^8 - 10^9\,M_{\odot}$, extending to ~ 100 pc, can be revealed up to redshift $z \lesssim 2$ by ALMA, thanks to its extraordinary sensitivity and exquisite spatial resolution. In fact, recently ALMA, though in a still incomplete technical configuration, has revealed CO, HCN, and HCO^+ emission lines in the very central regions of some nearby objects (see Combes et al. 2013; Fathi et al. 2013; Izumi et al. 2013).

In high redshift galaxies, the mass in cold gas/dust relative to that in stars is expected to be much larger than in local AGNs. In fact, CO emission lines have been detected by ALMA in a number of $z \sim 2-3$ objects (see Weiß et al. 2013). In addition, the potential efficiency of ALMA for these studies is boosted up in the case of strongly lensed (sub-)mm galaxies. As predicted by Negrello et al. (2007, 2010), and Blain et al. (2004), strongly lensed starforming galaxies can be efficiently selected with large area, relatively shallow (sub-)mm surveys.

In this context, González-Nuevo et al. (2012) have shown that about 10^3 strongly lensed starforming galaxies at $z \gtrsim 2$ can be easily extracted from the H-ATLAS survey, that covers ~ 550 deg^2. About 5% of them are magnified by a factor $\gtrsim 10$ (see Lapi et al. 2012; Bussmann et al. 2013). Additional starforming, strongly lensed galaxies have been detected by the HerMES (see Wardlow et al. 2013) and the South Pole Telescope (SPT) survey, of about 1200 deg^{-2}, at mm wavelengths (Vieira et al. 2013). Taking the Kawakatu et al. (2007, see their Fig. 2) model as a reference, one finds that lensing by factors $\gtrsim 10$ brings the apparent size of a reservoir with physical size $R_{\rm res} \approx 100$ pc to $\approx 0.07''$ (or to $0.015''$ for a physical size $R_{\rm res} \approx 20$ pc), well above the resolution achievable with ALMA for almost all CO transition lines.

Specifically, the CO emission lines with rotational angular momentum quantum number $J \geq 2$ are detectable in 12 hr at $5\,\sigma$ for $z \gtrsim 2$. CO$(6-5)$ and CO$(5-4)$ are detectable in about 4 hr (Kawakatu et al. 2007, see their Fig. 3). Even the HCN lines can be observed, at least for higher J (Kawakatu et al. 2007, see their Fig. 4). The C[II] 158 μm line can also be excited in the molecular torus by a combination of the AGN emission and of the

possible star formation (Pérez-Beaupuits, Wada & Spaans 2011). If so, ALMA will be able to produce detailed mapping of the C[II] emission in the torus up to large redshifts, in its final configuration.

We caution that the Kawakatu et al. (2007) model makes the classic assumption of a smooth, homogeneous dust distribution (e.g., Pier & Krolik 1992; Granato & Danese 1994; Efstathiou & Rowan-Robinson 1995). Clumpy torus models may be more realistic, as demonstrated by MIR observations of silicate emission features in local AGNs (see Nenkova et al. 2008a,b; Hönig et al. 2010; Kawaguchi & Mori 2011; Hönig et al. 2013).

Efstathiou et al. (2014) presented a detailed analysis on the spectrum of IRAS 08572+3915, a nearby starburst galaxy endowed with an AGN. Combining new *Herschel* observations with previous NIR and FIR datasets, they showed that the dusty torus illuminated by the AGN contributes to about 90% of the total IR luminosity. They also demonstrated that the FIR luminosity, in the wavelength range $40 \lesssim \lambda \lesssim 800\,\mu$m, of a smooth torus is a factor $\lesssim 2.5$ lower than that of a clumpy torus. Their measured total SED falls in between the smooth and the clumpy torus SEDs (cf. their Fig. 3). All in all, this result suggests that the FIR continuum emission of a smooth torus can be taken as a lower limit to the case of a clumpy torus.

Concerning the high-J CO emission lines, Kawakatu et al. (2007) found their results to agree with the outcomes from numerical simulations of 3D, non-local thermal equilibrium radiative transfer in inhomogeneous dusty tori (see Wada & Tomisaka 2005). In fact, recent observations of nearby Seyfert galaxies with *Herschel* (see Hailey-Dunsheath et al. 2012; Spinoglio et al. 2012; Pereira-Santaella et al. 2013) have revealed high-J CO emission lines roughly consistent with the expectations from homogeneous torus models.

We also remark that MIR emission from clumpy tori, as modeled by Hönig & Kishimoto (2010), and investigated by means of high-spatial resolution MIR spectrophotometry of Seyfert galaxies by Hönig et al. (2010), may be detectable with the JWST even in high-redshift galaxies, provided that they are gravitationally lensed at magnifications $\gtrsim 10$ (see Kawakatu & Ohsuga 2011).

Maps and velocity profiles of the molecular lines in strongly lensed starbursting galaxies will produce invaluable information on chemical composition, kinematic and mass of the reservoir during a crucial phase of galaxy evolution and BH accretion. In particular, in the instance of quite large gravitational amplification, we can even get estimates of the BH mass. These observations should be complemented by X-ray observations, which for magnification $\gtrsim 10$ will allow us to get a detailed view of the nuclear emission, even for highly obscured and quite low luminosity objects (Matt et al. 2004; Georgantopoulos, Rovilos & Comastri 2011).

The predicted intrinsic X-ray luminosity for typical lensed galaxies exceeds $L_X \gtrsim 10^{42}$ erg s^{-1}; the magnification by factors $\gtrsim 10$ makes them easily detectable in pointed observations up to $z \gtrsim 3$ with *Chandra* and the next generation of X-ray instruments.

In conclusion, coordinated, high-resolution ALMA and X-ray observations offer the possibility to probe the reservoir/torus and the AGN activity in lensed, FIR-selected galaxies. The outcome will provide an enormous progress in understanding the formation and coevolution of stars and SMBHs in primeval galaxies.

4.7.2 From the ISM to the reservoir

The first step for the ISM gas, in its path toward the central SMBH, is the reservoir. Our scenario prescribes that, when the star formation is vigorous in the host galaxy, some mechanism is able to drive a fraction of the ISM gas into the reservoir, at a rate proportional to the SFR. Several physical mechanisms can cause a fraction of the gas in galaxies to lose angular momentum and to pile up in the very central regions (see Alexander & Hickox 2012 for a comprehensive review).

A non exhaustive list includes gas drag, dynamical friction of gas plus star clumps, tidal fields, spiral waves, radiation drag, winds and bars (e.g., Norman & Scoville 1988; Shlosman, Frank & Begelman 1989; Shlosman, Begelman & Frank 1990; Shlosman & Noguchi 1993; Hernquist & Mihos 1995; Noguchi 1999; Umemura 2001; Kawakatu & Umemura 2002; Kawakatu, Umemura & Mori 2003; Thompson, Quataert & Murray 2005; Bournaud, Elmegreen & Elmegreen 2007; Bournaud et al. 2011; Hopkins & Quataert 2010, 2011). In general, the presence of clumps, which may be generated by fragmentation of gas already organized in an unstable disc or by inflow of gas and star subclumps, tends to increase the efficiency of such mechanisms.

Since the loss of angular momentum is a requirement also for the cold gas to collapse into clouds and to fragment into stars, the starburst activity and the AGN fueling have been often associated. Gravitational torques acting on gaseous and stellar discs can induce radial flows of the ISM (e.g., Shlosman, Frank & Begelman 1989; Shlosman, Begelman & Frank 1990), thus increasing the central surface density, triggering star formation in the inner kpc scale, and moving gas toward the internal 100 pc region. Such gravitational torques can be induced by external events, such as tidal encounters, orbital torques by satellites and minor/major mergers, or by internal instabilities related to infall, bars, or asymmetries generated during the evolution of the gas plus star structure.

Disc instabilities also grow gaseous clumps that migrate toward the central regions by dynamical friction (Shlosman & Noguchi 1993). The clumps can then contribute to the

formation of the bulge (Noguchi 1999; Genzel, Eisenhauer & Gillessen 2010; Genzel et al. 2011; Immeli et al. 2004; Ceverino, Dekel & Bournaud 2010; Bournaud, Elmegreen & Elmegreen 2007; Bournaud et al. 2014). All these processes are expected to establish a kind of relationship between the rate of star formation, at least in the inner kpc scale, and the rate at which the gas is delivered toward the very central regions of the galaxy.

Hopkins & Quataert (2010, 2011) have explored in detail the effects of gravitational torques (externally or internally induced), with numerical simulations. They show that part of the ISM gas is shocked, and dissipates energy and angular momentum, flowing toward the central regions. On scales of $1-30$ pc, such a gas can reach large surface densities, $\sim 10^{11}\,M_{\odot}$ kpc^{-2}. This gas can be identified with the reservoir/torus introduced in our framework.

In summary, there are several physical mechanisms, supported by observations, that can plausibly reduce the angular momentum, at least for a fraction of the diffuse ISM gas, and drive it to migrate from kpc to $\lesssim 100$ pc scale at a rate proportional to the SFR of the host galaxy.

4.7.3 From the reservoir to the accretion disc

Once low angular momentum gas has accumulated in the reservoir, additional loss/tranfer of angular momentum is required in order to bring the gas toward the accretion disc at sub-parsec scales. Some of the mechanisms at work on larger scales have been proposed to operate also on the smaller ones; for instance, bars-in-bars instabilities (Shlosman, Frank & Begelman 1989; Shlosman, Begelman & Frank 1990), gravitational interactions and dynamical friction in clumped discs (Kumar 1999) have been proposed.

Several authors have pointed out that, in the circumnuclear regions on parsec scales, the gas is very likely rich in metals and dust, prone to fragment in clumps and to form stars. On one side, the stellar feedback can remove part of the gas from the reservoir; on the other side, it can favor the gas to flow toward the accretion disc (e.g., Wada & Norman 2001, 2002; Thompson, Quataert & Murray 2005; Murray, Quataert & Thompson 2005; Kawakatu & Wada 2008).

For instance, in the model proposed by Kawakatu & Wada (2008), the gas turbulence supported by SN explosions transports angular momentum. As a result, $\sim 10-30\%$ of the gas flowing from larger scales can migrate toward the accretion disc. Moreover, in the numerical simulations by Hopkins & Quataert (2010), there is a correlation between the SFR in the circumnuclear disc and the rate of accretion onto the BH. Thompson,

Quataert & Murray (2005) found two possible classes of circumnuclear discs, depending on the rate at which the gas is supplied:

- discs with star formation large enough to consume most of the available gas, and with practically no accretion onto the central SMBH;
- discs with large star formation only at their periphery, which still retain enough gas in the internal regions to ensure significant accretion.

Storchi-Bergmann et al. (2012) detected star formation in the Seyfert 2 NCG 1068 on a scale of ~ 100 pc. Sani et al. (2012) confirmed this result for four additional nearby Seyfert galaxies, but concluded that the physical conditions of the gas in inner regions are not favorable to star formation. On the theoretical side, Begelman & Shlosman (2009) pointed out that, in the circumnuclear discs, highly turbulent continuous flows are relatively stable against fragmentation.

A relevant point is that the star formation, and its associated feedback in the reservoir, should *not* be too much efficient; otherwise, the amount of gas available to flow toward the SMBH will be substantially reduced, and, eventually, the relationship between stellar and BH mass will be erased (King & Pounds 2015). Likely, in the balance, the overall mass of long-living stars formed in the reservoir should be much less than the mass accreted onto the SMBH.

4.7.4 The accretion rate and the effect of feedback

Analytical approaches and hydrodynamical simulations have been used so far to explore possible effects of the AGN radiative power on the accretion rate (e.g., Begelman 1979; Abramowicz & Lasota 1980; Abramowicz et al. 1988; Watarai et al. 2000; Watarai 2006; Ohsuga 2007; Ohsuga & Mineshige 2011; Fabian 2012). In general, the rate $\dot{M}_{\rm acc}$ of gas accretion is possibly only a fraction of the rate $\dot{M}_{\rm inj}$ at which the gas is injected from the reservoir toward the BH:

$$\dot{M}_{\rm acc} = f_{\rm acc}\dot{M}_{\rm inj} \ , \tag{4.28}$$

due to possible outflows (Begelman 2012; Watarai 2006; Ohsuga 2007; Li 2012). The net effect is a kind of self-regulation (see Debuhr et al. 2010; Debuhr, Quataert & Ma 2011, 2012). We fiducially assume that most of the matter delivered from the reservoir toward the SMBH does accrete, and only a negligible fraction goes into winds, i.e. $f_{\rm acc} \sim 1$. As we already mentioned, this is required in order not to lose the correlation between the BH and the stellar mass. However, a significant variance in $f_{\rm acc}$ is expected, and should produce a variance in the final BH mass.

Moreover, we note that ϵ and $\lambda_{\rm Edd}$ are expected to fluctuate on very short timescales, depending on the local physical conditions, accretion, and outflow rates (e.g., Ohsuga 2007; Li 2012); we neglect these effects in our thesis, since we refer to quantities which are *averaged* over the timescale needed by the SMBH to acquire its final mass.

In order to fit the observed statistics of both (sub-)mm/FIR and X-ray selected objects at $z \gtrsim 2$, we assume that the accretion is self-regulated, with a time-averaged Eddington ratio $1 \lesssim \lambda_{\rm Edd} \lesssim 4$, depending on the redshift as described in Eq. 4.8, and a mass to energy conversion efficiency $0.03 \lesssim \epsilon \lesssim 0.1$, related to $\lambda_{\rm Edd}$ through Eq. 2.12. When the AGN feedback becomes dominant and the reservoir is no more fed, the accretion becomes supply-limited and sub-Eddington (see also Fig. 4.2). These outcomes can be compared to the predictions from theoretical treatments and numerical simulations concerning the accretion onto the central SMBH.

Watarai (2006) presented useful approximations of numerical and analytical results for thick/thin discs in the case of super/sub-Eddington accretion. If the accretion rate is parameterized as:

$$\xi = \dot{M}_{\rm acc} \, \frac{c^2}{L_{\rm Edd}} \ , \tag{4.29}$$

then the Eddington ratio can be approximated by:

$$\lambda_{\rm Edd} = \frac{L}{L_{\rm Edd}} \simeq 2 \, \ln \left[1 + \frac{\epsilon_0}{2} \, \xi \right] \ , \tag{4.30}$$

where $\epsilon_0 \approx 0.3$ is the efficiency for a maximally rotating BH; we recall that the spin of the BH rapidly increases to this maximal value during super-Eddington accretion episodes. The radiative efficiency during accretion is bound to be $\epsilon = \lambda_{\rm Edd}/\xi$. As a consequence, the accretion rate may exceed the Eddington one ($\xi > 1$), nevertheless keeping the ratio $\lambda_{\rm Edd} \lesssim 4$ and the radiative efficiency $\epsilon \lesssim 0.15$. For a QSO at $z = 6$, shining with a bolometric luminosity $L_{\rm AGN} \approx 3 \times 10^{47}$ erg s^{-1}, the approximation of Watarai (2006) yields $\lambda_{\rm Edd} \sim 3$ and $\epsilon \sim 0.13$, rather similar to the values adopted by us (see Fig. 4.2). Similar results have been found by Li (2012), who has also explored the possibility of having a largely super-Eddington regime followed by a sub-Eddington one, in order to explain the presence of the most massive BHs at $z \sim 6$.

The observed distribution of Eddington ratios in $z \sim 6$ quasars, estimated by Willott et al. (2010a), exhibits a lognormal distribution peaked at $\lambda_{\rm Edd} \sim 1$, with a dispersion of ~ 0.3 dex; for comparison, the distribution of $z \sim 2$ QSOs peaks at $\lambda_{\rm Edd} \sim 0.37$. The trend of decreasing Eddington ratio with redshift has been confirmed, exploiting quite large samples, by Kelly & Shen (2013), who also found that the Eddington ratio takes a maximum value of $\lambda_{\rm Edd} \sim 3$ for optical QSOs at $z \lesssim 5$. According to our framework, during the exponential growth of the BH, the maximum Eddington ratio is $\lambda_{\rm Edd} \sim 4$ at

$z \sim 6$, and $\lambda_{\rm Edd} \sim 2$ at $z \sim 2$, exponentially decreasing from those values during the optical bright phase (cf. dashed and dotted lines in Fig. 4.2), reproducing the observed behavior.

After the ejection of the cold gas by the QSO feedback, the mass in the reservoir, if not completely exhausted, is however no longer sufficient to sustain a super-Eddington accretion, because the BH mass is large; thus, a supply-limited, sub-Eddington accretion regime sets in during the declining phase of the AGN luminosity. We recall that the BH influence radius ($\approx G\,M_{\rm BH}/\sigma^2$) itself increases exponentially before the peak of the AGN activity, to attain values $\approx 70\,(M_{\rm BH}/10^9\,M_\odot)\,(\sigma/250\,{\rm km\ s^{-1}})^{-2}$ pc, close to the possible reservoir size. In these conditions, the standard theory of thin accretion discs should apply. A naive estimate of the accretion rate reads:

$$\dot{M}_{\rm acc} = \frac{M_{\rm res}}{\tau_{\rm visc}} = \frac{\sigma^3}{G\,\mathcal{R}_{\rm crit}}\,\frac{M_{\rm res}}{M_{\rm BH}}\ ; \tag{4.31}$$

here, according to standard prescriptions (e.g., Burkert & Silk (2001); Begelman (2012); King (2012)), the viscous timescale $\tau_{\rm visc} \sim \mathcal{R}_{\rm crit} \times \tau_{\rm dyn}$ is taken as the dynamical time $\tau_{\rm dyn} \approx GM_{\rm BH}/\sigma^2 \times 1/\sigma$ at the BH influence radius times the critical Reynolds number, $\mathcal{R}_{\rm crit} \sim 10^{2-3}$, for the onset of turbulence.

The accretion rates required by the data on the FIR detected fractions in X-ray selected AGN samples are lower than the simple limits derived above, amounting to $\dot{M}_{\rm acc} \sim 5\,(\epsilon/0.15)^{-1}\,M_\odot\ {\rm yr}^{-1}$. This may indicate that the fueling mechanism is very complex, as it does not depend solely on the amount of gas still available after the QSO ejection, but also on various other physical conditions. In fact, gas and dust spatial distribution, magnetic fields, viscosity, cooling and heating, radiative pressure and additional aspects have been recently introduced in hydrodynamical simulations to capture the main features of the mass transfer toward the central SMBH (see Narayan et al. 2012; Roth et al. 2012; Li, Ostriker & Sunyaev 2013; Liu et al. 2013). The results we have derived from observations in the present Chapter can help toward further, educated investigations.

4.7.5 Setting the parameters

On the basis of our analysis, we can now finally set the fiducial values of the parameters describing the AGN lightcurve (Eq. 4.5) and the SFR lightcurve (Eq. 4.12). We shall discuss the effect of varying them in Sec. 5.1.3 and Sec. 5.2.2.

In the AGN lightcurve, we adopt a descending timescale $\tau_D = 3\tau_{\rm ef}$, and a duration of the descending phase $\zeta \approx 3$ (in units of τ_D) for luminous AGNs with peak luminosity

$L \gtrsim 10^{13}\, L_\odot$, while $\tau_{\rm D} = 0$, i.e., the declining phase is almost absent, for low-luminosity objects. To interpolate continuously between these behaviors, we use a standard erfc-function smoothing:

$$\frac{\tau_{\rm D}}{\tau_{\rm ef}} = 3\left[1 - \frac{1}{2}\,{\rm erfc}\left(\frac{1}{2}\,\log\frac{L_{\rm AGN}}{10^{13} L_\odot}\right)\right] \tag{4.32}$$

which is illustrated in Fig. 4.15 (magenta line). The value of $\zeta = 3$ is fiducially adopted, since after a time $3\tau_{\rm D}$ after the peak, the BH mass has almost saturated to its final value.

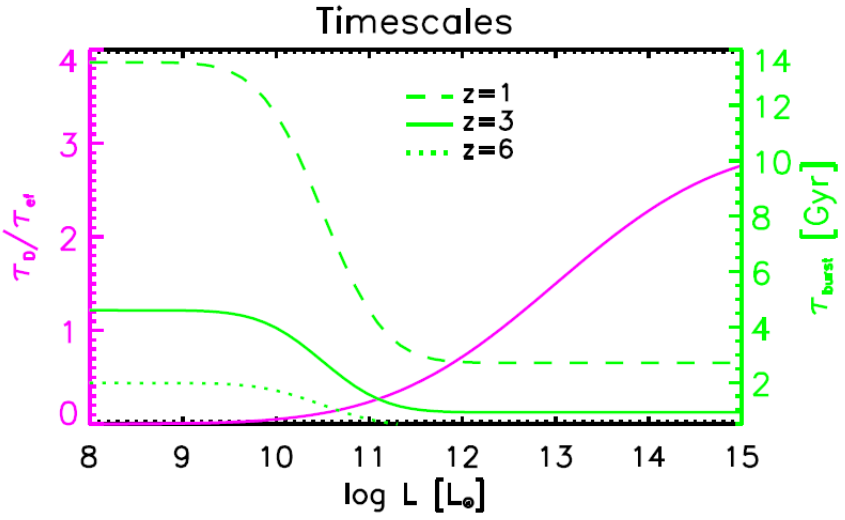

FIGURE 4.15: The characteristic timescale $\tau_{\rm D}/\tau_{\rm ef}$ of the AGN descending phase (magenta line and left axis) and the duration $\tau_{\rm burst}$ of the stellar burst (green lines and right axis) at redshift $z = 1$ (dashed), 3 (solid), and 6 (dotted), as a function of the peak AGN and of the SFR luminosity, respectively.

In the SFR lightcurve, we already set the duration of the starburst to be $\tau_{\rm burst} \sim 1$ Gyr for massive galaxies, supported by recent observations. On the other hand, longstanding data on stellar populations and chemical abundances of galaxies with final stellar masses $M_\star \lesssim 10^{10}\, M_\odot$ indicate that the star formation have proceeded for longer times, regulated by SN feedback (see reviews by Renzini 2006; Conroy 2013; Courteau et al. 2014, and references therein).

On this basis, we adopt a timescale for the duration of the starburst given by:

$$\tau_{\rm burst}(t) = 1\,{\rm Gyr}\left(\frac{1+z}{3.5}\right)^{-3/2}\left[1 + 2\,{\rm erfc}\left(\frac{4}{3}\,\log\frac{L_{\rm SFR}}{10^{10.5}\,L_\odot}\right)\right]\,. \tag{4.33}$$

The erfc-smoothing function connects continuously the behavior for bright and faint objects expected from the discussion above. The luminosity scale $3\times10^{10}\, L_\odot$ corresponds to $\dot{M}_\star \approx 5\, M_\odot\ {\rm yr}^{-1}$. At high redshift, as noted by Lapi et al. (2014), such a timescale is $\sim 0.5 - 1$ Gyr $\sim 15 - 20\,\tau_{\rm ef}$, in terms of the timescale of the hosted SMBH.

Chapter 5

Continuity Equation

Given an evolving population of astrophysical sources, we aim at linking the luminosity function $N(L,t)$ tracing a generic form of baryonic accretion (like that leading to the growth of the central SMBH or of the stellar content in the host galaxy) to the corresponding final mass function $N(M,t)$. To this purpose, we exploit the standard continuity equation approach (e.g., Small & Blandford 1992; Yu & Lu 2004), in the integral formulation:

$$N(L,t) = \int_0^\infty \mathrm{d}M \; [\partial_t N(M,t) - S(M,t)] \sum_i \frac{\mathrm{d}\tau_i}{\mathrm{d}L}(L|M,t) \; ; \tag{5.1}$$

here τ is the time elapsed since the triggering of the activity (the internal clock, different from the cosmological time t), and $\mathrm{d}\tau/\mathrm{d}L$ is the time spent by the object with final mass M in the luminosity range $[L, L+\mathrm{d}L]$ given a lightcurve $L(\tau|M,t)$; the sum allows for multiple solution τ_i of the equation $L = L(\tau|M,t)$. In addition, $S(M,t)$ is a source term due to 'dry' merging (i.e., not contributing to luminosity). In solving Eq. 5.1, we shall set the latter to zero. We will investigate the impact of dry merging in Sec. 5.3. Note that, by integrating Eq. 5.1 in $\mathrm{d}t$ from 0 to the present time t_0, we recover Eq. 18 of Yu & Lu (2004).

If the timescales τ_i (that encase the mass-to-energy conversion efficiency ϵ) are constant in redshift and luminosity, then a generalized Soltan (1982) argument, concerning the equivalence between the integrated luminosity density and the local, final mass density, can be straightforwardly recovered from Eq. 5.1 without source term, by multiplying by

L and integrating it over L and t:

$$\begin{aligned}\int_0^{t_0} \mathrm{d}t \int_0^{\infty} \mathrm{d}L\, L\, N(L,t) &= \int_0^{\infty} \mathrm{d}M\, N(M,t) \int_0^{\infty} \mathrm{d}L\, L \sum_i \frac{\mathrm{d}\tau_i}{\mathrm{d}L} \\ &= \mathrm{const} \times \int_0^{\infty} \mathrm{d}M\, M\, N(M,t)\ ,\end{aligned} \tag{5.2}$$

where the last equivalence holds since $\sum_i \int \mathrm{d}\tau_i\, L \equiv \mathrm{const} \times M$. Specifically, for the SMBH population, the constant is equal to $\epsilon\, c^2/(1-\epsilon)$. We will see in Sec. 5.2 that an analogous expression holds for the stellar component in galaxies.

More in general, Eq. 5.1 constitutes an integro-differential equation in the unknown function $N(M,t)$, that can be solved once the input luminosity function $N(L,t)$ and the lightcurve $L(\tau|M,t)$ have been specified.

5.1 Black Hole Mass Function

In this Section, we use Eq. 5.1 to derive the BHMF throughout the history of the Universe from the AGN LF. Remarkably, it can be solved in closed analytic form under the quite general assumptions we made on the AGN lightcurve.

5.1.1 Connection with standard approaches

It is useful to show the connection of Eq. 5.1 with the standard, differential form of the continuity equation for the evolution of the BHMF, as pioneered by Small & Blandford (1992), and then used in diverse contexts by many authors (e.g., Salucci et al. 1999; Yu & Tremaine 2002; Marconi et al. 2004; Shankar et al. 2004; Shankar, Weinberg & Miralda-Escudé 2009; Merloni & Heinz 2008; Cao 2010). Following Small & Blandford (1992), BHs are assumed to grow in a single accretion episode, emitting at a constant fraction λ_{Edd} of their Eddington luminosity. The resulting lightcurve can be written as:

$$L_{\mathrm{AGN}}(\tau|M_{\mathrm{BH}},t) = \frac{\lambda_{\mathrm{Edd}}\, M_{\mathrm{BH}}\, c^2}{t_{\mathrm{Edd}}}\, e^{(\tau-\tau_{\mathrm{burst}})/\tau_{\mathrm{ef}}} \qquad \tau \leq \tau_{\mathrm{burst}}\ ; \tag{5.3}$$

here M_{BH} is the final BH mass, $\tau_{\mathrm{burst}} = \int \mathrm{d}\tau$ is the total duration of the luminous accretion phase, and τ_{ef} is the $e-$folding time defined in Eq. 4.7. Then we have:

$$\frac{\mathrm{d}\tau}{\mathrm{d}L_{\mathrm{AGN}}} = \frac{\tau_{\mathrm{ef}}}{L_{\mathrm{AGN}}}\, \Theta_H \left[L_{\mathrm{AGN}} \leq L_{\mathrm{AGN}}(M_{\mathrm{BH}})\right]\ , \tag{5.4}$$

where the Heaviside step function $\Theta_H(\cdot)$ specifies that a BH with final mass $M_{\rm BH}$ cannot have shone at luminosity exceeding

$$L_{\rm AGN}(M_{\rm BH}) \equiv \frac{\lambda_{\rm Edd}}{t_{\rm Edd}}\, M_{\rm BH} c^2 \ . \tag{5.5}$$

Equivalently, only BHs with final masses exceeding

$$M_{\rm BH}(L_{\rm AGN}) \equiv L\, \frac{t_{\rm Edd}}{\lambda_{\rm Edd}}\, c^2 \tag{5.6}$$

have attained a luminosity $L_{\rm AGN}$, and so can contribute to the integral on the right hand side of Eq. 5.1. Hence, such an equation can be written as:

$$L_{\rm AGN}\, N(L_{\rm AGN}, t) = \int_{M_{\rm BH}(L_{\rm AGN})}^{\infty} {\rm d}M_{\rm BH}\, [\partial_t N(M_{\rm BH}, t) - S(M_{\rm BH}, t)]\, \tau_{\rm ef} \ . \tag{5.7}$$

Differentiating both sides with respect to L and rearranging terms yields:

$$\partial_t N(M_{\rm BH}, t) + \frac{1}{\tau_{\rm ef}}\, \partial_{M_{\rm BH}} [L_{\rm AGN}\, N(L_{\rm AGN}, t)]_{|L_{\rm AGN}(M_{\rm BH})} = S(M_{\rm BH}, t) \ . \tag{5.8}$$

Now we can formally write:

$$\begin{aligned} N(L_{\rm AGN}, t) &= N(M_{\rm BH}, t)\, \frac{{\rm d}M_{\rm BH}}{{\rm d}L_{\rm AGN}}\, \delta_{\rm AGN}(M_{\rm BH}, t) \\ \langle L_{\rm AGN} \rangle &= \delta_{\rm AGN}(M_{\rm BH}, t)\, L_{\rm AGN} \end{aligned} \tag{5.9}$$

in terms of the BH duty cycle:

$$\delta_{\rm AGN}(M_{\rm BH}, t) \equiv \tau_{\rm burst}(M_{\rm BH}, t)/t \lesssim 1 \ . \tag{5.10}$$

Since by definition:

$$\langle L_{\rm AGN} \rangle = \epsilon\, \langle \dot{M}_{\rm BH} \rangle\, c^2/(1-\epsilon) \ , \tag{5.11}$$

one finally obtains the continuity equation in the form:

$$\partial_t N(M_{\rm BH}, t) + \partial_{M_{\rm BH}} [\langle \dot{M}_{\rm BH} \rangle\, N(M_{\rm BH}, t)] = S(M_{\rm BH}, t) \ ; \tag{5.12}$$

the underlying rationale is that, although individual BHs turn on and off, the evolution of the SMBH population depends only on the mean accretion rate $\langle \dot{M}_{\rm BH} \rangle$.

5.1.2 Solution

Given the AGN lightcurve in Eq. 4.5, the fraction of the time spent by the BH per luminosity bin reads:

$$\sum_i \frac{\mathrm{d}\tau_i}{\mathrm{d}L_{\rm AGN}} = \frac{\tau_{\rm ef}+\tau_{\rm D}}{L_{\rm AGN}}\,\Theta_H\left[L_{\rm AGN}\leq L_{\rm AGN}(M_{\rm BH})\right]\ , \tag{5.13}$$

where $L_{\rm AGN}(M_{\rm BH})$ is the maximum luminosity corresponding to a final BH mass $M_{\rm BH}$, that can be written as:

$$L_{\rm AGN}(M_{\rm BH}) = \frac{\lambda_{\rm Edd}\,M_{\rm BH}c^2}{t_{\rm Edd}}\,\left[1+f_\epsilon\,\frac{\tau_{\rm D}}{\tau_{\rm ef}}\,(1-e^{-\zeta})\right]^{-1}\ ; \tag{5.14}$$

The epoch of the peak, τ_D, and the duration of the descending phase, ζ (in units of τ_D), have been determined in Sec. 4.7.5 on the basis of our analysis. As pointed out in Sec. 4.2, f_ϵ is a correction factor taking into account the modest change of the quantity $(1-\epsilon)/\epsilon$ along the declining phase. We have checked that $f_\epsilon \approx 0.8$ for any reasonable value of $\epsilon_{\rm thin}$. Eq. 5.14 highlights the relevance of the mass accretion during the AGN descending phase. This implies that the time spent in a luminosity bin is longer by a factor $\tau_{\rm D}$ than on assuming a simple growing exponential curve. We also note that Eq. 5.14 is implicit, since $\tau_{\rm D}/\tau_{\rm ef}$ is itself a function of the luminosity.

Using Eq. 5.13 in the continuity equation (neglecting merging, i.e., setting $S(M_{\rm BH},t)=0$) yields:

$$L_{\rm AGN}\,N(L_{\rm AGN},t) = \int_{M_{\rm BH}(L_{\rm AGN})}^{\infty} \mathrm{d}M_{\rm BH}\,\partial_t N(M_{\rm BH},t)\,\left[\tau_{\rm ef}+\tau_{\rm D}\right]\ , \tag{5.15}$$

where the minimum final mass that have shone at $L_{\rm AGN}$ is given by the inverse of Eq. 5.14, and $N(L_{\rm AGN},t)$ is the AGN bolometric LF, computed in Sec. 2.7.4 and shown in Fig. 2.4. To ease the reader, we report it here in Fig. 5.1.

We proceed by differentiating both sides with respect to $L_{\rm AGN}$ and by rearranging terms, to find:

$$\frac{L_{\rm AGN}}{f_{{\rm BH},L_{\rm AGN}}}\,\frac{\partial_{L_{\rm AGN}}\left[L_{\rm AGN}\,N(L_{\rm AGN},t)\right]}{\tau_{\rm ef}+\tau_{\rm D}} = -\left[\partial_t N(M_{\rm BH},t)\,M_{\rm BH}\right]_{|M_{\rm BH}(L_{\rm AGN})}\ . \tag{5.16}$$

In deriving this equation, we have defined:

$$f_{{\rm BH},L_{\rm AGN}} \equiv \frac{\mathrm{d}\log M_{\rm BH}}{\mathrm{d}\log L_{\rm AGN}}\ , \tag{5.17}$$

which is not equal to unity, since $\tau_{\rm D}/\tau_{\rm ef}$ depends on $L_{\rm AGN}$.

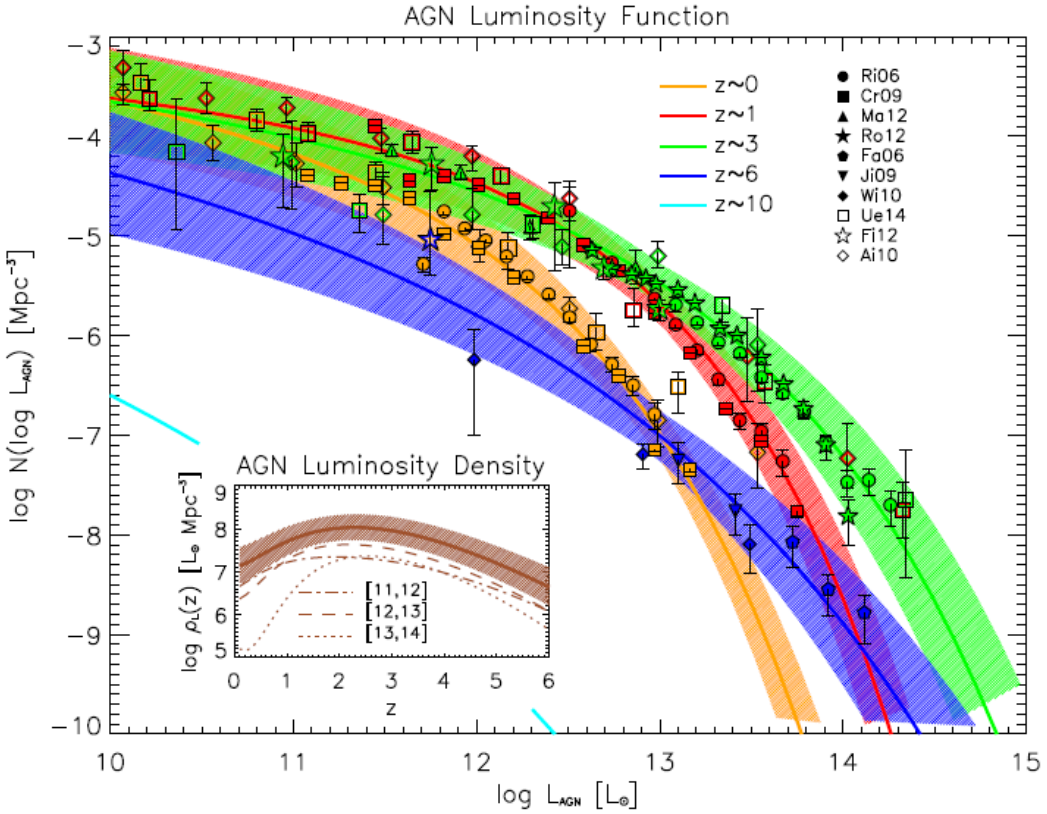

FIGURE 5.1: The bolometric AGN LF $N(\log L_{\rm AGN})$ at redshift $z = 0$ (orange), 1 (red), 3 (green), and 6 (blue). Optical data are from Richards et al. (2006, filled circles), Croom et al. (2009, filled squares), Masters et al. (2012, filled triangles), Ross et al. (2012, filled stars), Fan et al. (2006, filled pentagons), Jiang et al. (2009, filled reversed triangles), Willott et al. (2010b, filled diamonds); X-ray data are from Ueda et al. (2014, open squares), Fiore et al. (2012, open stars), and Aird et al. (2010, open diamonds). The optical and X-ray luminosities have been converted to bolometric ones by using the Hopkins, Richards & Hernquist (2007) corrections, while the number densities have been corrected for the presence of obscured AGNs according to Ueda et al. (2003, 2014). The solid lines illustrate the analytic rendition of the luminosity functions as described in Sec. 2.7.4, while the hatched areas represent the associated uncertainty; the cyan line is the extrapolation to $z = 10$, plotted for illustration. The inset shows the AGN luminosity density as a function of redshift, for the overall luminosity range probed by the data (solid line with hatched area), and for AGN bolometric luminosity $\log L_{\rm AGN}/L_{\odot}$ in the ranges $[11, 12]$ (dot-dashed line), $[12, 13]$ (dashed line), $[13, 14]$ (dotted line).

Finally, we integrate over the cosmic time, and pass to logarithmic bins. The outcome reads:

$$N(\log M_{\rm BH}, t) = -\int_0^t \frac{{\rm d}t'}{f_{{\rm BH},L_{\rm AGN}}} \frac{\partial_{\ln L_{\rm AGN}} \left[N(\log L_{\rm AGN})\right]}{\tau_{\rm ef}(L_{\rm AGN}, t') + \tau_{\rm D}(L_{\rm AGN}, t')}_{|L_{\rm AGN}(M_{\rm BH}, t')} \,. \qquad (5.18)$$

Note that, operatively, we have started the integration at $z_{\rm in} = 10$, assuming that the BHMF at that time was negligibly small. The solution in Eq. 5.18 constitutes a novel result. In the case with $\tau_{\rm D} = 0$, and when $\lambda_{\rm Edd}$ and ϵ are constant with redshift and luminosity, the above equation reduces to the form considered by Marconi et al. (2004).

5.1.3 Results

In Fig. 5.2, we illustrate our resulting BHMF at different representative redshifts. The outcomes can be fitted with the same functional shape used to render the AGN LF in Eq. 2.14, i.e., a modified Schechter function with evolving characteristic BH mass and slopes:

$$N(\log M_{\rm BH}, z) = \Phi(z) \left[\frac{M_{\rm BH}}{M_c(z)}\right]^{1-\alpha(z)} \exp\left\{-\left[\frac{M_{\rm BH}}{M_c(z)}\right]^{\omega(z)}\right\} . \tag{5.19}$$

The normalization $\log \Phi(z)$, the characteristic BH mass $\log M_c(z)$, and the characteristic slopes $\alpha(z)$ and $\omega(z)$ evolve with redshift according to the same parametrization:

$$p(z) = p_0 + k_{p1}\,\chi + k_{p2}\,\chi^2 + k_{p3}\,\chi^3 \ . \tag{5.20}$$

with $\chi = \log[(1+z)/(1+z_0)]$ and $z_0 = 0.1$. The parameter values are reported in Table 6.1; the resulting fits are accurate within 5% in the redshift range from 0 to 6, where the input AGN LFs are based on actual data.

In Fig. 5.2 two determinations of the local BHMF are also illustrated. One is from the collection of estimates by Shankar, Weinberg & Miralda-Escudé (2009), which have been built by combining the SMF or the VDF with the corresponding $M_{\rm BH} - M_\star$ (Häring & Rix 2004) or $M_{\rm BH} - \sigma$ (Tremaine et al. 2002) relations for elliptical galaxies and classical bulges. The other is the determination by Shankar et al. (2012), corrected to take into account the different relations followed by pseudobulges. In addition, we present the determination at $z = 0$ by Vika et al. (2009) based on an object-by-object analysis and on the $M_{\rm BH} - L$ (McLure & Dunlop 2004) relationship.

The BHMF at $z \approx 0$ from the continuity equation provides and almost perfect rendition of the local estimates by Shankar, Weinberg & Miralda-Escudé (2009) and Vika et al. (2009) when $\epsilon_{\rm thin} = 0.1$ is adopted. At $z \approx 1$, our BHMF is very similar to the local determination. Our result is in good shape (though on the high side), with the determination by Li, Ho & Wang (2011), based on the galaxy luminosity and mass functions, and on a mild evolution of the $M_{\rm BH} - L$ (or $M_{\rm BH} - M_\star$) relationships. The same also holds at $z \approx 2$, which is not plotted for clarity.

At $z \approx 3$, our BHMF is a factor ~ 10 below the local data, at the knee. We are in good agreement with the determination by Ueda et al. (2014), based on continuity equation models. This is expected, since we adopt similar bolometric LFs, and at $z \approx 3$ we have similar values of $\lambda_{\rm Edd}$ and ϵ. At $z \approx 6$, the BHMF is ~ 3 orders of magnitude smaller than the local data. We compare our result with the estimate by Willott et al. (2010a) in the range $M_{\rm BH} \sim 10^8 - 3 \times 10^9\,M_\odot$. This has been derived by combining the Eddington ratio distribution from single-epoch BH mass estimates to the optical

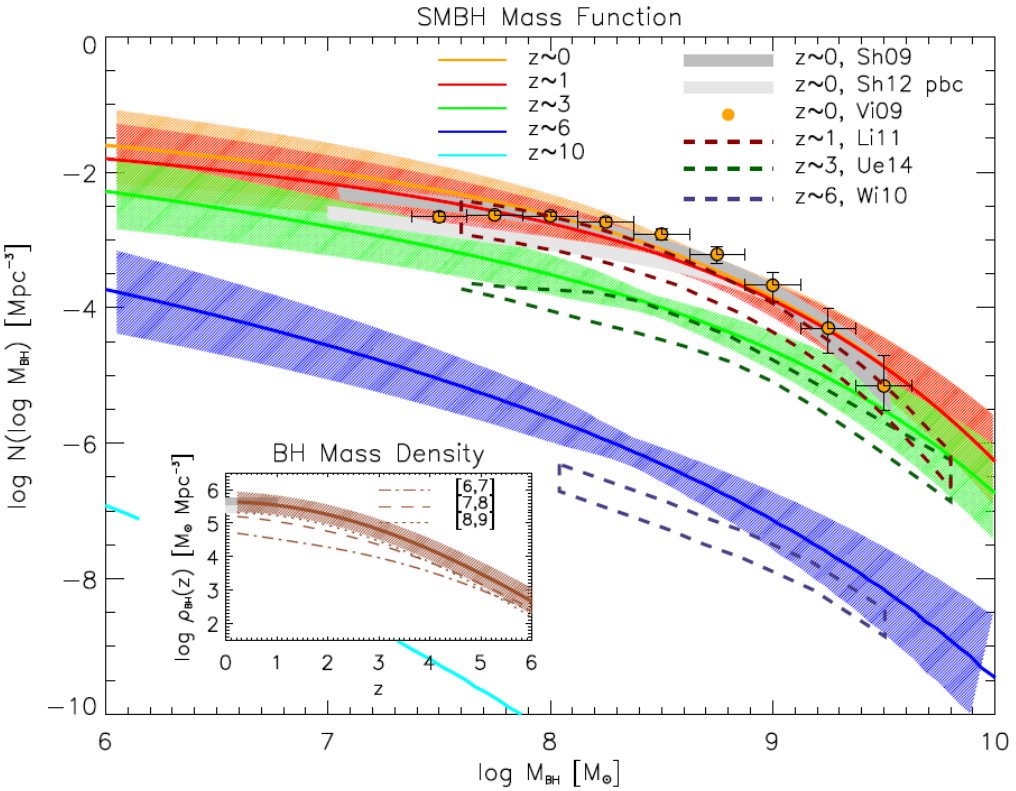

FIGURE 5.2: The BHMF $N(\log M_{\rm BH}, z)$ as a function of the final BH mass $M_{\rm BH}$. Results from the continuity equation (see Sec. 5.1.2) at redshift $z = 0$ (orange), 1 (red), 3 (green), and 6 (blue) are plotted as solid lines, with the hatched areas illustrating the associated uncertainty; the cyan line is the extrapolation to $z = 10$, plotted for illustration. The dark grey shaded area illustrates the collection of estimates by Shankar, Weinberg & Miralda-Escudé (2009), built by combining the SMF or the VDF with the $M_{\rm BH} - M_\star$ or $M_{\rm BH} - \sigma$ relations of elliptical galaxies; the light grey shaded area is the determination by Shankar et al. (2012), corrected to take into account the different relations followed by pseudobulges. The orange circles are the determination at $z = 0$ by Vika et al. (2009). The red dashed area illustrate the determination at $z \sim 1$ by Li, Ho & Wang (2011), the green dashed area shows the range of models by Ueda et al. (2014) at $z \sim 3$, and the blue dashed area the estimate by Willott et al. (2010a) at $z \sim 6$. The inset shows the BH mass density as a function of redshift computed from the continuity equation, for the overall mass range (solid line with hatched area), and for BH masses $\log M_{\rm BH}/M_\odot$ in the ranges $[6, 7]$ (dot-dashed line), $[7, 8]$ (dashed line), $[8, 9]$ (dotted line). The grey shaded areas illustrate the observational constraints on the local BH mass density from the above $z = 0$ BHMF by Shankar, Weinberg & Miralda-Escudé (2009); Shankar et al. (2012).

QSO LFs corrected for obscured objects. At the knee of the BHMF, we find a good agreement with our result based on the continuity equation, while we predict a slightly higher number of objects at lower masses.

The reasonable agreement with previous determinations in the range $0 \lesssim z \lesssim 6$ validates our prescriptions for the lightcurves, the redshift evolution of $\lambda_0(z)$, and the $\epsilon - \lambda$ relation of Eq. 2.12. Besides, we recall that we already independently tested them against the observed fractions of AGNs hosted in sub-mm galaxies and related statistics in Chapter 4 (see also Lapi et al. 2014).

Note that during the slim-accretion regime, where most of the BH mass is accumulated, the effective efficiency amounts to $\epsilon \lesssim 0.05$ given our assumed value $\epsilon_{\rm thin} \approx 0.1$ in Eq. 2.12 (see also Fig. 4.2). This requires to be discussed. As we have seen in Chapter 2, during a coherent disc accretion, the BH is expected to spin up very rapidly and, as a consequence, the efficiency is expected to attain values $\epsilon \gtrsim 0.15$ (Madau, Haardt & Dotti 2014), corresponding to $\epsilon_{\rm thin} \approx 0.3$ through Eq. 2.12. However, such a high value of the efficiency would produce a local BHMF in strong disagreement with the data. This can be understood on the basis of the standard Soltan argument. In fact, the BH mass density inferred from the AGN luminosity density would amount to:

$$\rho_{\rm BH} \approx 2 \times 10^4 \, \frac{(1-\epsilon)}{\epsilon} \, M_\odot \, {\rm Mpc}^{-3} \lesssim 10^5 \, M_\odot \, {\rm Mpc}^{-3} \, . \tag{5.21}$$

Plainly, the $z = 0$ result would fall short of the local observational determinations, that yields a fiducial mass density of $\rho_{\rm BH} \approx 4.5 \times 10^5 \, M_\odot \, {\rm Mpc}^{-3}$, using the Shankar, Weinberg & Miralda-Escudé (2009) BHMF. The discrepancy is even worse if one considers the local BHMF obtained by combining the VDF or SMF with the recently revised $M_{\rm BH} - \sigma$ or $M_{\rm BH} - M_\star$ relations by McConnell & Ma (2013) and Kormendy & Ho (2013), which feature a higher overall normalization.

Thus, an average slim-disc efficiency $\epsilon \lesssim 0.05$ is required. During the slim-disc accretion, such a low efficiency can be maintained by, e.g., chaotic accretion, efficient extraction of angular momentum by jets, or similar processes keeping the BH spin to low levels (King & Pringle 2006; Cao 2010; Li 2012; Barausse 2012; Sesana et al. 2014). We also remark that an efficiency $\epsilon \lesssim 0.05$ eases the formation of SMBHs at very high redshift ($z \gtrsim 6$), so alleviating any requirement on initial massive seeds (Volonteri 2010, see also Sec. 2.10). On the other hand, the BHMF only poorly constrains the values of the BH spin during the final thin-disc phase, which the current estimates suggest to be rather high (Reynolds 2013).

It will be shown in Sec. 5.3 that we have also tested the relevance of dry merging processes in shaping the BHMF over the range $M_{\rm BH} \approx 10^7 - 10^{10} \, M_\odot$. At $z \gtrsim 1$, BH merging

effects are found to be statistically negligible (see also Shankar, Weinberg & Miralda-Escudé 2009), although smaller mass BHs may undergo substantial merging activity, with a possible impact on the seed distribution (for a review, see Volonteri 2010). Our tests indicate that, at $z \lesssim 1$, the BHMF is mildly affected only for $M_{\rm BH} \gtrsim 10^9\,M_\odot$.

Bolometric corrections (Sec. 2.7.1) and obscured accretion (Sec. 2.7.2) can concur to alleviate the requirement of a low slim-disc efficiency. A large fraction of objects with accretion obscured at wavelengths ranging from X-ray to optical bands has been often claimed, also in connection with their contribution to the X-ray background (Comastri et al. 1995). The fraction compatible with it at substantial X-ray energies has been recently discussed by Ueda et al. (2014), and properly inserted in our AGN bolometric LFs (Sec. 2.7.4).

Concerning the overall evolution of the BHMF, we find that most of the SMBH mass growth occurs at higher redshifts for more massive objects (see the inset of Fig. 5.2), reflecting the downsizing behaviour of AGNs (e.g., Alexander & Hickox 2012; Brandt & Alexander 2015 and reference therein). The overall BH mass density at $z = 0$ amounts to $\rho_{\rm BH} \approx 4.5 \times 10^5\,M_\odot\,{\rm Mpc}^{-3}$, in excellent agreement with observational determinations.

In Fig. 5.3, we show how our results on the BHMF depend on various assumptions. The top and middle panels illustrate the effect of changing the parameters of the AGN lightcurve: radiative efficiency ϵ, Eddington ratio $\lambda_{\rm Edd}$, timescale of the descending phase $\tau_{\rm D}$ (in units of τ_D), and duration of the descending phase ζ. For clarity, we plot the results only at $z = 0$ and $z = 3$. We illustrate the output for our fiducial values, and compare it with the outcomes for values of the parameters decreased or increased relative to the reference ones.

To understand the various dependencies, it is useful to assume a simple, piecewise powerlaw shape of the AGN LF in the form:

$$N(\log L_{\rm AGN}) \propto L_{\rm AGN}^{-\eta}\ , \tag{5.22}$$

with $\eta \lesssim 1$ at the faint and $\eta > 1$ at the bright end. Then, it is easily seen from Eq. 5.18 that the resulting BHMF behaves as:

$$N(\log M_{\rm BH}) \propto \frac{1-\epsilon}{\epsilon}\,\lambda_{\rm Edd}^{1-\eta}\,\frac{[1+(\tau_{\rm D}/\tau_{\rm ef})\,(1-e^{-\zeta})]^\eta}{1+\tau_{\rm D}/\tau_{\rm ef}}\,\eta\,M_{\rm BH}^{-\eta}\ . \tag{5.23}$$

Thus, the BHMF features an almost inverse dependence on ϵ at given BH mass. The dependence on $\lambda_{\rm Edd}$ is inverse at the high-mass end, which is mostly contributed by high luminosities where $\eta > 1$. On the other hand, the dependence is direct at the low-mass end, mainly associated to faint sources with $\eta \lesssim 1$. The opposite applies to

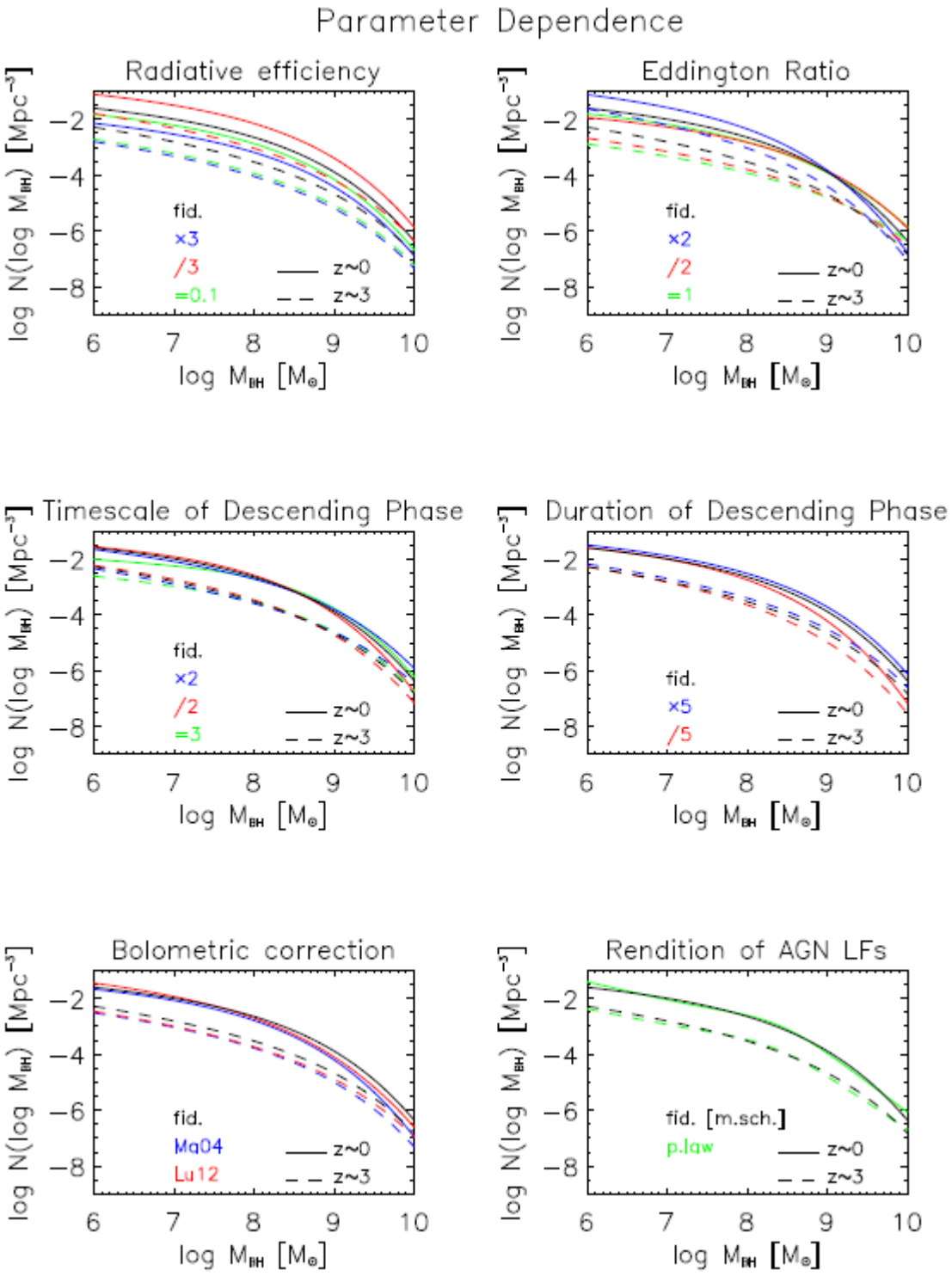

FIGURE 5.3: Comparison plot showing the dependence of the BHMF on the parameters of the assumed AGN lightcurve; for clarity, only results at $z = 0$ (solid lines) and at $z = 3$ (dashed lines) are plotted. In the top and middle panels, the black lines are for our fiducial values, while the red and blue lines refer to values of the parameters decreased or increased of the amount specified in the legend of each panel, and the green lines to constant values in redshift and luminosity. In the bottom left panel, we illustrate the effect of changing the optical/X-ray bolometric corrections: the black lines refer to our reference one by Hopkins, Richards & Hernquist (2007), while the blue and red lines refer to the ones proposed by Marconi et al. (2004) and by Lusso et al. (2012), respectively. In the bottom right panel, we illustrate the effect of changing the functional form used to analytically render the input AGN LF: the black lines refer to our fiducial rendition via a modified Schechter function (Eq. 2.14), while the green lines refer to a double powerlaw representation.

the dependence on $\tau_{\rm D}/\tau_{\rm ef}$, since roughly:

$$N(\log M_{\rm BH}) \propto (\frac{\tau_{\rm D}}{\tau_{\rm ef}})^{\eta-1} \ . \tag{5.24}$$

Finally, the dependence on ζ is mild, and nearly irrelevant for $\zeta \gtrsim 3$, since the exponential $e^{-\zeta}$ in Eq. 4.11 tends rapidly to zero. Differences in the results are more evident in the $z = 0$ than in the $z = 3$ BHMF, since this is an integrated quantity, as expressed by Eq. 5.18.

In the bottom left panel, we illustrate the effect of changing the optical/X-ray bolometric corrections: the black lines refer to our reference one by Hopkins, Richards & Hernquist (2007), while the blue and red lines refer to the ones proposed by Marconi et al. (2004) and by Lusso et al. (2012), respectively. It is easily seen that the impact on the BHMF is limited, actually well within the uncertainties associated to the input AGN LF and to the observational determinations of the local BHMF.

In the bottom right panel, we illustrate the effect of changing the functional form used to analytically render the AGN LF: the black lines refer to our fiducial rendition via a modified Schechter function (Eq. 2.14), while the green lines refer to a standard double powerlaw representation (e.g., Ueda et al. 2014; Aird et al. 2015). It can be seen that our results on the BHMF are marginally affected; this is because both shapes render comparably well the input AGN LFs.

In Fig. 5.4 we illustrate the Eddington ratio distribution $P(\log \lambda_{\rm Edd})$ associated to the overall adopted lightcurve at different redshifts and for different final BH masses. Typically, at given redshift and BH mass, the distribution features a Gaussian peak at high values of $\lambda_{\rm Edd}$, and then a powerlaw increase toward lower values of $\lambda_{\rm Edd}$ before an abrupt cutoff. The peak reflects the value of $\lambda_{\rm Edd}$ in the ascending part of the lightcurve. Actually, since $\lambda_{\rm Edd}(\tau)$ is constant there, the peak should be a Dirac $\delta-$function.

However, small variations around the central value and observational errors will broaden the peak to a narrow Gaussian, as plotted in the top panel; a dispersion of 0.3 dex has been safely adopted. The powerlaw behavior reflects the decrease of $\lambda_{\rm Edd}(\tau)$ during the declining part of the lightcurve at late times, and the cutoff in the distribution mirrors that of the lightcurve. The relative contribution of the Gaussian peak at high $\lambda_{\rm Edd}$, and of the powerlaw increase at low $\lambda_{\rm Edd}$, depends on the relative duration of the declining and ascending phases. Thus, at given redshift, small mass BHs feature a much more prominent peak and a less prominent powerlaw increase, relative to high mass ones. This happens because in small mass objects the descending phase is shorter. At given BH mass, the distributions shift to the left, i.e., toward smaller values of $\lambda_{\rm Edd}$, as the

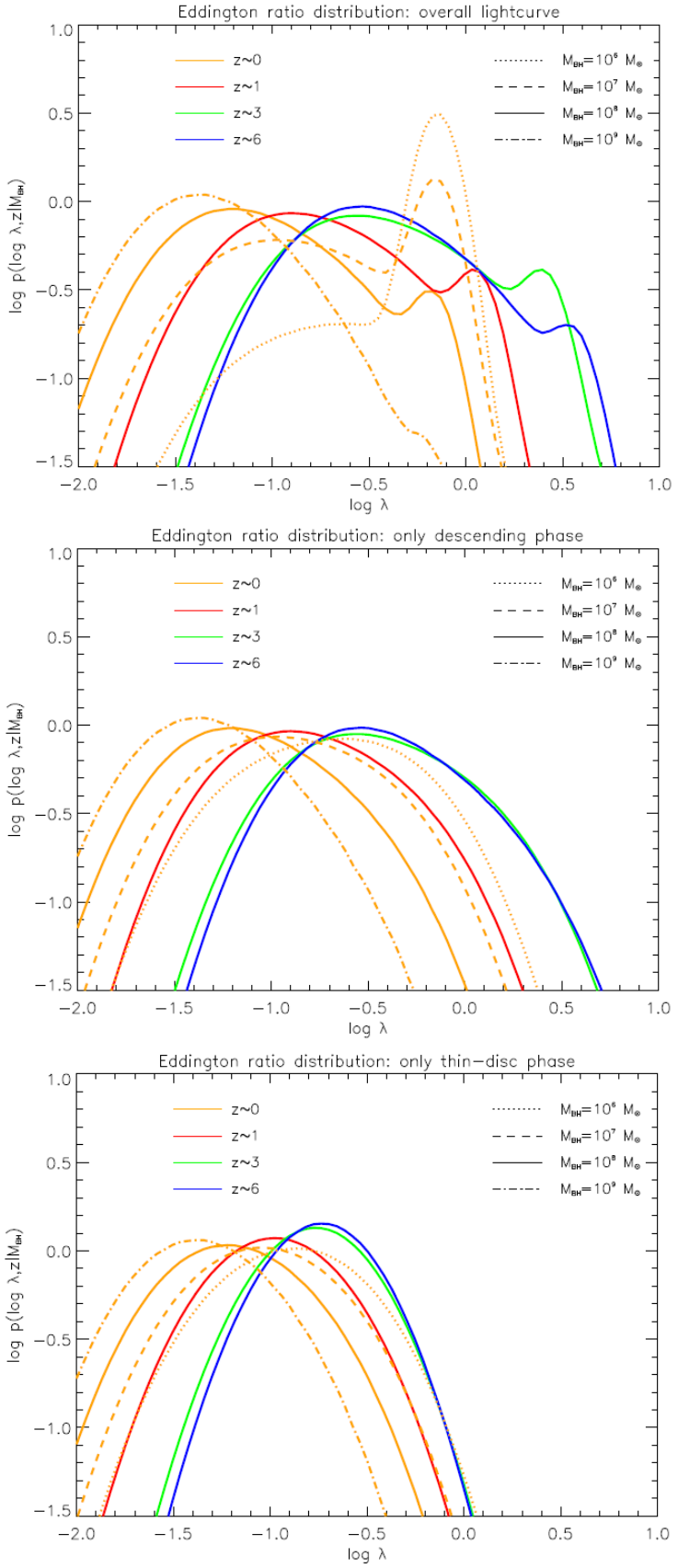

FIGURE 5.4: The Eddington ratio distribution $P(\log \lambda_{\rm Edd})$ associated to the overall lightcurve (top panel), only to the descending phase (middle panel), and only to the thin-disc phase (bottom panel), at redshift $z = 0$ (orange), 1 (red), 3 (green), and 6 (blue) and for different BH masses $M_{\rm BH} = 10^6$ (dotted), 10^7 (dashed), 10^8 (solid), and $10^9\,M_\odot$ (dot-dashed); for clarity the results relative to masses 10^6, 10^7 and $10^9\,M_\odot$ are plotted only at $z = 0$.

redshift decreases. This is because the initial value $\lambda_0(z)$ decreases with redshift, as prescribed by Eq. 4.8.

Such a distribution has been computed under the assumption that the overall lightcurve can be sampled. However, from an observational perspective, the Eddington ratio distribution is usually determined via single-epoch BH mass estimates of Type 1 AGNs. This implies that only a portion of the descending phase can be sampled. To ease the comparison with observations, we present in the middle and bottom panels of Fig. 5.4 the expected distribution, considering only the whole descending phase (including both the final portion of the slim-disc phase and the while thin-disc phase, i.e., $\lambda_{\rm Edd} \gtrsim 0.3$), and only the thin-disc phase (i.e., the portion with $\lambda_{\rm Edd} \lesssim 0.3$). The resulting distributions feature a powerlaw shape, whose slope depends on the portion of the declining phase that can be effectively sampled: the shorter this portion, the steeper the powerlaw.

The results are roughly consistent with the observational determinations by, e.g., Kelly & Shen (2013), although a direct comparison is difficult, due to observational selection effects. In fact, different observations are likely to sample diversely the initial part of the declining phase. Note that especially at $z \lesssim 1$, BH reactivations, which are not included in our treatment, can contribute to broaden the Eddington ratio distribution toward very low values of $\lambda_{\rm Edd} (\lesssim 10^{-2})$, as estimated in the local Universe (e.g., Kauffmann & Heckman 2009; Brandt & Alexander 2015).

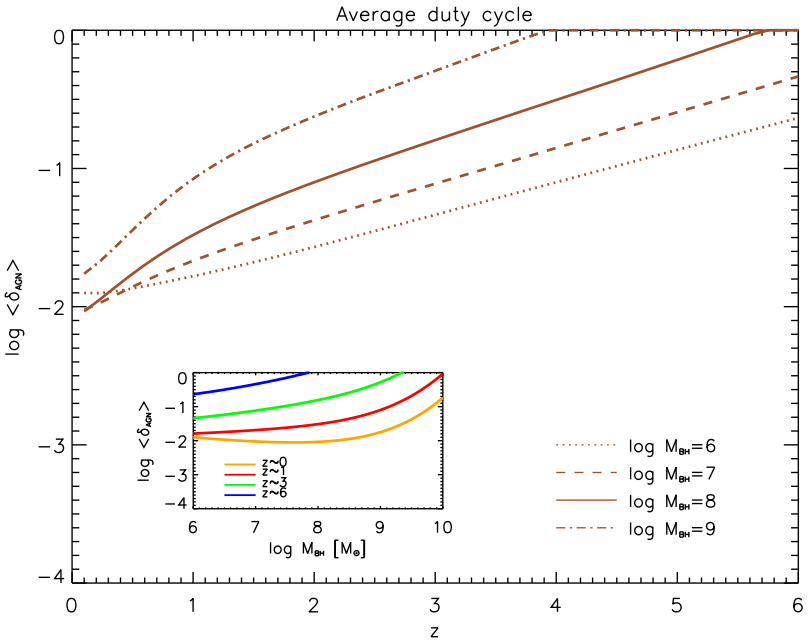

FIGURE 5.5: The average AGN duty cycle $\langle \delta_{\rm AGN} \rangle$ as a function of z, for different BH masses: $M_{\rm BH} = 10^6$ (dotted), 10^7 (dashed), 10^8 (solid), and $10^9\, M_\odot$ (dot-dashed). The inset illustrates the AGN duty cycle as a function of the BH mass at $z = 0$ (orange), 1 (red), 3 (green), and 6 (blue).

In Fig. 5.5, we present the AGN duty cycle, $\langle \delta_{\rm AGN} \rangle$, averaged over the Eddington ratio distribution associated to the adopted lightcurve. Specifically, it has been computed as:

$$\begin{aligned} \langle \delta_{\rm AGN} \rangle (M_{\rm BH}, t) &\equiv \frac{N_{\rm AGN}(\log M_{\rm BH}, t)}{N(\log M_{\rm BH}, t)} \\ &= \frac{1}{N(\log M_{\rm BH}, t)} \int {\rm d} \log \lambda_{\rm Edd} \; P(\log \lambda_{\rm Edd}, z) \times \\ &\times \, N(\log L_{\rm AGN}, t)_{|L_{\rm AGN}(M_{\rm BH}, \lambda_{\rm Edd})} \; , \end{aligned} \tag{5.25}$$

where $N_{\rm AGN}(\log M_{\rm BH}, t)$ represents the BHs which are in the "active" phase, mapped by the AGN LF, and $L_{\rm AGN}(M_{\rm BH}, \lambda)$ is given by Eq. 5.14. In our approach based on the continuity equation, the duty cycle is a quantity derived from the luminosity and mass functions. It provides an estimate for the fraction of active BHs relative to the total BH population. At given redshift, the average duty cycle increases with the BH mass, since more massive BHs are typically produced by more luminous objects, that feature the descending phase of the lightcurve. On the contrary, small mass BHs are originated mainly by low-luminosity objects, for which the descending phase is absent.

At given BH mass (see the inset of Fig. 5.5), the duty cycle increases with redshift, essentially because the BHs stay active for a larger fraction of the shorter cosmic time to attain the same final mass. This is especially true for BHs with high masses, up to the point that they are always active ($\delta_{\rm AGN} \approx 1$) for $z \gtrsim 3$. This agrees with the inferences from the strong clustering observed for high-redshift quasars (Shen et al. 2009; Shankar, Weinberg & Shen 2010; Willott et al. 2010a; Allevato et al. 2014); we will further discuss the issue in Sec. 6.2.5.

The increase of the duty cycle with BH mass is consistent with the active fraction measured by Bundy et al. (2008) and Xue et al. (2010), although the issue is still controversial, and strongly dependent on obscuration-corrections (see Schulze et al. 2015). On the other hand, we point out that our approach does not include AGN reactivations, which may strongly enhance the duty cycle for low-luminosity objects, especially at $z \lesssim 1$, accounting for the estimates by, e.g., Ho, Filippenko & Sargent (1997), Greene & Ho (2007), Goulding & Alexander (2009), Schulze & Wisotzki (2010).

In Fig. 5.6, we present the AGN Eddington ratio $\langle \lambda_{\rm Edd} \rangle$ averaged over the lightcurve, computed as:

$$\begin{aligned} \langle \lambda_{\rm Edd} \rangle (M_{\rm BH}, t) \equiv \frac{1}{N(\log M_{\rm BH})} \int {\rm d} \log \lambda_{\rm Edd} \; \lambda_{\rm Edd} \, P(\log \lambda_{\rm Edd}, z) \times \\ \times \, N(\log L_{\rm AGN})_{|L_{\rm AGN}(M_{\rm BH}, \lambda_{\rm Edd})} \; . \end{aligned} \tag{5.26}$$

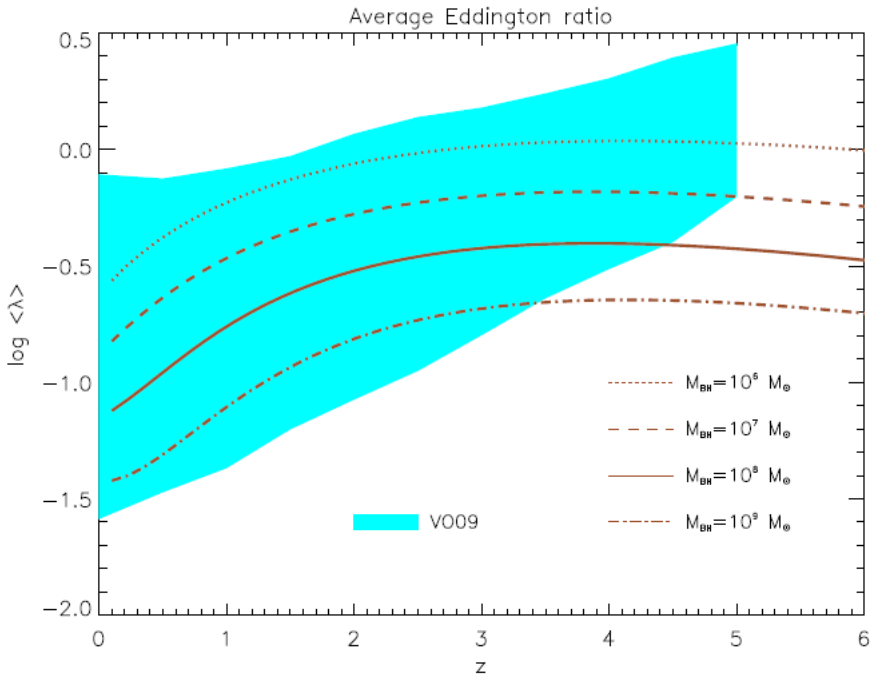

FIGURE 5.6: The average Eddington ratio $\langle \lambda_{\rm Edd} \rangle$ as a function of z, for different BH masses: $M_{\rm BH} = 10^6$ (dotted), 10^7 (dashed), 10^8 (solid), and $10^9\, M_\odot$ (dot-dashed). The cyan shaded area covers the range of measured values in the sample of quasars by Vestergaard & Osmer (2009).

At given BH mass, the Eddington ratio decreases toward lower redshifts, as a consequence of the dependence adopted in Eq. 4.8. The average values are consistent with those observed in the a sample of quasars by Vestergaard & Osmer (2009). Note that, to take into account the observational selection criteria, we have used the Eddington ratio distribution corresponding only to the descending phase, presented in the middle panel of Fig. 5.4.

In Fig. 5.7, (left panel) we show the Eddington ratio function, that has been computed as:

$$N(\log \lambda_{\rm Edd}, z) \equiv \int {\rm d} \log M_{\rm BH}\, P(\log \lambda_{\rm Edd} | M_{\rm BH}, z)\, N_{AGN}(\log M_{\rm BH}, z) \ ; \qquad (5.27)$$

The outcome is mildly sensitive to the lower integration limit, and we have adopted a value $M_{\rm BH} \sim 10^8 M_\odot$ to compare with the data (see Schulze et al. 2015). For the sake of completeness, we also present the results when using the Eddington ratio distribution associated to the thin-disc phase (cf. bottom panel of Fig. 5.4) or to the whole descending phase (cf. middle panel of Fig. 5.4); the outcomes for the overall lightcurve are very similar to this latter case. Our results from the continuity equation are confronted with the estimates from Schulze & Wisotzki (2010) at $z \sim 0$, and from Schulze et al. (2015) and Nobuta et al. (2012) at $z \sim 1-2$, finding a nice agreement within the observational uncertainties and the clear systematic differences between the datasets.

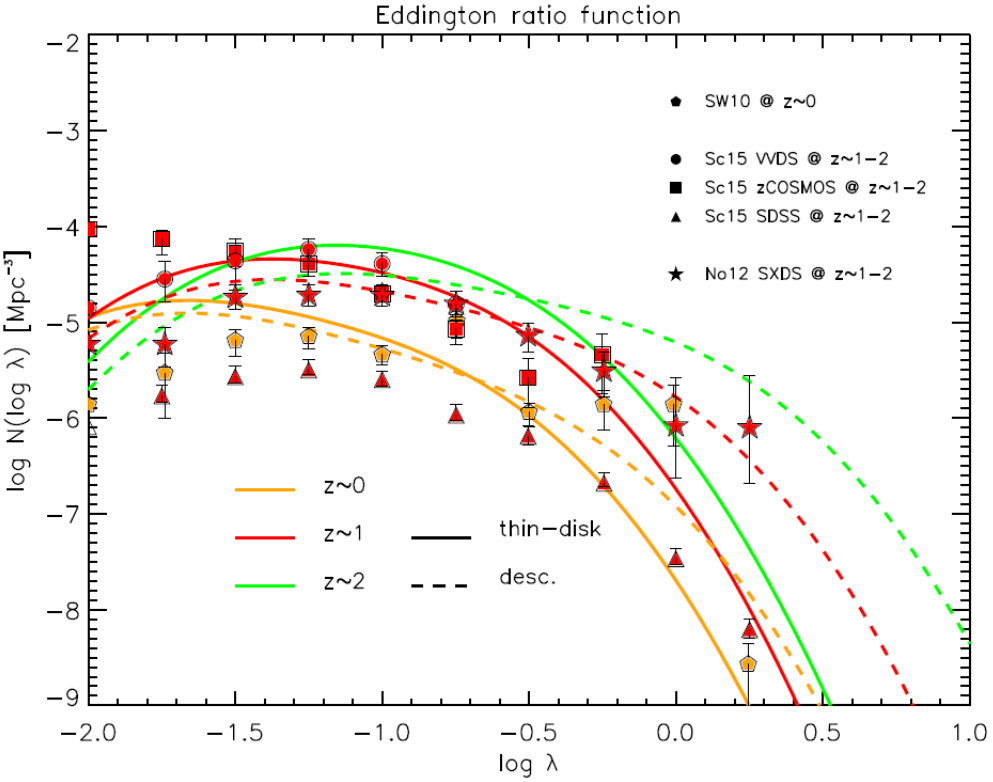

FIGURE 5.7: The Eddington ratio function at redshift $z = 0$ (orange), 1 (red), and 2 (green) associated to the thin-disc phase (solid lines) or to the descending phase (dashed lines; the outcomes when considering the overall lightcurve are very similar); observational estimates at $z \sim 0$ are from Schulze & Wisotzki (2010, orange diamonds), at $z \sim 1 - 2$ from Schulze et al. (2015, red circles for VVDS, squares for zCOSMOS, and triangles for SDSS), and from Nobuta et al. (2012, red stars for SXDS).

In Fig. 5.8, we present a related statistic: the fraction $F(\log \lambda_{\rm Edd}, M_\star)$ of galaxies, at given stellar mass, hosting an AGN (i.e., the active fraction) with a given Eddington ratio. It has been computed as:

$$F(\log \lambda_{\rm Edd}, M_\star) = \frac{P(\log \lambda_{\rm Edd}|M_{\rm BH}, z)\, N_{\rm AGN}(\log M_{\rm BH}, z)}{N(\log M_\star, z)} \ , \qquad (5.28)$$

where $N(\log M_\star, z)$ is the number of galaxies with given stellar mass $M_\star$ (the SMF, cf. Sec. 5.2). Plainly, $M_{\rm BH} \sim 2 \times 10^{-3}\, M_\star$ must be set to the BH mass corresponding to $M_\star$, the result being rather insensitive to the adopted $M_{\rm BH}/M_\star$ ratio; we further take into account a scatter of 0.3 dex in this relationship, whose effect is to make $F(\log \lambda_{\rm Edd}, M_\star)$ depend on $M_\star$ more weakly than $P(\log \lambda_{\rm Edd}|M_{\rm BH}, z)$ depends on $M_{\rm BH}$. We illustrate the outcome for a range of stellar masses from $M_\star \sim 10^{10.5} M_\odot$ to $M_\star \sim 10^{11.5} M_\odot$; the dependence on $M_\star$ is only mild, especially at $z \lesssim 2$, as also indicated by current observations.

In fact, our result can be compared with the observational estimates at $z \sim 0 - 2$ by Aird et al. (2012) and Bongiorno et al. (2012). The latter authors actually provide the

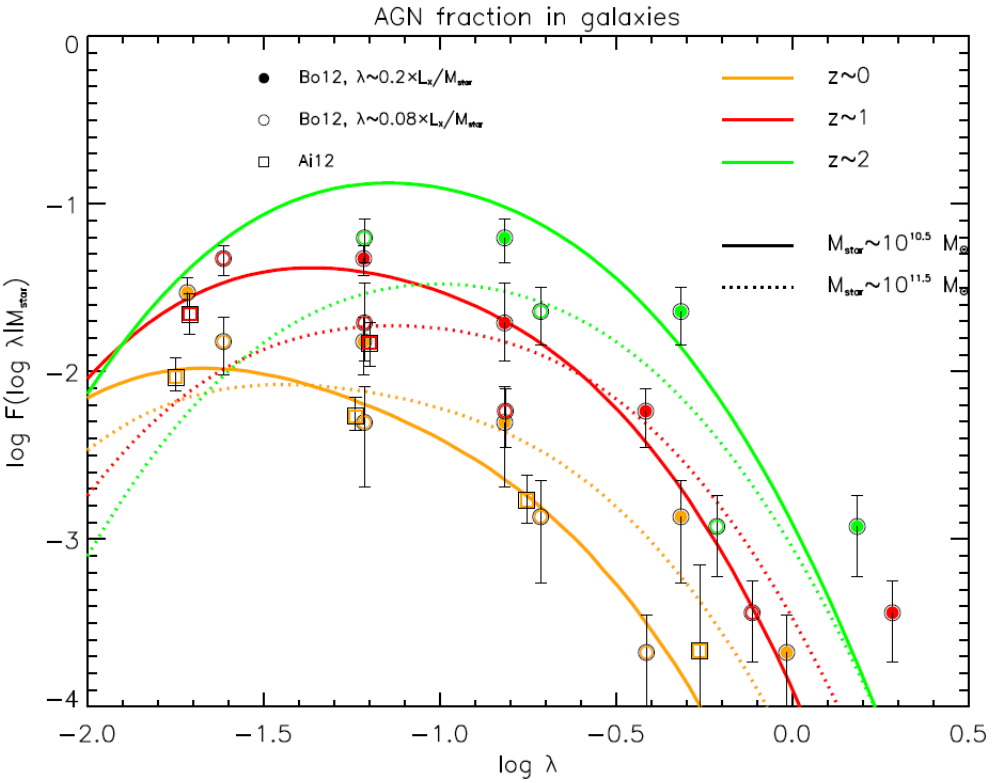

FIGURE 5.8: The fraction of galaxies of given stellar mass (solid lines for $M_\star \sim 10^{10.5} M_\star$ and dotted lines for $M_\star \sim 10^{11.5} M_\star$) hosting an AGN with given Eddington ratio at redshift $z = 0$ (orange), 1 (red), and 2 (green); data are from Aird et al. (2012, orange squares), and from Bongiorno et al. (2012, red and green circles), where the latter have been converted with the relation $\lambda_{\rm Edd} \equiv 0.2 L_X/M_\star$ (filled circles) or $\lambda_{\rm Edd} \equiv 0.08 L_X/M_\star$ (empty circle), see text for details.

active fraction as a function of the observable quantity $L_X/M_\star$, which can be converted into an Eddington ratio by assuming an X-ray bolometric correction and a value for the $M_{\rm BH}/M_\star$ ratio. The authors suggest an overall conversion factor $\lambda_{\rm Edd} \approx 0.2\, L_X/M_\star$ (here cgs units are used). We also plot their data points when using a conversion factor $\lambda_{\rm Edd} \approx 0.08\, L_X/M_\star$ (corresponding, e.g., to a larger ratio $M_{\rm BH}/M_\star$ or to a lower bolometric correction), giving more consistency with the determination by Aird et al. (2012).

All in all, our results from the continuity equation are found to be in good agreement with the observational estimates, reproducing their mild dependence on stellar mass and their shape for $z \lesssim 2$, down to $\lambda_{\rm Edd} \sim 10^{-2}$. On the other hand, AGNs at $z \lesssim 1$ with tiny accretion rates, corresponding to $\lambda_{\rm Edd} < 10^{-2}$, are likely triggered by reactivations, not included in our lightcurve, which can contribute to maintain a powerlaw shape of the Eddington ratio function and of the active fraction down to $\lambda_{\rm Edd} \sim 10^{-4}$ (Kauffmann & Heckman 2009; Aird et al. 2012; Brandt & Alexander 2015).

5.2 Stellar Mass Function

In this Section, we use Eq. 5.1 to derive the SMF at different redshifts from the SFR-LF, following the same procedure we used for the SMBHs. Also in this case, the continuity equation can be solved in a closed analytic form.

5.2.1 Solution

Given the lightcurve in Eq. 4.12, the fraction of the time spent per luminosity bin reads:

$$\sum_i \frac{\mathrm{d}\tau_i}{\mathrm{d}L_{\rm SFR}} = \tau_{\rm burst}\, \delta_D \left[L_{\rm SFR} - L_{\rm SFR}(M_\star)\right] \ , \tag{5.29}$$

with

$$L_{\rm SFR}(M_\star) = \kappa_\star \, \frac{M_{\star,\rm burst}}{\tau_{\rm burst}} \tag{5.30}$$

the SFR-luminosity associated to the *final* stellar mass $M_\star$; the Dirac delta-function $\delta_D(\cdot)$ specifies that, since the lightcurve is a constant, the luminosity associated to a stellar mass $M_\star$ must be in the luminosity bin $[L_{\rm SFR}, L_{\rm SFR} + \mathrm{d}L_{\rm SFR}]$.

Using this expression in the continuity equation (Eq. 5.1) without source term (i.e., setting $S(M_\star, t) = 0$) yields:

$$\frac{L_{\rm SFR}\, N(L_{\rm SFR}, t)}{\tau_{\rm burst}\, f_{\star, L_{\rm SFR}}} = \left[\partial_t N(M_\star, t)\, M_\star\right]_{|M_\star(L_{\rm SFR}, t)} \ , \tag{5.31}$$

where $N(L_{\rm SFR}, t)$ is the SLF computed in Sec. 3.5.3 and shown in Fig. 3.6. To ease the reader, we report it here in Fig. 5.9. The final stellar mass that have shone at $L_{\rm SFR}$ is given by:

$$M_\star(L_{\rm SFR}, t) = \frac{(1-R)\, L_{\rm SFR}\, \tau_{\rm burst}}{\kappa_\star} \ , \tag{5.32}$$

where $(1-R) \approx 1.6$, with R being the restituted fraction introduced in Sec. 3.1. In deriving Eq. 5.31, we have defined:

$$\frac{\mathrm{d}M_\star}{\mathrm{d}L_{\rm SFR}} \equiv f_{\star, L_{\rm SFR}} \, \frac{M_\star}{L_{\rm SFR}} \ . \tag{5.33}$$

On the same line of Sec. 5.1.2, we integrate over the cosmic time, and turn to logarithmic bins. The outcome reads:

$$N(\log M_\star, t) = \int_0^t \mathrm{d}t' \, \left[\frac{N(\log L_{\rm SFR})}{f_{\star, L_{\rm SFR}}\, \tau_{\rm burst}}\right]_{|L_{\rm SFR}(M_\star, t')} \ . \tag{5.34}$$

This solution constitutes a novel result. Note that our approach exploits the full SFR-LF in the continuity equation, and is almost insensitive to the initial conditions; in these

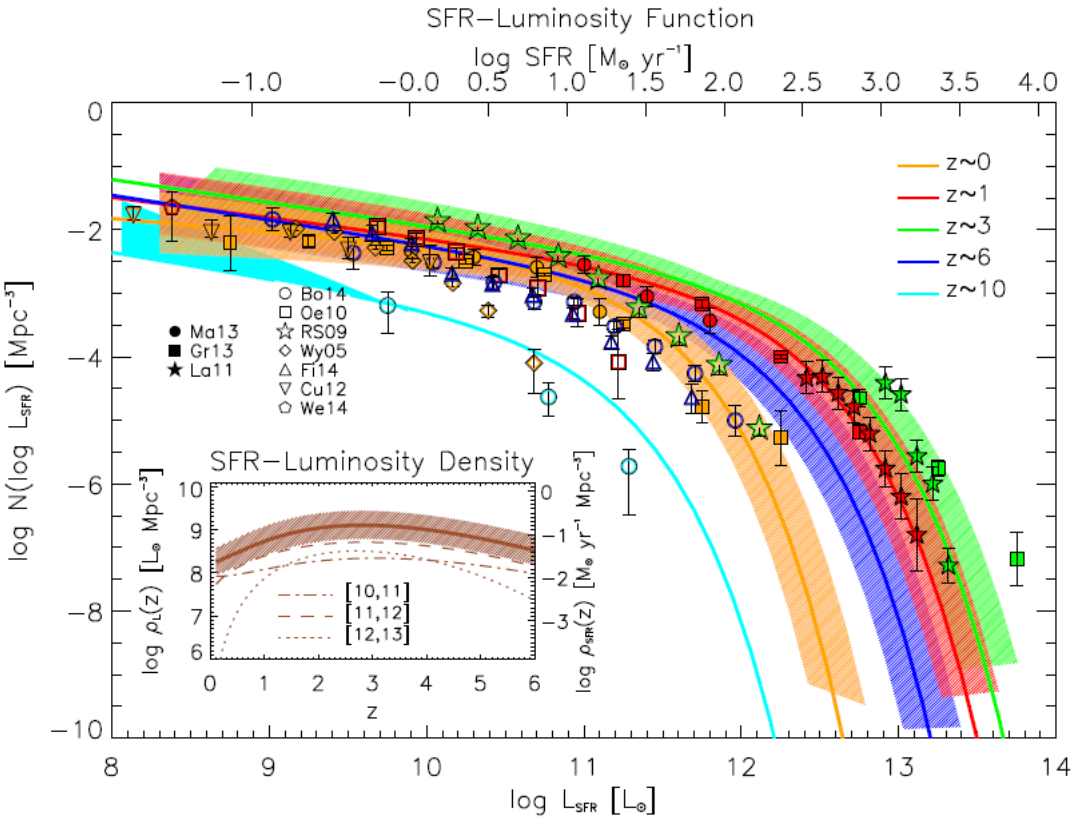

FIGURE 5.9: The SFR-LF $N(\log L_{\rm SFR})$ at redshift $z = 0$ (orange), 1 (red), 3 (green), and 6 (blue), vs. the bolometric luminosity $L_{\rm SFR}$ associated to the SFR (lower axis) and vs. the SFR (upper axis). IR data are from Magnelli et al. (2013, filled circles), Gruppioni et al. (2013, filled squares), and Lapi et al. (2011, filled stars); UV data (dust corrected, see text) are from Bouwens et al. (2014, open circles), Oesch et al. (2010, open squares), Reddy & Steidel (2009, open stars), Wyder et al. (2005, open diamonds), Finkelstein et al. (2014, open triangles), Cucciati et al. (2012, open reversed triangles), Weisz, Johnson & Conroy (2014, pentagons). The solid lines illustrate the analytic rendition of the SLF described in Sec. 3.5.3, while the hatched areas represent the associated uncertainty; the cyan line is the extrapolation to $z = 10$, plotted for illustration, with the shaded area representing the uncertainty on the faint-end slope. The inset shows the SFR-luminosity density as a function of redshift, for the overall luminosity range probed by the data (solid line with hatched area), and for bolometric luminosity $\log L_{\rm SFR}/L_\odot$ in the ranges $[10, 11]$ (dot-dashed line), $[11, 12]$ (dashed line), $[12, 13]$ (dotted line).

respects, it differs from the technique developed by Leja et al. (2015, see also Peng et al. 2010) to evolve the SMF backwards from $z \lesssim 2$ basing on the observed SFR$-M_\star$ relationship and the starforming fraction.

Interestingly, if $\tau_{\rm burst}$ is independent of $L_{\rm SFR}$, a Soltan-type argument can be extended to the stellar content. Infact, multiplying Eq. 5.34 by $M_\star$ and integrating over it, we obtain:

$$\int {\rm d}M_\star \, M_\star \, N(M_\star, t) = \frac{1-R}{\kappa_\star} \int_0^t {\rm d}t' \int {\rm d}L_{\rm SFR} \, L_{\rm SFR} \, N(L_{\rm SFR}, t') \; . \tag{5.35}$$

Comparing it with the classic expression for the BH population, it is evident that the role of the efficiency combination:

$$\frac{(1-\epsilon)}{\epsilon c^2} \approx 7 \times 10^{-14} \, \frac{(1-\epsilon)}{\epsilon} \, \mathrm{yr}^{-1} \, \frac{M_\odot}{L_\odot} \tag{5.36}$$

is played by the quantity:

$$\frac{(1-R)}{\kappa_\star} \approx 9 \times 10^{-11} \, \mathrm{yr}^{-1} \, \frac{M_\odot}{L_\odot} \ , \tag{5.37}$$

which mainly depends on the IMF (here the constant refers to the Chabrier IMF).

In passing, we notice that, for conventional IMFs, most of the stellar mass in galaxies resides in stars with mass $\lesssim 1 \, M_\odot$. Since these stars emit most of their luminosity in the NIR, the galaxy stellar mass $M_\star$ can be inferred by the NIR LFs. At variance with respect to the SMBH case, the so called 'remnants' are not dark, but luminous red stars. This provides a significant vantage point to estimate the MF of these 'remnants'. In fact, the SMF $N(M_\star, t)$ is worked out via the statistics of the SLF $N(L_\star, t)$, not to be confused with the SFR-LF $N(L_{\mathrm{SFR}}, t)$ used above.

5.2.2 Results

In Fig. 5.10, we illustrate our results on the SMF at different representative redshifts. The outcomes can be fitted with the same functional shape used for the BHMF in Eq. 5.19, with M_{BH} replaced by $M_\star$, and parameter values reported in Table 6.1; the resulting fits are accurate within 5% in the redshift range from 0 to 6, where the input SFR-LFs are based on actual data.

The outcome at $z \approx 0$ is compared with the determination of the local SMF by Bernardi et al. (2013). The outcomes at $z \approx 1$ and $z \approx 3$ are compared with the determinations by Santini et al. (2012a) and Ilbert et al. (2013), while the result at $z \approx 6$ is compared with the measurements by Stark et al. (2009) and Duncan et al. (2014). The results of the continuity equation and the observational estimates at different redshifts are in very good agreement, considering the associated uncertainties and systematic differences among the datasets.

Concerning the overall evolution, the high-mass end of the SMF is mainly built up at $z \gtrsim 1.5$, while the low-mass end is still forming at low z. The inset of Fig. 5.10 shows the progressive buildup of the stellar mass density as a function of redshift. The global stellar mass density at $z = 0$ reads $\rho_\star \approx 3 \times 10^8 \, M_\odot \, \mathrm{Mpc}^{-3}$, in good agreement with the observational determinations, and a factor $\sim 10^3$ above the local SMBH mass density. The stellar mass density at $z \sim 1$ is already very close to the local value.

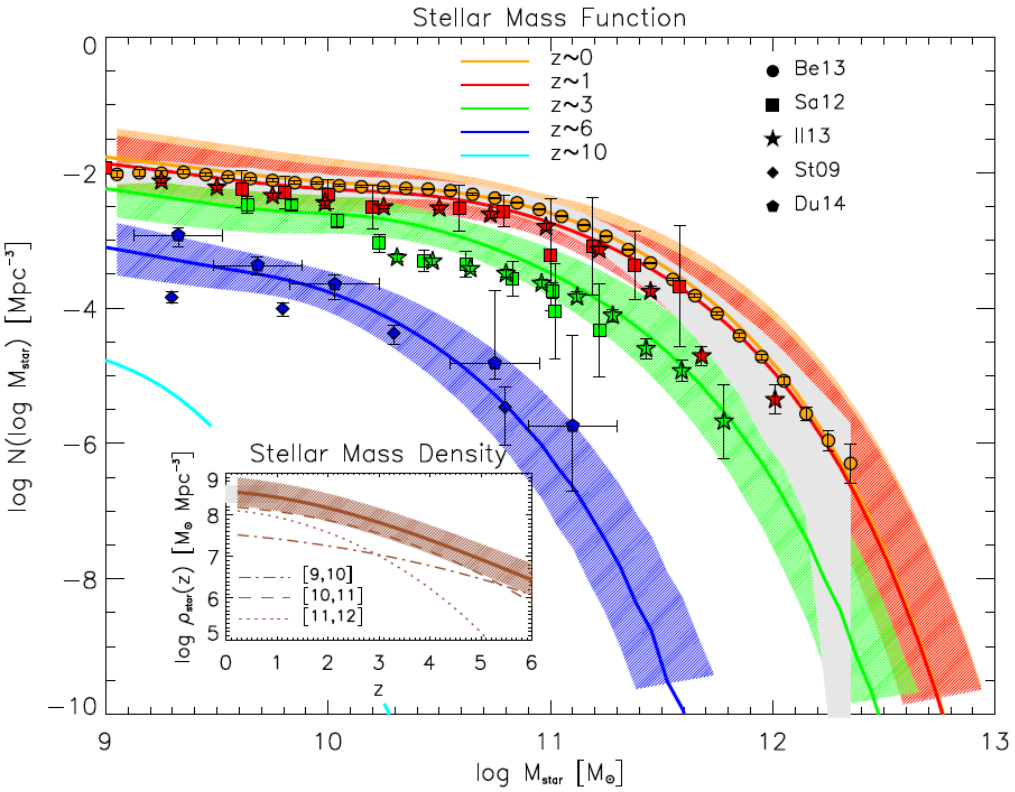

FIGURE 5.10: The SMF $N(\log M_\star)$ as a function of the final stellar mass $M_\star$ in solar units. Results from the continuity equation (see Sec. 5.2) at $z = 0$ (orange), 1 (red), 3 (green), and 6 (blue) are plotted as solid lines, with the hatched areas illustrating the associated uncertainty; the cyan line is the extrapolation to $z = 10$, plotted for illustration. High redshift data are from Ilbert et al. (2013, filled stars), Santini et al. (2012a, filled squares), Stark et al. (2009, filled diamonds), and Duncan et al. (2014, filled pentagon). Local data are from Bernardi et al. (2013): filled circles with errorbars illustrate their fiducial measurements with the associated statistical uncertainty, while the shaded area shows the systematic uncertainty related to light profile fitting. The inset shows the stellar mass density as a function of redshift computed from the continuity equation, for the overall mass range (solid line with hatched area), and for stellar masses $\log M_\star/M_\odot$ in the ranges $[9, 10]$ (dot-dashed line), $[10, 11]$ (dashed line), $[11, 12]$ (dotted line). The grey shaded area illustrates the observational constraints on the stellar mass density from the $z = 0$ MF by Bernardi et al. (2013).

In Fig. 5.11, we show how our results on the SMF depends on the parameters of the lightcurve: the timescale of the burst duration $\tau_{\rm burst}$ and the adopted IMF. To understand the various dependencies, it is useful to assume a simple, piecewise powerlaw shape of the SFR-LF in the form:

$$N(\log L_{\rm SFR}) \propto L_{\rm SFR}^{-\eta} \ , \tag{5.38}$$

with $\eta \lesssim 1$ at the faint end, and $\eta > 1$ at the bright end. Then, it can be seen from Eq. 5.34 that the resulting SMF behaves as:

$$N(\log M_\star) \propto \left(\frac{1-R}{\kappa_\star}\right)^{\eta} \tau_{\rm burst}^{\eta-1}\, \eta\, M_\star^{-\eta} \ . \tag{5.39}$$

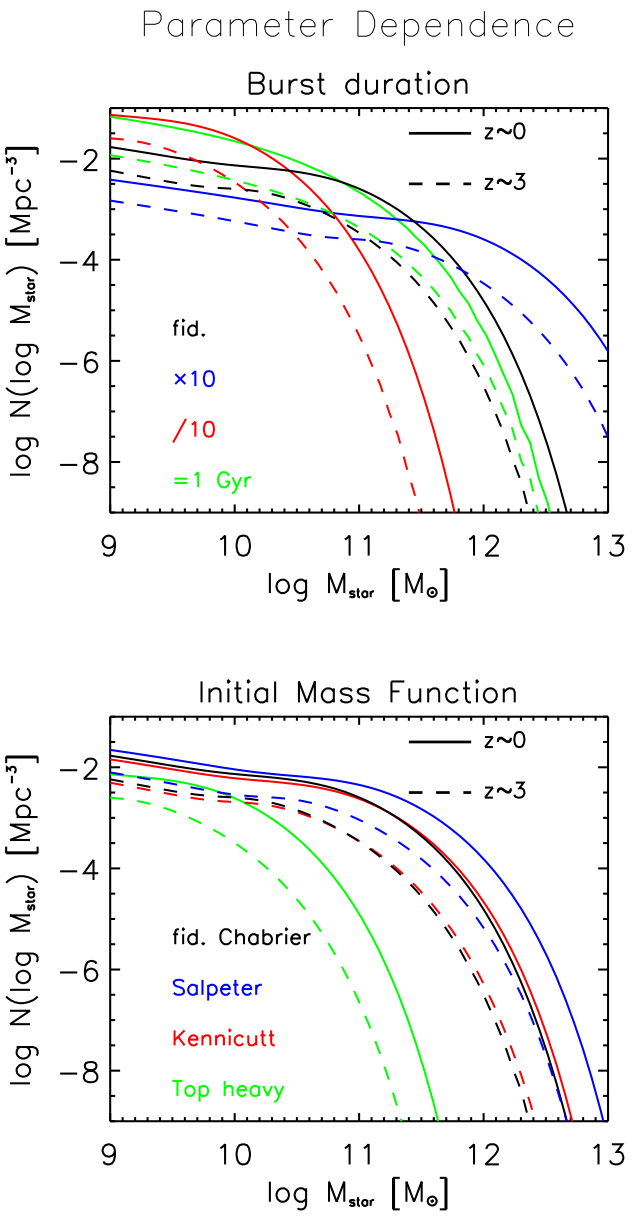

FIGURE 5.11: Comparison plot showing the dependence of the SMF on the parameters of the assumed stellar lightcurve; for clarity, only results at $z = 0$ (solid lines) and $z = 3$ (dashed lines) are plotted. In the top panel, the black lines are for our fiducial values, while the red and blue lines refer to values decreased or increased relative to the reference one; the green lines refers to a constant (in redshift and luminosity) value. In the bottom panel, the black lines refer to our fiducial Chabrier (2003) IMF, while the colored lines are for the Kennicutt (1983, red), the Salpeter (1955, blue), and a top-heavy Lacey et al. (2010, green) IMFs.

Thus, the SMF features an almost direct dependence on $\tau_{\rm burst}$ at the high-mass end, which is mostly contributed by high luminosities, where $\eta > 1$. On the other hand, the dependence is inverse at the low-mass end, mainly associated to faint sources with $\eta \lesssim 1$. The dependence on the IMF is related to the ratio $(1-R)/\kappa_\star$; e.g., passing from the Chabrier to the Salpeter IMF, the ratio increases by a factor of 2. More significant variations are originated when passing from the Chabrier to a top-heavy IMF (e.g., Lacey et al. 2010), which implies the ratio to be reduced by a factor ~ 8.

We have also tried to parameterize the stellar lightcurve with a decreasing or increasing exponential function $L_{\rm SFR} \propto e^{-\tau/\tau_\star}$; the solution of the continuity equation in these instances can be derived on the same route used for BHs. In this case, to reproduce the observed SMF at different redshifts, the typical timescale $\tau_\star$ of the exponential must be of the order of $\tau_{\rm burst}$, i.e., the lightcurve is required to be approximately constant over such a timescale, as we have indeed assumed.

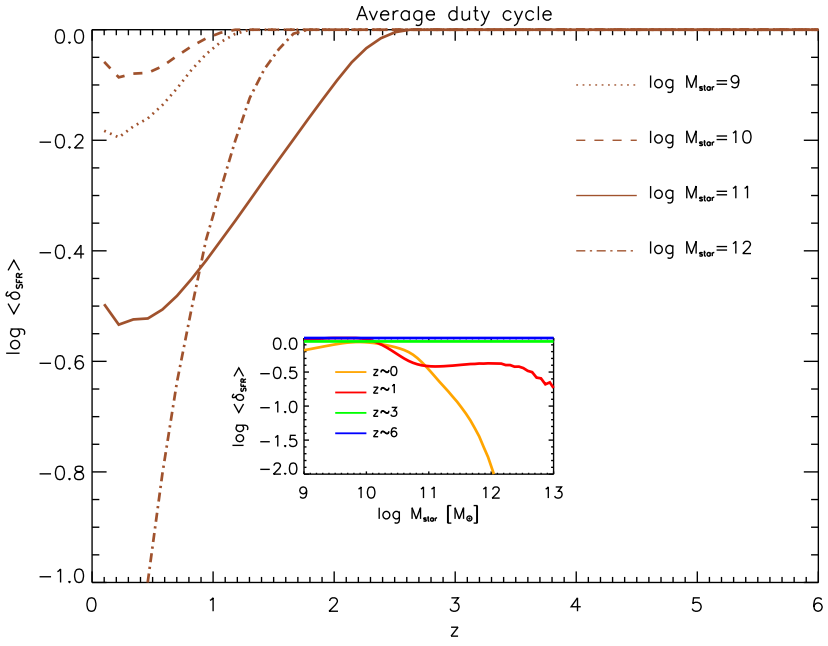

FIGURE 5.12: The average stellar duty cycle $\langle\delta_{\rm SFR}\rangle$ as a function of redshift, for $M_\star = 10^9$ (dotted), 10^{10} (dashed), 10^{11} (solid), and $10^{12}\,M_\odot$ (dot-dashed). The inset illustrates the duty cycle as a function of the stellar mass at $z = 0$ (orange), 1 (red), 3 (green), and 6 (blue).

Fig. 5.12 shows the average duty cycle $\langle\delta_{\rm SFR}\rangle$ of star formation in galaxies. In analogy to Eq. 5.25, it has been computed as:

$$\langle\delta_{\rm SFR}\rangle(M_\star, z) = \frac{N[\log M_\star(L_{\rm SFR}), z]}{N(\log M_\star, z)} \ , \tag{5.40}$$

where the relation between $L_{\rm SFR}$ and $M_\star$ is given by Eq. 5.30. At $z \gtrsim 1$, the duty cycle is almost unity, reflecting the build up of the SMF in real time. On the other hand, at $z \lesssim 1$ the duty cycle progressively drops down, dramatically for stellar masses $M_\star \gtrsim 10^{11}\,M_\odot$. This happens because the mass added by in-situ star formation becomes negligible.

Two related outcomes are extremely relevant in this context: the dust formation, and the role of merging. In Sec. 5.2.3, we will highlight the fundamental role of the dust, by comparing our fiducial results with those derived from the UV LF. We will show that the UV LF, even corrected for dust extinction, produces a SMF much lower than the observed one for $M_\star \gtrsim 2 \times 10^{10}\,M_\odot$ at any $z \lesssim 6$. In particular, we stress that our extrapolated FIR portion of the SFR-LF at $z \sim 6$ is validated by the good comparison with the SMF observed around that redshift. This implies that massive galaxies formed most of their stars in a dusty environment. We expect a large fraction of massive galaxies to be already passively-evolving (i.e., with quite low SFR and 'red' colors) at $z \gtrsim 1$, as indeed increasingly observed, even at substantial redshift ($z \sim 3$; Man et al. 2014; Marchesini et al. 2014).

The point is strengthened by Fig. 5.13, which shows an estimate of (actually an upper bound to) the dust 'formation' time $\tau_{\rm dust}$, computed multiplying the starformation timescale $\tau_{\rm burst}$ by the ratio of the UV LF to the total SFR-LF. At $z \approx 6$, galaxies with $\dot{M}_\star \approx 100\,M_\odot\ {\rm yr}^{-1}$ and $M_\star \gtrsim 3 \times 10^{10}\,M_\odot$ have a dust formation time of $\tau_{\rm dust} \approx 3 \times 10^7$ yr, implying a quite rapid metal/dust enrichment. Interestingly, this is much shorter than the fiducial time $\approx 15\,\tau_{\rm ef} \approx 10^8$ yr, required to grow the hosted final BH mass (cf. Sec. 4.4 and Sec. 4.5). Therefore, most of the BH growth must occur in dusty galaxies (e.g., Mortlock et al. 2011). At $z \gtrsim 2-3$, the upper bounds to $\tau_{\rm dust}$ for strongly starforming objects ($\dot{M}_\star \lesssim 100\,M_\odot\ {\rm yr}^{-1}$) stays almost constant at given SFR (see dot-dashed lines in Fig. 5.13). In moving toward $z \lesssim 2$, the dust formation time becomes shorter, even for moderately starforming objects ($\dot{M}_\star \lesssim 30\,M_\odot\ {\rm yr}^{-1}$). This can be interpreted as star formation episodes mainly occurring within dust-rich molecular clouds, in galaxies already evolved with respect to the chemical composition of their ISM.

In Sec. 5.3, we will investigate the impact of merging on the evolution of the SMF. In this context, it is worth stressing that the effect of dry merging is negligible at $z \gtrsim 1$, and can play some role only at lower redshift (see Fig. 5.17). These outcomes statistically ascertain that most of the stellar content in massive galaxies with $M_\star \gtrsim 3 \times 10^{10}\,M_\odot$ is formed *in situ*. However, we caveat that the observed SMF cannot currently be assessed for $M_\star \gtrsim 3 \times 10^{11}\,M_\odot$, given the substantial systematic uncertainties in the data (see discussion by Bernardi et al. 2013), and that the role of dry mergers can be of some

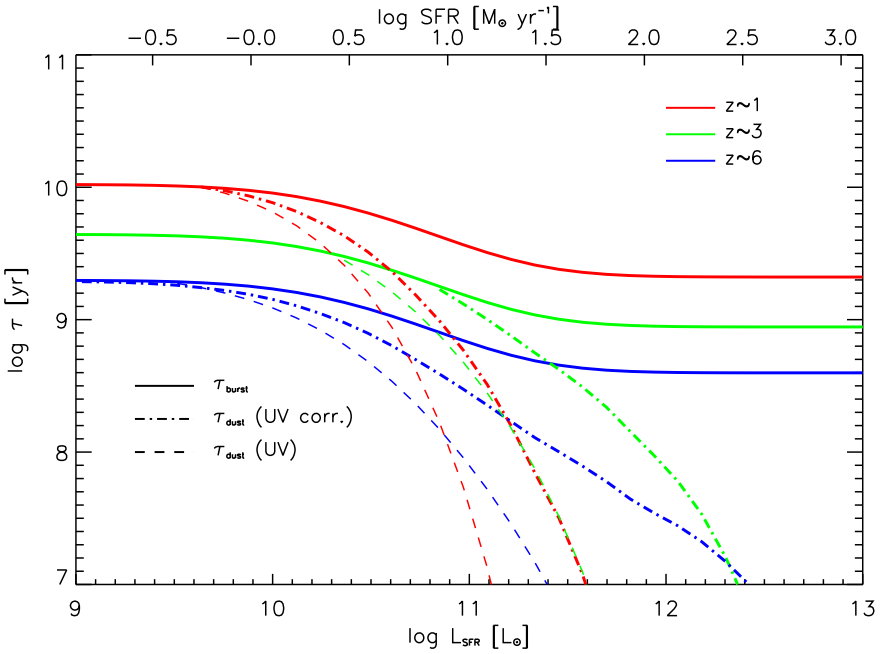

FIGURE 5.13: An estimate of (actually an upper bound to) the dust formation timescale as a function of the SFR-luminosity (lower scale) and of the SFR (upper scale) at $z = 1$ (red), 3 (green) and 6 (blue), computed from dust-corrected UV data (dot-dashed lines), and dust-uncorrected UV data (dotted lines); for comparison, the timescale of the burst duration is also shown (solid lines).

relevance in the growth of such extremely massive galaxies (see Liu et al. 2015; Shankar et al. 2015).

All in all, we stress the capability of the continuity equation in reconstructing the SFH in the Universe from the past SFR activity.

5.2.3 The complementarity of UV and FIR data

In this Section, we stress the importance of the FIR, in addition to the UV, data in probing the star formation process in high-redshift galaxies.

To this purpose, we present in Fig. 5.14 the SFR-LF estimated on the basis of dust-uncorrected UV data, dust-corrected UV data, and UV+FIR data. It is evident that, even when dust-corrected according to the prescriptions described in Sec. 3.5.3, UV data strongly undersample the bright end of the SLF. For example, at $z \sim 3$, the number of sources with $\dot{M}_\star \sim 300\, M_\odot$ yr^{-1}, which is not an extreme, but rather a typical value, is estimated to be 10^{-4} Mpc^{-3} from UV+FIR data, while it is inferred to be $\lesssim 10^{-6}$ Mpc^{-3} from dust-corrected UV data, and would be $\lesssim 10^{-10}$ Mpc^{-3} from dust-uncorrected UV data. We stress that, especially at $z \gtrsim 1.5$, the dust corrections routinely applied to the

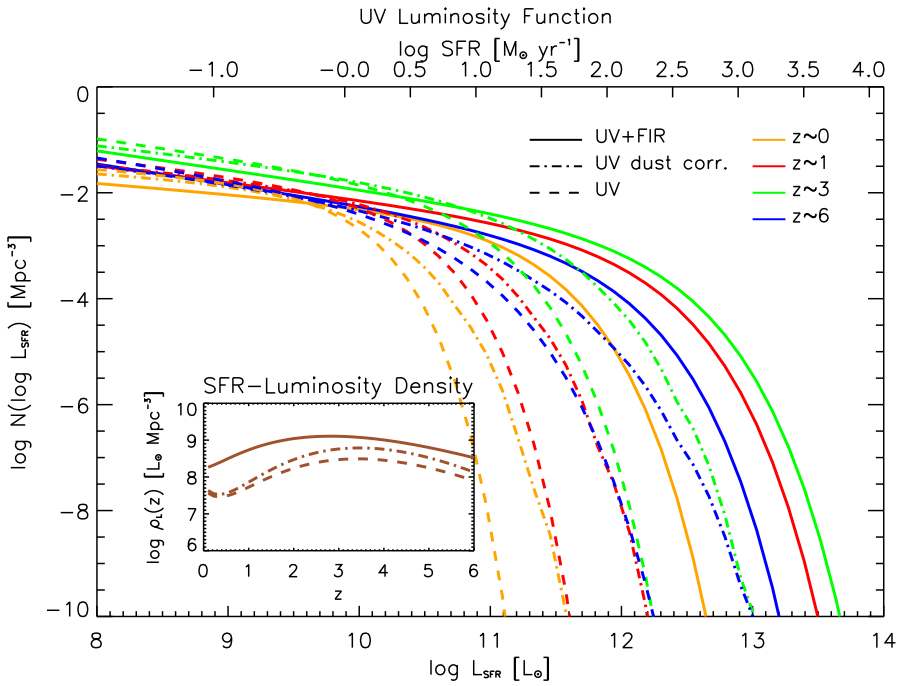

FIGURE 5.14: The SFR-LF $N(\log L_{\rm SFR})$ at $z = 0$ (orange), 1 (red), 3 (green), and 6 (blue), vs. the luminosity $L_{\rm SFR}$ associated to the SFR (lower axis) and vs. the SFR (upper axis). Solid lines is our rendition based on the UV data at the faint end and FIR data at the bright end (the same plotted in Fig. 5.9). Dot-dashed lines are a rendition based only on dust-corrected UV data, and dashed lines on dust-uncorrected UV data. The inset shows the corresponding SFR-luminosity densities. Data points have been omitted for clarity.

UV data are unable to fully account for the population of strongly starforming galaxies observed in the FIR band.

In Fig. 5.15, we illustrate the SMFs obtained via the continuity equation from the above input SLFs. We keep the same lightcurve of our fiducial model, which for UV-bright, low-luminosity objects yields a duration of the burst already close to the Hubble time. As it can be seen, when basing only on UV data (even if dust-corrected) the high mass end of the resulting SMF is strongly underpredicted relative to the FIR+UV results (which well reproduces observational estimates, see Fig. 5.10) at any redshift. Note that this mismatch can hardly be recovered by mass additions from dry merging events, since a factor ~ 10 in mass is needed from $z \approx 3$ to $z \approx 0$.

5.3 Dry merging

Many recent works (e.g., Shankar, Weinberg & Miralda-Escudé 2009, 2013; Moster et al. 2010; Moster, Naab & White 2013; Cisternas et al. 2011) have shown that the role of

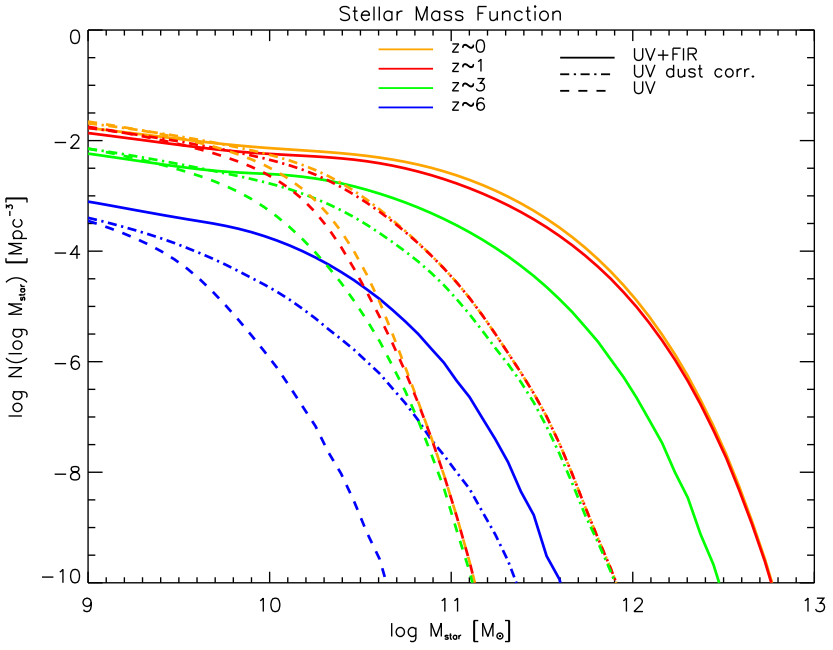

FIGURE 5.15: Effect of adopting the SFR-LFs obtained basing on FIR and UV data (solid lines), only dust-corrected UV data (dot-dashed lines) and only dust-uncorrected UV data (dashed lines) as input of the continuity equation to obtain the SMF. The solid lines are the same outputs shown in Fig. 5.10 to be in very good agreement with data points (here omitted for clarity).

dry mergers (i.e., addition of the whole mass content in stars or BHs of the merging halos, without significantly contributing to star formation or BH accretion) in building up the SMBH and stellar MFs is less important than accretion/in-situ star formation at $z \gtrsim 1.5$. This is simply because the evolutionary times associated to mergers are much longer than those associated to the in-situ BH/stellar mass growth.

On the other hand, at $z \lesssim 1.5$, the situation is expected to reverse. The reason is that the cold accreting or starforming gas within the DM halo gets progressively exhausted, or is ejected/heated by the energy feedback from SNe or from the AGN itself. In fact, the continuity equation with accretion only yields little evolution of the MFs from $z \sim 1$ to $z \sim 0$ (cf. Fig. 5.2, Fig. 5.10, and related insets). Thus, the low redshift ($z \lesssim 1$) evolution could be in principle more affected by dry merging. This is a hotly debated issue in the literature, especially in relation to the size evolution of massive, passively-evolving galaxies (e.g., Naab, Johansson & Ostriker 2009; Georgakakis et al. 2009; Fan et al. 2010; Nipoti et al. 2012; Shankar et al. 2015; Kulier et al. 2015).

In this Section, we highlight the impact of dry mergers on the SMBH and stellar MFs at $z \lesssim 1$. We start from the observed MFs at $z \sim 1$, then we evolve them down to $z = 0$, by taking into account both dry mergers and accretion in the continuity equation. The effect of dry mergers is numerically evaluated with a mid-point scheme computation that

divides the overall timegrid in sufficiently small steps δt, and then evolves the MF at each timestep t_i according to:

$$N(\log M, t_i + \delta t) = N(\log M, t_i) + \frac{\mathcal{P}}{2} N(\log \frac{M}{2}, t_i)\, \delta t - \mathcal{P}\, N(\log M, t_i)\, \delta t \ , \qquad (5.41)$$

where $\mathcal{P}$ is the probability of dry mergers. To compute it, we adopt the common simplifying assumption that dry merging of the associated stellar and BH components follows halo mergers of given mass ratio. We base on the DM merging rates provided by Stewart et al. (2009) via high-resolution $N-$body simulations, and write:

$$\mathcal{P}(>\zeta) \approx 0.02 \frac{\delta t}{\mathrm{Gyr}} (1+z)^{2.1} \frac{(1-\zeta)^{0.72}}{\zeta^{0.54}} \ , \qquad (5.42)$$

where ζ specifies the mass ratio above which mergers are considered; thus $\mathcal{P}(>0.5)$ is the probability of major mergers, while $\mathcal{P}(>0.1) - \mathcal{P}(>0.5)$ is that of minor mergers.

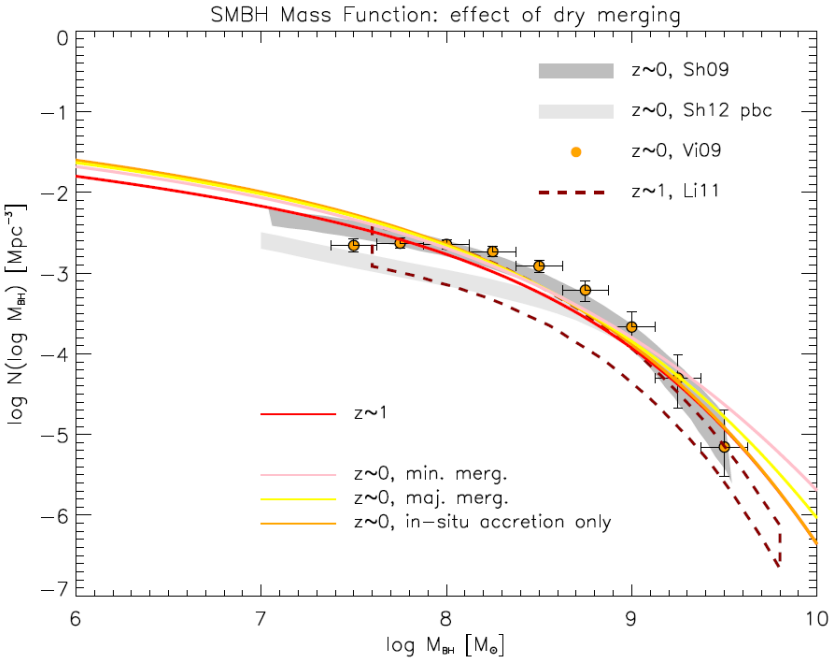

FIGURE 5.16: Effect of dry merging on the late ($z \lesssim 1$) evolution of the BHMF, as derived from the continuity equation. The red line represents the BHMF at $z \sim 1$ (merging effects are negligible at higher redshifts), while the other colored lines illustrates its evolution toward $z \sim 0$ due to merging and in-situ accretion. Specifically, the BH merging rate is assumed to mirror the DM merging rates, as given by Stewart et al. (2009) for major mergers (yellow line) and for minor mergers (pink line); for reference, the result for in-situ accretion only is plotted as an orange line. Data points and shaded areas as in Fig. 5.2.

The results on the SMBH and stellar MFs are illustrated in Fig. 5.16 and Fig. 5.17. The impact of dry mergers on the MFs is evident only at the high-mass end. Dry mergers moderately increase the space densities of SMBHs with mass $M_{\rm BH} \gtrsim 10^9\, M_\odot$, and boost

that of stellar masses $M_\star \gtrsim 10^{12}\,M_\odot$. We note that, in these ranges, the data are still statistically uncertain and/or affected by large systematics.

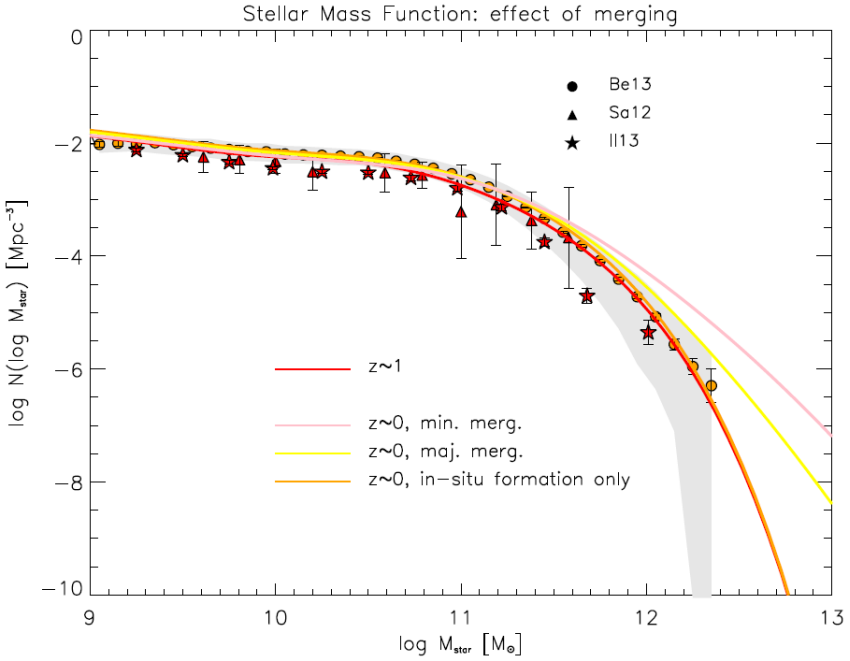

FIGURE 5.17: Effect of dry merging on the late ($z \lesssim 1$) evolution of the galaxy SMF, as derived from the continuity equation. The red line represents the SMF at $z \sim 1$ (merging effects are negligible at higher redshifts), while the other colored lines illustrate its evolution toward $z \sim 0$ due to merging and in-situ formation. Specifically, the galaxy merging rate is computed according to Stewart et al. (2009) for major mergers (yellow line) and for minor mergers (pink line); for reference, the result for in-situ formation only is plotted as an orange line. Data points and shaded areas as in Fig. 5.10.

Specifically, assuming that a dry merger follows any DM halo merger (either major of minor) yields a local BHMF still consistent with observational data, even considering the uncertainties on the bolometric corrections in converting from luminosity to mass (cf. Sec. 2.7.1). On the other hand, while major dry mergers produce a SMF consistent with the data (see also Liu et al. 2015), this is not the case for minor dry mergers. All that implies that the addition of stellar mass by (minor) dry mergers following the ones of DM halos must be only partial, possibly depending on the mass ratio, orbital parameters, tidal stripping, and structural properties (see Naab, Johansson & Ostriker 2009; Krogager et al. 2014).

Chapter 6

Abundance Matching

Having obtained a comprehensive view of the bolometric luminosity and mass functions for stars and SMBHs at different redshifts, we now aim at establishing a link among them and the gravitationally dominant DM component. To this purpose, we exploit the abundance matching technique, a standard way to derive a monotonic relationship between BH, galaxy and halo properties by matching their corresponding number densities (Vale & Ostriker 2004; Shankar et al. 2006; Moster et al. 2010; Moster, Naab & White 2013; Behroozi, Wechsler & Conroy 2013).

When dealing with stellar or BH mass, which we generically indicate with M, we derive the relation $M(M_{\rm H}, z)$ with the halo mass $M_{\rm H}$ by solving the equation (e.g., White, Martini & Cohn 2008; Shankar, Weinberg & Shen 2010):

$$\begin{aligned} &\int_{\log M}^{\infty} \mathrm{d}\log M'\, N(\log M', z) = \\ &= \int_{-\infty}^{+\infty} \mathrm{d}\log M'_{\rm H}\, N(\log M'_{\rm H}, z)\, \frac{1}{2}\,\mathrm{erfc}\left\{\frac{\log[M_{\rm H}(M)/M'_{\rm H}]}{\sqrt{2}\,\tilde{\sigma}_{\log M}}\right\}\,, \end{aligned} \tag{6.1}$$

which holds when a lognormal distribution of M at given $M_{\rm H}$ with dispersion $\sigma_{\log M}$ is adopted. In the above expression, we have defined:

$$\tilde{\sigma}_{\log M} = \frac{\sigma_{\log M}}{\mu}\,, \tag{6.2}$$

with $\mu \equiv \mathrm{d}\log M/\mathrm{d}\log M_{\rm H}$. On the basis of the investigation by Lapi et al. (2006, 2011, 2014) on the high-redshift galaxy and AGN LFs, we expect the $M_{\rm BH} - M_{\rm H}$ correlation to feature a quite large scatter ($\sigma_{\log M_{\rm BH}} \approx 0.4$ dex), while a smaller value ($\sigma_{\log M_\star} \approx 0.15$ dex) is expected for the correlation with the stellar component. We shall compare the correlations $M - M_{\rm H}$ obtained when such values for the scatter are considered, with those obtained by assuming one-to-one relationships, i.e., taking $\sigma_{\log M} = 0$.

In Eq. 6.1, the quantity $N(\log M_{\rm H})$ is the Galaxy Halo Mass Function (GHMF), i.e., the MF of halos hosting one individual galaxy. We do not simply rely on the overall halo mass function (HMF), because we aim at obtaining relationships valid for one single galaxy, not for a galaxy system like a group or a cluster. We defer the reader to Section 6.1 for the detailed description of this procedure.

The same abundance matching technique may also be applied to the stellar or AGN bolometric luminosity, generically indicated with L, looking for a relation $L(M_{\rm H}, z)$ specifying the typical luminosity to be expected in a halo of mass $M_{\rm H}$ at given redshift. When dealing with luminosities, it must be taken into account that galaxies and AGNs shine only for a fraction of the cosmic time. To deal with this, we use a modified abundance matching of the form:

$$\begin{aligned} &\int_{\log L}^{\infty} \mathrm{d}\log L' \, \frac{N(\log L', z)}{\langle\delta\rangle \times t} = \\ &= \int_{-\infty}^{+\infty} \mathrm{d}\log M'_{\rm H} \, \partial_t^+ N(\log M'_{\rm H}, z) \, \frac{1}{2} \, \mathrm{erfc}\left\{ \frac{\log[M_{\rm H}(L)/M'_{\rm H}]}{\sqrt{2}\,\tilde{\sigma}_{\log L}} \right\} \, , \end{aligned} \tag{6.3}$$

where $\langle\delta\rangle \times t$ is the duty cycle δ averaged over the lightcurve, multiplied by the cosmic time t, and $\partial_t^+ N(\log M_{\rm H}, z)$ is the formation rate of galactic halos, computed according to Lapi, Salucci & Danese (2013).

6.1 Galaxy Halo Mass Function

In order to investigate the relationships between the BH, stellar and DM content in galaxies, the mass function associated to halos hosting one individual galaxy has to been estimated. The computation actually includes two steps:

1. We account for the possibility of the presence of subhalos in a halo;
2. We probabilistically exclude halos corresponding to galaxy systems rather than to individual galaxies.

Our starting point is the subhalo MF, as recently determined by Jiang & van den Bosch (2014). The distribution of subhalos with mass between m and $m + \mathrm{d}m$ in a halo of mass $M_{\rm H}$ at redshift z can be well fitted by the function:

$$N(\log\psi) = \gamma \, \psi^{\alpha} \, e^{-\beta\,\psi^{\omega}} \, \ln 10 \, , \tag{6.4}$$

where $\psi = m/M_{\rm H}$. Actually, if m is taken as the subhalo mass at the infall time, the resulting *unevolved* subhalo MF is universal for any mass $M_{\rm H}$, and as such is described

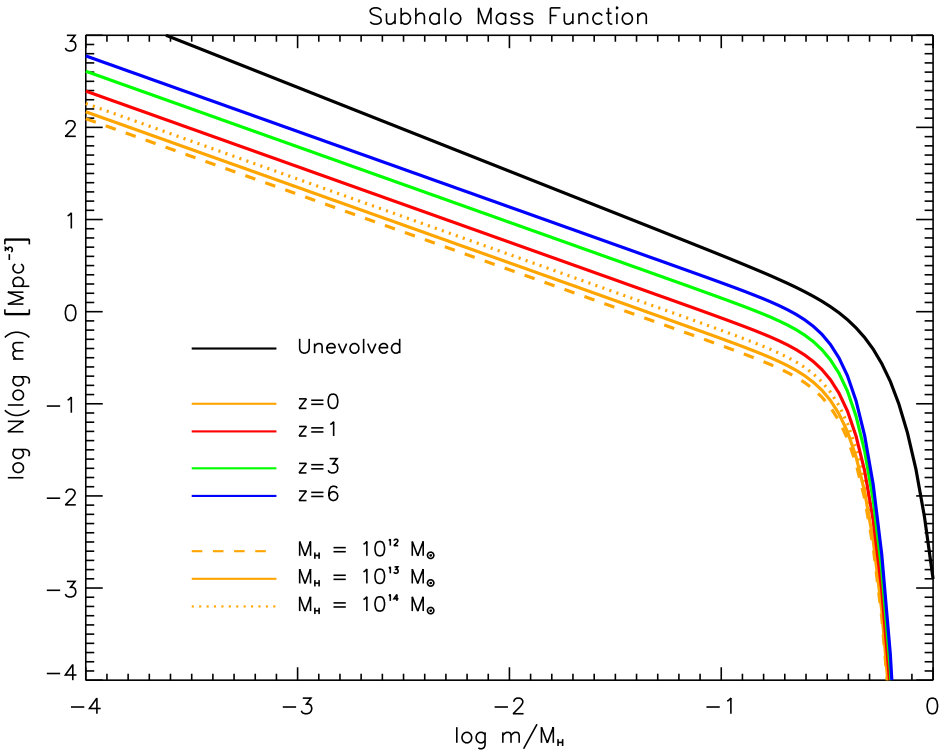

FIGURE 6.1: The subhalo MF $N(\log m)$ as a function of the ratio between the satellite and the halo masses $m/M_{\rm H}$, computed according to the prescriptions by Jiang & van den Bosch (2014). The black line refers to the unevolved MF, and colored lines to the evolved MFs at $z = 0$ (orange), 1 (red), 3 (green), and 6 (blue). At $z = 0$, the solid line refers to a host mass of $M_{\rm H} = 10^{13}\,M_\odot$, the dashed line to $10^{12}\,M_\odot$, and the dotted one to $10^{14}\,M_\odot$.

by the parameter set:

$$[\gamma, \alpha, \beta, \omega] = [0.22, -0.91, 6.00, 3.00]\ . \tag{6.5}$$

The subhalo MF is plotted in Fig. 6.1.

However, we are more interested in taking m as the mass of the surviving, self-bound entity at redshift z, which is reduced with respect to that at accretion due to mass stripping and dynamical friction. The resulting *evolved* subhalo MF is then described by the same functional shape in Eq. 6.4, but with a modified parameter set:

$$[\gamma, \alpha, \beta, \omega] = [0.31\,f_s, -0.82, 50.00, 4.00]\ , \tag{6.6}$$

which depends on the host halo mass and redshift through the quantity f_s. The latter may be determined as follows: first we obtain the half-mass redshift $z_{0.5}$ solving:

$$\delta_c(z_{0.5}) = \delta_c(z) + 1.19\,\sqrt{\sigma^2(M_{\rm H}/2) - \sigma^2(M_{\rm H})}\ , \tag{6.7}$$

$\delta_c(z)$ being the linear threshold for collapse at redshift z, and $\sigma^2(M)$ the mass variance at the scale M. Then we compute:

$$N_\tau = \int_{t(z)}^{t(z_{0.5})} \frac{\mathrm{d}t}{\tau_{\rm dyn}(t)} \ , \tag{6.8}$$

$\tau_{\rm dyn}$ being the halo dynamical time. Finally,

$$f_s = 0.3563\, N_\tau^{-0.6} - 0.075 \tag{6.9}$$

holds. The outcome is illustrated for different redshifts and host halo masses in Fig. 6.1.

Now we can compute the overall subhalo contribution to the Halo MF in the mass bin $[M_{\rm H}, M_{\rm H} + \mathrm{d}M_{\rm H}]$ as:

$$N_{\rm subH}(\log M_{\rm H}) = \int_0^\infty \mathrm{d}\log M'_{\rm H}\ N_{\rm H}(\log M'_{\rm H})\, N(\log\psi)_{|\psi=M_{\rm H}/M'_{\rm H}} \ , \tag{6.10}$$

where $N_{\rm H}(\log M_{\rm H})$ is the standard HMF (see Sheth & Tormen 1999; Tinker et al. 2008). Thus the total halo + subhalo MF just reads:

$$N_{\rm H+subH}(\log M_{\rm H}) = N_{\rm H}(\log M_{\rm H}) + N_{\rm subH}(\log M_{\rm H}) \ . \tag{6.11}$$

In Fig. 6.2, we plot at different redshifts the HMF, the overall subhalo MF, and the total halo + subhalo MF. It can be easily seen that the subhalo contribution is almost negligible for any redshifts in the mass range of interest for this thesis.

Now we turn to compute the probability distribution for a given halo to contain one individual galaxy. The first step is to obtain the halo occupation number (HON), i.e., the average number of subhalos inside a host halo of mass $M_{\rm H}$:

$$\langle N\rangle(M_{\rm H}, z) = \int_{\log m_{\rm min}/M_{\rm H}}^0 \mathrm{d}\log\psi\ N(\log\psi) \ . \tag{6.12}$$

Here, $m_{\rm min}$ represents a minimum mass for subhalos, required to avoid the divergence in the integral; it will be set by comparison with numerical simulations and observational datasets. The resulting HON as a function of $M_{\rm H}$ and redshift, for different minimum subhalo masses $m_{\rm min}$, is illustrated in Fig. 6.3. For $M_{\rm H} \gg m_{\rm min}$, the HON is well fitted by a power-law with logarithmic slope $\lesssim 1$, going into an abrupt cutoff for masses $M_{\rm H} \lesssim 3 - 5\, m_{\rm min}$.

The HON represents the *average* number of subhalos inside a host halo. Instead, we need the probability distribution $P(N|\langle N\rangle)$ of having N subhalos given the average number $\langle N\rangle(M_{\rm H}, z)$. Numerical simulations and halo occupation distribution (HOD) models,

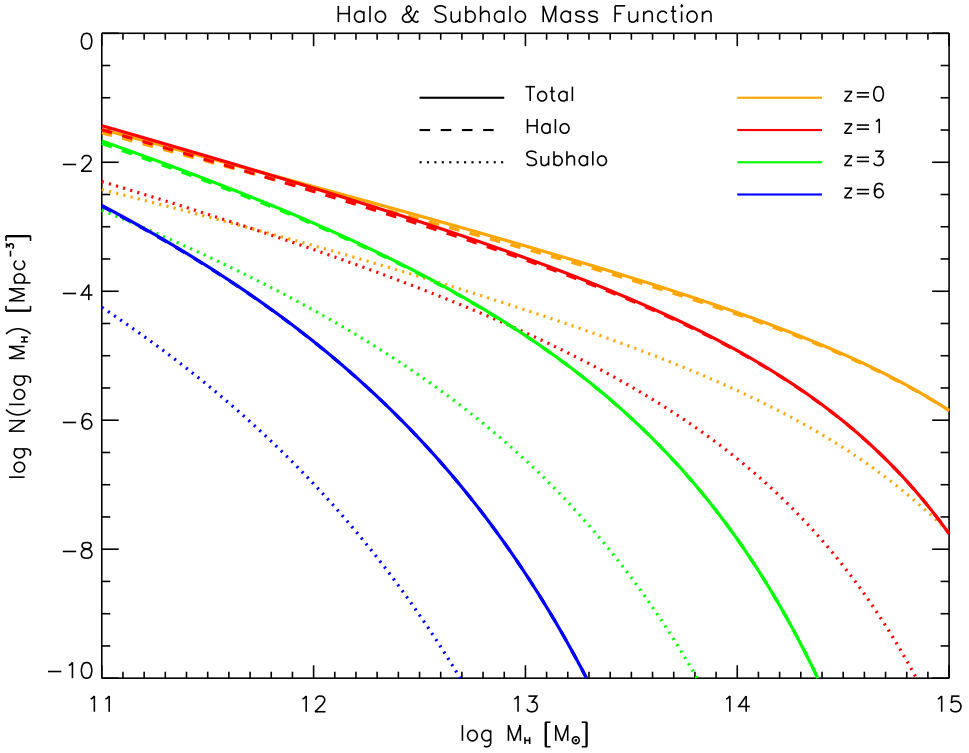

FIGURE 6.2: The overall contribution of subhalos to the HMF, as a function of the halo mass $M_{\rm H}$. Solid lines show the HMF including subhalos, dashed lines show the HMF without subhalos, and dotted lines show the subhalo contribution. Results are plotted at redshift $z = 0$ (orange), 1 (red), 3 (green), and 6 (blue).

aimed at reproducing various galaxy observables (Zehavi et al. 2005, 2011; Zheng, Coil & Zehavi 2007; Zheng et al. 2009; Tinker et al. 2013), indicate that such a distribution is well approximated by a Poissonian. Then, the cumulative probability $P(< N|\langle N\rangle)$ of having less than N subhalos can be easily computed. This reads:

$$P(< N|\langle N\rangle) = \frac{\Gamma(\underline{N+1}, \langle N\rangle)}{\underline{N}!} \ , \tag{6.13}$$

where $\Gamma(a,x) = \int_x^\infty {\rm d}t \ t^{a-1}\, e^{-t}$ is the incomplete complementary Γ-function, $\underline{x}$ is the floor function (the closest integer lower than x), and $n! = 1 \times 2 \times ... \times n$ the factorial function. We stress that, in such a probability, the dependence on host halo mass and redshift are encased into the HON $\langle N\rangle(M_{\rm H}, z)$.

Finally, the GHMF can be computed as:

$$N_{\rm GH}(\log M_{\rm H}) = N_{\rm H+subH}(\log M_{\rm H}) \times P(< N = 1|\langle N\rangle) \ . \tag{6.14}$$

The outcomes at different redshifts, adopting a minimum satellite mass of $m_{\rm min} = 10^{11}\, M_\odot$, are illustrated in Fig. 6.4. We stress that the determination of the GHMF

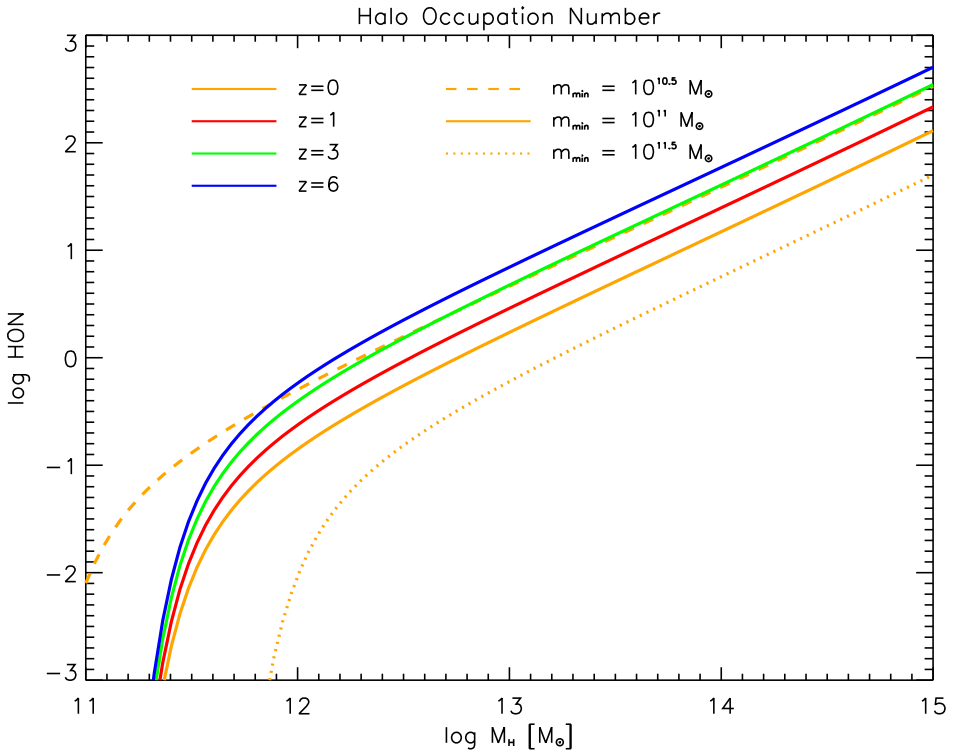

FIGURE 6.3: The HON as a function of the host halo mass $M_{\rm H}$. Results are plotted at $z = 0$ (orange), 1 (red), 3 (green), and 6 (blue). At $z = 0$, solid line refers to a minimum satellite mass $m_{\rm min} = 10^{11}\,M_\odot$, dashed to $10^{10.5}\,M_\odot$, and dotted to $10^{11.5}\,M_\odot$.

as a function of redshift constitutes in its stand a novel result. In the same figure, we also compare the GHMF to the overall HMF. The difference between the two, i.e. the galaxy system HMF at $z = 0$, is compared with local data to cross-check our approach. At the bright end, the GHMF drastically falls off, so that even at $z \lesssim 1$ galactic halo masses of $\approx 10^{14}\,M_\odot$ are very rare, since these masses pertain to galaxy systems. These findings agree with galaxy-galaxy weak lensing measurements (Kochanek et al. 2003; Mandelbaum et al. 2006; van Uitert et al. 2011; Leauthaud et al. 2012; Velander et al. 2014) and dynamical observations in nearby galaxies (Gerhard et al. 2001; Andreon et al. 2014, see also the review by Courteau et al. 2014).

With respect to the full halo + subhalo MF, the GHMF features a cutoff for host halo masses $M_{\rm H} \gtrsim 1-3\times10^{13}\,M_\odot$, more pronounced at lower redshift. This happens because the probability of hosting subhalos (hence more than one galaxy) increases strongly for large masses. In other words, such halos are more likely to host a galaxy group or cluster, than an individual galaxy.

We stress that both a minimum mass of $\sim 10^{11}\,M_\odot$ for satellite halos (corresponding to the adopted $m_{\rm min}$), and a maximal value of $\sim 10^{13}\,M_\odot$ for a halo to host an individual galaxy (corresponding to the resulting cutoff in the GHMF) are strongly indicated

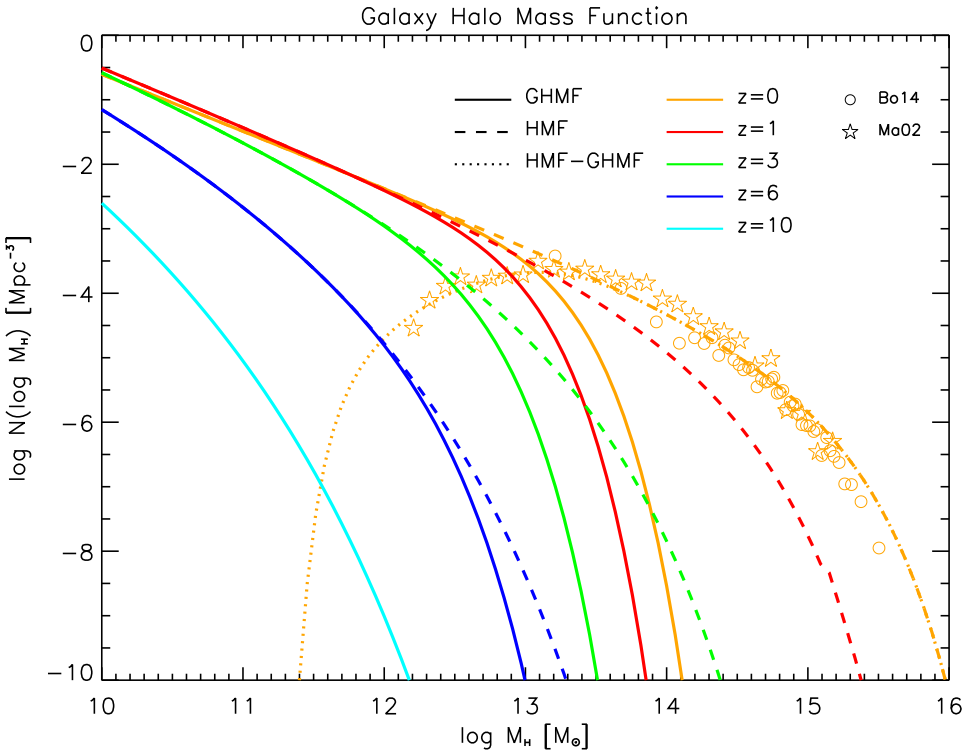

FIGURE 6.4: The GHMF $N_{\rm GH}(\log M_{\rm H})$ (solid lines) at $z = 0$ (orange), 1 (red), 3 (green), 6 (blue) and 10 (cyan), as a function of the halo mass $M_{\rm H}$ is solar units. This is obtained from the HMF (dashed lines) by adding the global subhalo MF and subtracting the MF of multiply-occupied halos (or equivalently multiplying by the probability of single occupation). At $z = 0$, we also report as a dotted line the resulting cluster and group HMF (obtained by subtraction of the solid from the dashed line); this is compared with the determinations by Böhringer, Chon & Collins (2014, circles) from X-ray observations of groups and clusters, and by Martínez et al. (2002, stars) from optical observations of loose groups.

by galaxy weak lensing observations (Mandelbaum et al. 2006; van Uitert et al. 2011; Leauthaud et al. 2012; Velander et al. 2014). Furthermore, such maximum galactic halo masses are also strongly suggested by dynamical observations of gas and stars in nearby galaxies (Gerhard et al. 2001; Andreon et al. 2014, see also the review by Courteau et al. 2014).

Finally, to provide a further observational test, we have computed the group and cluster MF by subtracting the GHMF from the overall halo + subhalo MF. This represents the HMF associated only to galaxy systems, and as such is expected to show a cutoff for $M_H \lesssim 10^{13}\, M_\odot$. The result at $z = 0$ is plotted as a dotted line in Fig. 6.4, and compared with the determinations by Böhringer, Chon & Collins (2014) from X-ray observations of groups and clusters, and by Martínez et al. (2002) from optical observations of loose groups; the agreement is quite impressive. We notice that the behavior in the range of poor clusters and groups is particularly sensitive to the parameter $m_{\rm min}$. Thus, the

agreement with the data is another indication that the adopted value $m_{\rm min} \sim 10^{11}\,M_\odot$ is appropriate.

The overall HMF and the GHMF can be fitted with the functional shape:

$$N(\log M_{\rm H}, z) = \Phi(z) \left[\frac{M_{\rm H}}{M_c(z)}\right]^{1-\alpha(z)} \exp\left\{-\left[\frac{M_{\rm H}}{M_c(z)}\right]^{\omega(z)}\right\}, \tag{6.15}$$

where the normalization $\log \Phi(z)$, the characteristic mass $\log M_c(z)$, and the characteristic slopes $\alpha(z)$ and $\omega(z)$ evolve with redshift according to the same parametrization:

$$p(z) = p_0 + k_{p1}\,\chi + k_{p2}\,\chi^2 + k_{p3}\,\chi^3 \tag{6.16}$$

with $\chi = \log[(1+z)/(1+z_0)]$ and $z_0 = 0.1$.

The parameter values are reported in Table 6.1. The resulting fits are accurate within 5% in the redshift range $0 \lesssim z \lesssim 10$, and halo mass range $10 \lesssim \log M_{\rm H}/\log M_\odot \lesssim 14$ for the GHMF, and $10 \lesssim \log M_{\rm H}/\log M_\odot \lesssim 16$ for the HMF.

6.2 Results

In this section, we present the results of the abundance matching technique among various statistical properties of SMBHs, galaxies, and host halos. Analytic fits to such outcomes can be found in Sec. 6.2.6 and in Table 6.2.

6.2.1 Black Hole vs. Halo properties

In Fig. 6.5, we show the relationship between the BH mass $M_{\rm BH}$ and the halo mass $M_{\rm H}$ from the abundance matching technique, at different redshifts. Since we are comparing BH and halo statistics at fixed z, the resulting relationship constitutes a snapshot, that can be operationally exploited in numerical works to properly populate halos at the reference redshift. On the other hand, the evolution of BHs and halos due to accretion is expected to modify the relation, though on different timescales, as the cosmological time passes. For example, if the cosmological growth of halos is dominant, then the relation would shift along the $M_{\rm H}$ axis. The relationship at a subsequent redshift takes into account such an evolution, although the number of evolved BHs and halos is generally subdominant with respect to the newly formed objects.

The top panel of Fig. 6.5 shows the results when a one-to-one (i.e., no scatter) $M_{\rm BH} - M_{\rm H}$ relationship is assumed, while bottom panel shows the resulting average relationship

Function	$\log \Phi_0$	$k_{\Phi 1}$	$k_{\Phi 2}$	$k_{\Phi 3}$	$\log X_0$	k_{X1}	k_{X2}	k_{X3}	$\alpha(z_0)$	$k_{\alpha 1}$	$k_{\alpha 2}$	$k_{\alpha 3}$	$\omega(z_0)$	$k_{\omega 1}$	$k_{\omega 2}$	$k_{\omega 2}$
$N(\log X, z) = \Phi(z) \left[\frac{X}{X_c(z)}\right]^{1-\alpha(z)} \exp\left\{-\left[\frac{X}{X_c(z)}\right]^{\omega(z)}\right\}$																
AGN LF	-3.80	0.45	-1.00	0.00	10.90	1.10	6.94	-11.55	1.40	-1.70	3.40	-1.75	0.36	0.62	-1.59	0.8
Stellar LF	-2.40	-2.30	6.20	-4.90	10.90	3.20	-1.40	-2.10	1.20	0.50	-0.50	0.20	0.70	-0.15	0.16	0.00
BH MF	-2.30	-0.40	-1.80	-1.50	8.07	-0.80	7.30	-9.20	1.35	-0.10	0.40	0.30	0.46	0.05	0.18	-0.55
Stellar MF	-2.10	-0.80	1.65	-3.10	10.85	0.00	0.00	-1.90	1.20	0.00	-0.40	0.55	0.65	0.00	-0.40	0.55
HMF	-3.97	0.00	0.00	1.50	14.00	-0.90	-1.90	-1.10	1.80	0.50	0.10	0.70	0.47	0.45	-0.10	-0.45
GHMF	-3.35	0.50	0.1	-1.50	13.05	-0.80	0.00	-1.30	1.88	0.30	-0.40	1.30	1.10	-0.10	0.00	-0.43

[a]

TABLE 6.1: Input/Output Generalized Schechter Functions

[a]Typical tolerance on the parameters is less than 10%. See Sec. 2.7.4, Sec. 3.5.3, Sec. 5.1.3, and Sec. 6.1 for details on the redshift evolution of the parameters.

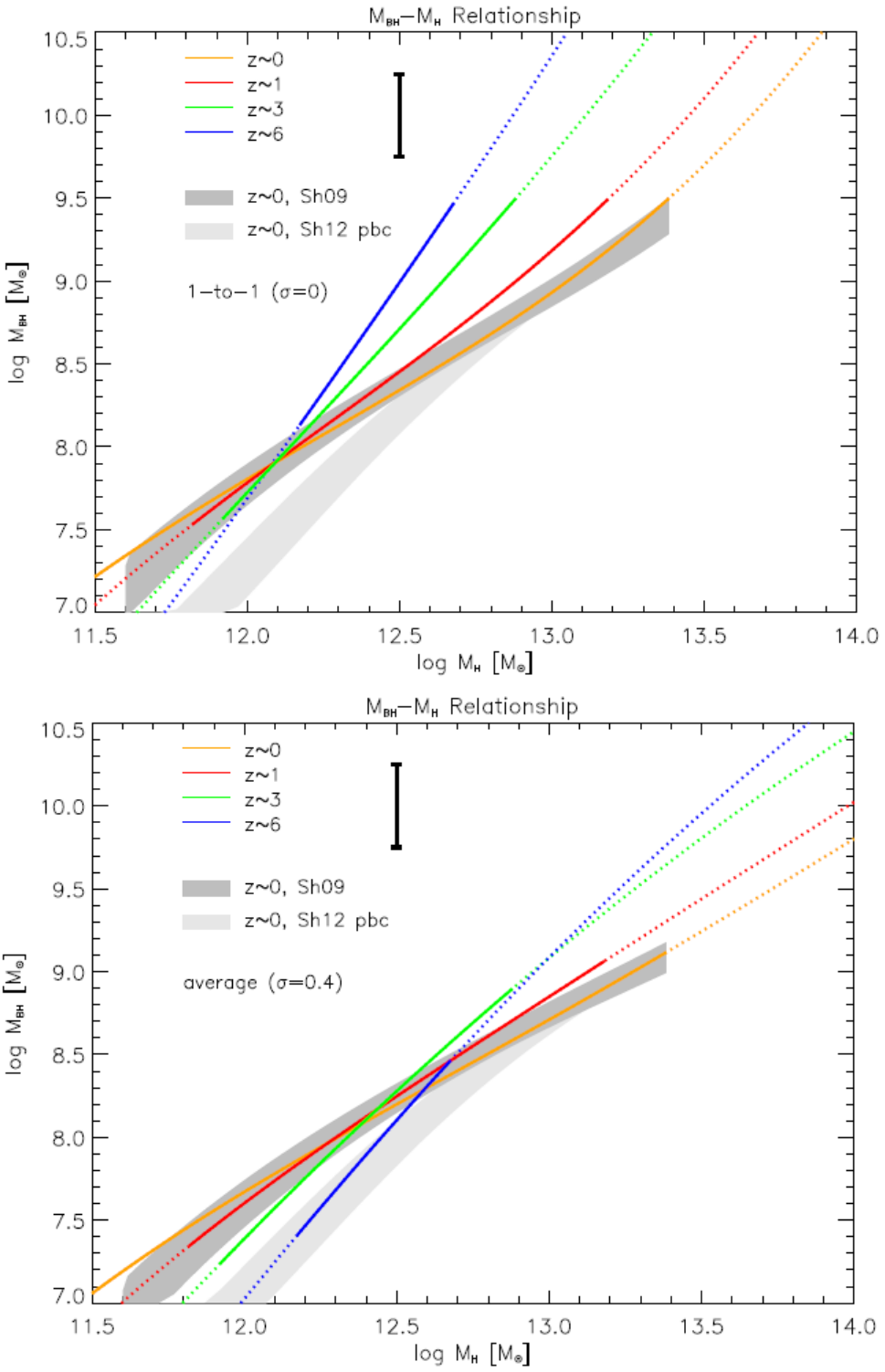

FIGURE 6.5: Relationship between BH mass $M_{\rm BH}$ and halo mass $M_{\rm H}$ from the abundance matching technique, at $z = 0$ (orange), 1 (red), 3 (green), and 6 (blue). Top panel shows the results when a one-to-one (i.e., no scatter) relationship $M_{\rm BH} - M_{\rm H}$ is assumed, while bottom panel shows the resulting average relationship when a Gaussian distribution in $M_{\rm BH}$ at given $M_{\rm H}$ with a scatter of 0.4 dex is assumed. In both panels the black errorbar illustrates the typical associated uncertainty, and the dotted lines highlight the ranges not covered by the current data on the BHMF. The grey shaded areas show the relations at $z = 0$ from the BHMF uncorrected (dark grey) and corrected (light grey) for pseudobulges by Shankar, Weinberg & Miralda-Escudé (2009) and Shankar et al. (2012), respectively.

when a Gaussian distribution in $M_{\rm BH}$ at given $M_{\rm H}$ with a scatter of 0.4 dex is adopted. The presence of scatter is particularly relevant at high redshift. Assuming a one-to-one relationship would yield, at $z \approx 6$, average BH masses $M_{\rm BH} \gtrsim 10^{10}\,M_{\odot}$ within halos of $M_{\rm H} \gtrsim 5 \times 10^{12}\,M_{\odot}$, much larger than at $z \approx 3$. This would imply a significant change in the physical mechanisms establishing the $M_{\rm BH} - M_{\rm H}$ relation over a relatively short timescale of ~ 1 Gyr. In the presence of scatter, instead, such large BH masses constitute only extreme instances, relative to much smaller average values ($M_{\rm BH} \approx 10^{9}\,M_{\odot}$), not very different from the lower redshift ones. In this scenario, such peculiar instances are precisely those picked by current observations at high-redshift, which are biased toward the more luminous AGNs powered by the more massive BHs. Thus, the one-to-one relationship offers a view of the observed properties at the given redshift, while the average relationship (with scatter) is helpful to provide a physical interpretation.

With scatter included, taking into account the considerable uncertainties, we can estimate that the logarithmic slope of the average relationship at $z \gtrsim 1$ is roughly $M_{\rm BH} \propto M_{\rm H}^{1-2}$, so encompassing the range suggested for AGN feedback processes (Silk & Rees 1998; Fabian 1999; King 2005; for recent reviews see King 2014; King & Pounds 2015). The average relationship can be considered unchanged, within the uncertainties, over the range $1 \lesssim z \lesssim 6$. Plainly, at $z = 0$ we find very good agreement with the relation inferred from the local BHMF by Shankar, Weinberg & Miralda-Escudé (2009).

In Fig. 6.6, we show the relationship between the AGN luminosity $L_{\rm AGN}$ and the halo mass $M_{\rm H}$, both with and without scatter. Concerning the scatter, the same comments of Fig. 6.5 apply. The flattening in the relation toward lower redshift is mainly driven by the evolution of the AGN LF, especially at the bright end. The one-to-one relationship, together with the duty cycle, is required to properly populate halos and derive the clustering properties of AGNs, which will be illustrated in Sec. 6.2.5.

6.2.2 Stellar vs. Halo properties

In Fig. 6.7, we show the relationship between the final stellar mass $M_{\star}$ and the halo mass $M_{\rm H}$, for different redshifts. The result at $z = 0$ is compared with the relationship inferred from the local SMF by Bernardi et al. (2013). We find a good agreement within the associated uncertainties. The $M_{\star} - M_{\rm H}$ relationship at given z can be described by a powerlaw with slope ~ 1 at the high-mass end, then steepening for halo masses $M_{\rm H} \lesssim 10^{12}\,M_{\odot}$. The presence of the 0.15 dex scatter does not appreciably affect the correlation. At $z \gtrsim 1$, the statistics of both stellar and halo masses are dominated by newly-created objects, so the mass evolution of the older population is irrelevant. From this perspective, the little - if no - evolution of the $M_{\star} - M_{\rm H}$ relationship can

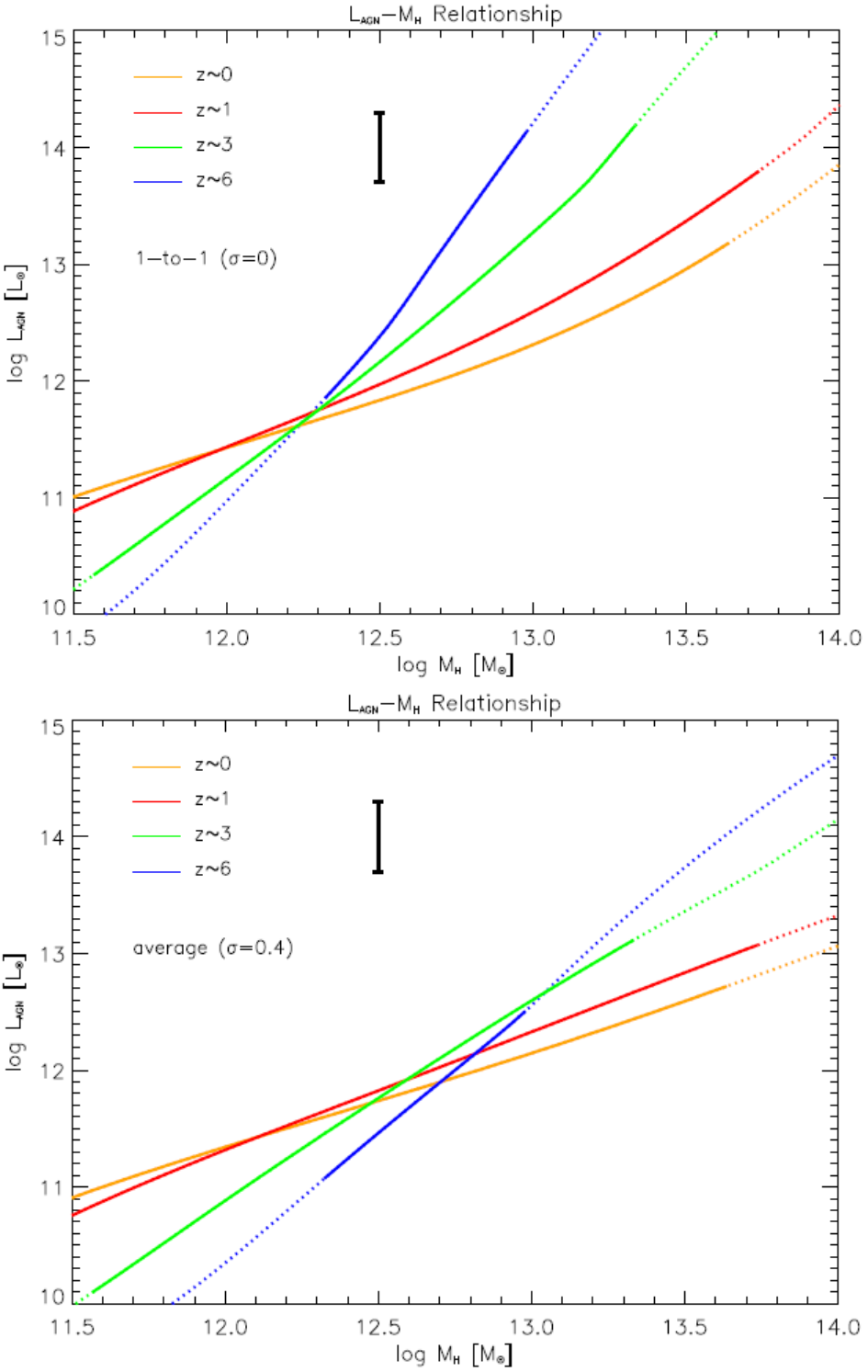

FIGURE 6.6: Relationship between bolometric AGN luminosity $L_{\rm AGN}$ and halo mass $M_{\rm H}$ from the abundance matching technique, at $z = 0$ (orange), 1 (red), 3 (green), and 6 (blue). Top panel shows the results when a one-to-one (i.e., no scatter) relationship $L_{\rm AGN} - M_{\rm H}$ is assumed, while bottom panel shows the resulting average relationship when a Gaussian distribution in $L_{\rm AGN}$ at given $M_{\rm H}$ with a scatter of 0.4 dex is assumed; in both panels, the black errorbar illustrates the typical associated uncertainty, and the dotted lines highlight the ranges not covered by the current data on the AGN LF.

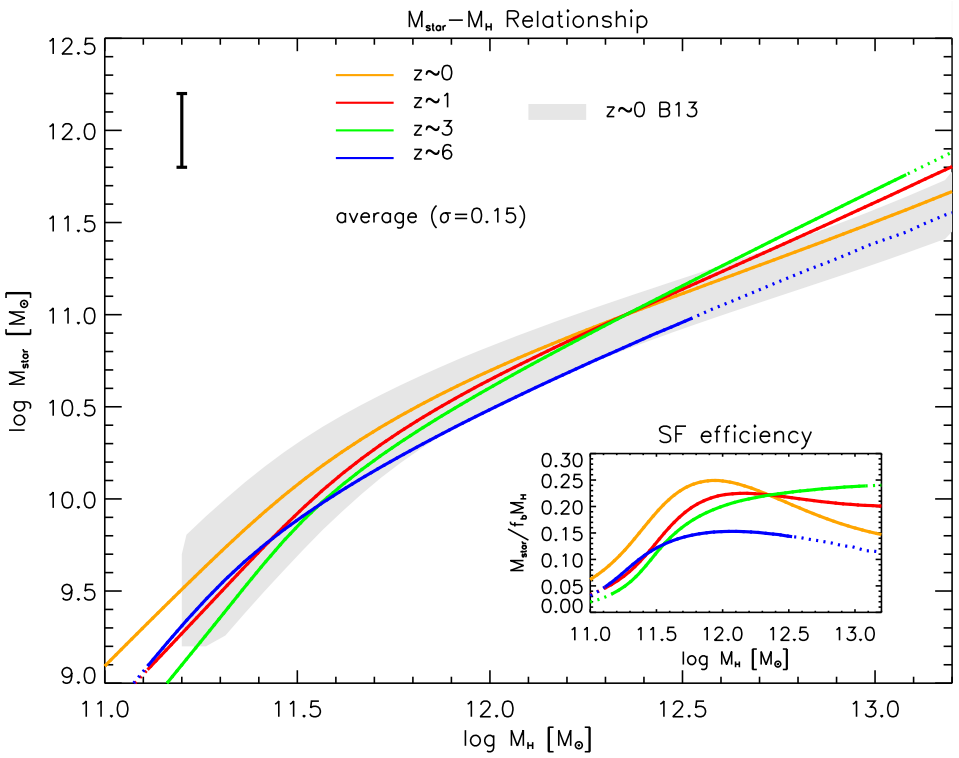

FIGURE 6.7: Relationship between stellar mass $M_{\rm star}$ and halo mass $M_{\rm H}$ from the abundance matching technique, at $z = 0$ (orange), 1 (red), 3 (green), and 6 (blue). The results refer to the average relationship when a Gaussian distribution in $M_\star$ at given $M_{\rm H}$ with a scatter of 0.15 dex is assumed (the one-to-one relationship is undistinguishable); the black errorbar illustrates the typical associated uncertainty, and the dotted lines highlight the ranges not covered by the current data on the SMF. The grey shaded area shows the relation at $z = 0$ obtained from the observed local SMF by Bernardi et al. (2013). The inset illustrates the efficiency $M_\star/f_{\rm b}\,M_{\rm H}$ for the conversion of the initial baryonic mass $f_{\rm b}\,M_{\rm H} = 0.2\,M_{\rm H}$ associated to the halo, into the final stellar mass $M_\star$.

be interpreted in the light of similar *in-situ* processes, regulating the star formation at different redshifts (Moster, Naab & White 2013). This may be seen more clearly in the inset, showing the star formation efficiency $M_\star/f_{\rm b}\,M_{\rm H}$, i.e., the efficiency of the conversion into stellar component of the original baryon content within the halo ($f_{\rm b}\,M_{\rm H}$), having adopted a cosmic initial baryon-to-DM ratio $f_{\rm b} = 0.2$. The star formation efficiency rises from values $\lesssim 10\%$ for halo masses $M_{\rm H} \lesssim 10^{11}\,M_\odot$ to a roughly constant values $\lesssim 25\%$ around halo masses $M_{\rm H} \approx 10^{12}\,M_\odot$. All in all, the star formation process in halos is highly inefficient.

From a physical point of view, this is usually interpreted in terms of competition between cooling and heating processes. In low-mass halos, the latter is provided by energy feedback from SN explosions. In massive halos, cooling rates are not significantly depressed by SN feedback, and the star formation can proceed at much higher levels, until the AGN attains enough power to abruptly quench it.

At $z \lesssim 1$ the interpretation is more complex, since the statistics of stars and halos are no longer dominated by newly-formed objects, and significant evolution in one of the two components may occur. Specifically, at high masses, the halo evolution dominates, and the $M_\star - M_\mathrm{H}$ relationship evolves shifting toward higher halo masses at almost constant stellar mass; contrariwise, at small masses, stellar mass evolution dominates over the halo one, and the relationship shifts upward, at almost constant halo mass.

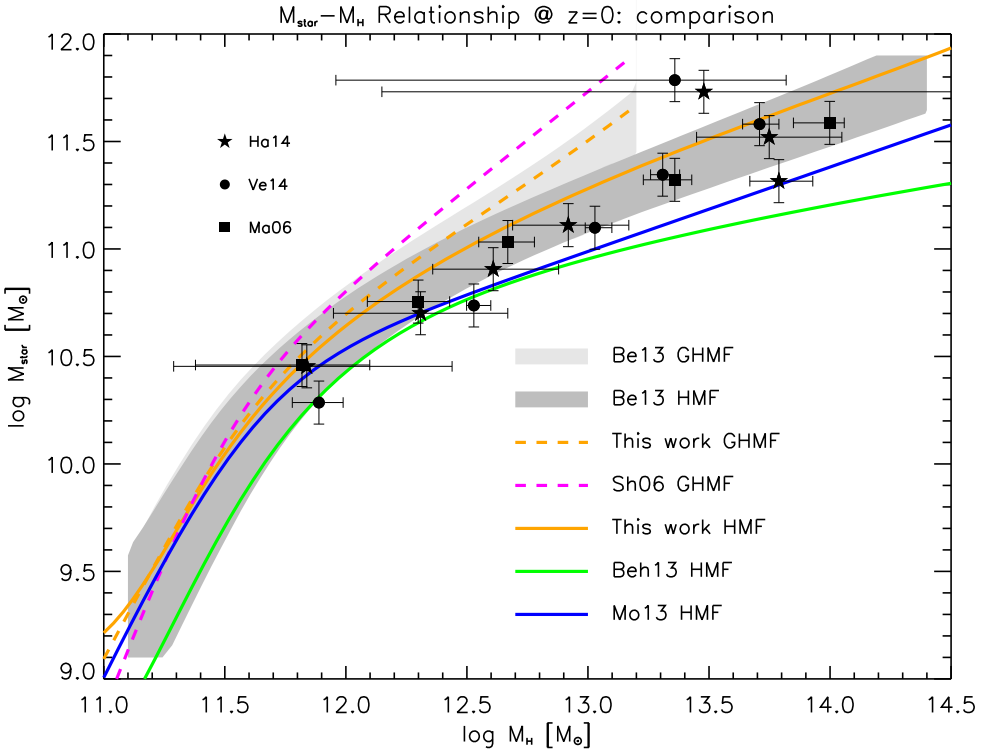

FIGURE 6.8: Relationship between stellar mass $M_\star$ and halo mass M_H from the abundance matching technique at $z = 0$ (orange line), when the GHMF (dashed) or the full HMF (solid) are adopted. The grey shaded areas show the relations at $z = 0$ obtained from the observed local SMF by Bernardi et al. (2013), matched with the galaxy (light grey) or the overall (dark grey) HMF. The green solid line refers to the result by Behroozi, Wechsler & Conroy (2013), the blue solid line to that by Moster, Naab & White (2013), and the magenta dashed line to that by Shankar et al. (2006). Data from gravitational lensing measurements in groups and clusters of galaxies are from Han et al. (2015, filled stars), Velander et al. (2014, filled circles), and Mandelbaum et al. (2006, filled squares).

In Fig. 6.8, we present a comparison of our $M_\star - M_\mathrm{H}$ relationship at $z = 0$ with literature determinations. Our result when the GHMF is exploited for the abundance matching (the same as in Fig. 6.7) can be directly compared with the determination by Shankar et al. (2006), based on the same abundance matching technique. The difference is mainly due to the dynamical $M_\star/L_{\star,K}$ ratio adopted by the authors to build up the SMF from the $K-$band LF. Our result, when the overall HMF is adopted, can be directly compared to the determinations based on the abundance matching by Behroozi, Wechsler & Conroy

(2013) and by Moster, Naab & White (2013). These are quite similar to ours at the low-mass end, while they are appreciably steeper at the high-mass end (see also Kravtsov, Vikhlinin & Meshscheryakov 2014; Shankar et al. 2014), where the Bernardi et al. (2013) SMF, adopted by us, contains relatively more objects.

The results based on the overall HMF can also be directly compared with the data from gravitational lensing measurements in groups and clusters of galaxies by Han et al. (2015), Velander et al. (2014), and Mandelbaum et al. (2006). The agreement is very nice. We note that, since gravitational lensing probes the mass projected along the line of sight, it is sensitive to the presence of groups and/or clusters surrounding the individual galactic halo.

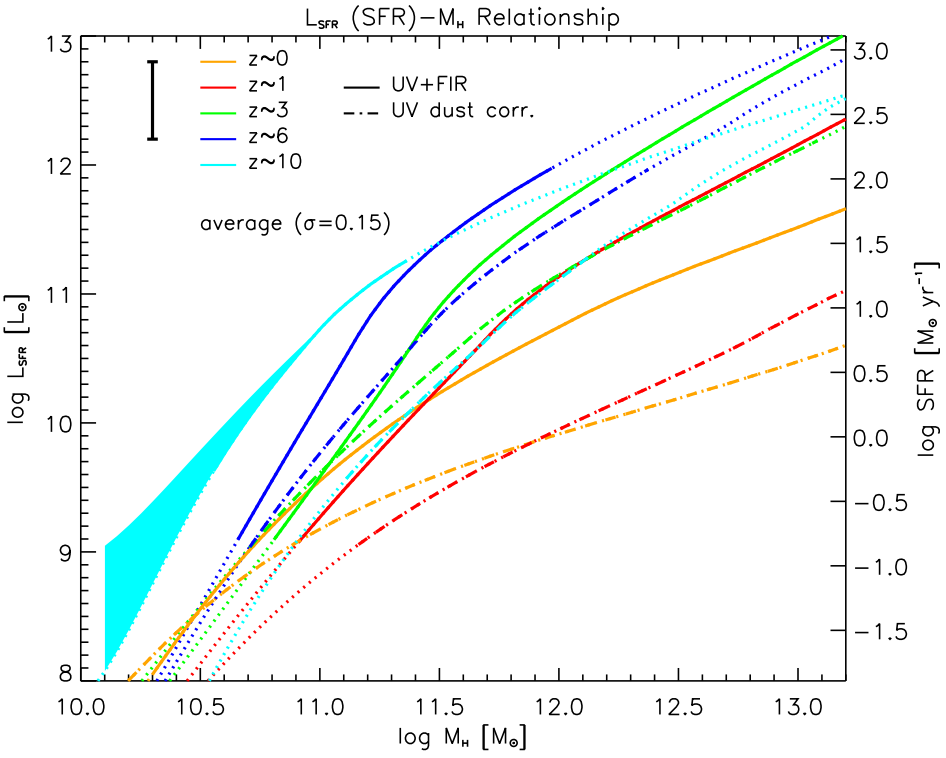

FIGURE 6.9: Average relationship between bolometric SFR-luminosity $L_{\rm SFR}$ and halo mass $M_{\rm H}$ from the abundance matching technique, at $z = 0$ (orange), 1 (red), 3 (green), 6 (blue), and 10 (cyan). A Gaussian distribution in $L_{\rm SFR}$ at given $M_{\rm H}$ with a scatter of 0.15 dex is assumed (the one-to-one relationship is undistinguishable). The black errorbar illustrates the typical associated uncertainty, and the dotted lines highlight the ranges not covered by the current data on the SFR-LF. Solid lines refer to the overall SFR-LF, while dot-dashed lines refers to dust-corrected UV LF only. At $z = 10$, the cyan shaded area for small halo masses illustrates the systematic uncertainty related to the faint-end slope of the SFR-LF.

In Fig. 6.9, we show the relationship between the luminosity $L_{\rm SFR}$ associated to the SFR and the halo mass $M_{\rm H}$, for different redshifts. The presence of the 0.15 dex scatter only marginally affects the average relationship. We show both the outcome based on the

overall SFR-LF, and the one based only on the dust-corrected UV LF. This has been determined by matching the GHMF with the SFR-LF of UV-selected galaxies corrected for dust extinction (see Sec. 5.2.3 and Fig. 5.14). It is evident from the figure that the typical UV data substantially underestimate the luminosity associated to the SFR. We stress once again that FIR data are crucial for an unbiased view of the star formation process.

In Fig. 6.9 we also plot the relationship expected at $z \approx 10$, although we caution that for $M_{\rm H} \lesssim 10^{11}\,M_{\odot}$ the relationship strongly depends on the faint-end slope of the SFR-LF. To illustrate the variance, we plot the relation corresponding to a faint-end slope -1.65 as a lower bound, and to -2 as an upper bound (Bouwens et al. 2014). The latter instance is required to keep the Universe ionized out to $z \lesssim 8.8$, corresponding to an electron-scattering optical depth $\tau_{\rm es} \lesssim 0.066$, as recently measured by the *Planck* Collaboration XIII et al. (2015). Our SFR-$M_{\rm H}$ relationship suggests that this value can be afforded by galaxies forming stars at rates $\gtrsim 10^{-2}\,M_{\odot}$ yr^{-1}, with UV magnitudes $M_{\rm UV} \gtrsim -13$, hosted within halos of masses $M_{\rm H} \gtrsim 10^{9}\,M_{\odot}$ (see also Cai et al. 2014).

6.2.3 SFR and sSFR vs. stellar mass and redshift

In Fig. 6.10, we plot the cosmic specific (sSFR), defined as:

$$\frac{\rho_{\rm SFR}}{\rho_{\star}} \equiv \frac{\int {\rm d}\log \dot{M}_{\star}\, \dot{M}_{\star}\, N(\log \dot{M}_{\star})}{\int {\rm d}\log M_{\star}\, M_{\star}\, N(\log M_{\star})}\ . \tag{6.17}$$

The resulting cosmic sSFR reflects the behavior for typical SFR and stellar masses at the knee of the corresponding distributions, and includes all galaxies, even the passively evolving ones (see also Madau & Dickinson 2014).

We report both the outcome based on the overall SFR-LF, and the one based on the dust-corrected UV LF only. It appears that the latter case underestimates the cosmic sSFR at any z (cf. Wilkins, Trentham & Hopkins 2008). We also illustrate the result by Madau & Dickinson (2014), which is similar to ours up to $z \sim 2$, and then approaches the UV-inferred result. As a matter of fact, their cosmic SFH at $z \gtrsim 3$ is based on UV data (see their Fig. 9).

It is worth noticing that the reported observational estimates refer to galaxy samples selected with different criteria. Specifically, at $z \gtrsim 3$, they mainly refer to UV-selected samples. This explains why they are better reproduced by our results for the UV dust-corrected case. On the other hand, at $z \lesssim 1.5$ they are mainly based on UV+near-IR data with ongoing star formation inferred from 24 μm or radio fluxes. In this redshift range, the sSFR estimated from the $\rho_{\rm SFR}/\rho_{\star}$ ratio lies below most of the data points, because

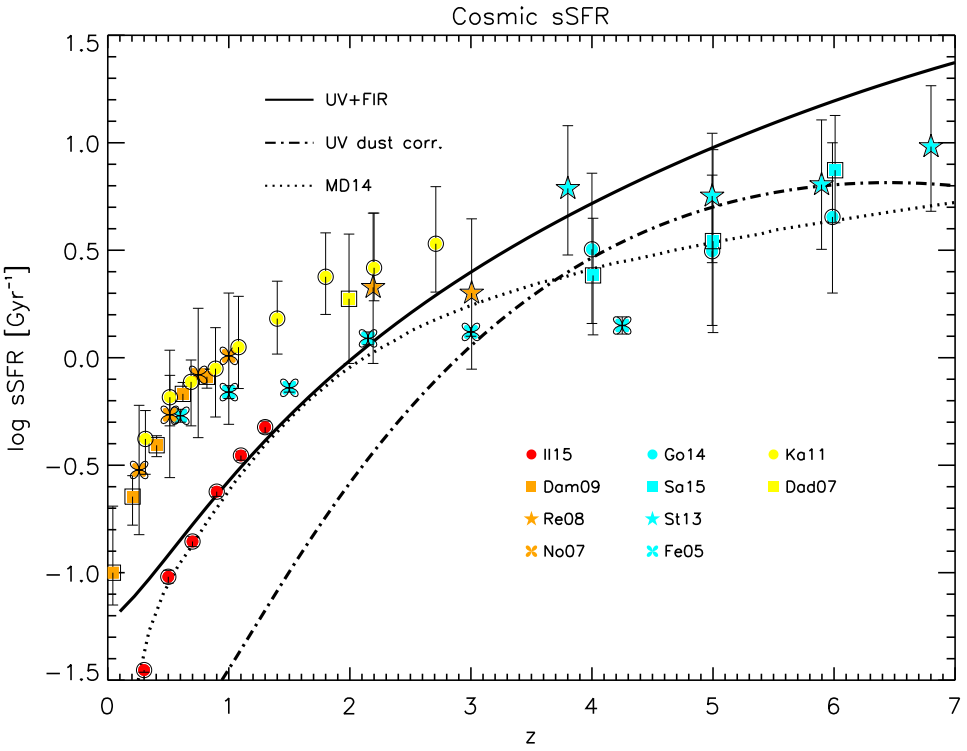

FIGURE 6.10: Cosmic sSFR as a function of redshift. The solid line refers to the overall SFR-LF, while the dot-dashed line to dust-corrected UV LF only. The dotted line illustrates the model by Madau & Dickinson (2014). IR data are from Ilbert et al. (2015, red circles), referring to $M_\star \gtrsim 10^{10.5}\,M_\odot$, Damen et al. (2009, orange squares), Reddy et al. (2008, orange stars), Noeske et al. (2007, orange clovers); UV data are from González et al. (2014, cyan circles), Salmon et al. (2015, cyan squares), Stark et al. (2013, cyan stars), Feulner et al. (2005, cyan clovers); radio data are from Karim et al. (2011, yellow circles), Daddi et al. (2007, yellow squares).

it includes an increasing fraction of objects in passive evolution, while observations refer to starforming galaxies only (see the discussion by Madau & Dickinson 2014). On the other hand, Ilbert et al. (2015) repost values of the sSFR closer to the ratio $\rho_{\rm SFR}/\rho_\star$, but a factor of $\sim 2-3$ lower than previous estimates in the literature. The authors attribute this difference to their more accurate treatment of the selection effects, leading to the inclusion of galaxies with lower sSFR, and to their more accurate statistics.

In Fig. 6.11, we show the relationship between the SFR and the stellar mass $M_\star$, at different redshifts; this is often referred to as the "main sequence" of starforming galaxies (e.g., Elbaz et al. 2011; Rodighiero et al. 2011). It is worth noticing that the outcome is obtained by matching the abundances of two observable quantities, the SFR-LF and the SMF (the halo mass is bypassed), including the star formation study cycle. From this point of view, the outcome is only mildly dependent on assumptions on the stellar lightcurve and the star formation timescales. As in Fig. 6.10, we report the outcome based on the overall SFR-LF, and the one based on dust-corrected UV LF only. We

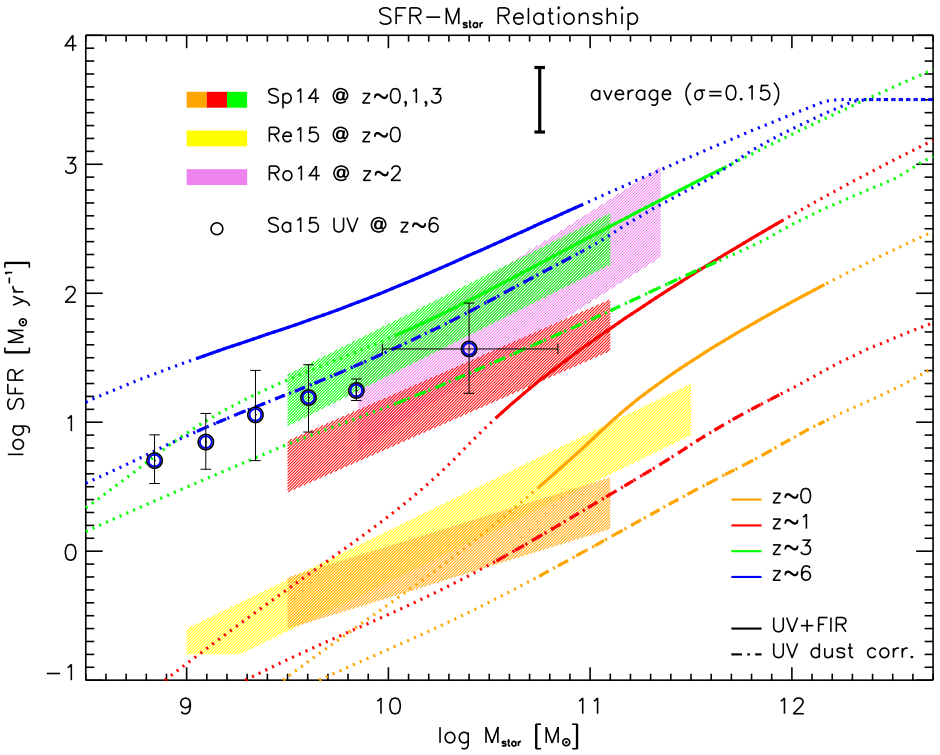

FIGURE 6.11: Relationship between the SFR and the final stellar mass from the abundance matching technique (the so called "main sequence" of starforming galaxies), at redshift z = 0 (orange), 1 (red), 3 (green), and 6 (blue). Results with and without scatter are almost undistinguishable. Solid lines refer to the overall SFR-LF, while dot-dashed lines to dust-corrected UV LF only. The black errorbar illustrates the typical associated uncertainty. The dotted lines highlight the ranges not covered by the current data on the SFR-LF and SMFs, or where the determination from the abundance matching technique is largely uncertain, due to the flatness of the SMF at the faint-end. Observational estimates are in the range $z \sim 0-3$ by Speagle et al. (2014, orange, red and green areas), at $z \sim 0$ by Renzini & Peng (2015, yellow area), at $z \sim 2$ by Rodighiero et al. (2014, violet area), and at $z \sim 6$ from UV determinations by Salmon et al. (2015, blue open circles).

compare the abundance matching results with the recent observational estimates by Rodighiero et al. (2014), Speagle et al. (2014), Salmon et al. (2015), and Renzini & Peng (2015), based on large samples of individual measurements of SFRs and stellar masses. We stress that, especially at $z \lesssim 1$, determinations of the main sequence by various authors differ, mainly due to the way galaxies are selected as being starforming (see the discussion by Renzini & Peng 2015). Further observations and analysis are needed to fully asses the main sequence, both regarding the overall normalization, and the slopes at the high and low mass end (that can even be different, see Whitaker et al. 2014).

At $z \lesssim 1$, our results from the abundance matching based on FIR+UV LFs well agree with the estimates by Rodighiero et al. (2014) and Speagle et al. (2014), based on

multiwavelength observations of galaxy samples. At $z \approx 6$, our result based on the UV LF is in excellent agreement with the data for UV-selected galaxies by Salmon et al. (2015). On the other hand, for $z \lesssim 1$, our results appear to be at variance with the observational determinations for $M_\star \lesssim 5 \times 10^{10} M_\odot$. However, in this mass range, the results from the abundance matching becomes loosely constraining, because of the large uncertainties introduced by the flatness of the SMF (cf. Fig. 5.10). This suggests that the SMF and the SFR-LF may not sample the same galaxy population at their respective faint ends. Nevertheless, at high stellar masses, the abundance matching technique is consistent with the current data, and actually extends the main sequence in a range where determinations from individual measurements are still scanty.

6.2.4 BH mass vs. Stellar mass

In Fig. 6.12, we illustrate the relationship between the BH mass and the stellar mass at different redshifts. The computation is performed through the abundance matching of the BHMF and the SMF obtained from the continuity equation, thus bypassing the halo mass. We show results both for the one-to-one case (top panel), and when a Gaussian scatter of 0.3 dex between $M_{\rm BH}$ and $M_\star$ is assumed (bottom panel). The presence of the scatter is increasingly relevant at higher redshift in biasing observations toward extreme values of the $M_{\rm BH}/M_\star$ ratio (shown in the inset). It is worth noticing that the evolution of the relationship, and hence of the $M_{\rm BH}/M_\star$ ratio, is quite small for $z \lesssim 3$, at variance with the claims by some authors (Peng 2007; Jahnke & Macciò 2011). This signals once again that the BH and stellar mass growth occurs *in parallel* by *in-situ* accretion and star formation processes.

Our results at $z = 0$ agree with the relations inferred from the abundance matching of the local determinations for the SMF by Bernardi et al. (2013) and for the BHMF by Shankar, Weinberg & Miralda-Escudé (2009). Our findings are in very good agreement with the individual determinations of BH and stellar masses based on dynamical measurements by Häring & Rix (2004). On the other hand, Kormendy & Ho (2013) propose a relation which is systematically higher by a factor ≈ 2.5. The Soltan argument would then imply an extremely high final SMBH mass density, and in turn a value $\epsilon \lesssim 0.02$ of the average efficiency during the slim-disc regime (see Sec. 5.1.3).

The *overmassive* BH at $z \sim 3.3$, with $M_{\rm BH} \sim 7 \times 10^9\, M_\odot$, hosted in a "regular" galaxy with $M_\star \sim 4 \times 10^{10}\, M_\odot$, claimed by Trakhtenbrot et al. (2015), lies well outside the relationships in Fig. 6.12. This powerful object is clearly extreme, as expected by the selection at high redshift. However, the analysis made by the authors must be taken with caution: indeed, it seems to give rather unreliable values of the Eddington ratio,

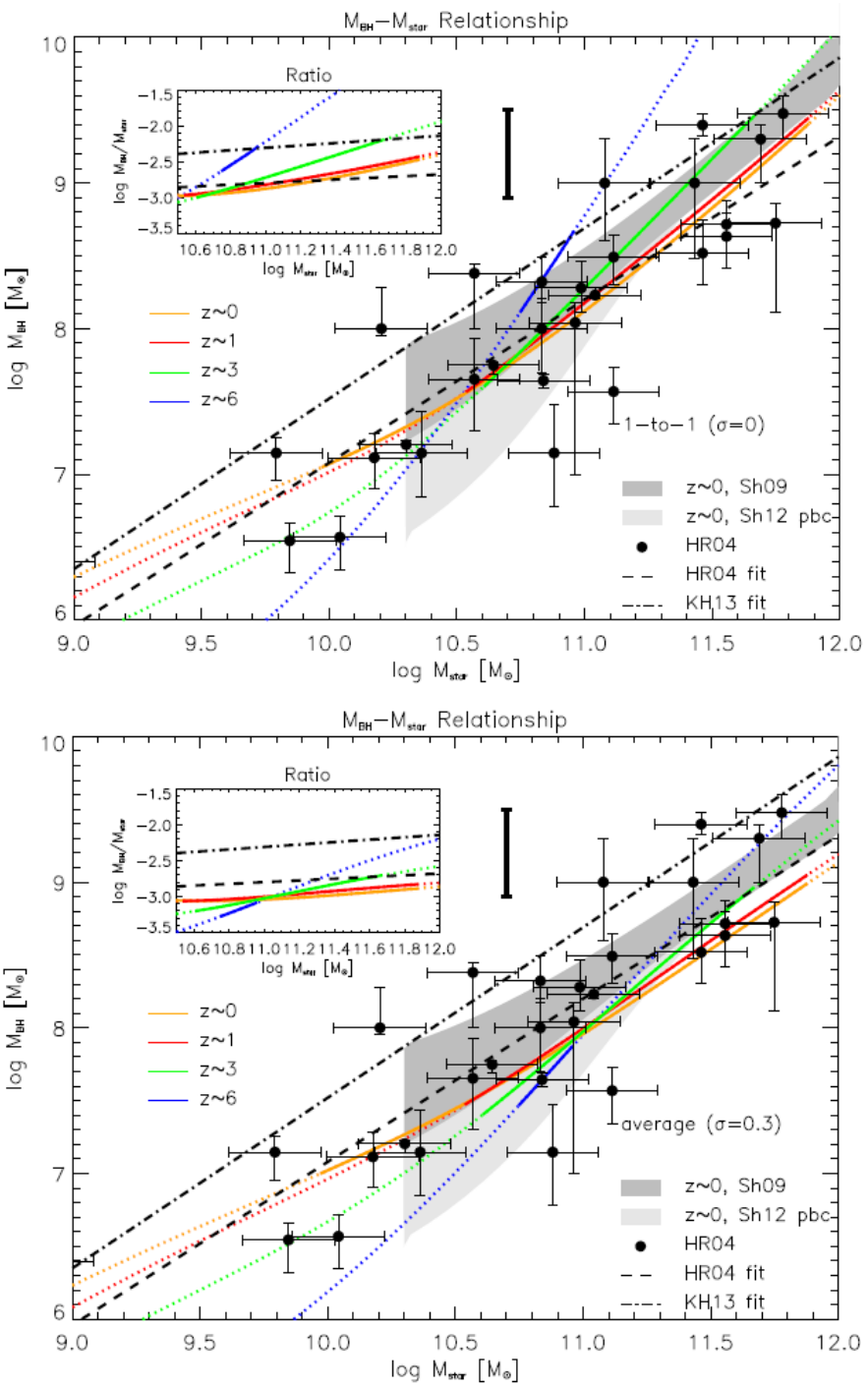

FIGURE 6.12: Relationship between BH mass $M_{\rm BH}$ and stellar mass $M_\star$ from the abundance matching technique, at $z = 0$ (orange), 1 (red), 3 (green), and 6 (blue). Top panel shows the results when a one-to-one (i.e., no scatter) relationship $M_{\rm BH} - M_{\rm H}$ is assumed, while bottom panel shows the resulting average relationship when a Gaussian distribution in $M_{\rm BH}$ at given $M_{\rm H}$ with a scatter of 0.3 dex is assumed; in both panels, the black errorbar illustrates the typical associated uncertainty, and the dotted lines highlight the ranges not covered by the current data of the BHMF and the SMF. The shaded areas show the relations at $z = 0$ obtained from the matching between the SMF and the BHMF, uncorrected (dark grey) and corrected (light grey) for pseudobulges. Data points are from the compilation by Häring & Rix (2004), with the dashed line representing their best-fit relation; the relation proposed by Kormendy & Ho (2013) is also shown as a dot-dashed line. The insets illustrate the corresponding $M_{\rm BH}/M_\star$ ratio as a function of $M_\star$.

$\lambda_{\rm Edd} \sim 0.02$, which cannot justify the high SFR ($\sim 400\,M_{\odot}$ yr^{-1}) estimated on the basis of FIR and sub-mm observations. The problem may stem from the single epoch estimators used to determine the BH mass, which could be influenced by the presence of observed outflows (see Sec. 2.8.6). On the other hand, assuming a value $\lambda_{\rm Edd} \lesssim 1$, characteristic of a slim (or even thin) disc, during the optically bright phase, we can recover $M_{\rm BH} \sim 10^8\,M_{\odot}$ for this object, consistent with the $M_{\rm BH} - M_{\star}$ relationships. Such values of the Eddington ratio have already been reported for similar objects at high redshift (De Rosa et al. 2014; Wu et al. 2015): they are more in line with our scenario, and strengthen our point. However, further careful investigations are needed to clarify this issue.

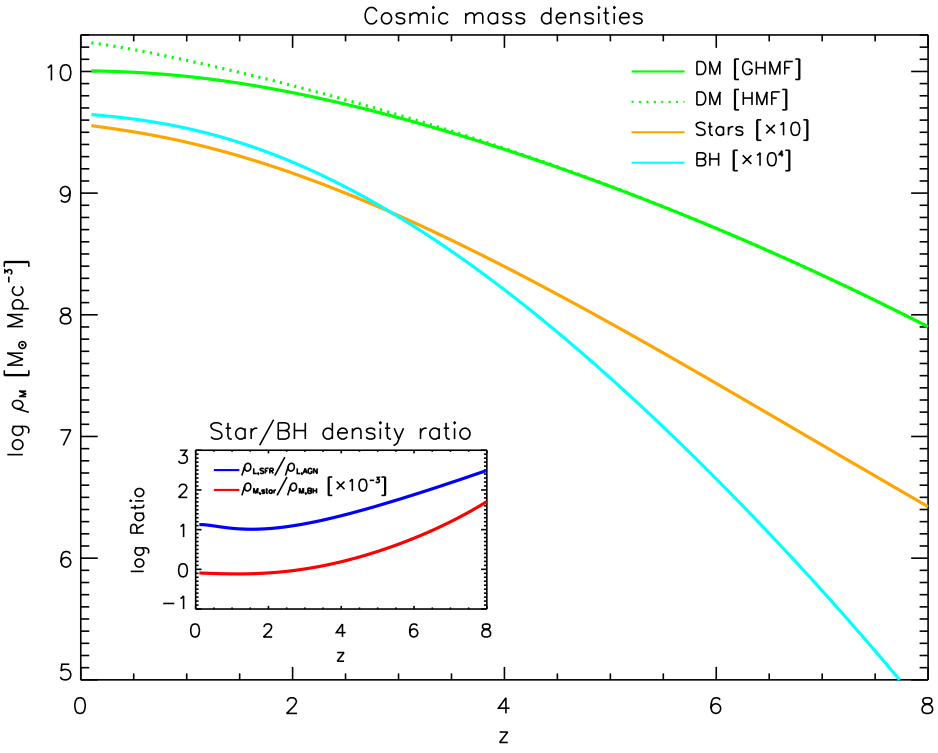

FIGURE 6.13: The evolution with z of the mass density in the overall DM halo population (dotted green line), in galactic DM halos (solid green line), in stars (solid orange line), and in BHs (solid cyan line). In the inset, the luminosity density ratio $\rho_{L_{\rm SFR}}/\rho_{L_{\rm AGN}}$ (blue line) and the mass density ratio $\rho_{M_{\star}}/\rho_{M_{\rm BH}}$ (red line) are illustrated.

In Fig. 6.13, we illustrate the evolution with z of the mass density in DM halos, stars, and BHs. The stellar mass density closely mirrors that of galactic DM halos, because the star to DM mass ratio (i.e., the star formation efficiency) stays roughly constant with z for typical galaxies at the knee of the SMF (see Fig. 6.7). On the other hand, for $z \lesssim 2$ the stellar mass density progressively differs from that of the overall halo population (including galaxy groups/clusters). Once again, this strengthens the point that star formation at high redshift occurs via *in-situ* processes within the central regions of

galactic halos. The stellar mass density is a factor $\sim 30-50$ lower than the galactic halo mass density, reflecting the inefficiency of galaxy formation due to feedback processes, as discussed in Sec. 6.2.2. The BH mass density has a considerably different shape, that toward higher z progressively steepens relative to the galactic halo and stellar mass density. This is due to two effects:

1. The number density of halos able to host massive BHs rapidly declines toward higher z;
2. The time needed to grow massive BHs becomes comparable with the age of the Universe, so making evident the delay of $\sim 10^8$ yr between the BH and stellar formation.

In the inset of Fig. 6.13, we show that the observed density ratio between the SFR and the AGN luminosity attains a minimum at $z \sim 1.5$, and it stays almost constant toward lower redshift. This happens because both luminosity densities decline in parallel (cf. insets in Fig. 5.1 and Fig. 5.9). The same considerations also applies for the trend of the corresponding mass density ratio.

6.2.5 Clustering

The clustering properties of QSOs/AGNs are an other important tool to investigate how the AGN activity is triggered and fueled, and to obtain information about the coevolution of AGNs and galaxies. Moreover, the connection between the SMBHs and the DM halos in which they reside can be further studied via clustering measurements, in the framework of the CDM structure formation scenario. Indeed, under the assumed cosmology, the bias of AGNs can be related to the typical mass of their host DM halos (Sheth & Tormen 1999; Sheth, Mo & Tormen 2001; Tinker et al. 2005, 2010; Allevato et al. 2011, 2014).

In Fig. 6.14, we show the luminosity- and BH mass-averaged AGN biases as a function of redshift. They have been computed as follows: we start from the linear halo bias model $b(M_{\rm H}, z)$ including excursion set peak prescriptions (Lapi & Danese 2014) for halos of mass $M_{\rm H}$ at redshift z (see also Sheth, Mo & Tormen 2001). Then, we associate to each halo mass $M_{\rm H}$ an AGN of luminosity $L_{\rm AGN}$, as prescribed according to the $L_{\rm AGN} - M_{\rm H}$ one-to-one relationship discussed in Sec. 6.2.1 and shown in the top panel of Fig 6.6. Finally, we compute the luminosity-weighted bias as a function of z as:

$$\bar{b}(z) = \frac{\int_{\log L_{\rm min}}^{\infty} {\rm d}\log L_{\rm AGN}\, N(\log L_{\rm AGN}, z)\, b(L_{\rm AGN}, z)}{\int_{\log L_{\rm min}}^{\infty} {\rm d}\log L_{\rm AGN}\, N(\log L_{\rm AGN}, z)} \ , \tag{6.18}$$

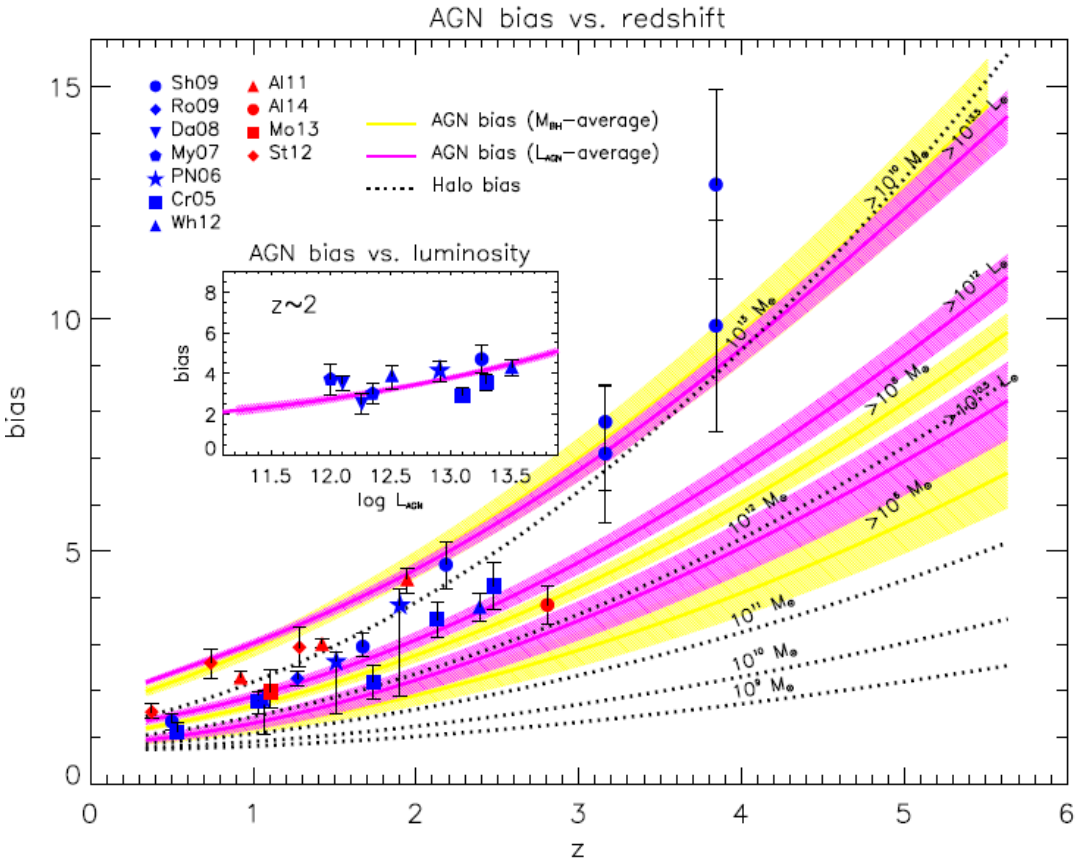

FIGURE 6.14: The AGN bias as a function of z. Results from the abundance matching technique are illustrated by magenta ($L_{\rm AGN}$-average bias) and yellow ($M_{\rm BH}$-average bias) continuous lines, with the hatched areas showing the associated uncertainties; specifically, the magenta curves refer to different AGN luminosities $L_{\rm AGN} > 10^{10.5}$, 10^{12}, and $10^{13.5}\,L_\odot$, and the yellow curves to different BH masses $M_{\rm BH} > 10^6$, 10^8, and $10^{10}\,M_\odot$ as labeled. For comparison, black dotted lines illustrate the halo bias referring to different halo masses from 10^9 to $10^{13}\,M_\odot$, as labeled. The inset shows the AGN bias from the abundance matching technique at $z = 2$ as a function of $L_{\rm AGN}$. Optical data are from Shen et al. (2009, blue circles), Ross et al. (2009, blue diamonds), da Ângela et al. (2008, blue reversed triangles), Myers et al. (2007, blue pentagons), Porciani & Norberg (2006, blue stars), Croom et al. (2005, blue squares), White et al. (2012, blue triangles); X-ray data are from Allevato et al. (2011, red triangles), Allevato et al. (2014, red circles), Mountrichas et al. (2013, red squares), Starikova et al. (2012, red diamonds).

where $L_{\rm min}$ is a minimum bolometric luminosity. The same procedure can be followed to obtain the $M_{\rm BH}$-averaged bias, through the one-to-one $M_{\rm BH} - M_{\rm H}$ relation and the average over the BHMF.

The resulting bias as a function of z, in Fig. 6.14, reproduces very well the observational data points from various optical and X-ray surveys. It is worth noticing that, while at $z \gtrsim 2$ the X-ray selected AGNs appear to be less clustered than the optical quasars, the opposite holds true at $z \lesssim 2$. This fact is somewhat puzzling, since X-ray AGNs feature generally lower bolometric luminosities, and is often interpreted in terms of a different

accretion mode becoming dominant at low z (e.g., sporadic reactivation episodes in place of continuous accretion, see discussion by Allevato et al. 2011, 2014).

However, direct comparison with these studies are difficult, because the selection of the reported datasets are diverse, and one has to consider the limitations of the various surveys used to obtain the bias, namely the area coverage and the limiting flux. These two elements determine the volume number density effectively sampled by the survey, which in turn directly impacts the possibility to yield accurate clustering measurements. The error bars reflect the difficulty arising when the sample size is not large enough, in particular at high redshift, where the sparceness of the objects increases.

Large and statistically complete samples over a wide area are needed for clustering measurements. Since the correlation signal has to be probed on very huge spatial volumes, the analysis of AGN clustering has become reliable only with the large-scale surveys, such as the SDSS (Myers et al. 2007; Shen et al. 2009; Ross et al. 2009), the 2dF QSO redshift survey (2QZ; Croom et al. 2005; Porciani & Norberg 2006), and the 2dF-Sloan Digital Sky Survey luminous red galaxy and QSO Survey (2SLAQ, an extension of the 2ZQ survey to fainter magnitudes; Richards et al. 2005; da Ângela et al. 2008), with areas of the order of thousands of deg^2. The last two surveys are characterized by a higher number density with respect to the SDSS main quasar sample, because they can reach a fainter portion of the quasar LF. In general, the optical surveys typically select quasars with luminosities $L_{\rm AGN} \gtrsim 10^{12} L_{\odot}$, while the X-ray data refer to AGNs with lower luminosity ($L_{\rm AGN} \gtrsim 10^{11} L_{\odot}$) and with a significant fraction of obscured sources with respect to the optical ones. Thanks to *Chandra* and *XMM-Newton*, large samples of X-ray AGNs are available, and clustering measurements of dimmer sources have become possible with a precision comparable, or even better, to that achievable with optical surveys. For example, data from the Baryon Oscillation Spectroscopic Survey (BOSS; White et al. 2012) can reach sensitivities almost 2 mag deeper than the SDSS at $2.2 < z < 3.5$. On the other hand, even though X-ray AGN samples are deeper, the surveyed areas are smaller, only of the order of tens to hundreds deg^2, or even smaller, such as the Cosmic Evolution Survey (COSMOS; Scoville et al. 2007; Mountrichas et al. 2013; Allevato et al. 2014), which has an area of 2.13 deg^2.

As a reference, in Fig. 6.14, the halo bias $b(M_{\rm H}, z)$ for various $M_{\rm H}$ is also shown. Typical host halos feature $M_{\rm H} \gtrsim 10^{12}\, M_{\odot}$, with a clear tendency for more massive halos to host more luminous AGNs and more massive BHs. In the inset, it can be seen that even the mild trend of the bias with luminosity at $z \approx 2$, claimed from optical surveys, is reproduced. On the other hand, the dependence on the luminosity is expected to significantly increase at $z \gtrsim 4$.

We stress that the clustering properties constitute a byproduct of our approach, and that the comparison with observations validate our results on the BHMF and the duty cycle (see also Shankar, Weinberg & Shen 2010). Note that past studies (Martini & Weinberg 2001) have instead exploited the clustering properties to constrain the AGN duty cycle. In comparing with previous works related to the AGN bias (e.g., White, Martini & Cohn 2008; Hopkins, Richards & Hernquist 2007; Wyithe & Loeb 2009; Bonoli et al. 2010; Shankar, Weinberg & Shen 2010), a few remarks are in order:

1. We stress that our adoption of the GHMF, in place of the routinely-used HMF, appreciably improves the agreement with observations of the bias for luminous AGNs/massive BHs at $z \gtrsim 3$;

2. We confirm that values of $\lambda_{\rm Edd} \gtrsim 3$ at $z \gtrsim 3$, implying a quite rapid growth of the BH during the ascending portion of the AGN lightcurve, are also required to meet the observational constraints;

3. We find that the weak dependence of the bias on luminosity at $z \sim 2$ is rather insensitive to the presence of the descending portion of the AGN lightcurve, that we recall is instead indicated in luminous objects by the observed fraction of star-forming hosts in optically-selected quasars (see Sec. 4.5.2).

In Fig. 6.15, we show the galaxy bias, both luminosity (or SFR)-averaged and stellar mass-averaged, for different values of minimum SFR or $M_\star$. These quantities have been computed following the same procedure for the AGN bias described above. As a reference, we also report the halo bias for different halo masses.

The bias computed from the abundance matching reproduces very well the determination at different redshifts for various populations of objects. In particular, UV-selected objects like LBGs and Lyman-α emitters feature low stellar masses ($M_\star \lesssim 10^9\,M_\odot$) and SFRs less than a few $M_\odot$ yr^{-1}, while FIR-selected objects are associated to much more violent SFRs ($\dot{M}_\star \gtrsim 10^2\,M_\odot$ yr^{-1}), and constitute the progenitors of massive galaxies with final stellar content $M_\star \gtrsim 10^{11}\,M_\odot$.

6.2.6 Analytic fits to abundance matching relationships

In this section, we provide analytic fits to the relationships derived from the abundance matching technique. To fit a relation of the form $Y - M$, we adopt a double powerlaw shape:

$$Y(M,z) = N(z) \times \left\{ \left[\frac{M}{M_b(z)} \right]^{\alpha(z)} + \left[\frac{M}{M_b(z)} \right]^{\omega(z)} \right\}^{\theta} , \qquad (6.19)$$

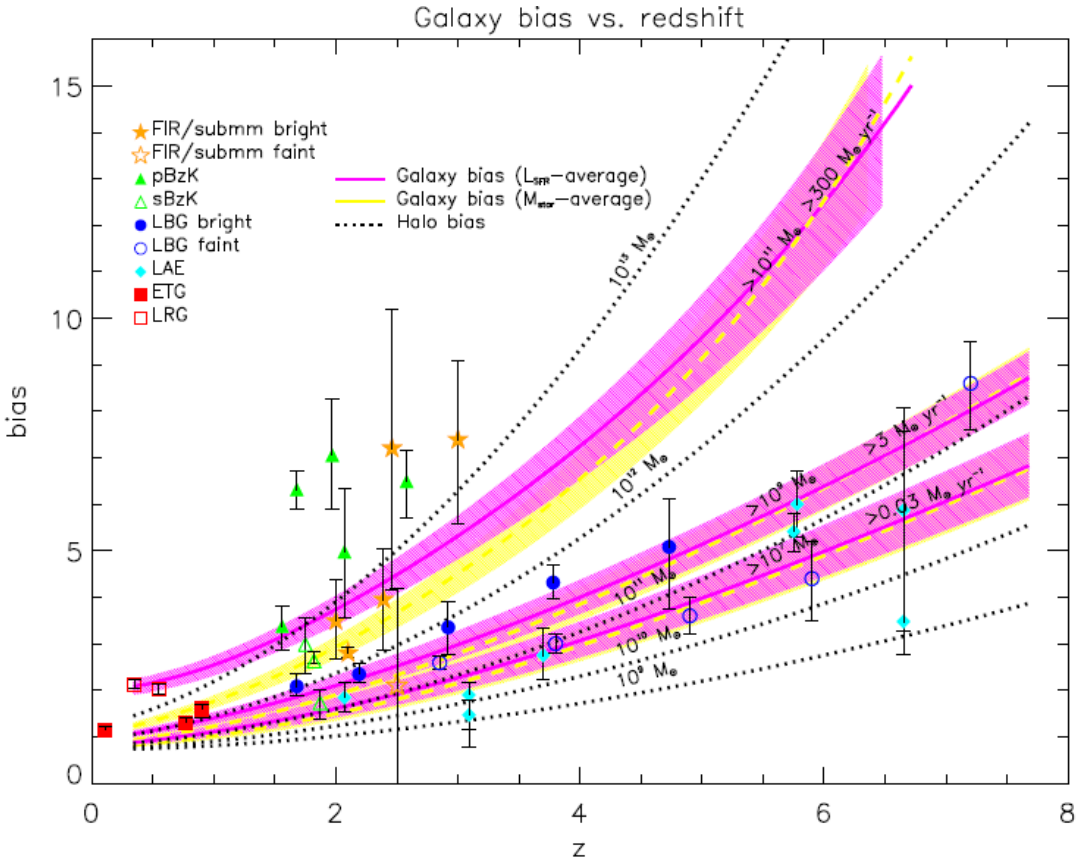

FIGURE 6.15: The galaxy bias as a function of z. Results from the abundance matching technique are illustrated by magenta ($L_{\rm SFR}$-average bias) and yellow ($M_\star$-average bias) continuous lines, with the hatched areas showing the associated uncertainty; specifically, the magenta curves refer to different SFRs$>$ 0.03, 3, and 300 $M_\odot$ yr^{-1} and the yellow curves to different stellar masses $M_\star > 10^7$, 10^9, and $10^{11}\,M_\odot$, as labeled. for comparison, black dotted lines illustrate the halo bias referring to different halo masses from 10^9 to $10^{13}\,M_\odot$, as labeled. Data for FIR/sub-mm bright galaxies (filled orange stars) are from Webb et al. (2003), Blain et al. (2004), Weiß et al. (2009), Hickox et al. (2012), Bianchini et al. (2015), for FIR/sub-mm faint galaxies (orange empty stars) are from Ono et al. (2014), for passive BzK galaxies (green filled triangles) are from Grazian et al. (2006), Quadri et al. (2007), Blanc et al. (2008), Furusawa et al. (2011), Lin et al. (2012), for starforming BzK galaxies (green empty triangles) are from Hayashi et al. (2007), Blanc et al. (2008), Furusawa et al. (2011), for bright LBGs (blue filled circles) are from Ouchi et al. (2004), Adelberger et al. (2005), Lee et al. (2006), Overzier et al. (2006), for faint LBGs (blue empty circles) are from Bielby et al. (2013), Barone-Nugent et al. (2014), for Lyman-α Emitters (cyan diamonds) are from Gawiser et al. (2007), Ouchi et al. (2010), Guaita et al. (2010), for passively-evolving ETGs (red filled squares) are from Hawkins et al. (2003), Guzzo et al. (2008), Georgakakis et al. (2014), for Luminous Red Galaxies (red empty squares) are from Tegmark et al. (2006), Ross et al. (2007).

with $\theta = -1$ for a convex or $\theta = +1$ for a concave relationship.

The normalization $\log N(z)$, the mass of the break $\log M_b(z)$, and the characteristic slopes $\alpha(z)$ and $\omega(z)$ evolve with the redshift according to the same parametrization:

$$p(z) = p_0 + k_{p1}\,\chi + k_{p2}\,\chi^2 + k_{p3}\,\chi^3 \tag{6.20}$$

with

$$\chi = \log\left(\frac{1+z}{1+z_0}\right) \tag{6.21}$$

and $z_0 = 0.1$. The parameter values are reported in Table 6.2.

These expressions can be exploited to interpolate and/or extrapolate the relationships all the way from $z \approx 0$ to $z \approx 6$. Interpolation is helpful to produce mock galaxy and AGN/BH catalogs, which can be used to compute gravitational lensing effects, to investigate clustering properties, to gauge sub-grid physics in numerical simulations, and to design observational setups. Moreover, extrapolation is particularly helpful to obtain specific predictions in redshift and mass ranges not currently probed by the data, but within the reach of upcoming experiments.

Function	$\log N_0$	k_{N1}	k_{N2}	k_{N3}	$\log M_{b0}$	k_{M1}	k_{M2}	k_{M3}	α_0	$k_{\alpha1}$	$k_{\alpha2}$	$k_{\alpha3}$	ω_0	$k_{\omega1}$	$k_{\omega2}$	$k_{\omega3}$
$Y = N \times \left[\left(\frac{X}{M_b}\right)^{\alpha} + \left(\frac{X}{M_b}\right)^{\omega}\right]^{-1}$																
$L_{\rm AGN} - M_{\rm H}$ (1to1)	12.25	-1.90	1.45	1.10	12.30	0.00	0.00	0.00	-1.65	1.20	-4.50	0.60	-0.65	-3.50	-0.40	0.80
$L_{\rm AGN} - M_{\rm H}$ (aver.)	12.33	-2.00	2.70	-1.30	12.50	0.00	0.00	0.00	-1.60	0.00	-3.30	1.30	-0.50	-2.10	-1.60	2.60
$L_{\rm SFR} - M_{\rm H}$ (aver.)	11.25	0.00	0.00	0.00	12.20	-1.20	0.00	0.00	-1.30	-3.00	-0.50	1.20	-0.50	-1.50	0.00	1.50
$M_{\rm BH} - M_{\rm H}$ (1to1)	8.00	-0.40	0.70	-0.80	11.90	0.00	0.00	0.00	-1.10	-0.80	-1.50	0.10	-1.10	-0.80	-1.50	0.10
$M_{\rm BH} - M_{\rm H}$ (aver.)	8.20	-0.20	0.80	-1.50	12.20	0.00	0.00	0.00	-1.40	-1.30	-0.30	0.10	-0.80	-0.40	-1.10	0.10
$M_\star - M_{\rm H}$ (aver.)	10.40	-0.80	0.80	-0.20	11.50	0.00	0.00	0.00	-2.20	-1.90	-1.60	4.70	-0.75	-0.30	-1.80	2.60
SFR$-M_\star$ (aver.)	1.90	0.00	0.00	0.00	11.60	-1.90	-2.50	1.70	-1.60	0.00	1.50	-0.20	-0.50	-1.70	3.50	-2.00
$Y = N \times \left[\left(\frac{X}{M_b}\right)^{\alpha} + \left(\frac{X}{M_b}\right)^{\omega}\right]$																
$M_{\rm BH} - M_\star$ (1to1)	7.33	0.10	-0.70	1.00	10.60	0.00	0.00	0.00	1.60	0.00	-0.20	2.80	0.60	0.40	-0.40	2.20
$M_{\rm BH} - M_\star$ (aver.)	7.15	0.00	-0.60	0.00	10.50	0.00	0.00	0.00	1.30	0.30	0.00	0.90	0.60	0.20	0.40	0.90

[a]

TABLE 6.2: Fits to Abundance Matching Results

[a]Typical tolerance on the parameters is less than 10%. See Sec. 6.2.6 for details on the redshift evolution of the parameters.

Chapter 7

Summary and Conclusions

In this thesis, we have employed different statistical tools to investigate the coevolution of SMBHs, their host galaxies, and their galactic DM halos. We have started by providing an overview of the main topics of interest, and by introducing the quantities useful for our discussions.

Chapter 2 has been dedicated to the relevant characteristics of SMBHs, the basic theory of BH growth, and some recent observational results.

In Chapter 3, we have presented the basic issues concerning the star formation process in galaxies, paying specific attention to the important role of the dust, and to the complementarity of UV and FIR data.

Equipped with this background, we have organized our work in three main parts.

In the first part (Chapter 4), we have exploited the recent wide samples of FIR-selected galaxies followed-up in X rays, and of X-ray/optically selected AGNs followed-up in the FIR band, at $z \gtrsim 1.5$, to infer the following scenario for the coevolution of SMBHs and massive host galaxies ($M_\star \gtrsim 10^{10.5}\,M_\odot$):

- The SFR in the host galaxy remains approximately constant for a time:

$$\tau_{\rm burst} \approx 0.5 - 1\,{\rm Gyr}\ , \tag{7.1}$$

  and then abruptly declines, because of the QSO feedback, on a very short time scale:

$$\tau_{\rm SFR} \approx \frac{\tau_{\rm ef}}{2} \approx \frac{\tau_{\rm burst}}{30}\ ; \tag{7.2}$$

- Part of the central ISM loses angular momentum and reaches the circumnuclear regions at a rate proportional to the SFR;

- The early accretion onto a small seed BH, $M_{\rm seed} \sim 10^{2-3}\,M_{\odot}$, occurs in a self-regulated regime with efficiency $\epsilon \approx 0.03$ and radiative power that can be just above the Eddington limit ($\lambda_{\rm Edd} \sim 4$), especially at the highest redshifts. Thus, the BH grows exponentially with an e-folding time:

$$\tau_{\rm ef} \approx 10^7\,{\rm yr}\ ; \tag{7.3}$$

- During the growth of the SMBH, a reservoir forms, with a size of $20-100$ pc, close to the influence radius of the SMBH at the end of its evolution; the reservoir mass is as large as the final SMBH mass, ready to be delivered in the last $2-3\,\tau_{\rm ef}$;

- In the case of massive BHs, the QSO feedback at the peak of the AGN lightcurve exceeds the stellar feedback, and is able to remove the ISM, stopping the star formation and the fueling of the reservoir; if the latter has retained enough gas, a phase of supply-limited accretion follows, with luminosity (and Eddington ratio) exponentially declining over a timescale:

$$\tau_D \approx 3\,\tau_{\rm ef}\ . \tag{7.4}$$

Interestingly, the time evolutions of both the host galaxy and the AGN can be characterized in terms of number of e-folding times; the coevolution takes $\sim 10-15\,\tau_{\rm ef}$ of the BH growth (see Fig. 4.7 and Fig. 4.12).

Our renditions of the SFR-LF for the host galaxies and of the bolometric AGN LF, based on recent data at different redshifts (see Fig. 2.4 and Fig. 3.6), have been used to compute the FIR and X-ray detected fractions. The results have been then compared with:

1. the available statistics on X-ray detections of FIR-selected galaxies (see Fig. 4.3, Fig. 4.4, Fig. 4.5, Fig. 4.6);

2. the available statistics on FIR detections of X-ray/optically selected AGNs (see Fig. 4.8, Fig. 4.10, Fig. 4.11, and Fig. 4.13);

3. the statistics of $M_{\rm BH}/M_{\star}$ ratio in FIR-selected galaxies and optically selected QSOs (see Sec. 4.6.1).

The time evolution of the SFR and of the BH accretion (namely, the timescales of the lightcurves described in Sec. 4.2), and the relation between them, have been fixed in order to comply with the current FIR and X-ray data. Moreover, we have considered the evolution of less massive galaxies ($M_{\star} \lesssim 10^{10}\,M_{\odot}$). In these objects, the declining

phase is almost absent, and the star formation may proceed for longer times, regulated by SN feedback, as indicated by longstanding data on stellar populations and chemical abundances (see Sec. 4.7.5).

We stress the importance of obtaining additional, accurate and well defined statistics on the SFR in X-ray selected AGNs/QSOs, and on the nuclear activity in FIR-selected galaxies, via coordinated observations from current and next generation of (sub-)mm and X-ray instruments. These observations will be crucial to follow in greater detail the different stages of the AGN/galaxy coevolution process, and in particular to pinpoint the ratio between the duration timescale of the star formation and the e-folding timescale of the BH accretion.

We have found that the ratio $L_{\rm SFR}/L_{\rm AGN}$ is the observational parameter that characterizes the time evolution of the galaxy plus AGN system (see Fig. 4.12); this ratio is a decreasing function of the galactic time, and marks the evolution from the epoch when the luminosity budget is dominated by the star formation to the epoch when the AGN/QSO takes over. The FIR selection elicits objects with $L_{\rm SFR}/L_{\rm AGN} \gtrsim 0.3$ and a $M_{\rm BH}/M_\star$ ratio smaller than the average local value $\Gamma_0 \approx 3 \times 10^{-3}$. The primary X-ray selection picks out objects spanning the whole range of the luminosity ratio; in particular, X-ray QSOs with large obscuration exhibit $0.3 \lesssim L_{\rm SFR}/L_{\rm AGN} \lesssim 5$. Instead, the optically selected QSOs show $0.01 \lesssim L_{\rm SFR}/L_{\rm AGN} \lesssim 0.3$, marking the decrease of the star formation on a short timescale, and the epoch of the reservoir exhaustion on longer timescales; the bright objects feature a mass ratio $M_{\rm BH}/M_\star \gtrsim \Gamma_0$.

Our findings indicate the following scenario, schematically illustrated in Fig. 4.1: AGNs begin their life as faint and obscured nuclei; during this phase, the SFR in the host galaxies dominates the radiative output, and these systems are observable at FIR wavelengths. Then, they evolve into obscured QSOs, mostly visible in the X-ray or in MIR bands, and eventually become bright QSOs, visible even in the optical band. In this framework, the role of the dust is crucial; it must form soon, at the beginning of the host evolution, in order to yield the appropriate FIR luminosity, and then it has to be largely removed soon after the onset of the optically bright AGN phase, in a couple of $\tau_{\rm ef}$. The nuclear activity is detectable at hard X-ray (rest-frame) energies for longer times, amounting to $4 - 5\,\tau_{\rm ef}$; this is in line with the increasing mean free path of the X-ray photons with increasing energy.

The time evolution of the star formation and BH accretion envisaged by our work can be compared with the results of other semi-analytical and numerical works, appeared in the recent literature. Khandai et al. (2012, see also Springel, Di Matteo & Hernquist 2005; Sijacki, Springel & Haehnelt 2009) exploited numerical simulations including galaxy mergers and cold gas streams, to investigate the growth of galaxies and hosted SMBHs

at high redshift. Their lightcurves (see Fig. 2 of Khandai et al. 2012) feature an early phase along which both the SFR and the BH accretion rate rise; the latter very rapidly attains $\sim \times 10^{-1}\, M_{\odot}\ \mathrm{yr}^{-1}$. As a result, the AGN bolometric luminosity exceeds $\sim 10^{45}$ erg s^{-1} over a rather long period, when the SFR keeps sustained at more than $100\, M_{\odot}$ yr^{-1}, so producing a very high fraction of X-ray detected AGNs in FIR-selected hosts. Subsequently, after the action of the AGN feedback, their lightcurves feature a mild, slow decline in the SFR, with the BH accretion still at appreciable values, implying a high fraction of FIR detections in X-ray/optically selected AGNs. Such high fractions are clearly at variance with current observational data (see Sec. 4.5). Part of these problems can be ascribed to the assumption of Bondi accretion strictly ceiled by the Eddington limit, the ensuing requirements on large BH seed masses ($\gtrsim 10^5\, M_{\odot}$), and the recipe for mild AGN feedback on the large-scale star formation activity.

Fanidakis et al. (2012, see also Cole et al. 2000; Baugh et al. 2005) exploit a semi-analytical model that includes BH accretion by galaxy merging and disc instabilities, to compute the evolution of AGNs across cosmic times. Their prescriptions (see Eqs. 1 and 2 of Fanidakis et al. 2012) imply a direct proportionality between the BH accretion rate and the SFR. With their adopted values for the fraction of stellar mass produced in the starburst that is accreted onto the BH (their parameter $f_{\mathrm{BH}} \approx 5 \times 10^{-3}$) and for the ratio between the accretion and the bulge dynamical timescale (their parameter $f_q \sim 1 - 10$), the resulting ratio of FIR to AGN bolometric luminosity stays almost constant with time at values $L_{\mathrm{FIR}}/L_{\mathrm{AGN}} \approx 2/f_q \sim 0.2 - 2$. This again implies a very high X-ray detected fraction in FIR-selected hosts. The problem can be mostly ascribed to the absence of the reservoir in their model, and to a prominent role of mergers in triggering the star formation and BH activity.

We have discussed the fueling of the reservoir (Sec. 4.7.2 and Sec. 4.7.3) and the physics of BH accretion (see Sec. 4.7.4) in the light of our scenario. We have shown that observations can be accounted for by prescribing a self-regulated, super-Eddington accretion associated to a slim-disc regime, characterized by a slightly super-Eddington radiative power ($\lambda_{\mathrm{Edd}} \lesssim 4$) and to a radiative efficiency $\epsilon \lesssim 0.05$. Subsequently, the exponential decline of the AGN luminosity, required by the data, implies that λ_{Edd} must exponentially decrease. Correspondingly, following the prescription of Eq. 2.12, the radiative efficiency is expected to rapidly increase up to $\epsilon \sim 0.1$, hence approaching the characteristic value of a thin disc regime (see dotted line in Fig. 4.2).

In the second part (Chapter 5), we have further investigated the coevolution of galaxies and hosted SMBHs throughout the history of the Universe, by adding information on how and when the stellar and the BH masses are accumulated. To do so, we implemented

our physically motivated lightcurves in a statistical approach based on the continuity equation. Our main results are the following:

- We have demonstrated that the BHMFs (Fig. 5.2) and the SMFs (Fig. 5.10) at different redshifts can be reconstructed from the SFR-LF and AGN LF via a continuity equation approach without source term (Sec. 5.1.2 and Sec. 5.2.1). This implies that the buildup of stars and SMBHs in galaxies occurs mainly via local, *in-situ* processes, with mergers playing a marginal role, at least for stellar masses $M_\star \lesssim 3 \times 10^{11}\, M_\odot$ and BH masses $M_{\rm BH} \lesssim 10^9\, M_\odot$, where the statistical data are more secure and less biased by systematic errors (see Sec. 5.3).
- Concerning the AGN/BH component, our analysis concurs with the observed Eddington ratio distributions in strongly suggesting that the fraction of AGNs observed in slim-disc regime increases with redshift, and that anyway most of the BH mass is accreted in such conditions (see Sec. 5.1.3).
- We show how the presence of the dust strongly affects the view of the star formation process in galaxies with $\dot{M}_\star \gtrsim 10\, M_\odot\ {\rm yr}^{-1}$ at any redshifts, even the quite large ones (see Sec. 5.2.3). In fact, we have shown that dust is formed on a timescale which is only a small fraction of the burst duration (Fig. 5.13). Such a behavior is also mirrored in the estimated cosmic SFR and sSFR density (see Fig. 6.10 and Fig. 6.11).
- Duty cycles for both the AGN and the stellar components have been derived (Fig. 5.5 and Fig. 5.12), and have been found to be close to unity at high-redshift.

In the last part (Chapter 6), we have established a link among the host galaxy + SMBH system and the gravitationally dominant DM component, by developing an improved abundance matching technique. Our main results are listed in the following:

- The relationships we have inferred between the stellar, BH, and DM components of galaxies at various redshifts (Sec. 6.2.1 and Sec. 6.2.2) imply that stellar and AGN feedback cooperate with gas cooling in the star formation process within halos, whose binding energy at formation is the most relevant feature. Specifically, in low-mass halos, SN explosions keep star formation low on long timescales, while in massive halos star formation can proceed at much higher levels, until the AGN abruptly quenches it. The same results are evident also when the DM halo is bypassed (see Sec. 6.2.3and Sec. 6.2.4). The relationships between galaxy/BH and halo properties constitute testbeds for galaxy formation and evolution models, and can be operationally implemented in numerical simulations to populate DM halos or to gauge subgrid physical prescriptions.

- We have derived the bias as a function of redshift and luminosity, both for the AGN (Fig. 6.14) and for various galaxy populations (Fig. 6.15). The clustering properties constitute a byproduct of our approach, and the nice agreement with observations *validate* our results on BH and stellar mass functions, and related duty cycles from the continuity equation (Fig. 5.5 and Fig. 5.12).

- The sSFR increases with redshift at least up to $z \sim 6$ (Fig. 6.10). In the range $0 < z < 3$, the results from the continuity equation agree with the so called 'main sequence' of starforming galaxies (Fig. 6.11), although we underline that the comparison with observations critically depends on sample selection.

- The low efficiency ($\lesssim 20\%$) in star formation (Fig. 6.7) elucidates that a fraction $\gtrsim 50\%$, up to $\sim 70\%$ (depending on mass), of the gas associated to a galaxy halo is always in warm/hot form.

- The $M_{\rm BH}/M_\star$ ratio (Fig. 6.12) mildly evolves, at least up to $z \lesssim 3$, signaling that the SMBH and the stellar mass growth occurs *in parallel*, by in-situ accretion and star formation processes.

- The negligible role of merging, and the inefficiency of star formation, imply that galaxy formation is basically a process inherent to the inner regions of halos, where most of the gas mass resides.

These evidences strongly motivate the development of hydrodynamical simulations at very high spatial resolutions. This would allow to perform detailed studies of the small-scale gravitational instabilities connected to gas cooling and condensation, star formation, BH accretion, and associated feedback processes.

From the technical point of view, the novel achievements of this thesis can be summarized as follows:

- We have set the timescales describing the SFR-luminosity and the AGN bolometric luminosity of the coevolving galaxy + SMBH systems of different masses and redshifts, on the basis of several observational statistics (Chapter 4).

- We have presented an analytical solution of the continuity equation for SMBHs, that holds under our physically motivated assumptions, including both a redshift and a luminosity dependence of Eddington ratio, radiative efficiency, and lightcurve timescales (Sec. 5.1).

- We have developed the continuity equation for the stellar component, solving it under our physically motivated assumptions on the lightcurve shape and timescales (Sec. 5.1.3).

- We have provided a continuous rendition of the overall SFR-LF, interpolating between the dust-corrected UV data at the faint end, and the FIR data at the bright end (Sec. 3.5.3). A posteriori, our approach is validated by the agreement between the SMF obtained via continuity equation and the observational determinations over the redshift range $z \sim 0 - 6$ (Fig. 5.10).

- We have developed a procedure to derive the GHMF at different redshifts (Sec. 6.1). This can be implemented in halo occupation distribution models.

- We have generalized the abundance matching technique to deal with relationships between both luminosity and mass, by considering the duty cycle of SMBHs and star formation in galaxies (Sec. 6.2).

Finally, some remarks are in order. As to the AGN/BH component, one of our major predictions is the formation of a reservoir in the circumnuclear regions; the reservoir hosted by typical star forming galaxies with $\dot{M}_\star \gtrsim 200\ M_\odot\ \mathrm{yr}^{-1}$ can reach a mass $M_{\rm res} \gtrsim 2 \times 10^8\ M_\odot$. In Sec. 4.7.1, we have pointed out that these hosts are easily selected by (sub-)mm surveys such as H-ATLAS, HerMES, and those performed with the SPT. Many tens of these hosts are strongly lensed by intervening galaxies, with amplification factors $\gtrsim 10$. In such cases, coordinated, high-resolution observations in the (sub-)mm band with ALMA, and in the X-ray band with *Chandra* and the next generation of X-ray telescopes, will allow us to study in detail the evolution of the SMBH and of its reservoir.

Moreover, large samples of AGNs with multiwavelength SEDs and single-epoch BH masses are strongly needed to test the statistics of the slim-disc fraction, and to measure the associated radiative efficiency (cf. Raimundo et al. 2012).

As to the stellar component, our analysis allows to extrapolate the SFR, stellar mass, and sSFR functions to higher redshifts, yet unexplored, but within the reach of future instrumentations like ALMA, JWST, and SKA. In particular, a crucial point will be to estimate the bright end of the SFR-LF at $z \gtrsim 4$, to obtain direct constraints on the timescale of dust formation in high-redshift galaxies.

Bibliography

Abel T., Bryan G. L., Norman M. L., 2000, ApJ, 540, 39

Abel T., Bryan G. L., Norman M. L., 2002, Science, 295, 93

Abramowicz M. A., Chen X., Kato S., Lasota J.-P., Regev O., 1995, ApJ, 438, L37

Abramowicz M. A., Czerny B., Lasota J. P., Szuszkiewicz E., 1988, ApJ, 332, 646

Abramowicz M. A., Fragile P. C., 2013, Living Reviews in Relativity, 16, 1

Abramowicz M. A., Lasota J. P., 1980, Acta Astron., 30, 35

Adelberger K. L., Steidel C. C., Pettini M., Shapley A. E., Reddy N. A., Erb D. K., 2005, ApJ, 619, 697

Aird J., Coil A. L., Georgakakis A., Nandra K., Barro G., Pérez-González P. G., 2015, MNRAS, 451, 1892

Aird J., Coil A. L., Moustakas J., Blanton M. R., Burles S. M., Cool R. J., Eisenstein D. J., Smith M. S. M., Wong K. C., Zhu G., 2012, ApJ, 746, 90

Aird J., Coil A. L., Moustakas J., Diamond-Stanic A. M., Blanton M. R., Cool R. J., Eisenstein D. J., Wong K. C., Zhu G., 2013, ApJ, 775, 41

Aird J., Nandra K., Laird E. S., Georgakakis A., Ashby M. L. N., Barmby P., Coil A. L., Huang J.-S., Koekemoer A. M., Steidel C. C., Willmer C. N. A., 2010, MNRAS, 401, 2531

Alexander D. M., Bauer F. E., Chapman S. C., Smail I., Blain A. W., Brandt W. N., Ivison R. J., 2005, ApJ, 632, 736

Alexander D. M., Brandt W. N., Smail I., Swinbank A. M., Bauer F. E., Blain A. W., Chapman S. C., Coppin K. E. K., Ivison R. J., Menéndez-Delmestre K., 2008, AJ, 135, 1968

Alexander D. M., Hickox R. C., 2012, New A Rev., 56, 93

Alexander D. M., Swinbank A. M., Smail I., McDermid R., Nesvadba N. P. H., 2010, MNRAS, 402, 2211

Aller M. C., Richstone D., 2002, AJ, 124, 3035

Allevato V., Finoguenov A., Cappelluti N., Miyaji T., Hasinger G., Salvato M., Brusa M., Gilli R., Zamorani G., Shankar F., James J. B., McCracken H. J., Bongiorno A., Merloni A., Peacock J. A., Silverman J., Comastri A., 2011, ApJ, 736, 99

Allevato V., Finoguenov A., Civano F., Cappelluti N., Shankar F., Miyaji T., Hasinger G., Gilli R., Zamorani G., Lanzuisi G., Salvato M., Elvis M., Comastri A., Silverman J., 2014, ApJ, 796, 4

Andreon S., Newman A. B., Trinchieri G., Raichoor A., Ellis R. S., Treu T., 2014, A&A, 565, A120

Antonucci R., 1993, ARA&A, 31, 473

Argon A. L., Greenhill L. J., Reid M. J., Moran J. M., Humphreys E. M. L., 2007, ApJ, 659, 1040

Assef R. J., Kochanek C. S., Ashby M. L. N., Brodwin M., Brown M. J. I., Cool R., Forman W., Gonzalez A. H., Hickox R. C., Jannuzi B. T., Jones C., Le Floc'h E., Moustakas J., Murray S. S., Stern D., 2011, ApJ, 728, 56

Aversa R., Lapi A., de Zotti G., Shankar F., Danese L., 2015, ApJ, 810, 74

Balbus S. A., Hawley J. F., 1998, Reviews of Modern Physics, 70, 1

Baldry I. K., Glazebrook K., 2003, ApJ, 593, 258

Baldry I. K., Glazebrook K., Brinkmann J., Ivezić Ž., Lupton R. H., Nichol R. C., Szalay A. S., 2004, ApJ, 600, 681

Banerji M., McMahon R. G., Hewett P. C., Alaghband-Zadeh S., Gonzalez-Solares E., Venemans B. P., Hawthorn M. J., 2012, MNRAS, 427, 2275

Banerji M., McMahon R. G., Hewett P. C., Gonzalez-Solares E., Koposov S. E., 2013, MNRAS, 429, L55

Barausse E., 2012, MNRAS, 423, 2533

Barger A. J., Cowie L. L., Chen C.-C., Owen F. N., Wang W.-H., Casey C. M., Lee N., Sanders D. B., Williams J. P., 2014, ApJ, 784, 9

Barger A. J., Wang W.-H., Cowie L. L., Owen F. N., Chen C.-C., Williams J. P., 2012, ApJ, 761, 89

Barone-Nugent R. L., Trenti M., Wyithe J. S. B., Bouwens R. J., Oesch P. A., Illingworth G. D., Carollo C. M., Su J., Stiavelli M., Labbe I., van Dokkum P. G., 2014, ApJ, 793, 17

Barth A. J., Martini P., Nelson C. H., Ho L. C., 2003, ApJ, 594, L95

Barth A. J., Sarzi M., Rix H.-W., Ho L. C., Filippenko A. V., Sargent W. L. W., 2001, ApJ, 555, 685

Baskin A., Laor A., 2005, MNRAS, 356, 1029

Basu-Zych A. R., Lehmer B. D., Hornschemeier A. E., Bouwens R. J., Fragos T., Oesch P. A., Belczynski K., Brandt W. N., Kalogera V., Luo B., Miller N., Mullaney J. R., Tzanavaris P., Xue Y., Zezas A., 2013, ApJ, 762, 45

Bauer F. E., Alexander D. M., Brandt W. N., Hornschemeier A. E., Vignali C., Garmire G. P., Schneider D. P., 2002, AJ, 124, 2351

Baugh C. M., Lacey C. G., Frenk C. S., Granato G. L., Silva L., Bressan A., Benson A. J., Cole S., 2005, MNRAS, 356, 1191

Begelman M. C., 1979, MNRAS, 187, 237

Begelman M. C., 2012, ApJ, 749, L3

Begelman M. C., Rees M. J., 1978, MNRAS, 185, 847

Begelman M. C., Shlosman I., 2009, ApJ, 702, L5

Begelman M. C., Volonteri M., Rees M. J., 2006, MNRAS, 370, 289

Behroozi P. S., Silk J., 2015, ApJ, 799, 32

Behroozi P. S., Wechsler R. H., Conroy C., 2013, ApJ, 770, 57

Beifiori A., Courteau S., Corsini E. M., Zhu Y., 2012, MNRAS, 419, 2497

Beifiori A., Sarzi M., Corsini E. M., Dalla Bontà E., Pizzella A., Coccato L., Bertola F., 2009, ApJ, 692, 856

Bell E. F., 2003, ApJ, 586, 794

Bell E. F., de Jong R. S., 2001, ApJ, 550, 212

Bennert V. N., Auger M. W., Treu T., Woo J.-H., Malkan M. A., 2011, ApJ, 742, 107

Bentz M. C., Peterson B. M., Netzer H., Pogge R. W., Vestergaard M., 2009a, ApJ, 697, 160

Bentz M. C., Peterson B. M., Pogge R. W., Vestergaard M., 2009b, ApJ, 694, L166

Bernardi M., Meert A., Sheth R. K., Vikram V., Huertas-Company M., Mei S., Shankar F., 2013, MNRAS, 436, 697

Bernardi M., Sheth R. K., Tundo E., Hyde J. B., 2007, ApJ, 660, 267

Berti E., Volonteri M., 2008, ApJ, 684, 822

Bianchini F., Bielewicz P., Lapi A., González-Nuevo J., Baccigalupi C., de Zotti G., Danese L., Bourne N., Cooray A., Dunne L., Dye S., Eales S., Ivison R., Maddox S., Negrello M., Scott D., Smith M. W. L., Valiante E., 2015, ApJ, 802, 64

Bielby R., Hill M. D., Shanks T., Crighton N. H. M., Infante L., Bornancini C. G., Francke H., Héraudeau P., Lambas D. G., Metcalfe N., Minniti D., Padilla N., Theuns T., Tummuangpak P., Weilbacher P., 2013, MNRAS, 430, 425

Blain A. W., Chapman S. C., Smail I., Ivison R., 2004, ApJ, 611, 725

Blanc G. A., Lira P., Barrientos L. F., Aguirre P., Francke H., Taylor E. N., Quadri R., Marchesini D., Infante L., Gawiser E., Hall P. B., Willis J. P., Herrera D., Maza J., MUSYC Collaboration, 2008, ApJ, 681, 1099

Blandford R. D., Begelman M. C., 1999, MNRAS, 303, L1

Blandford R. D., Begelman M. C., 2004, MNRAS, 349, 68

Böhringer H., Chon G., Collins C. A., 2014, A&A, 570, A31

Bolton J. S., Haehnelt M. G., Warren S. J., Hewett P. C., Mortlock D. J., Venemans B. P., McMahon R. G., Simpson C., 2011, MNRAS, 416, L70

Bonfield D. G., Jarvis M. J., Hardcastle M. J., Cooray A., Hatziminaoglou E., Ivison R. J., Page M. J., Stevens J. A., de Zotti G., Auld R., Baes M., Buttiglione S., Cava A., Dariush A., Dunlop J. S., Dunne L., Dye S., Eales S., Fritz J., Hopwood R., Ibar E., Maddox S. J., Michałowski M. J., Pascale E., Pohlen M., Rigby E. E., Rodighiero G., Serjeant S., Smith D. J. B., Temi P., van der Werf P., 2011, MNRAS, 416, 13

Bongiorno A., Merloni A., Brusa M., Magnelli B., Salvato M., Mignoli M., Zamorani G., Fiore F., Rosario D., Mainieri V., Hao H., Comastri A., Vignali C., Balestra I., Bardelli S., Berta S., Civano F., Kampczyk P., Le Floc'h E., Lusso E., Lutz D., Pozzetti L., Pozzi F., Riguccini L., Shankar F., Silverman J., 2012, MNRAS, 427, 3103

Bonoli S., Shankar F., White S. D. M., Springel V., Wyithe J. S. B., 2010, MNRAS, 404, 399

Borguet B. C. J., Arav N., Edmonds D., Chamberlain C., Benn C., 2013, ApJ, 762, 49

Borys C., Smail I., Chapman S. C., Blain A. W., Alexander D. M., Ivison R. J., 2005, ApJ, 635, 853

Bournaud F., Dekel A., Teyssier R., Cacciato M., Daddi E., Juneau S., Shankar F., 2011, ApJ, 741, L33

Bournaud F., Elmegreen B. G., Elmegreen D. M., 2007, ApJ, 670, 237

Bournaud F., Perret V., Renaud F., Dekel A., Elmegreen B. G., Elmegreen D. M., Teyssier R., Amram P., Daddi E., Duc P.-A., Elbaz D., Epinat B., Gabor J. M., Juneau S., Kraljic K., Le Floch' E., 2014, ApJ, 780, 57

Bourne N., Dunne L., Ivison R. J., Maddox S. J., Dickinson M., Frayer D. T., 2011, MNRAS, 410, 1155

Bouwens R. J., Illingworth G. D., Oesch P. A., Franx M., Labbé I., Trenti M., van Dokkum P., Carollo C. M., González V., Smit R., Magee D., 2012, ApJ, 754, 83

Bouwens R. J., Illingworth G. D., Oesch P. A., Labbé I., Trenti M., van Dokkum P., Franx M., Stiavelli M., Carollo C. M., Magee D., Gonzalez V., 2011, ApJ, 737, 90

Bouwens R. J., Illingworth G. D., Oesch P. A., Labbé I., van Dokkum P. G., Trenti M., Franx M., Smit R., Gonzalez V., Magee D., 2014, ApJ, 793, 115

Bouwens R. J., Illingworth G. D., Oesch P. A., Stiavelli M., van Dokkum P., Trenti M., Magee D., Labbé I., Franx M., Carollo C. M., Gonzalez V., 2010, ApJ, 709, L133

Bouwens R. J., Illingworth G. D., Oesch P. A., Trenti M., Labbé I., Bradley L., Carollo M., van Dokkum P. G., Gonzalez V., Holwerda B., Franx M., Spitler L., Smit R., Magee D., 2015, ApJ, 803, 34

Bouwens R. J., Oesch P. A., Illingworth G. D., Labbé I., van Dokkum P. G., Brammer G., Magee D., Spitler L. R., Franx M., Smit R., Trenti M., Gonzalez V., Carollo C. M., 2013, ApJ, 765, L16

Bower G. A., Green R. F., Danks A., Gull T., Heap S., Hutchings J., Joseph C., Kaiser M. E., Kimble R., Kraemer S., Weistrop D., Woodgate B., Lindler D., Hill R. S., Malumuth E. M., Baum S., Sarajedini V., Heckman T. M., Wilson A. S., Richstone D. O., 1998, ApJ, 492, L111

Bowler R. A. A., Dunlop J. S., McLure R. J., Rogers A. B., McCracken H. J., Milvang-Jensen B., Furusawa H., Fynbo J. P. U., Taniguchi Y., Afonso J., Bremer M. N., Le Fèvre O., 2014, MNRAS, 440, 2810

Boyle B. J., Shanks T., Croom S. M., Smith R. J., Miller L., Loaring N., Heymans C., 2000, MNRAS, 317, 1014

Braatz J. A., Reid M. J., Humphreys E. M. L., Henkel C., Condon J. J., Lo K. Y., 2010, ApJ, 718, 657

Brandt W. N., Alexander D. M., 2015, A&A Rev., 23, 1

Brandt W. N., Gallagher S. C., 2000, New A Rev., 44, 461

Brenneman L. W., Reynolds C. S., 2006, ApJ, 652, 1028

Brenneman L. W., Reynolds C. S., 2009, ApJ, 702, 1367

Bressan A., Chiosi C., Fagotto F., 1994, ApJS, 94, 63

Bressan A., Silva L., Granato G. L., 2002, A&A, 392, 377

Brightman M., Nandra K., Salvato M., Hsu L.-T., Aird J., Rangel C., 2014, MNRAS, 443, 1999

Brinchmann J., Ellis R. S., 2000, ApJ, 536, L77

Bromm V., Larson R. B., 2004, ARA&A, 42, 79

Bromm V., Loeb A., 2003, ApJ, 596, 34

Brusa M. et al., 2010, ApJ, 716, 348

Brusa M., Feruglio C., Cresci G., Mainieri V., Sargent M. T., Perna M., Santini P., Vito F., Marconi A., Merloni A., Lutz D., Piconcelli E., Lanzuisi G., Maiolino R., Rosario D., Daddi E., Bongiorno A., Fiore F., Lusso E., 2015, A&A, 578, A11

Bruzual A. G., Charlot S., 1993, ApJ, 405, 538

Buat V., Boselli A., Gavazzi G., Bonfanti C., 2002, A&A, 383, 801

Buat V., Iglesias-Páramo J., Seibert M., Burgarella D., Charlot S., Martin D. C., Xu C. K., Heckman T. M., Boissier S., Boselli A., Barlow T., Bianchi L., Byun Y.-I., Donas J., Forster K., Friedman P. G., Jelinski P., Lee Y.-W., Madore B. F., Malina R., Milliard B., Morissey P., Neff S., Rich M., Schiminovitch D., Siegmund O., Small T., Szalay A. S., Welsh B., Wyder T. K., 2005, ApJ, 619, L51

Buat V., Xu C., 1996, A&A, 306, 61

Buchner J., Georgakakis A., Nandra K., Brightman M., Menzel M.-L., Liu Z., Hsu L.-T., Salvato M., Rangel C., Aird J., Merloni A., Ross N., 2015, ApJ, 802, 89

Bundy K., Georgakakis A., Nandra K., Ellis R. S., Conselice C. J., Laird E., Coil A., Cooper M. C., Faber S. M., Newman J. A., Pierce C. M., Primack J. R., Yan R., 2008, ApJ, 681, 931

Burgarella D., Buat V., Iglesias-Páramo J., 2005, MNRAS, 360, 1413

Burkert A., Silk J., 2001, ApJ, 554, L151

Bussmann R. S., Pérez-Fournon I., Amber S., Calanog J., Gurwell M. A., Dannerbauer H., De Bernardis F., Fu H., Harris A. I., Krips M., Lapi A., Maiolino R., Omont A., Riechers D., Wardlow J., Baker A. J., Birkinshaw M., Bock J., Bourne N., Clements D. L., Cooray A., De Zotti G., Dunne L., Dye S., Eales S., Farrah D., Gavazzi R., González Nuevo J., Hopwood R., Ibar E., Ivison R. J., Laporte N., Maddox S., Martínez-Navajas P., Michalowski M., Negrello M., Oliver S. J., Roseboom I. G., Scott D., Serjeant S., Smith A. J., Smith M., Streblyanska A., Valiante E., van der Werf P., Verma A., Vieira J. D., Wang L., Wilner D., 2013, ApJ, 779, 25

Cai Z.-Y., Lapi A., Bressan A., De Zotti G., Negrello M., Danese L., 2014, ApJ, 785, 65

Cai Z.-Y., Lapi A., Xia J.-Q., De Zotti G., Negrello M., Gruppioni C., Rigby E., Castex G., Delabrouille J., Danese L., 2013, ApJ, 768, 21

Calzetti D., 1999, Ap&SS, 266, 243

Calzetti D., Armus L., Bohlin R. C., Kinney A. L., Koornneef J., Storchi-Bergmann T., 2000, ApJ, 533, 682

Calzetti D., Kinney A. L., Storchi-Bergmann T., 1994, ApJ, 429, 582

Cao X., 2010, ApJ, 725, 388

Cao X., Li F., 2008, MNRAS, 390, 561

Cappellari M., Bacon R., Bureau M., Damen M. C., Davies R. L., de Zeeuw P. T., Emsellem E., Falcón-Barroso J., Krajnović D., Kuntschner H., McDermid R. M., Peletier R. F., Sarzi M., van den Bosch R. C. E., van de Ven G., 2006, MNRAS, 366, 1126

Cappellari M., McDermid R. M., Alatalo K., Blitz L., Bois M., Bournaud F., Bureau M., Crocker A. F., Davies R. L., Davis T. A., de Zeeuw P. T., Duc P.-A., Emsellem E., Khochfar S., Krajnović D., Kuntschner H., Morganti R., Naab T., Oosterloo T., Sarzi M., Scott N., Serra P., Weijmans A.-M., Young L. M., 2013, MNRAS, 432, 1862

Cappellari M., Neumayer N., Reunanen J., van der Werf P. P., de Zeeuw P. T., Rix H.-W., 2009, MNRAS, 394, 660

Cappelluti N., Ajello M., Burlon D., Krumpe M., Miyaji T., Bonoli S., Greiner J., 2010, ApJ, 716, L209

Caputi K. I., Cirasuolo M., Dunlop J. S., McLure R. J., Farrah D., Almaini O., 2011, MNRAS, 413, 162

Carilli C. L., Bertoldi F., Rupen M. P., Fan X., Strauss M. A., Menten K. M., Kreysa E., Schneider D. P., Bertarini A., Yun M. S., Zylka R., 2001, ApJ, 555, 625

Carrera F. J., Ali A. K., Page M. J., Symeonidis M., Stevens J. A., Cao Orjales J. M., 2013, ArXiv e-prints

Carrera F. J., Page M. J., Stevens J. A., Ivison R. J., Dwelly T., Ebrero J., Falocco S., 2011, MNRAS, 413, 2791

Cavaliere A., Morrison P., Wood K., 1971, ApJ, 170, 223

Ceverino D., Dekel A., Bournaud F., 2010, MNRAS, 404, 2151

Chabrier G., 2003, PASP, 115, 763

Charlot S., Bruzual A. G., 1991, ApJ, 367, 126

Charlot S., Fall S. M., 2000, ApJ, 539, 718

Chartas G., Brandt W. N., Gallagher S. C., 2003, ApJ, 595, 85

Chartas G., Saez C., Brandt W. N., Giustini M., Garmire G. P., 2009, ApJ, 706, 644

Chen C.-T. J., Hickox R. C., Alberts S., Harrison C. M., Alexander D. M., Assef R., Brodwin M., Brown M. J. I., Del Moro A., Forman W. R., Gorjian V., Goulding A. D., Hainline K. N., Jones C., Kochanek C. S., Murray S. S., Pope A., Rovilos E., Stern D., 2015, ApJ, 802, 50

Choi J.-H., Shlosman I., Begelman M. C., 2013, ApJ, 774, 149

Choi J.-H., Shlosman I., Begelman M. C., 2015, MNRAS, 450, 4411

Chokshi A., Turner E. L., 1992, MNRAS, 259, 421

Cicone C., Maiolino R., Gallerani S., Neri R., Ferrara A., Sturm E., Fiore F., Piconcelli E., Feruglio C., 2015, A&A, 574, A14

Cirasuolo M., McLure R. J., Dunlop J. S., Almaini O., Foucaud S., Simpson C., 2010, MNRAS, 401, 1166

Cirasuolo M., Shankar F., Granato G. L., De Zotti G., Danese L., 2005, ApJ, 629, 816

Cisternas M., Jahnke K., Inskip K. J., Kartaltepe J., Koekemoer A. M., Lisker T., Robaina A. R., Scodeggio M., Sheth K., Trump J. R., Andrae R., Miyaji T., Lusso E., Brusa M., Capak P., Cappelluti N., Civano F., Ilbert O., Impey C. D., Leauthaud A., Lilly S. J., Salvato M., Scoville N. Z., Taniguchi Y., 2011, ApJ, 726, 57

Clemens M. S., Negrello M., De Zotti G., González-Nuevo J., Bonavera L., Cosco G., Guarese G., Boaretto L., Salucci P., Baccigalupi C., Clements D. L., Danese L., Lapi A., Mandolesi N., Partridge R. B., Perrotta F., Serjeant S., Scott D., Toffolatti L., 2013, MNRAS, 433, 695

Clements D. L., Rigby E., Maddox S., Dunne L., Mortier A., Pearson C., Amblard A., Auld R., Baes M., Bonfield D., Burgarella D., Buttiglione S., Cava A., Cooray A., Dariush A., de Zotti G., Dye S., Eales S., Frayer D., Fritz J., Gardner J. P., González-Nuevo J., Herranz D., Ibar E., Ivison R., Jarvis M. J., Lagache G., Leeuw L., Lopez-Caniego M., Negrello M., Pascale E., Pohlen M., Rodighiero G., Samui S., Serjeant S., Sibthorpe B., Scott D., Smith D. J. B., Temi P., Thompson M., Valtchanov I., van der Werf P., Verma A., 2010, A&A, 518, L8

Coil A. L., Georgakakis A., Newman J. A., Cooper M. C., Croton D., Davis M., Koo D. C., Laird E. S., Nandra K., Weiner B. J., Willmer C. N. A., Yan R., 2009, ApJ, 701, 1484

Colbert E. J. M., Heckman T. M., Ptak A. F., Strickland D. K., Weaver K. A., 2004, ApJ, 602, 231

Cole S., Lacey C. G., Baugh C. M., Frenk C. S., 2000, MNRAS, 319, 168

Comastri A., Setti G., Zamorani G., Hasinger G., 1995, A&A, 296, 1

Combes F., García-Burillo S., Casasola V., Hunt L., Krips M., Baker A. J., Boone F., Eckart A., Marquez I., Neri R., Schinnerer E., Tacconi L. J., 2013, A&A, 558, A124

Condon J. J., 1992, ARA&A, 30, 575

Conroy C., 2013, ARA&A, 51, 393

Conroy C., Graves G. J., van Dokkum P. G., 2014, ApJ, 780, 33

Coppin K. E. K., Swinbank A. M., Neri R., Cox P., Alexander D. M., Smail I., Page M. J., Stevens J. A., Knudsen K. K., Ivison R. J., Beelen A., Bertoldi F., Omont A., 2008, MNRAS, 389, 45

Cortese L., Boselli A., Buat V., Gavazzi G., Boissier S., Gil de Paz A., Seibert M., Madore B. F., Martin D. C., 2006, ApJ, 637, 242

Cortese L., Boselli A., Franzetti P., Decarli R., Gavazzi G., Boissier S., Buat V., 2008, MNRAS, 386, 1157

Courteau S., Cappellari M., de Jong R. S., Dutton A. A., Emsellem E., Hoekstra H., Koopmans L. V. E., Mamon G. A., Maraston C., Treu T., Widrow L. M., 2014, Reviews of Modern Physics, 86, 47

Croom S. M., Boyle B. J., Shanks T., Smith R. J., Miller L., Outram P. J., Loaring N. S., Hoyle F., da Ângela J., 2005, MNRAS, 356, 415

Croom S. M., Richards G. T., Shanks T., Boyle B. J., Strauss M. A., Myers A. D., Nichol R. C., Pimbblet K. A., Ross N. P., Schneider D. P., Sharp R. G., Wake D. A., 2009, MNRAS, 399, 1755

Croton D. J., Springel V., White S. D. M., De Lucia G., Frenk C. S., Gao L., Jenkins A., Kauffmann G., Navarro J. F., Yoshida N., 2006, MNRAS, 365, 11

Crummy J., Fabian A. C., Gallo L., Ross R. R., 2006, MNRAS, 365, 1067

Cucciati O., Tresse L., Ilbert O., Le Fèvre O., Garilli B., Le Brun V., Cassata P., Franzetti P., Maccagni D., Scodeggio M., Zucca E., Zamorani G., Bardelli S., Bolzonella M., Bielby R. M., McCracken H. J., Zanichelli A., Vergani D., 2012, A&A, 539, A31

Curtis-Lake E., McLure R. J., Dunlop J. S., Schenker M., Rogers A. B., Targett T., Cirasuolo M., Almaini O., Ashby M. L. N., Bradshaw E. J., Finkelstein S. L., Dickinson M., Ellis R. S., Faber S. M., Fazio G. G., Ferguson H. C., Fontana A., Grogin N. A., Hartley W. G., Kocevski D. D., Koekemoer A. M., Lai K., Robertson B. E., Vanzella E., Willner S. P., 2013, MNRAS, 429, 302

Czerny B., Elvis M., 1987, ApJ, 321, 305

Czerny B., Hryniewicz K., Nikołajuk M., Sądowski A., 2011, MNRAS, 415, 2942

Czerny B., Nikołajuk M., 2010, Mem. Soc. Astron. Italiana, 81, 281

da Ângela J., Shanks T., Croom S. M., Weilbacher P., Brunner R. J., Couch W. J., Miller L., Myers A. D., Nichol R. C., Pimbblet K. A., de Propris R., Richards G. T., Ross N. P., Schneider D. P., Wake D., 2008, MNRAS, 383, 565

da Cunha E., Charlot S., Elbaz D., 2008, MNRAS, 388, 1595

Daddi E., Dickinson M., Morrison G., Chary R., Cimatti A., Elbaz D., Frayer D., Renzini A., Pope A., Alexander D. M., Bauer F. E., Giavalisco M., Huynh M., Kurk J., Mignoli M., 2007, ApJ, 670, 156

Damen M., Labbé I., Franx M., van Dokkum P. G., Taylor E. N., Gawiser E. J., 2009, ApJ, 690, 937

Damjanov I., McCarthy P. J., Abraham R. G., Glazebrook K., Yan H., Mentuch E., Le Borgne D., Savaglio S., Crampton D., Murowinski R., Juneau S., Carlberg R. G., Jørgensen I., Roth K., Chen H.-W., Marzke R. O., 2009, ApJ, 695, 101

Davies R. I., Müller Sánchez F., Genzel R., Tacconi L. J., Hicks E. K. S., Friedrich S., Sternberg A., 2007, ApJ, 671, 1388

Davis S. W., Laor A., 2011, ApJ, 728, 98

de La Calle Pérez I., Longinotti A. L., Guainazzi M., Bianchi S., Dovčiak M., Cappi M., Matt G., Miniutti G., Petrucci P. O., Piconcelli E., Ponti G., Porquet D., Santos-Lleó M., 2010, A&A, 524, A50

De Rosa G., Venemans B. P., Decarli R., Gennaro M., Simcoe R. A., Dietrich M., Peterson B. M., Walter F., Frank S., McMahon R. G., Hewett P. C., Mortlock D. J., Simpson C., 2014, ApJ, 790, 145

Debuhr J., Quataert E., Ma C.-P., 2011, MNRAS, 412, 1341

Debuhr J., Quataert E., Ma C.-P., 2012, MNRAS, 420, 2221

Debuhr J., Quataert E., Ma C.-P., Hopkins P., 2010, MNRAS, 406, L55

Decarli R., Falomo R., Treves A., Labita M., Kotilainen J. K., Scarpa R., 2010, MNRAS, 402, 2453

Dekel A., Birnboim Y., 2006, MNRAS, 368, 2

Devecchi B., Volonteri M., 2009, ApJ, 694, 302

Devriendt J. E. G., Guiderdoni B., Sadat R., 1999, A&A, 350, 381

Di Matteo T., Springel V., Hernquist L., 2005, Nature, 433, 604

Diamond-Stanic A. M., Rieke G. H., 2012, ApJ, 746, 168

D'Odorico V., Cristiani S., Romano D., Granato G. L., Danese L., 2004, MNRAS, 351, 976

Done C., Davis S. W., Jin C., Blaes O., Ward M., 2012, MNRAS, 420, 1848

Done C., Jin C., Middleton M., Ward M., 2013, MNRAS, 434, 1955

Dotti M., Colpi M., Pallini S., Perego A., Volonteri M., 2013, ApJ, 762, 68

Draine B. T., Lazarian A., 1998, ApJ, 494, L19

Dressler A., 1989, in IAU Symposium, Vol. 134, Active Galactic Nuclei, Osterbrock D. E., Miller J. S., eds., p. 217

Duncan K., Conselice C. J., Mortlock A., Hartley W. G., Guo Y., Ferguson H. C., Davé R., Lu Y., Ownsworth J., Ashby M. L. N., Dekel A., Dickinson M., Faber S., Giavalisco M., Grogin N., Kocevski D., Koekemoer A., Somerville R. S., White C. E., 2014, MNRAS, 444, 2960

Dwelly T., Page M. J., 2006, MNRAS, 372, 1755

Eales S. A. et al., 2010, A&A, 518, L23

Ebisuzaki T., Makino J., Tsuru T. G., Funato Y., Portegies Zwart S., Hut P., McMillan S., Matsushita S., Matsumoto H., Kawabe R., 2001, ApJ, 562, L19

Efstathiou A., Pearson C., Farrah D., Rigopoulou D., Graciá-Carpio J., Verma A., Spoon H. W. W., Afonso J., Bernard-Salas J., Clements D. L., Cooray A., Cormier D., Etxaluze M., Fischer J., González-Alfonso E., Hurley P., Lebouteiller V., Oliver S. J., Rowan-Robinson M., Sturm E., 2014, MNRAS, 437, L16

Efstathiou A., Rowan-Robinson M., 1995, MNRAS, 273, 649

Efstathiou G., Ellis R. S., Peterson B. A., 1988, MNRAS, 232, 431

Eisenstein D. J., Loeb A., 1995, ApJ, 443, 11

Elbaz D. et al., 2011, A&A, 533, A119

Elvis M., Risaliti G., Zamorani G., 2002, ApJ, 565, L75

Elvis M., Wilkes B. J., McDowell J. C., Green R. F., Bechtold J., Willner S. P., Oey M. S., Polomski E., Cutri R., 1994, ApJS, 95, 1

Everett J. E., 2005, ApJ, 631, 689

Fabian A. C., 1999, MNRAS, 308, L39

Fabian A. C., 2012, ARA&A, 50, 455

Fabian A. C., Iwasawa K., 1999, MNRAS, 303, L34

Fan L., Chen Y., Er X., Li J., Lin L., Kong X., 2013, MNRAS, 431, L15

Fan L., Lapi A., Bressan A., Bernardi M., De Zotti G., Danese L., 2010, ApJ, 718, 1460

Fan L., Lapi A., De Zotti G., Danese L., 2008, ApJ, 689, L101

Fan L.-L., Lapi A., Bressan A., Nonino M., De Zotti G., Danese L., 2014, Research in Astronomy and Astrophysics, 14, 15

Fan X., 2006, New A Rev., 50, 665

Fan X., Narayanan V. K., Lupton R. H., Strauss M. A., Knapp G. R., Becker R. H., White R. L., Pentericci L., Leggett S. K., Haiman Z., Gunn J. E., Ivezić Ž., Schneider D. P., Anderson S. F., Brinkmann J., Bahcall N. A., Connolly A. J., Csabai I., Doi M., Fukugita M., Geballe T., Grebel E. K., Harbeck D., Hennessy G., Lamb D. Q., Miknaitis G., Munn J. A., Nichol R., Okamura S., Pier J. R., Prada F., Richards G. T., Szalay A., York D. G., 2001, AJ, 122, 2833

Fan X., Strauss M. A., Richards G. T., Hennawi J. F., Becker R. H., White R. L., Diamond-Stanic A. M., Donley J. L., Jiang L., Kim J. S., Vestergaard M., Young J. E., Gunn J. E., Lupton R. H., Knapp G. R., Schneider D. P., Brandt W. N., Bahcall N. A., Barentine J. C., Brinkmann J., Brewington H. J., Fukugita M., Harvanek M., Kleinman S. J., Krzesinski J., Long D., Neilsen, Jr. E. H., Nitta A., Snedden S. A., Voges W., 2006, AJ, 131, 1203

Fanidakis N., Baugh C. M., Benson A. J., Bower R. G., Cole S., Done C., Frenk C. S., Hickox R. C., Lacey C., Del P. Lagos C., 2012, MNRAS, 419, 2797

Fathi K., Lundgren A. A., Kohno K., Piñol-Ferrer N., Martín S., Espada D., Hatziminaoglou E., Imanishi M., Izumi T., Krips M., Matsushita S., Meier D. S., Nakai N., Sheth K., Turner J., van de Ven G., Wiklind T., 2013, ApJ, 770, L27

Ferrarese L., Ford H., 2005, Space Sci. Rev., 116, 523

Ferrarese L., Merritt D., 2000, ApJ, 539, L9

Feruglio C., Daddi E., Fiore F., Alexander D. M., Piconcelli E., Malacaria C., 2011, ApJ, 729, L4

Feruglio C., Maiolino R., Piconcelli E., Menci N., Aussel H., Lamastra A., Fiore F., 2010, A&A, 518, L155

Feulner G., Gabasch A., Salvato M., Drory N., Hopp U., Bender R., 2005, ApJ, 633, L9

Fine S., Croom S. M., Bland-Hawthorn J., Pimbblet K. A., Ross N. P., Schneider D. P., Shanks T., 2010, MNRAS, 409, 591

Fine S., Croom S. M., Hopkins P. F., Hernquist L., Bland-Hawthorn J., Colless M., Hall P. B., Miller L., Myers A. D., Nichol R., Pimbblet K. A., Ross N. P., Schneider D. P., Shanks T., Sharp R. G., 2008, MNRAS, 390, 1413

Finkelstein S. L., Papovich C., Giavalisco M., Reddy N. A., Ferguson H. C., Koekemoer A. M., Dickinson M., 2010, ApJ, 719, 1250

Finkelstein S. L., Papovich C., Salmon B., Finlator K., Dickinson M., Ferguson H. C., Giavalisco M., Koekemoer A. M., Reddy N. A., Bassett R., Conselice C. J., Dunlop J. S., Faber S. M., Grogin N. A., Hathi N. P., Kocevski D. D., Lai K., Lee K.-S., McLure R. J., Mobasher B., Newman J. A., 2012, ApJ, 756, 164

Finkelstein S. L., Ryan, Jr. R. E., Papovich C., Dickinson M., Song M., Somerville R., Ferguson H. C., Salmon B., Giavalisco M., Koekemoer A. M., Ashby M. L. N., Behroozi P., Castellano M., Dunlop J. S., Faber S. M., Fazio G. G., Fontana A., Grogin N. A., Hathi N., Jaacks J., Kocevski D. D., Livermore R., McLure R. J., Merlin E., Mobasher B., Newman J. A., Rafelski M., Tilvi V., Willner S. P., 2014, ArXiv e-prints

Finkelstein S. L., Song M., Behroozi P., Somerville R. S., Papovich C., Milosavljevic M., Dekel A., Narayanan D., Ashby M. L. N., Cooray A., Fazio G. G., Ferguson H. C., Koekemoer A. M., Salmon B. W., Willner S. P., 2015, ArXiv e-prints

Fioc M., Rocca-Volmerange B., 1997, A&A, 326, 950

Fiore F., Puccetti S., Brusa M., Salvato M., Zamorani G., Aldcroft T., Aussel H., Brunner H., Capak P., Cappelluti N., Civano F., Comastri A., Elvis M., Feruglio C., Finoguenov A., Fruscione A., Gilli R., Hasinger G., Koekemoer A., Kartaltepe J., Ilbert O., Impey C., Le Floc'h E., Lilly S., Mainieri V., Martinez-Sansigre A., McCracken H. J., Menci N., Merloni A., Miyaji T., Sanders D. B., Sargent M., Schinnerer E., Scoville N., Silverman J., Smolcic V., Steffen A., Santini P., Taniguchi Y., Thompson D., Trump J. R., Vignali C., Urry M., Yan L., 2009, ApJ, 693, 447

Fiore F., Puccetti S., Grazian A., Menci N., Shankar F., Santini P., Piconcelli E., Koekemoer A. M., Fontana A., Boutsia K., Castellano M., Lamastra A., Malacaria C., Feruglio C., Mathur S., Miller N., Pannella M., 2012, A&A, 537, A16

Fiore F., Puccetti S., Mathur S., 2012, Advances in Astronomy, 2012, 9

Frank J., King A., Raine D. J., 2002, Accretion Power in Astrophysics: Third Edition

Freitag M., Gürkan M. A., Rasio F. A., 2006, MNRAS, 368, 141

Freitag M., Rasio F. A., Baumgardt H., 2006, MNRAS, 368, 121

Frenk C. S., White S. D. M., 2012, Annalen der Physik, 524, 507

Fu H., Yan L., Scoville N. Z., Capak P., Aussel H., Le Floc'h E., Ilbert O., Salvato M., Kartaltepe J. S., Frayer D. T., Sanders D. B., Sheth K., Taniguchi Y., 2010, ApJ, 722, 653

Fukugita M., Peebles P. J. E., 2004, ApJ, 616, 643

Furusawa J., Sekiguchi K., Takata T., Furusawa H., Shimasaku K., Simpson C., Akiyama M., 2011, ApJ, 727, 111

Gallazzi A., Bell E. F., 2009, ApJS, 185, 253

Gammie C. F., Shapiro S. L., McKinney J. C., 2004, ApJ, 602, 312

Gawiser E., Francke H., Lai K., Schawinski K., Gronwall C., Ciardullo R., Quadri R., Orsi A., Barrientos L. F., Blanc G. A., Fazio G., Feldmeier J. J., Huang J.-s., Infante L., Lira P., Padilla N., Taylor E. N., Treister E., Urry C. M., van Dokkum P. G., Virani S. N., 2007, ApJ, 671, 278

Gebhardt K., Bender R., Bower G., Dressler A., Faber S. M., Filippenko A. V., Green R., Grillmair C., Ho L. C., Kormendy J., Lauer T. R., Magorrian J., Pinkney J., Richstone D., Tremaine S., 2000a, ApJ, 539, L13

Gebhardt K., Kormendy J., Ho L. C., Bender R., Bower G., Dressler A., Faber S. M., Filippenko A. V., Green R., Grillmair C., Lauer T. R., Magorrian J., Pinkney J., Richstone D., Tremaine S., 2000b, ApJ, 543, L5

Gebhardt K., Richstone D., Tremaine S., Lauer T. R., Bender R., Bower G., Dressler A., Faber S. M., Filippenko A. V., Green R., Grillmair C., Ho L. C., Kormendy J., Magorrian J., Pinkney J., 2003, ApJ, 583, 92

Gebhardt K., Thomas J., 2009, ApJ, 700, 1690

Genzel R., Eisenhauer F., Gillessen S., 2010, Reviews of Modern Physics, 82, 3121

Genzel R., Newman S., Jones T., Förster Schreiber N. M., Shapiro K., Genel S., Lilly S. J., Renzini A., Tacconi L. J., Bouché N., Burkert A., Cresci G., Buschkamp P., Carollo C. M., Ceverino D., Davies R., Dekel A., Eisenhauer F., Hicks E., Kurk J., Lutz D., Mancini C., Naab T., Peng Y., Sternberg A., Vergani D., Zamorani G., 2011, ApJ, 733, 101

Genzel R., Tacconi L. J., Combes F., Bolatto A., Neri R., Sternberg A., Cooper M. C., Bouché N., Bournaud F., Burkert A., Comerford J., Cox P., Davis M., Förster Schreiber N. M., Garcia-Burillo S., Gracia-Carpio J., Lutz D., Naab T., Newman S., Saintonge A., Shapiro K., Shapley A., Weiner B., 2012, ApJ, 746, 69

Georgakakis A., Coil A. L., Laird E. S., Griffith R. L., Nandra K., Lotz J. M., Pierce C. M., Cooper M. C., Newman J. A., Koekemoer A. M., 2009, MNRAS, 397, 623

Georgakakis A., Mountrichas G., Salvato M., Rosario D., Pérez-González P. G., Lutz D., Nandra K., Coil A., Cooper M. C., Newman J. A., Berta S., Magnelli B., Popesso P., Pozzi F., 2014, MNRAS, 443, 3327

Georgantopoulos I., Akylas A., Georgakakis A., Rowan-Robinson M., 2009, A&A, 507, 747

Georgantopoulos I., Rovilos E., Comastri A., 2011, A&A, 526, A46

Gerhard O., Kronawitter A., Saglia R. P., Bender R., 2001, AJ, 121, 1936

Ghez A. M., Salim S., Hornstein S. D., Tanner A., Lu J. R., Morris M., Becklin E. E., Duchêne G., 2005, ApJ, 620, 744

Ghez A. M., Salim S., Weinberg N. N., Lu J. R., Do T., Dunn J. K., Matthews K., Morris M. R., Yelda S., Becklin E. E., Kremenek T., Milosavljevic M., Naiman J., 2008, ApJ, 689, 1044

Giallongo E., D'Odorico S., Fontana A., Cristiani S., Egami E., Hu E., McMahon R. G., 1998, AJ, 115, 2169

Gierliński M., Done C., 2004, MNRAS, 349, L7

Gillessen S., Eisenhauer F., Fritz T. K., Bartko H., Dodds-Eden K., Pfuhl O., Ott T., Genzel R., 2009a, ApJ, 707, L114

Gillessen S., Eisenhauer F., Trippe S., Alexander T., Genzel R., Martins F., Ott T., 2009b, ApJ, 692, 1075

Gilli R., Su J., Norman C., Vignali C., Comastri A., Tozzi P., Rosati P., Stiavelli M., Brandt W. N., Xue Y. Q., Luo B., Castellano M., Fontana A., Fiore F., Mainieri V., Ptak A., 2011, ApJ, 730, L28

Glikman E., Helfand D. J., White R. L., Becker R. H., Gregg M. D., Lacy M., 2007, ApJ, 667, 673

González V., Bouwens R., Illingworth G., Labbé I., Oesch P., Franx M., Magee D., 2014, ApJ, 781, 34

González V., Labbé I., Bouwens R. J., Illingworth G., Franx M., Kriek M., 2011, ApJ, 735, L34

González-Nuevo J., Lapi A., Fleuren S., Bressan S., Danese L., De Zotti G., Negrello M., Cai Z.-Y., Fan L., Sutherland W., Baes M., Baker A. J., Clements D. L., Cooray A., Dannerbauer H., Dunne L., Dye S., Eales S., Frayer D. T., Harris A. I., Ivison R., Jarvis M. J., Michałowski M. J., López-Caniego M., Rodighiero G., Rowlands K.,

Serjeant S., Scott D., van der Werf P., Auld R., Buttiglione S., Cava A., Dariush A., Fritz J., Hopwood R., Ibar E., Maddox S., Pascale E., Pohlen M., Rigby E., Smith D., Temi P., 2012, ApJ, 749, 65

Goosmann R. W., Czerny B., Mouchet M., Ponti G., Dovčiak M., Karas V., Różańska A., Dumont A.-M., 2006, A&A, 454, 741

Gordon K. D., Clayton G. C., Witt A. N., Misselt K. A., 2000, ApJ, 533, 236

Goulding A. D., Alexander D. M., 2009, MNRAS, 398, 1165

Graham A. W., 2007, MNRAS, 379, 711

Graham A. W., Driver S. P., 2007, ApJ, 655, 77

Graham A. W., Erwin P., Caon N., Trujillo I., 2001, ApJ, 563, L11

Graham A. W., Li I.-h., 2009, ApJ, 698, 812

Graham A. W., Onken C. A., Athanassoula E., Combes F., 2011, MNRAS, 412, 2211

Granato G. L., Danese L., 1994, MNRAS, 268, 235

Granato G. L., De Zotti G., Silva L., Bressan A., Danese L., 2004, ApJ, 600, 580

Granato G. L., Silva L., Lapi A., Shankar F., De Zotti G., Danese L., 2006, MNRAS, 368, L72

Grazian A., Fontana A., Moscardini L., Salimbeni S., Menci N., Giallongo E., de Santis C., Gallozzi S., Nonino M., Cristiani S., Vanzella E., 2006, A&A, 453, 507

Greene J. E., Ho L. C., 2005, ApJ, 630, 122

Greene J. E., Ho L. C., 2007, ApJ, 667, 131

Greene J. E., Ho L. C., Barth A. J., 2008, ApJ, 688, 159

Greene J. E., Peng C. Y., Kim M., Kuo C.-Y., Braatz J. A., Impellizzeri C. M. V., Condon J. J., Lo K. Y., Henkel C., Reid M. J., 2010, ApJ, 721, 26

Greene J. E., Peng C. Y., Ludwig R. R., 2010, ApJ, 709, 937

Greene J. E., Seth A., den Brok M., Braatz J. A., Henkel C., Sun A.-L., Peng C. Y., Kuo C.-Y., Impellizzeri C. M. V., Lo K. Y., 2013, ApJ, 771, 121

Greene J. E., Zakamska N. L., Smith P. S., 2012, ApJ, 746, 86

Greenhill L. J., Kondratko P. T., Moran J. M., Tilak A., 2009, ApJ, 707, 787

Grier C. J., Peterson B. M., Horne K., Bentz M. C., Pogge R. W., Denney K. D., De Rosa G., Martini P., Kochanek C. S., Zu Y., Shappee B., Siverd R., Beatty T. G., Sergeev S. G., Kaspi S., Araya Salvo C., Bird J. C., Bord D. J., Borman G. A., Che X., Chen C., Cohen S. A., Dietrich M., Doroshenko V. T., Efimov Y. S., Free N., Ginsburg I., Henderson C. B., King A. L., Mogren K., Molina M., Mosquera A. M., Nazarov S. V., Okhmat D. N., Pejcha O., Rafter S., Shields J. C., Skowron J., Szczygiel D. M., Valluri M., van Saders J. L., 2013, ApJ, 764, 47

Groves B., Dopita M. A., Sutherland R. S., Kewley L. J., Fischera J., Leitherer C., Brandl B., van Breugel W., 2008, ApJS, 176, 438

Gruppioni C., Pozzi F., Andreani P., Rodighiero G., Cimatti A., Altieri B., Aussel H., Berta S., Bongiovanni A., Brisbin D., Cava A., Cepa J., Daddi E., Dominguez-Sanchez H., Elbaz D., Förster Schreiber N., Genzel R., Le Floc'h E., Lutz D., Magdis G., Magliocchetti M., Magnelli B., Maiolino R., Nordon R., Peréz-García A. M., Poglitsch A., Popesso P., Riguccini L., Saintonge A., Sanchez-Portal M., Santini P., Shao L., Sturm E., Tacconi L., Valtchanov I., 2010, A&A, 518, L27

Gruppioni C. et al., 2013, MNRAS, 432, 23

Guaita L., Gawiser E., Padilla N., Francke H., Bond N. A., Gronwall C., Ciardullo R., Feldmeier J. J., Sinawa S., Blanc G. A., Virani S., 2010, ApJ, 714, 255

Gültekin K., Richstone D. O., Gebhardt K., Lauer T. R., Pinkney J., Aller M. C., Bender R., Dressler A., Faber S. M., Filippenko A. V., Green R., Ho L. C., Kormendy J., Siopis C., 2009a, ApJ, 695, 1577

Gültekin K., Richstone D. O., Gebhardt K., Lauer T. R., Tremaine S., Aller M. C., Bender R., Dressler A., Faber S. M., Filippenko A. V., Green R., Ho L. C., Kormendy J., Magorrian J., Pinkney J., Siopis C., 2009b, ApJ, 698, 198

Guzzo L. et al., 2008, Nature, 451, 541

Haardt F., Maraschi L., 1991, ApJ, 380, L51

Haehnelt M. G., Rees M. J., 1993, MNRAS, 263, 168

Hailey-Dunsheath S., Sturm E., Fischer J., Sternberg A., Graciá-Carpio J., Davies R., González-Alfonso E., Mark D., Poglitsch A., Contursi A., Genzel R., Lutz D., Tacconi L., Veilleux S., Verma A., de Jong J. A., 2012, ApJ, 755, 57

Haiman Z., Loeb A., 2001, ApJ, 552, 459

Han J., Eke V. R., Frenk C. S., Mandelbaum R., Norberg P., Schneider M. D., Peacock J. A., Jing Y., Baldry I., Bland-Hawthorn J., Brough S., Brown M. J. I., Liske J., Loveday J., Robotham A. S. G., 2015, MNRAS, 446, 1356

Hao C.-N., Kennicutt R. C., Johnson B. D., Calzetti D., Dale D. A., Moustakas J., 2011, ApJ, 741, 124

Hao H., Elvis M., Civano F., Zamorani G., Ho L. C., Comastri A., Brusa M., Bongiorno A., Merloni A., Trump J. R., Salvato M., Impey C. D., Koekemoer A. M., Lanzuisi G., Celotti A., Jahnke K., Vignali C., Silverman J. D., Urry C. M., Schawinski K., Capak P., 2014, MNRAS, 438, 1288

Häring N., Rix H.-W., 2004, ApJ, 604, L89

Harris D. E., Krawczynski H., 2006, ARA&A, 44, 463

Harrison C. M., Alexander D. M., Mullaney J. R., Altieri B., Coia D., Charmandaris V., Daddi E., Dannerbauer H., Dasyra K., Del Moro A., Dickinson M., Hickox R. C., Ivison R. J., Kartaltepe J., Le Floc'h E., Leiton R., Magnelli B., Popesso P., Rovilos E., Rosario D., Swinbank A. M., 2012, ApJ, 760, L15

Hasinger G., 2008, A&A, 490, 905

Hawkins E., Maddox S., Cole S., Lahav O., Madgwick D. S., Norberg P., Peacock J. A., Baldry I. K., Baugh C. M., Bland-Hawthorn J., Bridges T., Cannon R., Colless M., Collins C., Couch W., Dalton G., De Propris R., Driver S. P., Efstathiou G., Ellis R. S., Frenk C. S., Glazebrook K., Jackson C., Jones B., Lewis I., Lumsden S., Percival W., Peterson B. A., Sutherland W., Taylor K., 2003, MNRAS, 346, 78

Hayashi M., Shimasaku K., Motohara K., Yoshida M., Okamura S., Kashikawa N., 2007, ApJ, 660, 72

Heckman T. M., Best P. N., 2014, ARA&A, 52, 589

Heckman T. M., Robert C., Leitherer C., Garnett D. R., van der Rydt F., 1998, ApJ, 503, 646

Heinis S., Buat V., Béthermin M., Bock J., Burgarella D., Conley A., Cooray A., Farrah D., Ilbert O., Magdis G., Marsden G., Oliver S. J., Rigopoulou D., Roehlly Y., Schulz B., Symeonidis M., Viero M., Xu C. K., Zemcov M., 2014, MNRAS, 437, 1268

Helou G., Soifer B. T., Rowan-Robinson M., 1985, ApJ, 298, L7

Hernquist L., Mihos J. C., 1995, ApJ, 448, 41

Herrnstein J. R., Moran J. M., Greenhill L. J., Trotter A. S., 2005, ApJ, 629, 719

Hickox R. C., Jones C., Forman W. R., Murray S. S., Kochanek C. S., Eisenstein D., Jannuzi B. T., Dey A., Brown M. J. I., Stern D., Eisenhardt P. R., Gorjian V., Brodwin M., Narayan R., Cool R. J., Kenter A., Caldwell N., Anderson M. E., 2009, ApJ, 696, 891

Hickox R. C., Myers A. D., Brodwin M., Alexander D. M., Forman W. R., Jones C., Murray S. S., Brown M. J. I., Cool R. J., Kochanek C. S., Dey A., Jannuzi B. T., Eisenstein D., Assef R. J., Eisenhardt P. R., Gorjian V., Stern D., Le Floc'h E., Caldwell N., Goulding A. D., Mullaney J. R., 2011, ApJ, 731, 117

Hickox R. C., Wardlow J. L., Smail I., Myers A. D., Alexander D. M., Swinbank A. M., Danielson A. L. R., Stott J. P., Chapman S. C., Coppin K. E. K., Dunlop J. S., Gawiser E., Lutz D., van der Werf P., Weiß A., 2012, MNRAS, 421, 284

Hirashita H., Inoue A. K., Kamaya H., Shibai H., 2001, A&A, 366, 83

Hiroi K., Ueda Y., Akiyama M., Watson M. G., 2012, ApJ, 758, 49

Ho L. C., Filippenko A. V., Sargent W. L. W., 1997, ApJ, 487, 568

Ho L. C., Kim M., 2014, ApJ, 789, 17

Hönig S. F., Kishimoto M., 2010, A&A, 523, A27

Hönig S. F., Kishimoto M., Gandhi P., Smette A., Asmus D., Duschl W., Polletta M., Weigelt G., 2010, A&A, 515, A23

Hönig S. F., Kishimoto M., Tristram K. R. W., Prieto M. A., Gandhi P., Asmus D., Antonucci R., Burtscher L., Duschl W. J., Weigelt G., 2013, ApJ, 771, 87

Hopkins A. M., Connolly A. J., Haarsma D. B., Cram L. E., 2001, AJ, 122, 288

Hopkins P. F., Hernquist L., Cox T. J., Kereš D., 2008, ApJS, 175, 356

Hopkins P. F., Quataert E., 2010, MNRAS, 407, 1529

Hopkins P. F., Quataert E., 2011, MNRAS, 415, 1027

Hopkins P. F., Richards G. T., Hernquist L., 2007, ApJ, 654, 731

Hopkins P. F., Robertson B., Krause E., Hernquist L., Cox T. J., 2006, ApJ, 652, 107

Howarth I. D., 1983, MNRAS, 203, 301

Howell J. H., Armus L., Mazzarella J. M., Evans A. S., Surace J. A., Sanders D. B., Petric A., Appleton P., Bothun G., Bridge C., Chan B. H. P., Charmandaris V., Frayer D. T., Haan S., Inami H., Kim D.-C., Lord S., Madore B. F., Melbourne J., Schulz B., U V., Vavilkin T., Veilleux S., Xu K., 2010, ApJ, 715, 572

Hu J., 2008, MNRAS, 386, 2242

Hughes M. A., Axon D., Atkinson J., Alonso-Herrero A., Scarlata C., Marconi A., Batcheldor D., Binney J., Capetti A., Carollo C. M., Dressel L., Gerssen J., Macchetto D., Maciejewski W., Merrifield M., Ruiz M., Sparks W., Stiavelli M., Tsvetanov Z., 2005, AJ, 130, 73

Hughes S. A., Blandford R. D., 2003, ApJ, 585, L101

Ikarashi S., Ivison R. J., Caputi K. I., Aretxaga I., Dunlop J. S., Hatsukade B., Hughes D., Iono D., Izumi T., Kawabe R., Kohno K., Lagos C. P., Motohara K., Nakanishi K., Ohta K., Tamura Y., Umehata H., Wilson G., Yabe K., Yun M. S., 2014, ArXiv e-prints

Ilbert O., Arnouts S., Le Floc'h E., Aussel H., Bethermin M., Capak P., Hsieh B.-C., Kajisawa M., Karim A., Le Fèvre O., Lee N., Lilly S., McCracken H. J., Michel-Dansac L., Moutard T., Renzini M. A., Salvato M., Sanders D. B., Scoville N., Sheth K., Silverman J. D., Smolčić V., Taniguchi Y., Tresse L., 2015, A&A, 579, A2

Ilbert O., McCracken H. J., Le Fèvre O., Capak P., Dunlop J., Karim A., Renzini M. A., Caputi K., Boissier S., Arnouts S., Aussel H., Comparat J., Guo Q., Hudelot P., Kartaltepe J., Kneib J. P., Krogager J. K., Le Floc'h E., Lilly S., Mellier Y., Milvang-Jensen B., Moutard T., Onodera M., Richard J., Salvato M., Sanders D. B., Scoville N., Silverman J. D., Taniguchi Y., Tasca L., Thomas R., Toft S., Tresse L., Vergani D., Wolk M., Zirm A., 2013, A&A, 556, A55

Ilbert O., Tresse L., Arnouts S., Zucca E., Bardelli S., Zamorani G., Adami C., Cappi A., Garilli B., Le Fèvre O., Maccagni D., Meneux B., Scaramella R., Scodeggio M., Vettolani G., Zanichelli A., 2004, MNRAS, 351, 541

Immeli A., Samland M., Gerhard O., Westera P., 2004, A&A, 413, 547

Ishibashi W., Fabian A. C., 2012, MNRAS, 427, 2998

Ivison R. J. et al., 2010, A&A, 518, L31

Iwasawa K., Gilli R., Vignali C., Comastri A., Brandt W. N., Ranalli P., Vito F., Cappelluti N., Carrera F. J., Falocco S., Georgantopoulos I., Mainieri V., Paolillo M., 2012, A&A, 546, A84

Izumi T., Kohno K., Martín S., Espada D., Harada N., Matsushita S., Hsieh P.-Y., Turner J. L., Meier D. S., Schinnerer E., Imanishi M., Tamura Y., Curran M. T., Doi A., Fathi K., Krips M., Lundgren A. A., Nakai N., Nakajima T., Regan M. W., Sheth K., Takano S., Taniguchi A., Terashima Y., Tosaki T., Wiklind T., 2013, PASJ, 65, 100

Jahnke K., Macciò A. V., 2011, ApJ, 734, 92

Jarvis M. J., Smith D. J. B., Bonfield D. G., Hardcastle M. J., Falder J. T., Stevens J. A., Ivison R. J., Auld R., Baes M., Baldry I. K., Bamford S. P., Bourne N., Buttiglione S., Cava A., Cooray A., Dariush A., de Zotti G., Dunlop J. S., Dunne L., Dye S., Eales S., Fritz J., Hill D. T., Hopwood R., Hughes D. H., Ibar E., Jones D. H., Kelvin L., Lawrence A., Leeuw L., Loveday J., Maddox S. J., Michałowski M. J., Negrello M., Norberg P., Pohlen M., Prescott M., Rigby E. E., Robotham A., Rodighiero G., Scott D., Sharp R., Temi P., Thompson M. A., van der Werf P., van Kampen E., Vlahakis C., White G., 2010, MNRAS, 409, 92

Jiang F., van den Bosch F. C., 2014, ArXiv e-prints

Jiang L., Fan X., Bian F., Annis J., Chiu K., Jester S., Lin H., Lupton R. H., Richards G. T., Strauss M. A., Malanushenko V., Malanushenko E., Schneider D. P., 2009, AJ, 138, 305

Johnson S. P., Wilson G. W., Wang Q. D., Williams C. C., Scott K. S., Yun M. S., Pope A., Lowenthal J., Aretxaga I., Hughes D., Kim M. J., Kim S., Tamura Y., Kohno K., Ezawa H., Kawabe R., Oshima T., 2013, MNRAS, 431, 662

Kara E., Fabian A. C., Lohfink A. M., Parker M. L., Walton D. J., Boggs S. E., Christensen F. E., Hailey C. J., Harrison F. A., Matt G., Reynolds C. S., Stern D., Zhang W. W., 2015, MNRAS, 449, 234

Karim A., Schinnerer E., Martínez-Sansigre A., Sargent M. T., van der Wel A., Rix H.-W., Ilbert O., Smolčić V., Carilli C., Pannella M., Koekemoer A. M., Bell E. F., Salvato M., 2011, ApJ, 730, 61

Karim A., Swinbank A. M., Hodge J. A., Smail I. R., Walter F., Biggs A. D., Simpson J. M., Danielson A. L. R., Alexander D. M., Bertoldi F., de Breuck C., Chapman S. C., Coppin K. E. K., Dannerbauer H., Edge A. C., Greve T. R., Ivison R. J., Knudsen K. K., Menten K. M., Schinnerer E., Wardlow J. L., Weiß A., van der Werf P., 2013, MNRAS, 432, 2

Kaspi S., Maoz D., Netzer H., Peterson B. M., Vestergaard M., Jannuzi B. T., 2005, ApJ, 629, 61

Kaspi S., Smith P. S., Netzer H., Maoz D., Jannuzi B. T., Giveon U., 2000, ApJ, 533, 631

Kauffmann G., Haehnelt M., 2000, MNRAS, 311, 576

Kauffmann G., Heckman T. M., 2009, MNRAS, 397, 135

Kawaguchi T., Mori M., 2011, ApJ, 737, 105

Kawaguchi T., Shimura T., Mineshige S., 2001, ApJ, 546, 966

Kawakatu N., Andreani P., Granato G. L., Danese L., 2007, ApJ, 663, 924

Kawakatu N., Ohsuga K., 2011, MNRAS, 417, 2562

Kawakatu N., Umemura M., 2002, MNRAS, 329, 572

Kawakatu N., Umemura M., Mori M., 2003, ApJ, 583, 85

Kawakatu N., Wada K., 2008, ApJ, 681, 73

Kelly B. C., Bechtold J., Siemiginowska A., Aldcroft T., Sobolewska M., 2007, ApJ, 657, 116

Kelly B. C., Merloni A., 2012, Advances in Astronomy, 2012, 7

Kelly B. C., Shen Y., 2013, ApJ, 764, 45

Kelly B. C., Vestergaard M., Fan X., 2009, ApJ, 692, 1388

Kennicutt R. C., Evans N. J., 2012, ARA&A, 50, 531

Kennicutt, Jr. R. C., 1983, ApJ, 272, 54

Kennicutt, Jr. R. C., 1998, ARA&A, 36, 189

Kennicutt, Jr. R. C., Hao C.-N., Calzetti D., Moustakas J., Dale D. A., Bendo G., Engelbracht C. W., Johnson B. D., Lee J. C., 2009, ApJ, 703, 1672

Khandai N., Feng Y., DeGraf C., Di Matteo T., Croft R. A. C., 2012, MNRAS, 423, 2397

King A., 2003, ApJ, 596, L27

King A., 2005, ApJ, 635, L121

King A., 2012, Mem. Soc. Astron. Italiana, 83, 466

King A., 2014, Space Sci. Rev., 183, 427

King A., Pounds K., 2015, ArXiv e-prints

King A. R., Pringle J. E., 2006, MNRAS, 373, L90

King A. R., Pringle J. E., Hofmann J. A., 2008, MNRAS, 385, 1621

Kochanek C. S., White M., Huchra J., Macri L., Jarrett T. H., Schneider S. E., Mader J., 2003, ApJ, 585, 161

Kollmeier J. A., Onken C. A., Kochanek C. S., Gould A., Weinberg D. H., Dietrich M., Cool R., Dey A., Eisenstein D. J., Jannuzi B. T., Le Floc'h E., Stern D., 2006, ApJ, 648, 128

Kondratko P. T., Greenhill L. J., Moran J. M., 2006, ApJ, 652, 136

Konigl A., Kartje J. F., 1994, ApJ, 434, 446

Kormendy J., Bender R., 2009, ApJ, 691, L142

Kormendy J., Ho L. C., 2013, ARA&A, 51, 511

Kormendy J., Richstone D., 1995, ARA&A, 33, 581

Koushiappas S. M., Bullock J. S., Dekel A., 2004, MNRAS, 354, 292

Koutoulidis L., Plionis M., Georgantopoulos I., Fanidakis N., 2013, MNRAS, 428, 1382

Krajnović D., McDermid R. M., Cappellari M., Davies R. L., 2009, MNRAS, 399, 1839

Kravtsov A., Vikhlinin A., Meshscheryakov A., 2014, ArXiv e-prints

Kriek M., Labbé I., Conroy C., Whitaker K. E., van Dokkum P. G., Brammer G. B., Franx M., Illingworth G. D., Marchesini D., Muzzin A., Quadri R. F., Rudnick G., 2010, ApJ, 722, L64

Krips M., Martín S., Eckart A., Neri R., García-Burillo S., Matsushita S., Peck A., Stoklasová I., Petitpas G., Usero A., Combes F., Schinnerer E., Humphreys E., Baker A. J., 2011, ApJ, 736, 37

Krogager J.-K., Zirm A. W., Toft S., Man A., Brammer G., 2014, ApJ, 797, 17

Kroupa P., 2001, MNRAS, 322, 231

Kroupa P., Tout C. A., Gilmore G., 1993, MNRAS, 262, 545

Kulier A., Ostriker J. P., Natarajan P., Lackner C. N., Cen R., 2015, ApJ, 799, 178

Kumar P., 1999, ApJ, 519, 599

Kuo C. Y., Braatz J. A., Condon J. J., Impellizzeri C. M. V., Lo K. Y., Zaw I., Schenker M., Henkel C., Reid M. J., Greene J. E., 2011, ApJ, 727, 20

Kurucz R. L., 1979, ApJS, 40, 1

Lacey C. G., Baugh C. M., Frenk C. S., Benson A. J., Orsi A., Silva L., Granato G. L., Bressan A., 2010, MNRAS, 405, 2

Lacki B. C., Thompson T. A., 2010, ApJ, 717, 196

Laird E. S., Nandra K., Adelberger K. L., Steidel C. C., Reddy N. A., 2005, MNRAS, 359, 47

Laird E. S., Nandra K., Hobbs A., Steidel C. C., 2006, MNRAS, 373, 217

Laird E. S., Nandra K., Pope A., Scott D., 2010, MNRAS, 401, 2763

Laor A., Netzer H., 1989, MNRAS, 238, 897

Laor A., Netzer H., Piran T., 1990, MNRAS, 242, 560

Lapi A., Cavaliere A., 2011, ApJ, 743, 127

Lapi A., Danese L., 2014, J. Cosmology Astropart. Phys., 7, 44

Lapi A., González-Nuevo J., Fan L., Bressan A., De Zotti G., Danese L., Negrello M., Dunne L., Eales S., Maddox S., Auld R., Baes M., Bonfield D. G., Buttiglione S., Cava A., Clements D. L., Cooray A., Dariush A., Dye S., Fritz J., Herranz D., Hopwood R., Ibar E., Ivison R., Jarvis M. J., Kaviraj S., López-Caniego M., Massardi M., Michałowski M. J., Pascale E., Pohlen M., Rigby E., Rodighiero G., Serjeant S., Smith D. J. B., Temi P., Wardlow J., van der Werf P., 2011, ApJ, 742, 24

Lapi A., Negrello M., González-Nuevo J., Cai Z.-Y., De Zotti G., Danese L., 2012, ApJ, 755, 46

Lapi A., Raimundo S., Aversa R., Cai Z.-Y., Negrello M., Celotti A., De Zotti G., Danese L., 2014, ApJ, 782, 69

Lapi A., Salucci P., Danese L., 2013, ApJ, 772, 85

Lapi A., Shankar F., Mao J., Granato G. L., Silva L., De Zotti G., Danese L., 2006, ApJ, 650, 42

Lauer T. R., Gebhardt K., Faber S. M., Richstone D., Tremaine S., Kormendy J., Aller M. C., Bender R., Dressler A., Filippenko A. V., Green R., Ho L. C., 2007, ApJ, 664, 226

Leauthaud A., Tinker J., Bundy K., Behroozi P. S., Massey R., Rhodes J., George M. R., Kneib J.-P., Benson A., Wechsler R. H., Busha M. T., Capak P., Cortês M., Ilbert O., Koekemoer A. M., Le Fèvre O., Lilly S., McCracken H. J., Salvato M., Schrabback T., Scoville N., Smith T., Taylor J. E., 2012, ApJ, 744, 159

Lee K.-S., Dey A., Reddy N., Brown M. J. I., Gonzalez A. H., Jannuzi B. T., Cooper M. C., Fan X., Bian F., Glikman E., Stern D., Brodwin M., Cooray A., 2011, ApJ, 733, 99

Lee K.-S., Giavalisco M., Gnedin O. Y., Somerville R. S., Ferguson H. C., Dickinson M., Ouchi M., 2006, ApJ, 642, 63

Lehmer B. D., Alexander D. M., Bauer F. E., Brandt W. N., Goulding A. D., Jenkins L. P., Ptak A., Roberts T. P., 2010, ApJ, 724, 559

Lehmer B. D., Brandt W. N., Alexander D. M., Bauer F. E., Conselice C. J., Dickinson M. E., Giavalisco M., Grogin N. A., Koekemoer A. M., Lee K.-S., Moustakas L. A., Schneider D. P., 2005, AJ, 129, 1

Leipski C., Meisenheimer K., Walter F., Besel M.-A., Dannerbauer H., Fan X., Haas M., Klaas U., Krause O., Rix H.-W., 2013, ApJ, 772, 103

Leitherer C., Schaerer D., Goldader J. D., Delgado R. M. G., Robert C., Kune D. F., de Mello D. F., Devost D., Heckman T. M., 1999, ApJS, 123, 3

Leja J., van Dokkum P. G., Franx M., Whitaker K. E., 2015, ApJ, 798, 115

Li J., Ostriker J., Sunyaev R., 2013, ApJ, 767, 105

Li L.-X., 2012, MNRAS, 424, 1461

Li Y.-R., Ho L. C., Wang J.-M., 2011, ApJ, 742, 33

Lin L., Dickinson M., Jian H.-Y., Merson A. I., Baugh C. M., Scott D., Foucaud S., Wang W.-H., Yan C.-H., Yan H.-J., Cheng Y.-W., Guo Y., Helly J., Kirsten F., Koo D. C., Lagos C. d. P., Meger N., Messias H., Pope A., Simard L., Grogin N. A., Wang S.-Y., 2012, ApJ, 756, 71

Liu C., Yuan F., Ostriker J. P., Gan Z., Yang X., 2013, MNRAS, 434, 1721

Liu F. S., Lei F. J., Meng X. M., Jiang D. F., 2015, MNRAS, 447, 1491

Lo K. Y., 2005, ARA&A, 43, 625

Lodato G., Natarajan P., 2006, MNRAS, 371, 1813

Loeb A., Rasio F. A., 1994, ApJ, 432, 52

Lorenzoni S., Bunker A. J., Wilkins S. M., Caruana J., Stanway E. R., Jarvis M. J., 2013, MNRAS, 429, 150

Lupi A., Colpi M., Devecchi B., Galanti G., Volonteri M., 2014, MNRAS, 442, 3616

Lusso E., Comastri A., Simmons B. D., Mignoli M., Zamorani G., Vignali C., Brusa M., Shankar F., Lutz D., Trump J. R., Maiolino R., Gilli R., Bolzonella M., Puccetti S., Salvato M., Impey C. D., Civano F., Elvis M., Mainieri V., Silverman J. D., Koekemoer A. M., Bongiorno A., Merloni A., Berta S., Le Floc'h E., Magnelli B., Pozzi F., Riguccini L., 2012, MNRAS, 425, 623

Lusso E., Comastri A., Vignali C., Zamorani G., Brusa M., Gilli R., Iwasawa K., Salvato M., Civano F., Elvis M., Merloni A., Bongiorno A., Trump J. R., Koekemoer A. M., Schinnerer E., Le Floc'h E., Cappelluti N., Jahnke K., Sargent M., Silverman J., Mainieri V., Fiore F., Bolzonella M., Le Fèvre O., Garilli B., Iovino A., Kneib J. P., Lamareille F., Lilly S., Mignoli M., Scodeggio M., Vergani D., 2010, A&A, 512, A34

Lutz D., Mainieri V., Rafferty D., Shao L., Hasinger G., Weiß A., Walter F., Smail I., Alexander D. M., Brandt W. N., Chapman S., Coppin K., Förster Schreiber N. M., Gawiser E., Genzel R., Greve T. R., Ivison R. J., Koekemoer A. M., Kurczynski P., Menten K. M., Nordon R., Popesso P., Schinnerer E., Silverman J. D., Wardlow J., Xue Y. Q., 2010, ApJ, 712, 1287

Lynden-Bell D., 1971, MNRAS, 155, 95

Macchetto F., Marconi A., Axon D. J., Capetti A., Sparks W., Crane P., 1997, ApJ, 489, 579

Maciejewski W., Binney J., 2001, MNRAS, 323, 831

Madau P., Dickinson M., 2014, ARA&A, 52, 415

Madau P., Haardt F., Dotti M., 2014, ApJ, 784, L38

Magnelli B., Popesso P., Berta S., Pozzi F., Elbaz D., Lutz D., Dickinson M., Altieri B., Andreani P., Aussel H., Béthermin M., Bongiovanni A., Cepa J., Charmandaris V., Chary R.-R., Cimatti A., Daddi E., Förster Schreiber N. M., Genzel R., Gruppioni C., Harwit M., Hwang H. S., Ivison R. J., Magdis G., Maiolino R., Murphy E., Nordon R., Pannella M., Pérez García A., Poglitsch A., Rosario D., Sanchez-Portal M., Santini P., Scott D., Sturm E., Tacconi L. J., Valtchanov I., 2013, A&A, 553, A132

Magorrian J., Tremaine S., Richstone D., Bender R., Bower G., Dressler A., Faber S. M., Gebhardt K., Green R., Grillmair C., Kormendy J., Lauer T., 1998, AJ, 115, 2285

Mahmood A., Devriendt J. E. G., Silk J., 2005, MNRAS, 359, 1363

Mainieri V. et al., 2011, A&A, 535, A80

Mainieri V., Hasinger G., Cappelluti N., Brusa M., Brunner H., Civano F., Comastri A., Elvis M., Finoguenov A., Fiore F., Gilli R., Lehmann I., Silverman J., Tasca L., Vignali C., Zamorani G., Schinnerer E., Impey C., Trump J., Lilly S., Maier C., Griffiths R. E., Miyaji T., Capak P., Koekemoer A., Scoville N., Shopbell P., Taniguchi Y., 2007, ApJS, 172, 368

Maiolino R., 2008, New A Rev., 52, 339

Maiolino R., Gallerani S., Neri R., Cicone C., Ferrara A., Genzel R., Lutz D., Sturm E., Tacconi L. J., Walter F., Feruglio C., Fiore F., Piconcelli E., 2012, MNRAS, 425, L66

Maiolino R., Marconi A., Salvati M., Risaliti G., Severgnini P., Oliva E., La Franca F., Vanzi L., 2001, A&A, 365, 28

Maiolino R., Oliva E., Ghinassi F., Pedani M., Mannucci F., Mujica R., Juarez Y., 2004, A&A, 420, 889

Man A. W. S., Greve T. R., Toft S., Magnelli B., Karim A., Ilbert O., Salvato M., Le Floc'h E., Bertoldi F., Casey C. M., Lee N., Li Y., Navarrete F., Sheth K., Smolcic V., Sanders D. B., Schinnerer E., Zirm A. W., 2014, ArXiv e-prints

Mancuso C., Lapi A., Cai Z.-Y., Negrello M., De Zotti G., Bressan A., Bonato M., Perrotta F., Danese L., 2015, ArXiv e-prints

Mandelbaum R., Seljak U., Cool R. J., Blanton M., Hirata C. M., Brinkmann J., 2006, MNRAS, 372, 758

Mao J., Lapi A., Granato G. L., de Zotti G., Danese L., 2007, ApJ, 667, 655

Mao M. Y., Huynh M. T., Norris R. P., Dickinson M., Frayer D., Helou G., Monkiewicz J. A., 2011, ApJ, 731, 79

Maraston C., 1998, MNRAS, 300, 872

Maraston C., 2005, MNRAS, 362, 799

Maraston C., Daddi E., Renzini A., Cimatti A., Dickinson M., Papovich C., Pasquali A., Pirzkal N., 2006, ApJ, 652, 85

Maraston C., Pforr J., Henriques B. M., Thomas D., Wake D., Brownstein J. R., Capozzi D., Tinker J., Bundy K., Skibba R. A., Beifiori A., Nichol R. C., Edmondson E., Schneider D. P., Chen Y., Masters K. L., Steele O., Bolton A. S., York D. G., Weaver B. A., Higgs T., Bizyaev D., Brewington H., Malanushenko E., Malanushenko V., Snedden S., Oravetz D., Pan K., Shelden A., Simmons A., 2013, MNRAS, 435, 2764

Maraston C., Pforr J., Renzini A., Daddi E., Dickinson M., Cimatti A., Tonini C., 2010, MNRAS, 407, 830

Marchesini D., Muzzin A., Stefanon M., Franx M., Brammer G. G., Marsan C. Z., Vulcani B., Fynbo J. P. U., Milvang-Jensen B., Dunlop J. S., Buitrago F., 2014, ApJ, 794, 65

Marchesini D., van Dokkum P. G., Förster Schreiber N. M., Franx M., Labbé I., Wuyts S., 2009, ApJ, 701, 1765

Marchesini D., Whitaker K. E., Brammer G., van Dokkum P. G., Labbé I., Muzzin A., Quadri R. F., Kriek M., Lee K.-S., Rudnick G., Franx M., Illingworth G. D., Wake D., 2010, ApJ, 725, 1277

Marconi A., Axon D. J., Capetti A., Maciejewski W., Atkinson J., Batcheldor D., Binney J., Carollo C. M., Dressel L., Ford H., Gerssen J., Hughes M. A., Macchetto D., Merrifield M. R., Scarlata C., Sparks W., Stiavelli M., Tsvetanov Z., van der Marel R. P., 2003, ApJ, 586, 868

Marconi A., Capetti A., Axon D. J., Koekemoer A., Macchetto D., Schreier E. J., 2001, ApJ, 549, 915

Marconi A., Hunt L. K., 2003, ApJ, 589, L21

Marconi A., Risaliti G., Gilli R., Hunt L. K., Maiolino R., Salvati M., 2004, MNRAS, 351, 169

Marcum P. M., O'Connell R. W., Fanelli M. N., Cornett R. H., Waller W. H., Bohlin R. C., Neff S. G., Roberts M. S., Smith A. M., Cheng K.-P., Collins N. R., Hennessy G. S., Hill J. K., Hill R. S., Hintzen P., Landsman W. B., Ohl R. G., Parise R. A., Smith E. P., Freedman W. L., Kuchinski L. E., Madore B., Angione R., Palma C., Talbert F., Stecher T. P., 2001, ApJS, 132, 129

Marigo P., Girardi L., Bressan A., Groenewegen M. A. T., Silva L., Granato G. L., 2008, A&A, 482, 883

Martin D. C., Fanson J., Schiminovich D., Morrissey P., Friedman P. G., Barlow T. A., Conrow T., Grange R., Jelinsky P. N., Milliard B., Siegmund O. H. W., Bianchi L., Byun Y.-I., Donas J., Forster K., Heckman T. M., Lee Y.-W., Madore B. F., Malina R. F., Neff S. G., Rich R. M., Small T., Surber F., Szalay A. S., Welsh B., Wyder T. K., 2005, ApJ, 619, L1

Martínez H. J., Zandivarez A., Merchán M. E., Domínguez M. J. L., 2002, MNRAS, 337, 1441

Martínez-Sansigre A., Taylor A. M., 2009, ApJ, 692, 964

Martini P., Weinberg D. H., 2001, ApJ, 547, 12

Marziani P., Sulentic J. W., 2012, New A Rev., 56, 49

Mashian N., Oesch P., Loeb A., 2015, ArXiv e-prints

Mason K. O., Breeveld A., Much R., Carter M., Cordova F. A., Cropper M. S., Fordham J., Huckle H., Ho C., Kawakami H., Kennea J., Kennedy T., Mittaz J., Pandel D.,

Priedhorsky W. C., Sasseen T., Shirey R., Smith P., Vreux J.-M., 2001, A&A, 365, L36

Masters D., Capak P., Salvato M., Civano F., Mobasher B., Siana B., Hasinger G., Impey C. D., Nagao T., Trump J. R., Ikeda H., Elvis M., Scoville N., 2012, ApJ, 755, 169

Mateos S., Barcons X., Carrera F. J., Ceballos M. T., Hasinger G., Lehmann I., Fabian A. C., Streblyanska A., 2005, A&A, 444, 79

Matt G., Bianchi S., Guainazzi M., Molendi S., 2004, A&A, 414, 155

McAlary C. W., Rieke G. H., 1988, ApJ, 333, 1

McConnell N. J., Ma C.-P., 2013, ApJ, 764, 184

McConnell N. J., Ma C.-P., Gebhardt K., Wright S. A., Murphy J. D., Lauer T. R., Graham J. R., Richstone D. O., 2011, Nature, 480, 215

McConnell N. J., Ma C.-P., Murphy J. D., Gebhardt K., Lauer T. R., Graham J. R., Wright S. A., Richstone D. O., 2012, ApJ, 756, 179

McLure R. J., Dunlop J. S., 2001, MNRAS, 327, 199

McLure R. J., Dunlop J. S., 2002, MNRAS, 331, 795

McLure R. J., Dunlop J. S., 2004, MNRAS, 352, 1390

McLure R. J., Dunlop J. S., Bowler R. A. A., Curtis-Lake E., Schenker M., Ellis R. S., Robertson B. E., Koekemoer A. M., Rogers A. B., Ono Y., Ouchi M., Charlot S., Wild V., Stark D. P., Furlanetto S. R., Cirasuolo M., Targett T. A., 2013, MNRAS, 432, 2696

McLure R. J., Jarvis M. J., 2002, MNRAS, 337, 109

Melbourne J., Peng C. Y., Soifer B. T., Urrutia T., Desai V., Armus L., Bussmann R. S., Dey A., Matthews K., 2011, AJ, 141, 141

Merloni A., 2004, MNRAS, 353, 1035

Merloni A. et al., 2010, ApJ, 708, 137

Merloni A., Bongiorno A., Brusa M., Iwasawa K., Mainieri V., Magnelli B., Salvato M., Berta S., Cappelluti N., Comastri A., Fiore F., Gilli R., Koekemoer A., Le Floc'h E., Lusso E., Lutz D., Miyaji T., Pozzi F., Riguccini L., Rosario D. J., Silverman J., Symeonidis M., Treister E., Vignali C., Zamorani G., 2014, MNRAS, 437, 3550

Merloni A., Heinz S., 2008, MNRAS, 388, 1011

Merloni A., Heinz S., di Matteo T., 2003, MNRAS, 345, 1057

Merloni A., Heinz S., Di Matteo T., 2005, Ap&SS, 300, 45

Merritt D., Ferrarese L., 2001, ApJ, 547, 140

Meurer G. R., Heckman T. M., Calzetti D., 1999, ApJ, 521, 64

Miller G. E., Scalo J. M., 1979, ApJS, 41, 513

Miller M. C., Hamilton D. P., 2002, MNRAS, 330, 232

Mineshige S., Kawaguchi T., Takeuchi M., Hayashida K., 2000, PASJ, 52, 499

Miyoshi M., Moran J., Herrnstein J., Greenhill L., Nakai N., Diamond P., Inoue M., 1995, Nature, 373, 127

Mobasher B., Dahlen T., Ferguson H. C., Acquaviva V., Barro G., Finkelstein S. L., Fontana A., Gruetzbauch R., Johnson S., Lu Y., Papovich C. J., Pforr J., Salvato M., Somerville R. S., Wiklind T., Wuyts S., Ashby M. L. N., Bell E., Conselice C. J., Dickinson M. E., Faber S. M., Fazio G., Finlator K., Galametz A., Gawiser E., Giavalisco M., Grazian A., Grogin N. A., Guo Y., Hathi N., Kocevski D., Koekemoer A. M., Koo D. C., Newman J. A., Reddy N., Santini P., Wechsler R. H., 2015, ApJ, 808, 101

Mor R., Netzer H., Trakhtenbrot B., Shemmer O., Lira P., 2012, ApJ, 749, L25

Moran J. M., 2008, in Astronomical Society of the Pacific Conference Series, Vol. 395, Frontiers of Astrophysics: A Celebration of NRAO's 50th Anniversary, Bridle A. H., Condon J. J., Hunt G. C., eds., p. 87

Mortlock D. J., Warren S. J., Venemans B. P., Patel M., Hewett P. C., McMahon R. G., Simpson C., Theuns T., Gonzáles-Solares E. A., Adamson A., Dye S., Hambly N. C., Hirst P., Irwin M. J., Kuiper E., Lawrence A., Röttgering H. J. A., 2011, Nature, 474, 616

Moster B. P., Naab T., White S. D. M., 2013, MNRAS, 428, 3121

Moster B. P., Somerville R. S., Maulbetsch C., van den Bosch F. C., Macciò A. V., Naab T., Oser L., 2010, ApJ, 710, 903

Mountrichas G., Georgakakis A., Finoguenov A., Erfanianfar G., Cooper M. C., Coil A. L., Laird E. S., Nandra K., Newman J. A., 2013, MNRAS, 430, 661

Mullaney J. R., Alexander D. M., Goulding A. D., Hickox R. C., 2011, MNRAS, 414, 1082

Mullaney J. R., Daddi E., Béthermin M., Elbaz D., Juneau S., Pannella M., Sargent M. T., Alexander D. M., Hickox R. C., 2012a, ApJ, 753, L30

Mullaney J. R., Pannella M., Daddi E., Alexander D. M., Elbaz D., Hickox R. C., Bournaud F., Altieri B., Aussel H., Coia D., Dannerbauer H., Dasyra K., Dickinson M., Hwang H. S., Kartaltepe J., Leiton R., Magdis G., Magnelli B., Popesso P., Valtchanov I., Bauer F. E., Brandt W. N., Del Moro A., Hanish D. J., Ivison R. J., Juneau S., Luo B., Lutz D., Sargent M. T., Scott D., Xue Y. Q., 2012b, MNRAS, 419, 95

Müller Sánchez F., Davies R. I., Genzel R., Tacconi L. J., Eisenhauer F., Hicks E. K. S., Friedrich S., Sternberg A., 2009, ApJ, 691, 749

Murphy E. J., 2009, ApJ, 706, 482

Murphy E. J., Bremseth J., Mason B. S., Condon J. J., Schinnerer E., Aniano G., Armus L., Helou G., Turner J. L., Jarrett T. H., 2012, ApJ, 761, 97

Murphy E. J., Condon J. J., Schinnerer E., Kennicutt R. C., Calzetti D., Armus L., Helou G., Turner J. L., Aniano G., Beirão P., Bolatto A. D., Brandl B. R., Croxall K. V., Dale D. A., Donovan Meyer J. L., Draine B. T., Engelbracht C., Hunt L. K., Hao C.-N., Koda J., Roussel H., Skibba R., Smith J.-D. T., 2011, ApJ, 737, 67

Murray N., Chiang J., Grossman S. A., Voit G. M., 1995, ApJ, 451, 498

Murray N., Quataert E., Thompson T. A., 2005, ApJ, 618, 569

Myers A. D., Brunner R. J., Nichol R. C., Richards G. T., Schneider D. P., Bahcall N. A., 2007, ApJ, 658, 85

Naab T., Johansson P. H., Ostriker J. P., 2009, ApJ, 699, L178

Narayan R., McClintock J. E., 2008, New A Rev., 51, 733

Narayan R., SÄ dowski A., Penna R. F., Kulkarni A. K., 2012, MNRAS, 426, 3241

Narayan R., Yi I., 1994, ApJ, 428, L13

Negrello M. et al., 2010, Science, 330, 800

Negrello M., Hopwood R., Dye S., Cunha E. d., Serjeant S., Fritz J., Rowlands K., Fleuren S., Bussmann R. S., Cooray A., Dannerbauer H., González-Nuevo J., Lapi A., Omont A., Amber S., Auld R., Baes M., Buttiglione S., Cava A., Danese L., Dariush A., De Zotti G., Dunne L., Eales S., Ibar E., Ivison R. J., Kim S., Leeuw L., Maddox S., Michałowski M. J., Massardi M., Pascale E., Pohlen M., Rigby E., Smith D. J. B., Sutherland W., Temi P., Wardlow J., 2014, MNRAS, 440, 1999

Negrello M., Perrotta F., González-Nuevo J., Silva L., de Zotti G., Granato G. L., Baccigalupi C., Danese L., 2007, MNRAS, 377, 1557

Nenkova M., Sirocky M. M., Ivezić Ž., Elitzur M., 2008a, ApJ, 685, 147

Nenkova M., Sirocky M. M., Nikutta R., Ivezić Ž., Elitzur M., 2008b, ApJ, 685, 160

Neri R., Downes D., Cox P., Walter F., 2014, A&A, 562, A35

Netzer H., Lira P., Trakhtenbrot B., Shemmer O., Cury I., 2007, ApJ, 671, 1256

Netzer H., Trakhtenbrot B., 2014, MNRAS, 438, 672

Nipoti C., Treu T., Leauthaud A., Bundy K., Newman A. B., Auger M. W., 2012, MNRAS, 422, 1714

Nobuta K., Akiyama M., Ueda Y., Watson M. G., Silverman J., Hiroi K., Ohta K., Iwamuro F., Yabe K., Tamura N., Moritani Y., Sumiyoshi M., Takato N., Kimura M., Maihara T., Dalton G., Lewis I., Bonfield D., Lee H., Curtis-Lake E., Macaulay E., Clarke F., Sekiguchi K., Simpson C., Croom S., Ouchi M., Hanami H., Yamada T., 2012, ApJ, 761, 143

Noeske K. G., Faber S. M., Weiner B. J., Koo D. C., Primack J. R., Dekel A., Papovich C., Conselice C. J., Le Floc'h E., Rieke G. H., Coil A. L., Lotz J. M., Somerville R. S., Bundy K., 2007, ApJ, 660, L47

Noguchi M., 1999, ApJ, 514, 77

Noll S., Burgarella D., Giovannoli E., Buat V., Marcillac D., Muñoz-Mateos J. C., 2009, A&A, 507, 1793

Norman C., Scoville N., 1988, ApJ, 332, 124

Oesch P. A., Bouwens R. J., Carollo C. M., Illingworth G. D., Magee D., Trenti M., Stiavelli M., Franx M., Labbé I., van Dokkum P. G., 2010, ApJ, 725, L150

Oesch P. A., Bouwens R. J., Illingworth G. D., Labbé I., Franx M., van Dokkum P. G., Trenti M., Stiavelli M., Gonzalez V., Magee D., 2013, ApJ, 773, 75

Oesch P. A., van Dokkum P. G., Illingworth G. D., Bouwens R. J., Momcheva I., Holden B., Roberts-Borsani G. W., Smit R., Franx M., Labbé I., González V., Magee D., 2015, ApJ, 804, L30

Ohsuga K., 2007, ApJ, 659, 205

Ohsuga K., Mineshige S., 2011, ApJ, 736, 2

Omont A., Beelen A., Bertoldi F., Cox P., Carilli C. L., Priddey R. S., McMahon R. G., Isaak K. G., 2003, A&A, 398, 857

Omont A., Cox P., Bertoldi F., McMahon R. G., Carilli C., Isaak K. G., 2001, A&A, 374, 371

Omont A., McMahon R. G., Cox P., Kreysa E., Bergeron J., Pajot F., Storrie-Lombardi L. J., 1996, A&A, 315, 1

Omont A., Willott C. J., Beelen A., Bergeron J., Orellana G., Delorme P., 2013, A&A, 552, A43

Omukai K., Schneider R., Haiman Z., 2008, ApJ, 686, 801

Onken C. A., Ferrarese L., Merritt D., Peterson B. M., Pogge R. W., Vestergaard M., Wandel A., 2004, ApJ, 615, 645

Onken C. A., Kollmeier J. A., 2008, ApJ, 689, L13

Ono Y., Ouchi M., Kurono Y., Momose R., 2014, ApJ, 795, 5

Ouchi M., Shimasaku K., Furusawa H., Saito T., Yoshida M., Akiyama M., Ono Y., Yamada T., Ota K., Kashikawa N., Iye M., Kodama T., Okamura S., Simpson C., Yoshida M., 2010, ApJ, 723, 869

Ouchi M., Shimasaku K., Okamura S., Furusawa H., Kashikawa N., Ota K., Doi M., Hamabe M., Kimura M., Komiyama Y., Miyazaki M., Miyazaki S., Nakata F., Sekiguchi M., Yagi M., Yasuda N., 2004, ApJ, 611, 685

Overzier R. A., Bouwens R. J., Illingworth G. D., Franx M., 2006, ApJ, 648, L5

Overzier R. A., Heckman T. M., Wang J., Armus L., Buat V., Howell J., Meurer G., Seibert M., Siana B., Basu-Zych A., Charlot S., Gonçalves T. S., Martin D. C., Neill J. D., Rich R. M., Salim S., Schiminovich D., 2011, ApJ, 726, L7

Page M. J., Carrera F. J., Stevens J. A., Ebrero J., Blustin A. J., 2011, MNRAS, 416, 2792

Page M. J., Stevens J. A., Ivison R. J., Carrera F. J., 2004, ApJ, 611, L85

Page M. J. et al., 2012, Nature, 485, 213

Pancoast A., Brewer B. J., Treu T., 2014, MNRAS, 445, 3055

Panter B., Heavens A. F., Jimenez R., 2004, MNRAS, 355, 764

Papovich C., Dickinson M., Ferguson H. C., 2001, ApJ, 559, 620

Patel S. G., Fumagalli M., Franx M., van Dokkum P. G., van der Wel A., Leja J., Labbé I., Brammer G., Skelton R. E., Momcheva I., Whitaker K. E., Lundgren B., Muzzin A., Quadri R. F., Nelson E. J., Wake D. A., Rix H.-W., 2013, ApJ, 778, 115

Patrick A. R., Reeves J. N., Porquet D., Markowitz A. G., Braito V., Lobban A. P., 2012, MNRAS, 426, 2522

Peng C. Y., 2007, ApJ, 671, 1098

Peng C. Y., Impey C. D., Ho L. C., Barton E. J., Rix H.-W., 2006, ApJ, 640, 114

Peng Y.-j. et al., 2010, ApJ, 721, 193

Pereira-Santaella M., Spinoglio L., Busquet G., Glenn J., Isaak K., Kamenetzky J., Rangwala N., Schirm M. R. P., Baes M., Barlow M. J., Boselli A., Cooray A., Cormier D., 2013, ArXiv e-prints

Pérez-Beaupuits J. P., Wada K., Spaans M., 2011, ApJ, 730, 48

Pérez-González P. G., Rieke G. H., Villar V., Barro G., Blaylock M., Egami E., Gallego J., Gil de Paz A., Pascual S., Zamorano J., Donley J. L., 2008, ApJ, 675, 234

Perrotta F., Magliocchetti M., Baccigalupi C., Bartelmann M., De Zotti G., Granato G. L., Silva L., Danese L., 2003, MNRAS, 338, 623

Persic M., Rephaeli Y., Braito V., Cappi M., Della Ceca R., Franceschini A., Gruber D. E., 2004, A&A, 419, 849

Peterson B. M., 2014, Space Sci. Rev., 183, 253

Pier E. A., Krolik J. H., 1992, ApJ, 401, 99

Planck Collaboration XIII, Ade P. A. R., Aghanim N., Arnaud M., Ashdown M., Aumont J., Baccigalupi C., Banday A. J., Barreiro R. B., Bartlett J. G., et al., 2015, ArXiv e-prints

Planck Collaboration XVI, Ade P. A. R., Aghanim N., Armitage-Caplan C., Arnaud M., Ashdown M., Atrio-Barandela F., Aumont J., Baccigalupi C., Banday A. J., et al., 2014, A&A, 571, A16

Planck Collaboration XX, Ade P. A. R., Aghanim N., Arnaud M., Ashdown M., Aumont J., Baccigalupi C., Balbi A., Banday A. J., Barreiro R. B., et al., 2011, A&A, 536, A20

Planck Collaboration XXV, Ade P. A. R., Aghanim N., Armitage-Caplan C., Arnaud M., Ashdown M., Atrio-Barandela F., Aumont J., Baccigalupi C., Banday A. J., et al., 2014, A&A, 571, A25

Polletta M., Tajer M., Maraschi L., Trinchieri G., Lonsdale C. J., Chiappetti L., Andreon S., Pierre M., Le Fèvre O., Zamorani G., Maccagni D., Garcet O., Surdej J., Franceschini A., Alloin D., Shupe D. L., Surace J. A., Fang F., Rowan-Robinson M., Smith H. E., Tresse L., 2007, ApJ, 663, 81

Porciani C., Norberg P., 2006, MNRAS, 371, 1824

Portegies Zwart S. F., Baumgardt H., Hut P., Makino J., McMillan S. L. W., 2004, Nature, 428, 724

Portegies Zwart S. F., McMillan S. L. W., 2002, ApJ, 576, 899

Pozzetti L., Bolzonella M., Lamareille F., Zamorani G., Franzetti P., Le Fèvre O., Iovino A., Temporin S., Ilbert O., Arnouts S., Charlot S., Brinchmann J., Zucca E., Tresse L., Scodeggio M., Guzzo L., Bottini D., Garilli B., Le Brun V., Maccagni D., Picat J. P., Scaramella R., Vettolani G., Zanichelli A., Adami C., Bardelli S., Cappi A., Ciliegi P., Contini T., Foucaud S., Gavignaud I., McCracken H. J., Marano B., Marinoni C., Mazure A., Meneux B., Merighi R., Paltani S., Pellò R., Pollo A., Radovich M., Bondi M., Bongiorno A., Cucciati O., de la Torre S., Gregorini L., Mellier Y., Merluzzi P., Vergani D., Walcher C. J., 2007, A&A, 474, 443

Priddey R. S., Isaak K. G., McMahon R. G., Omont A., 2003, MNRAS, 339, 1183

Prochaska J. X., Hennawi J. F., 2009, ApJ, 690, 1558

Proga D., Stone J. M., Kallman T. R., 2000, ApJ, 543, 686

Prouton O. R., Bressan A., Clemens M., Franceschini A., Granato G. L., Silva L., 2004, A&A, 421, 115

Quadri R., van Dokkum P., Gawiser E., Franx M., Marchesini D., Lira P., Rudnick G., Herrera D., Maza J., Kriek M., Labbé I., Francke H., 2007, ApJ, 654, 138

Rafferty D. A., Brandt W. N., Alexander D. M., Xue Y. Q., Bauer F. E., Lehmer B. D., Luo B., Papovich C., 2011, ApJ, 742, 3

Raimundo S. I., Fabian A. C., 2009, MNRAS, 396, 1217

Raimundo S. I., Fabian A. C., Vasudevan R. V., Gandhi P., Wu J., 2012, MNRAS, 419, 2529

Ranalli P., Comastri A., Setti G., 2003, A&A, 399, 39

Ratnam C., Salucci P., 2000, New A, 5, 427

Rawle T. D., Egami E., Bussmann R. S., Gurwell M., Ivison R. J., Boone F., Combes F., Danielson A. L. R., Rex M., Richard J., Smail I., Swinbank A. M., Altieri B., Blain A. W., Clement B., Dessauges-Zavadsky M., Edge A. C., Fazio G. G., Jones T., Kneib J.-P., Omont A., Pérez-González P. G., Schaerer D., Valtchanov I., van der Werf P. P., Walth G., Zamojski M., Zemcov M., 2014, ApJ, 783, 59

Reddy N. A., Erb D. K., Pettini M., Steidel C. C., Shapley A. E., 2010, ApJ, 712, 1070

Reddy N. A., Steidel C. C., 2004, ApJ, 603, L13

Reddy N. A., Steidel C. C., 2009, ApJ, 692, 778

Reddy N. A., Steidel C. C., Pettini M., Adelberger K. L., Shapley A. E., Erb D. K., Dickinson M., 2008, ApJS, 175, 48

Rees M. J., 1984, ARA&A, 22, 471

Rees M. J., Ostriker J. P., 1977, MNRAS, 179, 541

Reid M. J., Braatz J. A., Condon J. J., Greenhill L. J., Henkel C., Lo K. Y., 2009, ApJ, 695, 287

Renzini A., 2006, ARA&A, 44, 141

Renzini A., Peng Y.-j., 2015, ApJ, 801, L29

Reynolds C. S., 2013, Classical and Quantum Gravity, 30, 244004

Reynolds C. S., 2014, Space Sci. Rev., 183, 277

Richards G. T., Croom S. M., Anderson S. F., Bland-Hawthorn J., Boyle B. J., De Propris R., Drinkwater M. J., Fan X., Gunn J. E., Ivezić Ž., Jester S., Loveday J., Meiksin A., Miller L., Myers A., Nichol R. C., Outram P. J., Pimbblet K. A., Roseboom I. G., Ross N., Schneider D. P., Shanks T., Sharp R. G., Stoughton C., Strauss M. A., Szalay A. S., Vanden Berk D. E., York D. G., 2005, MNRAS, 360, 839

Richards G. T., Strauss M. A., Fan X., Hall P. B., Jester S., Schneider D. P., Vanden Berk D. E., Stoughton C., Anderson S. F., Brunner R. J., Gray J., Gunn J. E., Ivezić Ž., Kirkland M. K., Knapp G. R., Loveday J., Meiksin A., Pope A., Szalay A. S., Thakar A. R., Yanny B., York D. G., Barentine J. C., Brewington H. J., Brinkmann J., Fukugita M., Harvanek M., Kent S. M., Kleinman S. J., Krzesiński J., Long D. C., Lupton R. H., Nash T., Neilsen, Jr. E. H., Nitta A., Schlegel D. J., Snedden S. A., 2006, AJ, 131, 2766

Riechers D. A. et al., 2013, Nature, 496, 329

Riechers D. A., Carilli C. L., Capak P. L., Scoville N. Z., Smolčić V., Schinnerer E., Yun M., Cox P., Bertoldi F., Karim A., Yan L., 2014, ApJ, 796, 84

Risaliti G., Harrison F. A., Madsen K. K., Walton D. J., Boggs S. E., Christensen F. E., Craig W. W., Grefenstette B. W., Hailey C. J., Nardini E., Stern D., Zhang W. W., 2013, Nature, 494, 449

Rodighiero G., Brusa M., Daddi E., Negrello M., Mullaney J. R., Delvecchio I., Lutz D., Renzini A., Franceschini A., Baronchelli I., Pozzi F., Gruppioni C., Strazzullo V., Cimatti A., Silverman J., 2015, ApJ, 800, L10

Rodighiero G., Daddi E., Baronchelli I., Cimatti A., Renzini A., Aussel H., Popesso P., Lutz D., Andreani P., Berta S., Cava A., Elbaz D., Feltre A., Fontana A., Förster Schreiber N. M., Franceschini A., Genzel R., Grazian A., Gruppioni C., Ilbert O., Le Floch E., Magdis G., Magliocchetti M., Magnelli B., Maiolino R., McCracken H., Nordon R., Poglitsch A., Santini P., Pozzi F., Riguccini L., Tacconi L. J., Wuyts S., Zamorani G., 2011, ApJ, 739, L40

Rodighiero G., Renzini A., Daddi E., Baronchelli I., Berta S., Cresci G., Franceschini A., Gruppioni C., Lutz D., Mancini C., Santini P., Zamorani G., Silverman J., Kashino D., Andreani P., Cimatti A., Sánchez H. D., Le Floch E., Magnelli B., Popesso P., Pozzi F., 2014, MNRAS, 443, 19

Rodighiero G., Vaccari M., Franceschini A., Tresse L., Le Fevre O., Le Brun V., Mancini C., Matute I., Cimatti A., Marchetti L., Ilbert O., Arnouts S., Bolzonella M., Zucca E., Bardelli S., Lonsdale C. J., Shupe D., Surace J., Rowan-Robinson M., Garilli B., Zamorani G., Pozzetti L., Bondi M., de la Torre S., Vergani D., Santini P., Grazian A., Fontana A., 2010, A&A, 515, A8

Roediger J. C., Courteau S., 2015, MNRAS, 452, 3209

Roming P. W. A., Kennedy T. E., Mason K. O., Nousek J. A., Ahr L., Bingham R. E., Broos P. S., Carter M. J., Hancock B. K., Huckle H. E., Hunsberger S. D., Kawakami H., Killough R., Koch T. S., McLelland M. K., Smith K., Smith P. J., Soto J. C., Boyd P. T., Breeveld A. A., Holland S. T., Ivanushkina M., Pryzby M. S., Still M. D., Stock J., 2005, Space Sci. Rev., 120, 95

Rosa-González D., Terlevich E., Terlevich R., 2002, MNRAS, 332, 283

Rosario D. J., Santini P., Lutz D., Shao L., Maiolino R., Alexander D. M., Altieri B., Andreani P., Aussel H., Bauer F. E., Berta S., Bongiovanni A., Brandt W. N., Brusa M., Cepa J., Cimatti A., Cox T. J., Daddi E., Elbaz D., Fontana A., Förster Schreiber N. M., Genzel R., Grazian A., Le Floch E., Magnelli B., Mainieri V., Netzer

H., Nordon R., Pérez Garcia I., Poglitsch A., Popesso P., Pozzi F., Riguccini L., Rodighiero G., Salvato M., Sanchez-Portal M., Sturm E., Tacconi L. J., Valtchanov I., Wuyts S., 2012, A&A, 545, A45

Ross N. P., da Ângela J., Shanks T., Wake D. A., Cannon R. D., Edge A. C., Nichol R. C., Outram P. J., Colless M., Couch W. J., Croom S. M., de Propris R., Drinkwater M. J., Eisenstein D. J., Loveday J., Pimbblet K. A., Roseboom I. G., Schneider D. P., Sharp R. G., Weilbacher P. M., 2007, MNRAS, 381, 573

Ross N. P., Myers A. D., Sheldon E. S., Yèche C., Strauss M. A., Bovy J., Kirkpatrick J. A., Richards G. T., Aubourg É., Blanton M. R., Brandt W. N., Carithers W. C., Croft R. A. C., da Silva R., Dawson K., Eisenstein D. J., Hennawi J. F., Ho S., Hogg D. W., Lee K.-G., Lundgren B., McMahon R. G., Miralda-Escudé J., Palanque-Delabrouille N., Pâris I., Petitjean P., Pieri M. M., Rich J., Roe N. A., Schiminovich D., Schlegel D. J., Schneider D. P., Slosar A., Suzuki N., Tinker J. L., Weinberg D. H., Weyant A., White M., Wood-Vasey W. M., 2012, ApJS, 199, 3

Ross N. P., Shen Y., Strauss M. A., Vanden Berk D. E., Connolly A. J., Richards G. T., Schneider D. P., Weinberg D. H., Hall P. B., Bahcall N. A., Brunner R. J., 2009, ApJ, 697, 1634

Ross R. R., Fabian A. C., 2005, MNRAS, 358, 211

Roth N., Kasen D., Hopkins P. F., Quataert E., 2012, ApJ, 759, 36

Rovilos E., Comastri A., Gilli R., Georgantopoulos I., Ranalli P., Vignali C., Lusso E., Cappelluti N., Zamorani G., Elbaz D., Dickinson M., Hwang H. S., Charmandaris V., Ivison R. J., Merloni A., Daddi E., Carrera F. J., Brandt W. N., Mullaney J. R., Scott D., Alexander D. M., Del Moro A., Morrison G., Murphy E. J., Altieri B., Aussel H., Dannerbauer H., Kartaltepe J., Leiton R., Magdis G., Magnelli B., Popesso P., Valtchanov I., 2012, A&A, 546, A58

Rowlands K., Dunne L., Dye S., Aragón-Salamanca A., Maddox S., da Cunha E., Smith D. J. B., Bourne N., Eales S., Gomez H. L., Smail I., Alpaslan M., Clark C. J. R., Driver S., Ibar E., Ivison R. J., Robotham A., Smith M. W. L., Valiante E., 2014, MNRAS, 441, 1017

Runnoe J. C., Brotherton M. S., Shang Z., 2012, MNRAS, 422, 478

Rupke D. S. N., Veilleux S., 2011, ApJ, 729, L27

Rusli S. P., Thomas J., Saglia R. P., Fabricius M., Erwin P., Bender R., Nowak N., Lee C. H., Riffeser A., Sharp R., 2013, AJ, 146, 45

Salim S., Rich R. M., Charlot S., Brinchmann J., Johnson B. D., Schiminovich D., Seibert M., Mallery R., Heckman T. M., Forster K., Friedman P. G., Martin D. C., Morrissey P., Neff S. G., Small T., Wyder T. K., Bianchi L., Donas J., Lee Y.-W., Madore B. F., Milliard B., Szalay A. S., Welsh B. Y., Yi S. K., 2007, ApJS, 173, 267

Salmon B., Papovich C., Finkelstein S. L., Tilvi V., Finlator K., Behroozi P., Dahlen T., Davé R., Dekel A., Dickinson M., Ferguson H. C., Giavalisco M., Long J., Lu Y., Mobasher B., Reddy N., Somerville R. S., Wechsler R. H., 2015, ApJ, 799, 183

Salpeter E. E., 1955, ApJ, 121, 161

Salucci P., Szuszkiewicz E., Monaco P., Danese L., 1999, MNRAS, 307, 637

Sandage A., Tammann G. A., Yahil A., 1979, ApJ, 232, 352

Sanders D. B., Phinney E. S., Neugebauer G., Soifer B. T., Matthews K., 1989, ApJ, 347, 29

Sanders D. B., Soifer B. T., Elias J. H., Madore B. F., Matthews K., Neugebauer G., Scoville N. Z., 1988, ApJ, 325, 74

Sani E., Davies R. I., Sternberg A., Graciá-Carpio J., Hicks E. K. S., Krips M., Tacconi L. J., Genzel R., Vollmer B., Schinnerer E., García-Burillo S., Usero A., Orban de Xivry G., 2012, MNRAS, 424, 1963

Sani E., Marconi A., Hunt L. K., Risaliti G., 2011, MNRAS, 413, 1479

Santini P., Fontana A., Grazian A., Salimbeni S., Fontanot F., Paris D., Boutsia K., Castellano M., Fiore F., Gallozzi S., Giallongo E., Koekemoer A. M., Menci N., Pentericci L., Somerville R. S., 2012a, A&A, 538, A33

Santini P., Rosario D. J., Shao L., Lutz D., Maiolino R., Alexander D. M., Altieri B., Andreani P., Aussel H., Bauer F. E., Berta S., Bongiovanni A., Brandt W. N., Brusa M., Cepa J., Cimatti A., Daddi E., Elbaz D., Fontana A., Förster Schreiber N. M., Genzel R., Grazian A., Le Floc'h E., Magnelli B., Mainieri V., Nordon R., Pérez Garcia A. M., Poglitsch A., Popesso P., Pozzi F., Riguccini L., Rodighiero G., Salvato M., Sanchez-Portal M., Sturm E., Tacconi L. J., Valtchanov I., Wuyts S., 2012b, A&A, 540, A109

Sargent W. L. W., Young P. J., Lynds C. R., Boksenberg A., Shortridge K., Hartwick F. D. A., 1978, ApJ, 221, 731

Sarzi M., Rix H.-W., Shields J. C., McIntosh D. H., Ho L. C., Rudnick G., Filippenko A. V., Sargent W. L. W., Barth A. J., 2002, ApJ, 567, 237

Sauvage M., Thuan T. X., 1992, ApJ, 396, L69

Sawicki M., Yee H. K. C., 1998, AJ, 115, 1329

Scalo J. M., 1986, in IAU Symposium, Vol. 116, Luminous Stars and Associations in Galaxies, De Loore C. W. H., Willis A. J., Laskarides P., eds., pp. 451–466

Scannapieco C., Wadepuhl M., Parry O. H., Navarro J. F., Jenkins A., Springel V., Teyssier R., Carlson E., Couchman H. M. P., Crain R. A., Dalla Vecchia C., Frenk C. S., Kobayashi C., Monaco P., Murante G., Okamoto T., Quinn T., Schaye J., Stinson G. S., Theuns T., Wadsley J., White S. D. M., Woods R., 2012, MNRAS, 423, 1726

Schmidt M., 1968, ApJ, 151, 393

Schmidt M., Green R. F., 1983, ApJ, 269, 352

Schmoll S., Miller J. M., Volonteri M., Cackett E., Reynolds C. S., Fabian A. C., Brenneman L. W., Miniutti G., Gallo L. C., 2009, ApJ, 703, 2171

Schulze A., Bongiorno A., Gavignaud I., Schramm M., Silverman J., Merloni A., Zamorani G., Hirschmann M., Mainieri V., Wisotzki L., Shankar F., Fiore F., Koekemoer A. M., Temporin G., 2015, MNRAS, 447, 2085

Schulze A., Gebhardt K., 2011, ApJ, 729, 21

Schulze A., Wisotzki L., 2010, A&A, 516, A87

Schulze A., Wisotzki L., Husemann B., 2009, A&A, 507, 781

Schwarzschild M., 1979, ApJ, 232, 236

Schwarzschild M., 1993, ApJ, 409, 563

Scoville N., Aussel H., Benson A., Blain A., Calzetti D., Capak P., Ellis R. S., El-Zant A., Finoguenov A., Giavalisco M., Guzzo L., Hasinger G., Koda J., Le Fèvre O., Massey R., McCracken H. J., Mobasher B., Renzini A., Rhodes J., Salvato M., Sanders D. B., Sasaki S. S., Schinnerer E., Sheth K., Shopbell P. L., Taniguchi Y., Taylor J. E., Thompson D. J., 2007, ApJS, 172, 150

Scoville N., Aussel H., Sheth K., Scott K. S., Sanders D., Ivison R., Pope A., Capak P., Vanden Bout P., Manohar S., Kartaltepe J., Robertson B., Lilly S., 2014, ApJ, 783, 84

Scoville N., Sheth K., Aussel H., Vanden Bout P., Capak P., Bongiorno A., Casey C. M., Murchikova L., Koda J., Pope A., Toft S., Ivison R., Sanders D., Manohar S., Lee N., 2015, ArXiv e-prints

Seaton M. J., 1979, MNRAS, 187, 73P

Serjeant S. et al., 2010, A&A, 518, L7

Sesana A., Barausse E., Dotti M., Rossi E. M., 2014, ApJ, 794, 104

Shakura N. I., Sunyaev R. A., 1973, A&A, 24, 337

Shankar F., 2013, Classical and Quantum Gravity, 30, 244001

Shankar F., Buchan S., Rettura A., Bouillot V. R., Moreno J., Licitra R., Bernardi M., Huertas-Company M., Mei S., Ascaso B., Sheth R., Delaye L., Raichoor A., 2015, ApJ, 802, 73

Shankar F., Guo H., Bouillot V., Rettura A., Meert A., Buchan S., Kravtsov A., Bernardi M., Sheth R., Vikram V., Marchesini D., Behroozi P., Zheng Z., Maraston C., Ascaso B., Lemaux B. C., Capozzi D., Huertas-Company M., Gal R. R., Lubin L. M., Conselice C. J., Carollo M., Cattaneo A., 2014, ApJ, 797, L27

Shankar F., Lapi A., Salucci P., De Zotti G., Danese L., 2006, ApJ, 643, 14

Shankar F., Marulli F., Mathur S., Bernardi M., Bournaud F., 2012, A&A, 540, A23

Shankar F., Salucci P., Granato G. L., De Zotti G., Danese L., 2004, MNRAS, 354, 1020

Shankar F., Weinberg D. H., Miralda-Escudé J., 2009, ApJ, 690, 20

Shankar F., Weinberg D. H., Miralda-Escudé J., 2013, MNRAS, 428, 421

Shankar F., Weinberg D. H., Shen Y., 2010, MNRAS, 406, 1959

Shao L., Lutz D., Nordon R., Maiolino R., Alexander D. M., Altieri B., Andreani P., Aussel H., Bauer F. E., Berta S., Bongiovanni A., Brandt W. N., Brusa M., Cava A., Cepa J., Cimatti A., Daddi E., Dominguez-Sanchez H., Elbaz D., Förster Schreiber N. M., Geis N., Genzel R., Grazian A., Gruppioni C., Magdis G., Magnelli B., Mainieri V., Pérez García A. M., Poglitsch A., Popesso P., Pozzi F., Riguccini L., Rodighiero G., Rovilos E., Saintonge A., Salvato M., Sanchez Portal M., Santini P., Sturm E., Tacconi L. J., Valtchanov I., Wetzstein M., Wieprecht E., 2010, A&A, 518, L26

Shapley A. E., Steidel C. C., Adelberger K. L., Dickinson M., Giavalisco M., Pettini M., 2001, ApJ, 562, 95

Shen Y., 2013, Bulletin of the Astronomical Society of India, 41, 61

Shen Y., Greene J. E., Strauss M. A., Richards G. T., Schneider D. P., 2008, ApJ, 680, 169

Shen Y., Kelly B. C., 2010, ApJ, 713, 41

Shen Y., Kelly B. C., 2012, ApJ, 746, 169

Shen Y., Liu X., 2012, ApJ, 753, 125

Shen Y., Richards G. T., Strauss M. A., Hall P. B., Schneider D. P., Snedden S., Bizyaev D., Brewington H., Malanushenko V., Malanushenko E., Oravetz D., Pan K., Simmons A., 2011, ApJS, 194, 45

Shen Y., Strauss M. A., Ross N. P., Hall P. B., Lin Y.-T., Richards G. T., Schneider D. P., Weinberg D. H., Connolly A. J., Fan X., Hennawi J. F., Shankar F., Vanden Berk D. E., Bahcall N. A., Brunner R. J., 2009, ApJ, 697, 1656

Sheth R. K., Mo H. J., Tormen G., 2001, MNRAS, 323, 1

Sheth R. K., Tormen G., 1999, MNRAS, 308, 119

Shields J. C., Rix H.-W., Sarzi M., Barth A. J., Filippenko A. V., Ho L. C., McIntosh D. H., Rudnick G., Sargent W. L. W., 2007, ApJ, 654, 125

Shlosman I., Begelman M. C., Frank J., 1990, Nature, 345, 679

Shlosman I., Frank J., Begelman M. C., 1989, Nature, 338, 45

Shlosman I., Noguchi M., 1993, ApJ, 414, 474

Sijacki D., Springel V., Haehnelt M. G., 2009, MNRAS, 400, 100

Silk J., 2013, ApJ, 772, 112

Silk J., Rees M. J., 1998, A&A, 331, L1

Silva L., Granato G. L., Bressan A., Danese L., 1998, ApJ, 509, 103

Simpson J. M., Swinbank A. M., Smail I., Alexander D. M., Brandt W. N., Bertoldi F., de Breuck C., Chapman S. C., Coppin K. E. K., da Cunha E., Danielson A. L. R., Dannerbauer H., Greve T. R., Hodge J. A., Ivison R. J., Karim A., Knudsen K. K., Poggianti B. M., Schinnerer E., Thomson A. P., Walter F., Wardlow J. L., Weiß A., van der Werf P. P., 2014, ApJ, 788, 125

Siopis C., Gebhardt K., Lauer T. R., Kormendy J., Pinkney J., Richstone D., Faber S. M., Tremaine S., Aller M. C., Bender R., Bower G., Dressler A., Filippenko A. V., Green R., Ho L. C., Magorrian J., 2009, ApJ, 693, 946

Small T. A., Blandford R. D., 1992, MNRAS, 259, 725

Smit R., Bouwens R. J., Franx M., Illingworth G. D., Labbé I., Oesch P. A., van Dokkum P. G., 2012, ApJ, 756, 14

Soltan A., 1982, MNRAS, 200, 115

Somerville R. S., Davé R., 2014, ArXiv e-prints

Spaans M., Meijerink R., 2008, ApJ, 678, L5

Speagle J. S., Steinhardt C. L., Capak P. L., Silverman J. D., 2014, ApJS, 214, 15

Spinoglio L., Pereira-Santaella M., Busquet G., Schirm M. R. P., Wilson C. D., Glenn J., Kamenetzky J., Rangwala N., Maloney P. R., Parkin T. J., Bendo G. J., Madden S. C., Wolfire M. G., Boselli A., Cooray A., Page M. J., 2012, ApJ, 758, 108

Springel V., Di Matteo T., Hernquist L., 2005, MNRAS, 361, 776

Starikova S., Berta S., Franceschini A., Marchetti L., Rodighiero G., Vaccari M., Vikhlinin A., 2012, ApJ, 751, 126

Stark D. P., Ellis R. S., Bunker A., Bundy K., Targett T., Benson A., Lacy M., 2009, ApJ, 697, 1493

Stark D. P., Schenker M. A., Ellis R., Robertson B., McLure R., Dunlop J., 2013, ApJ, 763, 129

Stecher T. P., Cornett R. H., Greason M. R., Landsman W. B., Hill J. K., Hill R. S., Bohlin R. C., Chen P. C., Collins N. R., Fanelli M. N., Hollis J. I., Neff S. G., O'Connell R. W., Offenberg J. D., Parise R. A., Parker J., Roberts M. S., Smith A. M., Waller W. H., 1997, PASP, 109, 584

Steidel C. C., Pettini M., Adelberger K. L., 2001, ApJ, 546, 665

Stevens J. A., Page M. J., Ivison R. J., Carrera F. J., Mittaz J. P. D., Smail I., McHardy I. M., 2005, MNRAS, 360, 610

Stewart K. R., Bullock J. S., Barton E. J., Wechsler R. H., 2009, ApJ, 702, 1005

Storchi-Bergmann T., Riffel R. A., Riffel R., Diniz M. R., Borges Vale T., McGregor P. J., 2012, ApJ, 755, 87

Sturm E., González-Alfonso E., Veilleux S., Fischer J., Graciá-Carpio J., Hailey-Dunsheath S., Contursi A., Poglitsch A., Sternberg A., Davies R., Genzel R., Lutz D., Tacconi L., Verma A., Maiolino R., de Jong J. A., 2011, ApJ, 733, L16

Sulentic J. W., Bachev R., Marziani P., Negrete C. A., Dultzin D., 2007, ApJ, 666, 757

Sunyaev R. A., Trümper J., 1979, Nature, 279, 506

Symeonidis M., Georgakakis A., Seymour N., Auld R., Bock J., Brisbin D., Buat V., Burgarella D., Chanial P., Clements D. L., Cooray A., Eales S., Farrah D., Franceschini A., Glenn J., Griffin M., Hatziminaoglou E., Ibar E., Ivison R. J., Mortier A. M. J., Oliver S. J., Page M. J., Papageorgiou A., Pearson C. P., Pérez-Fournon I., Pohlen M., Rawlings J. I., Raymond G., Rodighiero G., Roseboom I. G., Rowan-Robinson M., Scott D., Smith A. J., Tugwell K. E., Vaccari M., Vieira J. D., Vigroux L., Wang L., Wright G., 2011, MNRAS, 417, 2239

Symeonidis M., Rosario D., Georgakakis A., Harker J., Laird E. S., Page M. J., Willmer C. N. A., 2010, MNRAS, 403, 1474

Tamura N., Ohta K., Ueda Y., 2006, MNRAS, 365, 134

Tanaka T., Haiman Z., 2009, ApJ, 696, 1798

Targett T. A., Dunlop J. S., McLure R. J., 2012, MNRAS, 420, 3621

Taylor E. N., Hopkins A. M., Baldry I. K., Brown M. J. I., Driver S. P., Kelvin L. S., Hill D. T., Robotham A. S. G., Bland-Hawthorn J., Jones D. H., Sharp R. G., Thomas D., Liske J., Loveday J., Norberg P., Peacock J. A., Bamford S. P., Brough S., Colless M., Cameron E., Conselice C. J., Croom S. M., Frenk C. S., Gunawardhana M., Kuijken K., Nichol R. C., Parkinson H. R., Phillipps S., Pimbblet K. A., Popescu C. C., Prescott M., Sutherland W. J., Tuffs R. J., van Kampen E., Wijesinghe D., 2011, MNRAS, 418, 1587

Tegmark M. et al., 2006, Phys. Rev. D, 74, 123507

Thompson T. A., Quataert E., Murray N., 2005, ApJ, 630, 167

Thorne K. S., 1974, ApJ, 191, 507

Tinker J., Kravtsov A. V., Klypin A., Abazajian K., Warren M., Yepes G., Gottlöber S., Holz D. E., 2008, ApJ, 688, 709

Tinker J. L., Leauthaud A., Bundy K., George M. R., Behroozi P., Massey R., Rhodes J., Wechsler R. H., 2013, ApJ, 778, 93

Tinker J. L., Robertson B. E., Kravtsov A. V., Klypin A., Warren M. S., Yepes G., Gottlöber S., 2010, ApJ, 724, 878

Tinker J. L., Weinberg D. H., Zheng Z., Zehavi I., 2005, ApJ, 631, 41

Tozzi P., Gilli R., Mainieri V., Norman C., Risaliti G., Rosati P., Bergeron J., Borgani S., Giacconi R., Hasinger G., Nonino M., Streblyanska A., Szokoly G., Wang J. X., Zheng W., 2006, A&A, 451, 457

Trakhtenbrot B., 2014, ApJ, 789, L9

Trakhtenbrot B., Netzer H., 2012, MNRAS, 427, 3081

Trakhtenbrot B., Urry C. M., Civano F., Rosario D. J., Elvis M., Schawinski K., Suh H., Bongiorno A., Simmons B. D., 2015, Science, 349, 168

Treister E., Schawinski K., Volonteri M., Natarajan P., Gawiser E., 2011, Nature, 474, 356

Treister E., Urry C. M., 2006, ApJ, 652, L79

Tremaine S., Gebhardt K., Bender R., Bower G., Dressler A., Faber S. M., Filippenko A. V., Green R., Grillmair C., Ho L. C., Kormendy J., Lauer T. R., Magorrian J., Pinkney J., Richstone D., 2002, ApJ, 574, 740

Treyer M., Schiminovich D., Johnson B., Seibert M., Wyder T., Barlow T. A., Conrow T., Forster K., Friedman P. G., Martin D. C., Morrissey P., Neff S. G., Small T., Bianchi L., Donas J., Heckman T. M., Lee Y.-W., Madore B. F., Milliard B., Rich R. M., Szalay A. S., Welsh B. Y., Yi S. K., 2007, ApJS, 173, 256

Tundo E., Bernardi M., Hyde J. B., Sheth R. K., Pizzella A., 2007, ApJ, 663, 53

Turner T. J., Miller L., 2009, A&A Rev., 17, 47

Ueda Y., Akiyama M., Hasinger G., Miyaji T., Watson M. G., 2014, ApJ, 786, 104

Ueda Y., Akiyama M., Ohta K., Miyaji T., 2003, ApJ, 598, 886

Ueda Y., Hiroi K., Isobe N., Hayashida M., Eguchi S., Sugizaki M., Kawai N., Tsunemi H., Mihara T., Matsuoka M., Ishikawa M., Kimura M., Kitayama H., Kohama M., Matsumura T., Morii M., Nakagawa Y. E., Nakahira S., Nakajima M., Negoro H., Serino M., Shidatsu M., Sootome T., Sugimori K., Suwa F., Toizumi T., Tomida H., Tsuboi Y., Ueno S., Usui R., Yamamoto T., Yamaoka K., Yamazaki K., Yoshida A., 2011, PASJ, 63, 937

Umemura M., 2001, ApJ, 560, L29

Urry C. M., Padovani P., 1995, PASP, 107, 803

Vale A., Ostriker J. P., 2004, MNRAS, 353, 189

van den Bosch R. C. E., de Zeeuw P. T., 2010, MNRAS, 401, 1770

van den Bosch R. C. E., van de Ven G., Verolme E. K., Cappellari M., de Zeeuw P. T., 2008, MNRAS, 385, 647

van der Marel R. P., van den Bosch F. C., 1998, AJ, 116, 2220

van Uitert E., Hoekstra H., Velander M., Gilbank D. G., Gladders M. D., Yee H. K. C., 2011, A&A, 534, A14

Vasudevan R. V., Fabian A. C., 2007, MNRAS, 381, 1235

Vasudevan R. V., Fabian A. C., Gandhi P., Winter L. M., Mushotzky R. F., 2010, MNRAS, 402, 1081

Vasudevan R. V., Mushotzky R. F., Reynolds C. S., Fabian A. C., Lohfink A. M., Zoghbi A., Gallo L. C., Walton D., 2014, ApJ, 785, 30

Vazdekis A., 1999, ApJ, 513, 224

Vega O., Clemens M. S., Bressan A., Granato G. L., Silva L., Panuzzo P., 2008, A&A, 484, 631

Velander M., van Uitert E., Hoekstra H., Coupon J., Erben T., Heymans C., Hildebrandt H., Kitching T. D., Mellier Y., Miller L., Van Waerbeke L., Bonnett C., Fu L., Giodini S., Hudson M. J., Kuijken K., Rowe B., Schrabback T., Semboloni E., 2014, MNRAS, 437, 2111

Venemans B. P., Findlay J. R., Sutherland W. J., De Rosa G., McMahon R. G., Simcoe R., González-Solares E. A., Kuijken K., Lewis J. R., 2013, ApJ, 779, 24

Venemans B. P., McMahon R. G., Walter F., Decarli R., Cox P., Neri R., Hewett P., Mortlock D. J., Simpson C., Warren S. J., 2012, ApJ, 751, L25

Verdoes Kleijn G. A., van der Marel R. P., Noel-Storr J., 2006, AJ, 131, 1961

Vestergaard M., 2002, ApJ, 571, 733

Vestergaard M., Fan X., Tremonti C. A., Osmer P. S., Richards G. T., 2008, ApJ, 674, L1

Vestergaard M., Osmer P. S., 2009, ApJ, 699, 800

Vestergaard M., Peterson B. M., 2006, ApJ, 641, 689

Vieira J. D. et al., 2010, ApJ, 719, 763

Vieira J. D. et al., 2013, Nature, 495, 344

Vignali C., Pozzi F., Fritz J., Comastri A., Gruppioni C., Bellocchi E., Fiore F., Brusa M., Maiolino R., Mignoli M., La Franca F., Pozzetti L., Zamorani G., Merloni A., 2009, MNRAS, 395, 2189

Vika M., Driver S. P., Graham A. W., Liske J., 2009, MNRAS, 400, 1451

Vito F., Gilli R., Vignali C., Comastri A., Brusa M., Cappelluti N., Iwasawa K., 2014, MNRAS, 445, 3557

Vito F., Vignali C., Gilli R., Comastri A., Iwasawa K., Brandt W. N., Alexander D. M., Brusa M., Lehmer B., Bauer F. E., Schneider D. P., Xue Y. Q., Luo B., 2013, MNRAS, 428, 354

Volonteri M., 2010, A&A Rev., 18, 279

Volonteri M., Madau P., Quataert E., Rees M. J., 2005, ApJ, 620, 69

Volonteri M., Rees M. J., 2006, ApJ, 650, 669

Volonteri M., Sikora M., Lasota J.-P., 2007, ApJ, 667, 704

Volonteri M., Silk J., Dubus G., 2015, ApJ, 804, 148

Wada K., Norman C. A., 2001, ApJ, 547, 172

Wada K., Norman C. A., 2002, ApJ, 566, L21

Wada K., Tomisaka K., 2005, ApJ, 619, 93

Walcher J., Groves B., Budavári T., Dale D., 2011, Ap&SS, 331, 1

Walsh J. L., Barth A. J., Sarzi M., 2010, ApJ, 721, 762

Walsh J. L., van den Bosch R. C. E., Barth A. J., Sarzi M., 2012, ApJ, 753, 79

Walter F., Riechers D., Cox P., Neri R., Carilli C., Bertoldi F., Weiss A., Maiolino R., 2009, Nature, 457, 699

Walterbos R. A. M., Greenawalt B., 1996, ApJ, 460, 696

Walton D. J., Nardini E., Fabian A. C., Gallo L. C., Reis R. C., 2013, MNRAS, 428, 2901

Wandel A., Peterson B. M., Malkan M. A., 1999, ApJ, 526, 579

Wang B., Heckman T. M., 1996, ApJ, 457, 645

Wang J., Navarro J. F., Frenk C. S., White S. D. M., Springel V., Jenkins A., Helmi A., Ludlow A., Vogelsberger M., 2011a, MNRAS, 413, 1373

Wang J.-M., Chen Y.-M., Zhang F., 2006, ApJ, 647, L17

Wang J.-M., Du P., Li Y.-R., Ho L. C., Hu C., Bai J.-M., 2014, ApJ, 792, L13

Wang J.-M., Du P., Valls-Gabaud D., Hu C., Netzer H., 2013a, Physical Review Letters, 110, 081301

Wang J.-M., Hu C., Li Y.-R., Chen Y.-M., King A. R., Marconi A., Ho L. C., Yan C.-S., Staubert R., Zhang S., 2009, ApJ, 697, L141

Wang R., Carilli C. L., Neri R., Riechers D. A., Wagg J., Walter F., Bertoldi F., Menten K. M., Omont A., Cox P., Fan X., 2010, ApJ, 714, 699

Wang R., Carilli C. L., Wagg J., Bertoldi F., Walter F., Menten K. M., Omont A., Cox P., Strauss M. A., Fan X., Jiang L., Schneider D. P., 2008, ApJ, 687, 848

Wang R., Wagg J., Carilli C. L., Neri R., Walter F., Omont A., Riechers D. A., Bertoldi F., Menten K. M., Cox P., Strauss M. A., Fan X., Jiang L., 2011b, AJ, 142, 101

Wang R., Wagg J., Carilli C. L., Walter F., Lentati L., Fan X., Riechers D. A., Bertoldi F., Narayanan D., Strauss M. A., Cox P., Omont A., Menten K. M., Knudsen K. K., Neri R., Jiang L., 2013b, ApJ, 773, 44

Wang S. X., Brandt W. N., Luo B., Smail I., Alexander D. M., Danielson A. L. R., Hodge J. A., Karim A., Lehmer B. D., Simpson J. M., Swinbank A. M., Walter F., Wardlow J. L., Xue Y. Q., Chapman S. C., Coppin K. E. K., Dannerbauer H., De Breuck C., Menten K. M., van der Werf P., 2013c, ApJ, 778, 179

Wardle M., Yusef-Zadeh F., 2012, ApJ, 750, L38

Wardlow J. L. et al., 2013, ApJ, 762, 59

Watarai K.-y., 2006, ApJ, 648, 523

Watarai K.-y., Fukue J., Takeuchi M., Mineshige S., 2000, PASJ, 52, 133

Watarai K.-y., Mizuno T., Mineshige S., 2001, ApJ, 549, L77

Watson D., Christensen L., Knudsen K. K., Richard J., Gallazzi A., Michałowski M. J., 2015, Nature, 519, 327

Webb T. M., Eales S., Foucaud S., Lilly S. J., McCracken H., Adelberger K., Steidel C., Shapley A., Clements D. L., Dunne L., Le Fèvre O., Brodwin M., Gear W., 2003, ApJ, 582, 6

Weiß A. et al., 2013, ApJ, 767, 88

Weiß A., Kovács A., Coppin K., Greve T. R., Walter F., Smail I., Dunlop J. S., Knudsen K. K., Alexander D. M., Bertoldi F., Brandt W. N., Chapman S. C., Cox P., Dannerbauer H., De Breuck C., Gawiser E., Ivison R. J., Lutz D., Menten K. M., Koekemoer A. M., Kreysa E., Kurczynski P., Rix H.-W., Schinnerer E., van der Werf P. P., 2009, ApJ, 707, 1201

Weisz D. R., Johnson B. D., Conroy C., 2014, ApJ, 794, L3

Werner M. W., Roellig T. L., Low F. J., Rieke G. H., Rieke M., Hoffmann W. F., Young E., Houck J. R., Brandl B., Fazio G. G., Hora J. L., Gehrz R. D., Helou G., Soifer B. T., Stauffer J., Keene J., Eisenhardt P., Gallagher D., Gautier T. N., Irace W., Lawrence C. R., Simmons L., Van Cleve J. E., Jura M., Wright E. L., Cruikshank D. P., 2004, ApJS, 154, 1

Whitaker K. E., Franx M., Leja J., van Dokkum P. G., Henry A., Skelton R. E., Fumagalli M., Momcheva I. G., Brammer G. B., Labbé I., Nelson E. J., Rigby J. R., 2014, ApJ, 795, 104

White M., Martini P., Cohn J. D., 2008, MNRAS, 390, 1179

White M., Myers A. D., Ross N. P., Schlegel D. J., Hennawi J. F., Shen Y., McGreer I., Strauss M. A., Bolton A. S., Bovy J., Fan X., Miralda-Escude J., Palanque-Delabrouille N., Paris I., Petitjean P., Schneider D. P., Viel M., Weinberg D. H., Yeche C., Zehavi I., Pan K., Snedden S., Bizyaev D., Brewington H., Brinkmann J., Malanushenko V., Malanushenko E., Oravetz D., Simmons A., Sheldon A., Weaver B. A., 2012, MNRAS, 424, 933

White S. D. M., Rees M. J., 1978, MNRAS, 183, 341

Wilkins D. R., Gallo L. C., 2015, MNRAS, 448, 703

Wilkins S. M., Trentham N., Hopkins A. M., 2008, MNRAS, 385, 687

Williams O. R., Turner M. J. L., Stewart G. C., Saxton R. D., Ohashi T., Makishima K., Kii T., Inoue H., Makino F., Hayashida K., Koyama K., 1992, ApJ, 389, 157

Willott C. J., 2011, ApJ, 742, L8

Willott C. J., Albert L., Arzoumanian D., Bergeron J., Crampton D., Delorme P., Hutchings J. B., Omont A., Reylé C., Schade D., 2010a, AJ, 140, 546

Willott C. J., Bergeron J., Omont A., 2015, ApJ, 801, 123

Willott C. J., Delfosse X., Forveille T., Delorme P., Gwyn S. D. J., 2005, ApJ, 633, 630

Willott C. J., Delorme P., Omont A., Bergeron J., Delfosse X., Forveille T., Albert L., Reylé C., Hill G. J., Gully-Santiago M., Vinten P., Crampton D., Hutchings J. B., Schade D., Simard L., Sawicki M., Beelen A., Cox P., 2007, AJ, 134, 2435

Willott C. J., Delorme P., Reylé C., Albert L., Bergeron J., Crampton D., Delfosse X., Forveille T., Hutchings J. B., McLure R. J., Omont A., Schade D., 2010b, AJ, 139, 906

Willott C. J., Omont A., Bergeron J., 2013, ApJ, 770, 13

Worthey G., 1994, ApJS, 95, 107

Wright E. L., Eisenhardt P. R. M., Mainzer A. K., Ressler M. E., Cutri R. M., Jarrett T., Kirkpatrick J. D., Padgett D., McMillan R. S., Skrutskie M., Stanford S. A., Cohen M., Walker R. G., Mather J. C., Leisawitz D., Gautier, III T. N., McLean I., Benford D., Lonsdale C. J., Blain A., Mendez B., Irace W. R., Duval V., Liu F., Royer D., Heinrichsen I., Howard J., Shannon M., Kendall M., Walsh A. L., Larsen M., Cardon J. G., Schick S., Schwalm M., Abid M., Fabinsky B., Naes L., Tsai C.-W., 2010, AJ, 140, 1868

Wu S., Lu Y., Zhang F., Lu Y., 2013, MNRAS, 436, 3271

Wu X.-B., Wang F., Fan X., Yi W., Zuo W., Bian F., Jiang L., McGreer I. D., Wang R., Yang J., Yang Q., Thompson D., Beletsky Y., 2015, Nature, 518, 512

Wu X.-B., Wang R., Kong M. Z., Liu F. K., Han J. L., 2004, A&A, 424, 793

Wyder T. K., Treyer M. A., Milliard B., Schiminovich D., Arnouts S., Budavári T., Barlow T. A., Bianchi L., Byun Y.-I., Donas J., Forster K., Friedman P. G., Heckman T. M., Jelinsky P. N., Lee Y.-W., Madore B. F., Malina R. F., Martin D. C., Morrissey P., Neff S. G., Rich R. M., Siegmund O. H. W., Small T., Szalay A. S., Welsh B. Y., 2005, ApJ, 619, L15

Wyithe J. S. B., Loeb A., 2002, ApJ, 581, 886

Wyithe J. S. B., Loeb A., 2003, ApJ, 595, 614

Wyithe J. S. B., Loeb A., 2009, MNRAS, 395, 1607

Xue Y. Q., Brandt W. N., Luo B., Rafferty D. A., Alexander D. M., Bauer F. E., Lehmer B. D., Schneider D. P., Silverman J. D., 2010, ApJ, 720, 368

Yu Q., Lu Y., 2004, ApJ, 602, 603

Yu Q., Lu Y., 2008, ApJ, 689, 732

Yu Q., Tremaine S., 2002, MNRAS, 335, 965

Yun M. S., Reddy N. A., Condon J. J., 2001, ApJ, 554, 803

Zamorani G., Henry J. P., Maccacaro T., Tananbaum H., Soltan A., Avni Y., Liebert J., Stocke J., Strittmatter P. A., Weymann R. J., Smith M. G., Condon J. J., 1981, ApJ, 245, 357

Zdziarski A. A., Poutanen J., Johnson W. N., 2000, ApJ, 542, 703

Zehavi I., Zheng Z., Weinberg D. H., Blanton M. R., Bahcall N. A., Berlind A. A., Brinkmann J., Frieman J. A., Gunn J. E., Lupton R. H., Nichol R. C., Percival W. J., Schneider D. P., Skibba R. A., Strauss M. A., Tegmark M., York D. G., 2011, ApJ, 736, 59

Zehavi I., Zheng Z., Weinberg D. H., Frieman J. A., Berlind A. A., Blanton M. R., Scoccimarro R., Sheth R. K., Strauss M. A., Kayo I., Suto Y., Fukugita M., Nakamura O., Bahcall N. A., Brinkmann J., Gunn J. E., Hennessy G. S., Ivezić Ž., Knapp G. R., Loveday J., Meiksin A., Schlegel D. J., Schneider D. P., Szapudi I., Tegmark M., Vogeley M. S., York D. G., SDSS Collaboration, 2005, ApJ, 630, 1

Zhao D. H., Mo H. J., Jing Y. P., Börner G., 2003, MNRAS, 339, 12

Zheng Z., Coil A. L., Zehavi I., 2007, ApJ, 667, 760

Zheng Z., Zehavi I., Eisenstein D. J., Weinberg D. H., Jing Y. P., 2009, ApJ, 707, 554

Zibetti S., Charlot S., Rix H.-W., 2009, MNRAS, 400, 1181

Zubovas K., King A., 2013, ApJ, 769, 51

Zubovas K., Nayakshin S., Sazonov S., Sunyaev R., 2013, MNRAS, 431, 793